UNIVERSITÉ D'ORLÉANS

ÉCOLE DOCTORALE Énergie - Matériaux - Sciences de la Terre et de l'Univers
INSTITUT DES SCIENCES DE LA TERRE D'ORLEANS

THÈSE présentée par :

Viktor GREDICAK

soutenue le : **4 juillet 2025**

pour obtenir le grade de : **Docteur de l'Université d'Orléans**

Discipline/ Spécialité : Sciences de l'Univers

Microfluidic Study of Mass Transfer at Fluid–Fluid Interfaces in Porous Media with Plasma-Induced Wettability Control and Raman Spectroscopy

Approche microfluidique du transfert de masse aux interfaces fluide–fluide dans les milieux poreux avec contrôle de mouillabilité par plasma et analyse par spectroscopie Raman

THÈSE dirigée par :

ROMAN Sophie	Maîtresse de conférences HDR, Université d'Orléans (ISTO)
SLODCZYK Aneta	Ingénieure de recherche HDR, CNRS (ISTO, CEMHTI)
DOUAT Claire	Maîtresse de conférences HDR, Université d'Orléans (GREMI)

RAPPORTEURS :

JIMENEZ-MARTINEZ Joaquin	Professeur adjoint, Eawag & ETH Zurich
MORENT Rino	Professeur, Université de Gand

JURY :

KOVACEVIC Eva	Université d'Orléans (GREMI), **Présidente du jury**
DOUAT Claire	Maîtresse de conférences HDR, Université d'Orléans (GREMI), invitée
JIMENEZ-MARTINEZ Joaquin	Professeur adjoint, Eawag & ETH Zurich, Rapporteur
MEHEUST Yves	Maître de conférences HDR, Université Rennes 1, examinateur
MORENT Rino	Professeur, Université de Gand, Rapporteur
ROUET Jean-Louis	Professeur, Université d'Orléans (ISTO), examinateur
ROMAN Sophie	Maîtresse de conférences HDR, Université d'Orléans (ISTO) invitée
SLODCZYK Aneta	Ingénieure de recherche HDR, CNRS (ISTO, CEMHTI), invitée

Acknowledgements

And so, the PhD journey in Orleans is completed. In a distant 2021, I arrived first time to France having accepted a 6-month internship where a goal was to investigate the influence of porous media on mass transfer behavior across fluid-fluid interfaces. I was warmly welcomed in ISTO by Sophie, Aneta and Cyprien who introduced me to geoscientific research. In the following months I started exploring microfluidics and Raman spectroscopy, being fueled by curiosity and excitement of observing new, interesting phenomena. During the internship I finished my master's degree for which I sincerely thank Cyprien for his guidance and patience in transferring knowledge of computer simulations. The internship then turned into PhD under supervision of Sophie, Aneta, Claire and Lionel, each contributing to my scientific development within their respective expertise. Together we started developing plasma technology, discussing results of two-phase microfluidic experiments and analyzing Raman signatures. This journey was marked with many scientific and practical challenges which were eventually successfully resolved. Besides scientific progress, I would also like to thank all my supervisors on their availability and frequent meetings, which gave me confidence in presenting my work at many conferences, and finally, defending the thesis with ease. Moreover, I wish to express my special gratitude to Sophie who has been very professional but also very human in her approach with me; always available and ready to help despite her super busy schedule and private struggles. Thus, I look up to You, Sophie, as my professional and personal role model.

I would also like to acknowledge tremendous practical and language support coming from my friend and officemate Nathan who also drove me to the hospital when I couldn't walk due to my back pain. A favor I will never forget. Moreover, Nathan and Walid have always been there to take a break with me, discuss our struggles and support each other to make the work easier but also to make conferences memorable and cheese tastings more proficient, among other things. In that direction, I would also like to mention Tibo, Carolina, Gabriel, Nathan, Gina and many others who made working hours more exciting by indulging in prank activities but also giving me company and motivation for before/after-work swimming sessions.

Friends that started this journey with me, from the first flat party, first trip together, first birthday BBQ, following with countless dinner and dance nights, outdoors activities and multitude of other memorable moments, they hold special place in my heart. Monica's first bloody dance, fascinating skills to create new words and delicious pistaccio carbonara; Claudio's sarcasm, life experience sharing and wonderful guidance in Rome; Fede Siciliana's cooking skills, elegance, work diligence and pressure resilience; Fede Blondy's amazing social skills to connect people and organize events; Hector's (travieso) outstanding (exotic) dance, singing and entertaining skills in addition to great hugs; Albo's impressive climbing skills, his mature and kind nature making him best French person I have ever met; and many other wonderful moments with Camille, sin Andrea, Marina, Tania, Diletta, Alessandra, Khashi, Julia, Mahdi, etc..

With most emphasis I want to thank Kristijan, Mateja, Fellipe and Elena.

Veliki, hvala ti na vrlo prijateljskom pristupu od samog početka kad sam došel u Orleans. Uvijek si bio primjer i uzor u akademskom smislu kroz svoju upornost, ambicioznost i komunikacijske vještine. Neizmjerno ti hvala na opuštenim razgovorima, podršci, savjetima i svim posjetama iz Engleske. Uvijek se prisjetim i svih naših sportskih aktivnosti, od penjanja prve godine, slackline-a, pétanque-a, kajakiranja, planinarenja, itd. Ne sumnjam da se danas družim s budućom velikom facom iz svijeta geologije!

Barica, suseda moja najdraža, ako je neko testirao koliko daleko idu dobrosusjedski odnosi kroz nebrojene hitne pozive tokom noći, onda sam to ja. A ti kao najbolja susjeda, uvijek si bila spremna za zvati popiere, hitnu, otvoriti svoju kućnu ljekarnu i naći ključ rješenja za sve francuske administrativne probleme. U najmanju ruku bili su tu nedjeljni ručkovi sa nepresušnim tekućim pitanjima svih vrsta, ali uvijek vrhunske kvalitete. Uz to kakva šetnja na svježem zraku da ohladimo glavu ili kakav dubokoumni razgovor da ju zagrijemo temama o prošlosti, sadašnjosti ili budućnosti, na osobnoj ili globalnoj sceni. Bara je suseda za navek!

Oi Fellipe, muito obrigado per me insegniare questa lingua italo-braziliana che io parlo e tu non ascuta 😉. Hai mi mostrato un nuovo punto di vista sulla vita, una cultura diversa. Le tue abilita culinarie sono incomparabili e hanno migliorato mie giornate tante volte. Sono grato per tutti i viaggi insieme per conoscere il mundo, massaggi a mi schiena malata e tuo sorriso bello e altri tipi di supporte durante il mio dottorato. Grande baccio pra voce!

And finally, Elena, a magmatic chamber, my faithful friend, climbing and dance partner, teatime therapist and a hug maniac just like me. To this day I recall your uncontained happiness when I got accepted for a PhD, the reaction that actually gave me motivation to go for it. From then on, we shared countless moments, big and small. Countless closed office conversations (even when Kiki interrupted the moment), innumerable hugs, scratches and massages, plenty of “I miss you” messages, and all other close moments that intrigued others. There are number of highlights, well documented in our pictures portraying the emotion only we can recall in our hearts. One such memory is a night walk in Salamanca resulting in completely unexpected and unique wedding experience with you. I’m so happy to have met you and I can confidently say that I’ve found a friend for life, despite our differences on the topic of glitter.

In the memory of us all, there stands a grafted cherry tree named Victoria, planted in spring of 2024 in honor of us all being once in Orleans, being friends, successfully completing PhDs, thus showing resilience, courage, ability to learn, grow and adapt.

With one final note, I would like to thank all my friends from Croatia and elsewhere for believing in me and express my appreciation to all my family members on their support throughout my education, especially to my grandma who came to France for my defense despite being 90 years young.

Résumé étendu en francais

Cette thèse vise à apporter une meilleure compréhension des mécanismes de piégeage du CO_2 dans les réservoirs souterrains pour les procédés de stockage géologique du carbone. Pour cela nous avons développé une approche expérimentale à l'échelle des pores pour étudier les mécanismes de déplacement et d'interactions entre le CO_2 et l'eau en milieux poreux.

La thèse est structurée en 6 chapitres, chacun abordant une question scientifique clé.

Le premier **chapitre introductif (1)** présente les principes fondamentaux du stockage souterrain du CO_2, en soulignant l'importance des propriétés de mouillabilité des milieux dans les mécanismes de transfert d'espèces et de piégeage du CO_2. Dans ce chapitre, nous soulignons les limites des capacités prédictives actuelles qui viennent de la variabilité des données et de la rareté des ensembles de données complets. Nous soulevons la nécessité d'études expérimentales à l'échelle du pore, ce qui constitue la principale motivation de cette thèse.

Plus précisément, comprendre les relations entre les propriétés de mouillabilité, et les comportements fluide-fluide, fluide-solide est essentielle pour une bonne prédiction du processus de stockage géologique du CO_2. Pour y parvenir, nous donnons une définition des propriétés de mouillabilité, nous identifions les paramètres qui l'influencent et comment quantifier leurs effets. Au cours des dernières décennies, des efforts considérables ont été déployés pour caractériser la mouillabilité des minéraux de subsurface dans les systèmes CO_2-saumure. Les données disponibles indiquent que la plupart des minéraux et des roches de subsurface présentent un comportement mouillant vis à vis de l''eau, avec quelques exceptions présentant des caractéristiques de mouillabilité intermédiaire. Cependant, la variabilité substantielle des données rapportées suggère que la mouillabilité est influencée par de multiples facteurs, ce qui nécessite des recherches supplémentaires pour réduire les incertitudes expérimentales et améliorer notre compréhension de son rôle dans les mécanismes de piégeage du CO_2, en particulier le piégeage capillaire et le piégeage par solubilité.

Si la solubilité du CO_2 dans l'eau ou la saumure dans des conditions thermodynamiques d'équilibre est bien comprise, la cinétique du transfert de masse dans des environnements influencés par la mouillabilité reste moins étudiée. Il existe notamment une boucle de rétroaction dans laquelle la mouillabilité affecte la dissolution du CO_2, tandis que le CO_2 dissous peut, à son tour, modifier la mouillabilité des minéraux. En outre, l'interaction entre les différents mécanismes de piégeage et les complexités inhérentes aux échelles spatiales et temporelles dans les milieux poreux naturels rendent compliquées les capacités de prédiction pour la modélisation du stockage du CO_2. Les implications de la mouillabilité pour le stockage du CO_2 sont importantes, car elle influence directement la capacité d'étanchéité des roches, détermine le potentiel de stockage et régit la distribution du CO_2 stocké entre les différents mécanismes de piégeage. En outre, la mouillabilité joue un rôle essentiel dans l'optimisation des stratégies d'injection et dans la garantie de la sécurité

du confinement à long terme. Pour améliorer la fiabilité des simulations numériques à grande échelle, des études fondamentales à l'échelle du pore, à la fois expérimentales et numériques, doivent être intégrées afin d'incorporer avec précision des paramètres physicochimiques clés tels que la mouillabilité. Les techniques expérimentales telles que la microfluidique offrent un outil puissant pour relever ces défis en isolant des effets spécifiques qui sont difficiles à distinguer dans les études à l'échelle du réservoir et qui ne sont pas pris en compte dans les simulations. Nous terminons ce chapitre en annonçant les objectifs de la thèse qui sont (i) évaluer si le plasma peut être propagé et utilisé pour le traitement de surface *in situ* des dispositifs microfluidiques en verre, (ii) déterminer comment la mouillabilité influence le piégeage capillaire et le transfert de masse interfacial à l'échelle des pores, et (iii) suivre le processus de transfert de masse interfacial fluide-fluide en suivant l'évolution des espèces chimiques à l'aide de la spectroscopie Raman.

Le **chapitre (2)** détaille le dispositif expérimental général, les techniques de mesure communes et les outils utilisés tout au long de la thèse, détaillant en particulier la conception de dispositifs microfluidiques. Comme son nom l'indique, la microfluidique est la technologie qui permet de manipuler de petits volumes de fluides dans un espace confiné de dimensions micrométriques. Par rapport aux études sur des échantillons naturels centrimétiques, les dispositifs microfluidiques offrent plusieurs avantages clés, notamment l'observation visuelle en temps réel des processus dynamiques et la compatibilité avec diverses techniques d'analyse *in situ*.

Parmi les différentes géométries que nous avons conçues pour imiter les milieux poreux de la roche, cette étude se concentre sur deux géométries distinctes : la géométrie à poche unique et la géométrie à pores en L. Ces deux géométries contiennent un microcanal rectangulaire de 4 cm de long et de profondeur uniforme de 100 µm. Un motif géométrique est conçu pour piéger un fluide alors qu'un autre s'écoule dans le canal. La poche unique est une géométrie carrée avec une longueur de côté de 500 µm. Comme son nom l'indique, la géométrie à pores en L est attachée au microcanal principal, formant une forme de L. La réalisation d'expériences sur plusieurs géométries nous permet d'analyser l'effet d'une complexité géométrique croissante et d'évaluer l'influence directe de la mouillabilité sur les résultats expérimentaux.

Dans le **chapitre (3)**, nous nous sommes concentrés sur le développement d'une nouvelle méthode de modification de la mouillabilité. Notre principale question scientifique était de savoir si un plasma pouvait être propagé et utilisé pour le traitement *in situ* de la mouillabilité de dispositifs microfluidiques en verre fermés.

Sur la base de l'analyse de la littérature, nous avons justifié l'utilisation du plasma à pression atmosphérique en tant qu'outil prometteur pour la modification de la mouillabilité et nous avons mis au point un dispositif adapté aux dispositifs microfluidiques en verre fermés. Nous avons choisi un plasma à pression atmosphérique d'hélium kHz dans une configuration de type DBD en raison de sa capacité à pénétrer et à se propager dans les microcanaux, de sa nature froide et non thermique et de la chimie réactive du plasma, qui permet de modifier la surface *in situ* tout en préservant le matériau.

Nous avons démontré que notre installation produit effectivement un plasma froid (< 100° C) d'une puissance de plusieurs centaines de mW qui se propage avec succès dans des microcanaux de 4 cm de long et de largeur variable. L'analyse de la propagation du plasma indique que la configuration des électrodes joue un rôle majeur dans la manipulation de la propagation du plasma, en particulier sur les modèles géométriques plus complexes. Une analyse des espèces du plasma par spectrométrie à émission optique (OES) indique une chimie du plasma riche allant bien au-delà de l'hélium, qui est le gaz dominant.

La section centrale de ce chapitre se concentre sur les performances en matière de mouillabilité. Pour cela l'angle de contact entre l'eau et le CO_2 est mesuré l'intérieur de nos canaux, avant et après traitement plasma. Nous avons obtenu un traitement de surface rapide en une minute environ, les performances de vieillissement dépendant du milieu de stockage. Les dispositifs stockés dans l'air ont présenté une stabilité de l'angle de contact la plus faible d'une durée de un jour, qui s'est prolongée jusqu'à environ trois jours lorsqu'ils ont été stockés dans l'eau. Les dispositifs microfluidiques stockés dans l'air ont retrouvé leur état initial de mouillabilité. Les micromodèles stockés dans l'eau garde un état hydrophile pendant plusieurs semaines. Le retraitement a montré des résultats de mouillabilité reproductifs, soulignant la possibilité de réutiliser des dispositifs microfluidiques en verre conçus avec précision et difficiles à fabriquer, ce qui est avantageux compte tenu de leur coût de production élevé.

Des analyses OES et des analyses de spectroscopie Raman ont permis de mieux comprendre les mécanismes sous-jacents à l'altération de la mouillabilité. Des recherches plus approfondies à l'aide de la méthode XPS (Spectrométrie photoélectronique X) ont attribué les changements de mouillabilité au nettoyage et à la fonctionnalisation des surfaces du verre. Le traitement au plasma réduit la contamination de la surface par le carbone en exposant la couche de verre naturellement hydrophile et en attachant divers groupes fonctionnels hydrophiles (carboxyles, aminés, etc.), la stabilité de ces groupes dépend du milieu de stockage.

Ce traitement *in situ de* la mouillabilité facilite le traitement des dispositifs microfluidiques fermés couramment achetés auprès des fabricants, permettant le traitement de toutes les parois des microcanaux tout en minimisant la dégradation des propriétés de surface qui peut se produire pendant le collage. Dans l'ensemble, l'application du plasma à pression atmosphérique en tant que traitement *in situ* représente une méthode nouvelle et efficace pour modifier la mouillabilité, particulièrement adaptée aux systèmes microfluidiques fermés.

Avec une procédure établie pour contrôler la mouillabilité, nous avons étudié dans **le chapitre 4** la question centrale de cette thèse, à savoir l'influence de la mouillabilité sur le piégeage capillaire et le transfert de masse interfacial à l'échelle des pores.

Après une introduction sur les quelques données disponibles dans la littérature sur l'influence de la mouillabilité sur le piégeage résiduel et le piégeage capillaire, nous présentons nos procédures expérimentales. Les expériences ont été réalisées sur deux géométries microfluidiques mentionnées précédemment, en utilisant du CO_2 et de l'eau comme analogues des fluides injectés lors du

stockage de CO_2. Dans chaque géométrie, nous avons effectué des drainages et des imbibitions. Pendant le drainage, l'objectif était de piéger l'eau et d'étudier l'évaporation, tandis que pendant l'imbibition, nous avons cherché à immobiliser le CO_2 et à évaluer les processus de dissolution. Les résultats de chaque géométrie sont évalués sur deux conditions de mouillabilité distinctes sur la gamme des différences de pression imposées, simulant différentes conditions d'écoulement.

Avant les expériences principales, nous avons cherché à caractériser les écoulements dans nos géométries en monophasique et en diphasique à l'aide de la méthode de PIV (Vélocimétrie par Images de Particules). L'analyse des écoulements d'eau a révélé que l'apparition des premières recirculations se produit autour de 65 mbar (entre l'entrée et la sortie du canal). Dans cette plage de différence de pression, le nombre de Reynolds est resté inférieur à 20, tandis que le nombre capillaire correspondant pendant l'écoulement diphasique était d'environ 10^{-3}, ces deux valeurs sont typiques des conditions de stockage de CO_2. Pendant le drainage (CO_2 déplaçant l'eau), l'eau piégée montre un mouvement advectif entraîné par le transfert de quantité de mouvement à l'interface CO_2-eau. En outre, sur les surfaces traitées au plasma, le drainage était caractérisé par une forte présence et un fort écoulement de films. Ces deux observations se sont révélées cruciales pour l'interprétation du comportement du transfert de masse par la suite.

La suite de ce chapitre se consacre à la caractérisation de l'influence de la mouillabilité sur le piégeage capillaire, puis sur le transfert de masse aux interfaces.

Nous nous intéressons dans un premier temps au piégeage capillaire du CO_2 lors d'une imbibition. La bulle initiale de CO_2 piégée présente une large gamme de formes différentes influencées par la géométrie des pores et la mouillabilité. À des angles de contact faibles, l'interface de la bulle reste plus arrondie et courbée, principalement guidée par la tension interfaciale plutôt que par la géométrie de l'élément de piégeage. Dans la géométrie à poche unique, la bulle reste constamment en contact avec la surface solide, tandis que dans la géométrie à pores en L dans des conditions superhydrophiles (0°), la bulle n'entre pas en contact avec les surfaces en verre.

La mouillabilité ne semble pas affecter de manière significative la taille initiale des bulles dans la géométrie à poche unique. De même, la taille initiale des bulles dans la géométrie à pores en L ne dépend pas de la mouillabilité ou de l'anisotropie de l'écoulement. Toutefois, dans la géométrie à pores en L, les bulles de CO_2 ne restent pas piégées pour des conditions superhydrophiles (0°) lorsque la différence de pression imposée dépasse 35 mbar. Nos résultats suggèrent que l'effet combiné de l'anisotropie de l'écoulement et de la mouillabilité peut influencer le potentiel de piégeage capillaire du CO_2.

Lors d'un drainage, c'est l'eau qui se retrouve immobilisée dans l'élément de piégeage. En raison de la nature hydrophile des surfaces en verre, d'importants volumes d'eau restent piégés après le déplacement initial par le CO_2. Ces volumes piégés sont présents sous forme de films d'eau, de gouttelettes et de films de coins le long des microcanaux, en plus du volume principal à l'intérieur de l'élément de piégeage.

Lorsque l'on évalue la quantité d'eau initialement piégée dans la géométrie à poche unique, des volumes significativement plus importants sont retenus pour un angle de contact de 23° par rapport à 53°. De manière surprenante, dans la géométrie à pores en L, les surfaces modérément mouillantes (angle de contact de 59°) retiennent en moyenne plus d'eau que les surfaces superhydrophiles (0°). Bien que l'influence exacte de la mouillabilité ne soit pas claire, son effet est évident, ce qui suggère qu'un facteur supplémentaire peut contribuer au comportement de piégeage observé. En outre, aucune différence significative dans le piégeage de l'eau n'a été observée dans la géométrie des pores L lors de la modification de la direction de l'écoulement.

Finalement, si l'on considère les deux géométries et les deux fluides, les effets de la mouillabilité sont les plus prononcés dans le piégeage capillaire de l'eau pendant le drainage, alors qu'ils semblent négligeables pour le piégeage du CO_2. Cette différence s'explique probablement par le fait que toutes les surfaces testées étaient hydrophiles, assurant un contact constant avec l'eau, alors que le CO_2, en tant que phase non mouillante, reste largement insensible aux variations de la mouillabilité des solides.

En comparant les volumes piégés des différents fluides dans la même géométrie, la géométrie à poche unique retient plus d'eau que de CO_2, alors que dans la géométrie à pores en L, aucune différence significative n'est observée entre les deux fluides. Alors que les milieux hydrophiles devraient favoriser une plus grande rétention d'eau, la complexité géométrique accrue de nos milieux semble atténuer cet effet, ce qui se traduit par un comportement de piégeage comparable pour les deux fluides dans la géométrie à pores en L.

En testant à la fois le piégeage résiduel de l'eau et du CO_2 pour des géométries simples et en conditions contrôlées, nous montrons pour la première fois que la mouillabilité régit fortement la rétention de l'eau mais pas le piégeage du CO_2 - un résultat rendu possible par l'élimination de l'hétérogénéité de la géométrie, contrairement à la plupart des expériences multi-pores antérieures.

Dans un second temps, nous nous sommes intéressés au tranferts de masse aux interfaces fluide-fluide et à l'impact de la mouillabilité. Tout d'abord, lors du piégeage du CO_2 dans la géométrie à poche unique, la dissolution du CO_2 dans l'eau présente deux phases distinctes : une période initiale de dissolution rapide dominée par l'advection et une phase ultérieure plus lente contrôlée par la diffusion. Alors que la mouillabilité n'influence pas de manière significative la phase de dissolution rapide, la phase lente et les valeurs du coefficient de transfert de masse montrent une tendance claire, avec des taux de dissolution plus élevés observés à un angle de contact plus faible (23°). Les taux de transfert de masse moyens sont de l'ordre de quelques μm/s, ce qui correspond bien aux résultats d'études antérieures. Une comparaison des formulations de transfert de masse avec et sans normalisation à l'aire interfaciale révèle que la mouillabilité influence la dissolution non seulement en augmentant l'aire interfaciale, mais aussi en modifiant la courbure interfaciale, ce qui modifie la pression capillaire.

Par ailleurs, une expérience statique, pour laquelle une bulle de CO_2 est piégée dans le pore et l'eau dans le canal ne s'écoule pas, a démontré que la dissolution du CO_2 dans de telles conditions

prendrait des mois, alors qu'en conditions d'écoulement la dissolution totale de la bulle prend 100 to 250 sec. Cela souligne l'importance d'assurer le confinement du CO_2 au cours de la période initiale par des mécanismes de piégeage physique, tels que le piégeage structurel et capillaire, avant que des mécanismes chimiques tels que la dissolution et la minéralisation ne puissent assurer la sécurité du stockage à long terme.

Dans le cas de la géométrie à pores en L, nous avons rencontré une grande variabilité des résultats due au déplacement des bulles initialement piégées ou lors de la dissolution. Cela met en évidence l'instabilité potentielle du piégeage capillaire, mais limite également la robustesse statistique de nos données de transfert de masse. En outre, la croissance des bulles de CO_2 a été observée sur des surfaces à mouillabilité intermédiaire, ce qui suggère un processus d'exsolution plutôt que de dissolution.

Malgré la diversité des données expérimentales et l'impact significatif de la mouillabilité, de la géométrie de l'élément de piégeage et de son anisotropie sur les mécanismes de dissolution, les périodes caractéristiques de dissolution rapide et lente restent distinctes. Comme dans le cas de la géométrie à poche unique, la phase initiale de dissolution rapide ne dépend pas de la mouillabilité, alors que la phase lente et les taux de transfert de masse globaux présentent une tendance claire en faveur d'une dissolution plus rapide à des angles de contact plus faibles (0°). Sur les surfaces modérément hydrophiles (59°), les taux de dissolution globaux sont de l'ordre de 10^{-1} μm/s, tandis que sur les surfaces superhydrophiles (0°), les taux varient entre 10^0 et 10^1 μm/s. La direction de l'écoulement ne semble pas affecter les taux de transfert de masse globaux.

Lorsque l'eau est piégée dans la géométrie à pore unique, celle-ci s'évapore dans le CO_2. L'évaporation de l'eau pendant le drainage suit un comportement biphasé, composé d'une période humide et d'une période sèche. Pendant la période humide, d'importants volumes d'eau sous forme de films, de petites gouttelettes et de films de coins restent sur les surfaces des microcanaux. Pendant la période sèche, seul le volume principal des gouttelettes à l'intérieur de l'élément de piégeage persiste. Les conditions de mouillabilité ont un impact important sur l'évaporation en modifiant le type et la quantité des volumes d'eau pendant la période humide. Sur les surfaces à angle de contact de 53°, une pente plus forte est observée pendant la période sèche, indiquant que les taux d'évaporation sont plus élevés lorsque le flux de CO_2 n'est pas saturé en vapeur d'eau. Contrairement aux volumes d'eau immobilisés sur les surfaces à 53°, les volumes d'eau sur les surfaces à angle de contact de 23° se déplacent, entrant et sortant de l'élément de piégeage de façon imprévisible, créant de multiples tendances non linéaires au cours de la période humide.

Par conséquent, les données expérimentales des taux de transfert de masse sur des surfaces d'angle de contact de 53° montrent moins de dispersion, avec une tendance claire à l'augmentation du transfert de masse global avec de la différence de pression appliquée entre l'entrée et la sortie du canal. À des différences de pression appliquées plus faibles, les deux conditions de mouillabilité présentent des taux d'évaporation globaux similaires. Cependant, lorsque les différences de pression augmentent, les taux d'évaporation divergent, favorisant la surface à angle de contact plus

faible (23°). Les taux d'évaporation globaux sont de l'ordre de 10^{-1} µm/s, ce qui est un ordre de grandeur inférieur aux taux de dissolution du CO_2.

Nos résultats comblent un manque de données expérimentales sur l'évaporation de l'eau dans le CO_2 en conditions contrôlées. Ces données pourront servir à la comparaison aux modèles numériques en développements. De plus, nos mesures rapportent des taux d'évaporation globaux de l'ordre de 10^{-1} µm/s, offrant de nouveaux repères expérimentaux pour les futurs efforts de modélisation dans le contexte du stockage géologique du CO_2.

Le comportement d'évaporation dans la géométrie à pores en L est plus difficile à analyser car nous observons un drainage progressif mais rapide de l'eau de l'élément de piégeage par les films aux parois et aux coins des canaux. Le drainage presque complet de la gouttelette piégée se produit en 15 secondes environ sur les surfaces à angle de contact de 59° et en 6 secondes seulement sur les surfaces à 0°, ce qui correspond à des taux de vidange élevés de l'ordre de 10^5 µm^2/s. Ainsi, le drainage est un processus prévalent par rapport au transfert de masse interfacial que nous attribuons à la présence de rugosité aux parois des canaux qui favorise l'écoulement par les films. Par conséquent, la comparaison directe entre les taux d'évaporation des deux géométries, ainsi que la comparaison entre les taux de dissolution et d'évaporation sur cette géométrie n'est pas pertinente.

Dans l'ensemble, cette recherche révèle que la mouillabilité, la géométrie des pores et les différences de pression appliquées influencent la complexité du comportement du transfert de masse aux interfaces. Malgré des variations dans les mécanismes, un comportement à deux périodes est observé pour toutes nos configurations. La mouillabilité devient un facteur ominant pour une des périodes avec des mécanismes sous-jacents différents. Lors de l'imbibition et la dissolution du CO_2, la mouillabilité influence le transfert de masse pendant la période dominée par un régime diffusif. Au cours du drainage et de l'évaporation de l'eau, la mouillabilité joue un rôle plus critique dans la période humide initiale, où les surfaces hydrophiles favorisent la formation et l'advection de films d'eau et de volumes de coin.

Dans l'ensemble, le transfert de masse, que ce soit par dissolution ou par évaporation, tend à être plus efficace dans des conditions hydrophiles. Cette amélioration est due à de multiples mécanismes, notamment l'augmentation de la surface interfaciale, l'augmentation de la pression capillaire due à une plus grande courbure interfaciale et la présence de films et de volumes de coins, qui non seulement étendent la surface interfaciale disponible mais régulent également le volume piégé par une dynamique directe.

Les résultats de cette étude ont des implications significatives pour la réduction des incertitudes et l'amélioration des modèles de prévision liés au stockage géologique du CO_2 dans les aquifères salins. En particulier, l'influence observée de la mouillabilité sur le piégeage par capillarité et par solubilité souligne la nécessité d'incorporer les effets de la mouillabilité dans les modèles prédictifs, surtout si l'on considère que ces effets deviennent dominants au cours des étapes ultérieures dans des conditions contrôlées par la diffusion. En élucidant les mécanismes fondamentaux de transfert de masse basés sur les premiers principes de la physique dans le contexte du stockage du CO_2, ces

connaissances peuvent également être étendues à une large gamme de systèmes biphasés dans des environnements poreux.

Alors que dans le chapitre 4 l'analyse du transfert de masse aux interfaces est faite à partir de données optiques de visualisation directe, le **chapitre** suivant **(5)** s'intéresse au développement d'une méthode pour suivre les espèces dissoutes et leur répartition lors de la dissolution. Pour cela nous évaluons la faisabilité de mesures de spectroscopie Raman *in situ*. Comme dans les chapitres précédents, nous commençons par présenter un état des lieux du processus de dissolution du CO_2 et de l'application de la spectroscopie Raman à la microfluidique. Sur la base d'un examen de l'état actuel des connaissances, nous avons justifié l'utilisation de la spectroscopie Raman, en particulier sa capacité à détecter les espèces chimiques gazeuses et dissoutes. Notre objectif était non seulement de valider la faisabilité des mesures dans les environnements microfluidiques, mais aussi de développer un dispositif expérimental optimisé capable de capturer des signatures chimiques clés dans des conditions dynamiques à basse pression. Pour atteindre cet objectif, nous avons conçu une procédure adaptée aux dispositifs microfluidiques en verre, en tenant compte des défis spécifiques rencontrés lors de l'acquisition du signal. Une attention particulière a été accordée à la suppression des effets de fluorescence, qui apparaissent au-dessus de 2000 cm^{-1} et interfèrent avec le signal d'étirement OH de l'eau. Heureusement, le principal signal du CO_2, la résonance de Fermi, apparaît dans une région faiblement affectée par la fluorescence, ce qui nous a permis de nous concentrer sur le comportement du CO_2 à la fois en phase gazeuse et en solution.

Pour le CO_2 gazeux, une échelle linéaire de l'intensité du pic d'une résonance de Fermi avec la pression a été observée, ce qui est cohérent avec les études précédentes et confirme la sensibilité des spectres Raman aux variations de pression. Lors de la dissolution du CO_2 dans l'eau, les pics de la résonance de Fermi se sont élargis et déplacés vers des nombres d'ondes plus faibles, ce qui est cohérent avec les résultats de la littérature. Le but ultime était de suivre la cinétique de la réaction *in situ* en surveillant l'évolution des espèces chimiques pendant la dissolution du CO_2 dans des conditions de drainage dynamique. Le mode drainage a été préféré à l'imbibition en raison de son mouvement interfacial plus lent, ce qui a permis des temps d'acquisition plus longs et donc un meilleur rapport signal sur bruit à basse pression (< 1 bar). Il s'agit là d'une différence significative par rapport à la plupart des études de la littérature, qui opèrent généralement sous une pression plus élevée et bénéficient donc de signaux Raman plus forts. Malgré ces conditions moins favorables, des intensités de signal relativement stables ont été obtenues sur la géométrie à poche unique, ce qui suggère une dissolution rapide et un quasi-équilibre entre les phases CO_2 et eau pendant le temps d'acquisition. Des variations mineures de l'intensité Raman ont été observées entre les différents états de mouillabilité et les gradients de pression, mais elles n'étaient pas suffisamment significatives pour modifier la tendance générale ou l'interprétation du signal. Cependant, nous avons pu observer qualitativement l'influence des différents états de mouillabilité et des gradients de pression imposés au moment où l'interface gaz-liquide a traversé le spot laser (positionné à 100 µm de la paroi la plus éloignée de la géométrie), marqué par un changement distinct du signal Raman de $CO_{2(aq)}$ à $CO_{2(g)}$. La complexité géométrique accrue des dispositifs à pores en L a entraîné

une évolution plus progressive de l'intensité du signal Raman au fil du temps, probablement en raison de la plus grande distance du spot laser par rapport à l'interface gaz-liquide.

Ces résultats confirment que la spectroscopie Raman permet de suivre qualitativement et semi-quantitativement l'évolution chimique pendant le transfert de masse dans des géométries confinées, même dans des conditions de basse pression. Toutefois, l'interprétation quantitative complète reste limitée par l'absence de corrélation directe entre le signal Raman et la concentration réelle des espèces dissoutes. Les travaux futurs viseront à remédier à cette limitation par un étalonnage par rapport à des normes connues ou à des modèles thermodynamiques. En outre, les améliorations apportées au système, telles que l'incorporation de lasers avec d'autres longueurs d'onde pour atténuer la fluorescence, l'utilisation de détecteurs plus rapides pour capturer la dynamique transitoire et la mise en œuvre de techniques de cartographie spatiale, devraient permettre d'élargir l'applicabilité de la méthode. Des systèmes réagissant plus lentement, tels que le méthane et l'eau, pourraient également être étudiés afin de sonder davantage la cinétique du transfert de masse de manière plus contrôlée et d'étendre la recherche à d'autres paires de fluides.

Ensemble, ces améliorations ouvriront la voie à une analyse Raman robuste, résolue dans l'espace et quantitative des processus interfaciaux en microfluidique.

Enfin, le dernier **chapitre (6)** avait pour objectif de résumer notre travail, de mettre en évidence les principales conclusions et d'esquisser les perspectives de recherche future. Ainsi, avec notre approche expérimentale multidisciplinaire à l'échelle du pore, déployant la microfluidique, le plasma et la spectroscopie Raman, nous démontrons l'importance de la mouillabilité sur le stockage géologique du CO_2 principalement en évaluant le piégeage capillaire et le piégeage par solubilité. Nous soulignons l'importance des données expérimentales à l'échelle du pore pour évaluer la cinétique et les principes fondamentaux du transfert de masse influencé par la mouillabilité afin de développer, valider et/ou calibrer des modèles à l'échelle du pore, puis d'extrapoler ces modèles et d'améliorer les capacités prédictives des simulations à l'échelle des réservoirs.

Abstract

This PhD thesis is part of the INTER-AQ project within CNRS, an interdisciplinary research initiative aiming to unravel the complex and coupled dynamics of mass transfer and fluid redistribution at fluid-fluid interfaces within porous media. The project combines experimental microfluidics to replicate subsurface environments, vibrational spectroscopy for *in situ* chemical quantification, and novel plasma-based techniques to tailor pore surface properties. These integrated approaches target key environmental and energy challenges, such as geological CO_2 storage. Within this framework, the PhD research contributes to a pore-scale perspective, advancing experimental methods to investigate how interfacial phenomena influence fluid behavior in porous systems.

The objective of this thesis is to address a fundamental gap in our understanding of mass transfer at the pore scale, specifically how wettability affects fluid/fluid interfacial mass transfer processes and fluid trapping in geological porous media. The research focuses on the development of an experimental platform that integrates microfluidics and μRaman spectroscopy to track CO_2-water interfacial mass transfer in real time. Microfluidic devices are transparent pore networks made of channels of rectangular cross-sections, mimicking subsurface porous environments and allowing direct visualization of fluid behaviors. Crucially, the study introduces *in situ* atmospheric pressure plasma treatment as a new tool for modifying wettability within closed glass microfluidic devices. This allows precise control over surface characteristics, enabling systematic investigation of wettability impacts on interfacial dynamics. The insights of wettability influenced interfacial mass transfer gained in this study are expected to improve the calibration of both pore- and field-scale models, increasing the accuracy of predictions for carbon storage in geological reservoirs.

Three core research questions structure the investigation. First, the feasibility of propagating atmospheric plasma within closed microfluidic channels is explored to determine whether *in situ* wettability tuning is technically viable. The work demonstrates that plasma jets can be successfully introduced and controlled within the devices, enabling reliable alteration of surface wettability. Results obtained by *in situ* contact angle measurement on images indicate uniform wettability treatment with increased hydrophilic properties after only 1 min of plasma treatment. The wettability achieved on glass with our setup offers stability for up to 70 days, depending on the plasma treatment and storage parameters. Second, the study examines how wettability conditions affect capillary trapping and interfacial mass transfer. By employing microfluidic devices with increasing geometrical complexity, the experiments reveal how surface wettability indeed influences fluid displacement/ retention, water evaporation and CO_2 dissolution under a range of flow conditions. Our results demonstrate the influence of wettability on fluid-fluid displacement and mass transfer processes. Third, the potential of μRaman spectroscopy for *in situ*, semi-quantitative analysis of CO_2 dissolution is assessed. Raman analysis is able to capture the temporal evolution of dissolved species, providing complementary chemical data to visual flow observations and enabling the quantification of interfacial mass transfer rates.

In summary, this research establishes an integrated atmospheric-plasma-microfluidic-μRaman experimental framework that allows for the systematic study of pore-scale interfacial mass transfer under controlled wettability conditions. By leveraging plasma technology for surface modification and spectroscopic techniques for chemical analysis on microfluidic devices, the thesis delivers new insights into the mechanisms that govern CO_2 trapping in porous media and that are critical for the design and optimization of carbon sequestration strategies.

Table of Contents

Chapter 1 - The role of wettability for underground carbon storage

In this chapter, we introduce the principles and challenges of carbon capture, utilization and storage (CCUS), with a focus on underground carbon storage. We point out the importance of experimental pore-scale investigations and thus introduce microfluidics as a technique suitable for such research. Then we describe wettability characterization, measurements and its role for carbon storage, with an emphasis on capillary and solubility trapping. Finally, we outline the objectives and the scope of the thesis.

I. Carbon storage in geological formations

Understanding the mechanisms of carbon dioxide (CO_2) storage (Iglauer *et al.*, 2011; Ringrose, 2020; Sifuentes *et al.*, 2009; Taheri *et al.*, 2012) in geological porous media, as a part of the carbon capture, utilization and storage (CCUS) framework (IEA, 2021a; IPCC, 2005) (see Figure 1), is becoming increasingly important to combat accelerating climate changes (IEA, 2021b). The principle of CO_2 storage is injecting CO_2 in supercritical conditions ($scCO_2$ - above the critical temperature of 31 °C, and critical pressure 7.4 MPa) through drilled wells into the geological reservoir. The reason for supercritical injection is due to increased density and relatively low viscosity, which favors storage capacity. Once injected, supercritical CO_2 displaces the fluid in the porous system and interacts with its environment (pore fluid and rock matrix). Injection of CO_2 into geological formations initiates a multicomponent, multiphase flow system under highly non-equilibrium conditions.

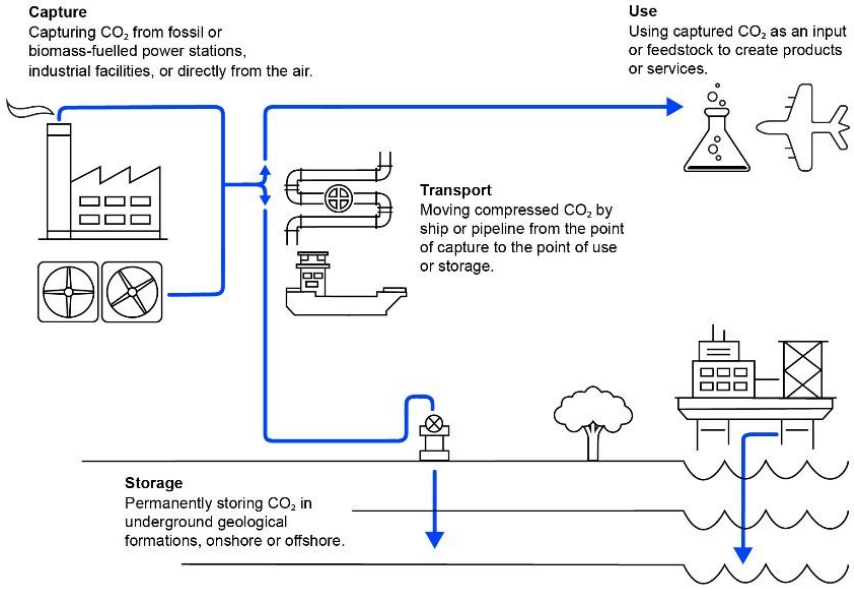

Figure 1 CCUS schematics. Taken from IEA (2021a).

Numerous geological structures and reservoirs have been considered for storage. Injection into the oil wells is already common under the terms enhanced oil recovery (EOR) or improved oil recovery (IOR). Brown natural gas reservoirs (Khan *et al.*, 2013), coal seams (Liu *et al*., 2019) and even gas hydrate depositions (Liu *et al.*, 2023) are also some of the explored options. Yet, saline aquifers are perceived as the best potential due to their abundance and largest identified storage capacity overall (Celia *et al.*, 2015; IPCC, 2005) (Figure 2). Aquifers are geological formations that store water within the pores and fractures of the rock. Also, the water found in these geological reservoirs at great depths is usually salty and it is referred to as brine. Besides geological storage, the marine environment offers enormous storage capacity, however it is beyond the scope of this thesis.

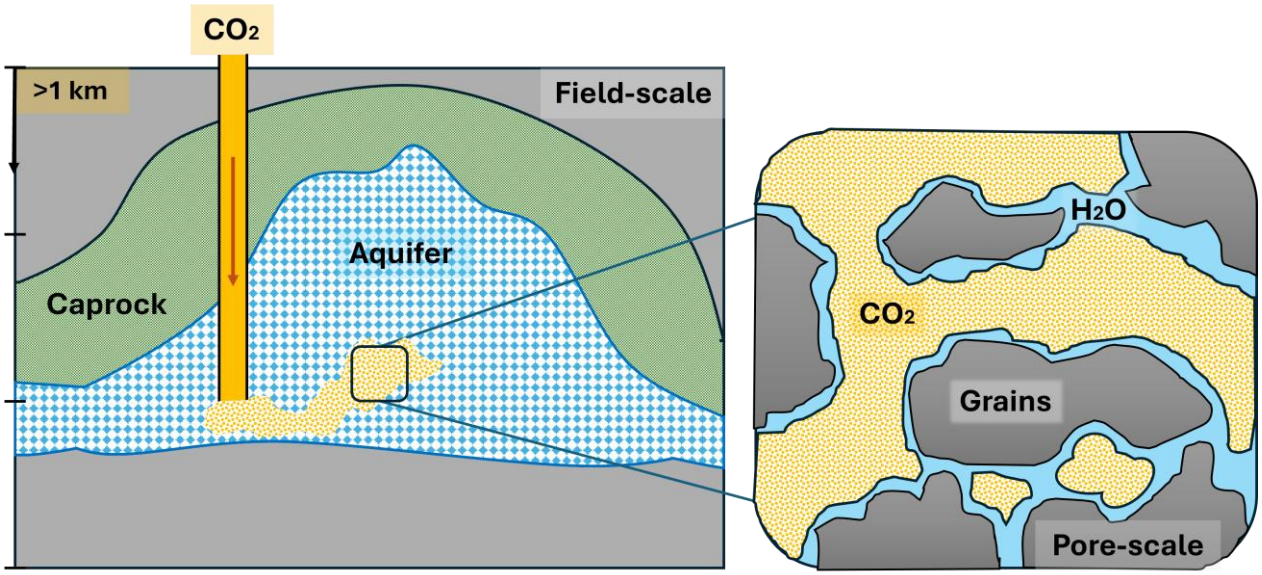

Figure 2 Carbon dioxide storage in saline aquifers with representations on the field and pore scale.

Several physicochemical mechanisms are responsible for the trapping of CO_2 with evolving contribution over time (see Figure 3). At first, injected CO_2 tends to rise to an impermeable layer called caprock due to buoyancy, being structurally or stratigraphically trapped (Hesse *et al.*, 2008; Iglauer *et al.*, 2015). On its migration pathway, part of the CO_2 will be left behind, isolated and immobile in the pore network, through a mechanism called residual or capillary trapping (Juanes *et al.*, 2006; Saadatpoor *et al.*, 2010). During the entire time, CO_2 will be in contact with reservoir fluid (brine), allowing for continuous mass transfer, which contributes to dissolution trapping (Bachu and Adams, 2003; Riaz *et al.*, 2006) and mineral trapping (Gaus, 2010; Xu *et al.*, 2003). The general concern associated with the geological storage of CO_2 is the potential of CO_2 to escape into the atmosphere through natural pathways such as faults and fractures or man-made channels such as wells.

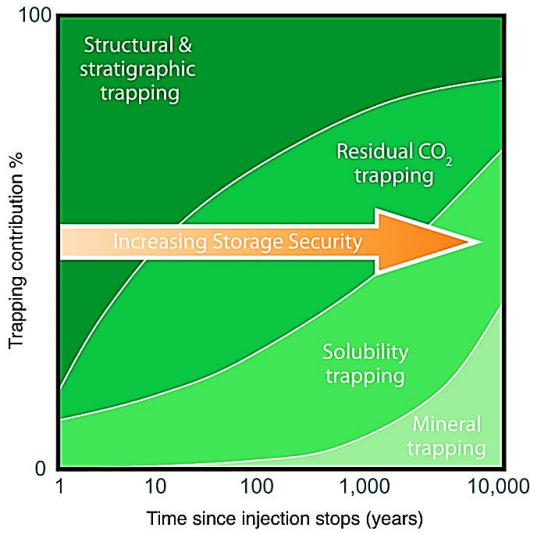

Figure 3 The relative contribution of trapping mechanisms over time. Taken from IPCC (2005).

As the storage processes transpire hundreds or thousands of meters below the surface without our direct view and control, many questions associated with the storage remain to be fully answered. How effective is CCUS in reducing greenhouse gas emissions? What are the potential risks and environmental impacts of CCUS? Are there and what are the possible remediation methods in case of uncontrolled underground migration and leakage? What are the best options for capturing carbon dioxide (technically and economically)? Which geological structures are the best storage option and why? How can we accurately measure, monitor and predict the amount of carbon dioxide that can be stored underground? How can we improve the efficiency of CCUS technology to make it more economically feasible? What are the long-term effects of storing carbon dioxide underground? What is the actual timescale of trapping mechanisms? How well do we understand trapping? These and many more are questions of great importance before starting large-scale CCUS operations.

Focus of current CCUS models (Ajayi *et al.*, 2019; Furre *et al.*, 2020; Mishra *et al.*, 2015; Saraf and Bera, 2021; Sifuentes *et al.*, 2009; Tatomir *et al.*, 2019) and field-scale engineering projects (like Sleipner CO_2 storage, Orca and Silverstone to mention a few) is generally related to capacity assessment, injection rates, and later control and forecast of the flow and storage dynamics (Agada *et al.*, 2017; Munkejord *et al.*, 2021). Besides technical/operational parameters imposed from the surface at the injection site, intrinsic properties of geological structures play an influential role in reducing uncertainty, increasing efficiency and enhancing the financial viability of the CCUS projects. Geometry and volume of the reservoir, pressure and temperature, absolute and effective porosity, absolute and relative permeability, capillary pressure (Busch and Müller, 2011; Fleury *et al.*, 2010; Saraf and Bera, 2021; Worden, 2023); and heterogeneity and anisotropy of all mentioned properties (Bouquet *et al.*, 2013; Rasheed *et al.*, 2020; Taheri *et al.*, 2012; Worden, 2023) are just some of the entry-level parameters to consider.

On a large scale, Darcy's law, originally formulated for single-phase flow, is used to describe fluid movement through porous media. It establishes a proportional relationship between the volumetric flow rate (Q) over a certain cross section (A) and the pressure gradient (∇p), modulated by the medium's permeability (k) and the fluid's viscosity (μ), according to the equation below

$$Q = \frac{kA\nabla p}{\mu}. \tag{1}$$

This law is valid at the Representative Elementary Volume (REV) scale, a sufficiently large volume where macroscopic properties such as porosity and permeability are statistically homogeneous. In a multiphase system, we consider an extension of Darcy's law that takes into account relative permeability. Relative permeability quantifies the ability of each fluid phase to move through the porous matrix, depending on its saturation and interactions with other phases. When two fluids are in contact, we also consider capillary pressure. Capillary pressure, governed by the Young-Laplace law, represents the pressure difference across the interface between the wetting (p_w) and non-wetting phase (p_{nw}). This pressure difference is influenced by interfacial tension (σ), contact angle (θ), and the radius of the capillary (r) as shown in the equation below.

$$p_c = p_{nw} - p_w = \frac{2\sigma\cos\theta}{r} \tag{2}$$

Both relative permeability and capillary pressure define fluid distribution in porous media and are thus typically expressed as functions of saturation. Fluid saturation represents the fraction of pore volume occupied by a given phase, while residual saturation is the irreducible saturation at which a fluid becomes immobile due to capillary forces. Overall, a fluid saturation distribution following the injection is defined through sweep and displacement efficiency. Sweep efficiency describes the fraction of the total reservoir volume contacted by the injected fluid, whereas displacement efficiency refers to the effectiveness of one fluid in mobilizing and displacing another in a contacted sweep zone. Understanding these parameters is crucial for optimizing reservoir performance and designing efficient injection strategies.

All of those parameters are already being implemented across the existing core (Roels *et al.*, 2014; Worden, 2023) and field-scale models and projects (Leetaru *et al.*, 2012; Shariati Pour *et al.*, 2012). To apply constitutive relationships like capillary pressure and relative permeabilities into large-scale models, traditional core-scale experimental methods (Akbarabadi and Piri, 2013; Busch and Müller, 2011; Müller, 2011; Williams *et al.*, 2018) have been used as an information input. Core acquisition and experiments are however expensive, sample-dependent, time-consuming, and often yield uncertain measurements. By performing core-scale two-phase experiments, Aryana and Kovscek (2012) have shown that flow processes are not adequately described by generalized Darcy's law. Thus, these models still fail to fully explain the phenomena of flow, trapping, dissolution, mineralization and other physicochemical processes in complex and heterogeneous multi-phase systems.

Understanding large-scale phenomena in CO_2 storage requires investigating the fundamental processes occurring at the pore scale, where fluid-fluid and fluid-solid interactions take place, thus permitting the underlying physics to be explicitly captured, rather than expressed through averaged or lumped parameters as in continuum-scale models. Consequently, pore-scale research has become a key approach in studying storage mechanisms in saline aquifers, using two complementary methods: numerical simulations and experimental investigations. In recent years, pore-scale simulations have gained significant popularity. These models allow researchers to explore phase behavior and predict CO_2 migration and trapping under different conditions (see Figure 4), exploiting parameters such as pressure, temperature, porous media and fluid properties. Common dimensionless numbers used to describe fluid-fluid-solid behavior are: the mobility ratio (M), which compares the viscosities of displacing and displaced fluids; the capillary number (Ca), the ratio of viscous to capillary forces; the Bond number, which relates gravitational to capillary forces; the Reynolds number (Re), expressing the ratio of inertial to viscous forces; the Damköhler number (Da), comparing the rate of chemical reaction to that of convective or diffusive transport; and the Peclet number (Pe), which compares advective and diffusive transport. These parameters play a crucial role in controlling capillary and solubility trapping in porous media (Iglauer *et al.*, 2015; Oliveira *et al.*, 2023; Primkulov *et al.*, 2021; Tokunaga and Wan, 2013; Wan *et al.*, 2023).

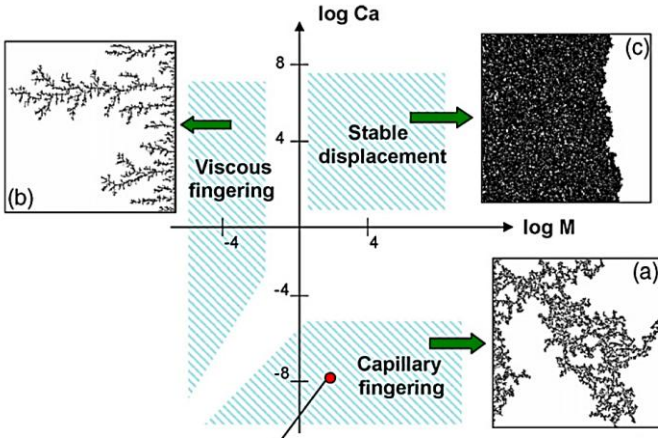

Figure 4 Lenormand diagram depicting fluid behavior as a function of capillary number (Ca) and mobility (viscosity) ratio (M). Taken from Sinha and Wang (2007).

Despite significant progress, numerical modelling of multiphase flow remains a complex challenge. The difficulties are twofold: on one side, numerical models require further refinement including dynamic calculation of interface curvature, fluid composition tracking and faster simulation times. On the other hand, the physical description of interfacial properties remains incomplete, particularly regarding the wettability conditions and thin film behavior. Ongoing research aims to tackle these challenges by developing reliable and efficient pore-scale simulators for multiphase flow (Soulaine *et al.*, 2021). In addition, high-resolution experimental research is needed to augment these models by providing data to verify predictions and by analyzing the physico-chemical processes behind the interfacial properties.

In this context, the present thesis contributes to the advancement of pore-scale experimental studies, specifically by investigating the role of wettability in CO_2 storage processes. The work is conducted as part of the INTER-AQ project ("Mass transfer at fluid/fluid interfaces in geological porous media: aquifer-on-a-chip" funded by CNRS MITI Prime), which focuses on CO_2 storage in saline aquifers and the parameters influencing capillary trapping and solubility of CO_2 in resident fluids. To uncover the physics behind these mechanisms, the study downscales from the traditional REV, i.e., Darcy-scale (m - cm), to the pore-scale (mm - µm - nm). Rather than using actual rock samples, we utilize synthetic porous media that allow for controlled geometries, the elimination of rock-fluid chemical interactions, and the visual tracking of key processes. A parameter of particular interest in this project is wettability, which this thesis explores in relation to its influence on both capillary trapping and interfacial mass transfer during CO_2 injection and storage. Further details on the specific goals and methodology of this thesis are presented in Section V, while Chapter 4 provides an in-depth discussion of pore-scale investigations into capillary trapping and mass transfer in the context of CO_2 storage, with a particular emphasis on wettability.

II. Microfluidics to mimic subsurface environments

As the name suggests, microfluidics is the technology where small volumes of fluids are manipulated in a contained space of micrometer dimensions. A microfluidic device, microfluidic chip or micromodel is the core part of our setup. It consists of an inlet and outlet (one or multiple) between which there is a geometry of interest etched in the material of choice (Tang *et al*., 2021). Geometries vary from simple straight microchannels to complex 3D shapes. The technology is also famous under the term " (geological) lab on a chip" (Jahanbakhsh *et al*., 2020; Morais *et al*., 2016). In geosciences, devices frequently feature 2D geometries of heterogeneous pore networks, derived from real rock pore structures captured via CT imaging (e.g., from Digital Rock Portal by Prodanovic *et al*. (2015)).

There are several major advantages to microfluidics over core samples as a porous media representative. Microfluidic devices offer real-time visual observation of dynamic processes and compatibility with various *in situ* analytical techniques. Great flexibility is reflected in customizable designs with controlled properties that ensure a reproducible process environment of micro dimensions and facilitate low-volume consumable usage for faster, more efficient studies (Zhu and Wang, 2022). Even elevated pressure and temperature requirements are no longer a significant limitation, as advancements in materials and fabrication techniques now allow for robust designs that withstand subsurface-relevant conditions (Marre *et al*., 2009). Many single-use and reusable designs are also readily accessible and cost-effective compared to core samples sourced from deep boreholes (Qi *et al*., 2018).

III. Wettability of porous materials and importance for carbon storage

1. Wettability characterization and measurement

a) Wettability theory

Wettability is a characteristic of a fluid-fluid-solid system, where one fluid preferentially adheres to the surface of a specific material more than the other fluid (Craig, 1971). Wettability is commonly described using the water-air contact angle (WCA), unless specified otherwise. Accordingly, surfaces are usually classified as hydrophilic (water-wet) or hydrophobic (non-water-wet), depending on their attraction or repulsion of water. Further divisions may include terms such as super-, strongly, moderately and weakly (-wet/hydrophilic/hydrophobic). One such example is given in Figure 5. Although the contact angle range (0 - 180°) does not have a fixed division, it is generally considered that 0° represents an ideal wetting condition, where the surface fully attracts one fluid. A contact angle around 90° indicates a neutral surface, interacting equally with both fluids in the system. Angles greater than 90° suggest that the surface is more readily wetted by the other fluid. In nature and on a larger scale, some surfaces can also be considered mixed-wet or amphiphilic, meaning some parts of the domain are wetted by one fluid while others are wetted by another fluid. As a rule of thumb, liquids have stronger preferential wetting to surfaces compared to gases.

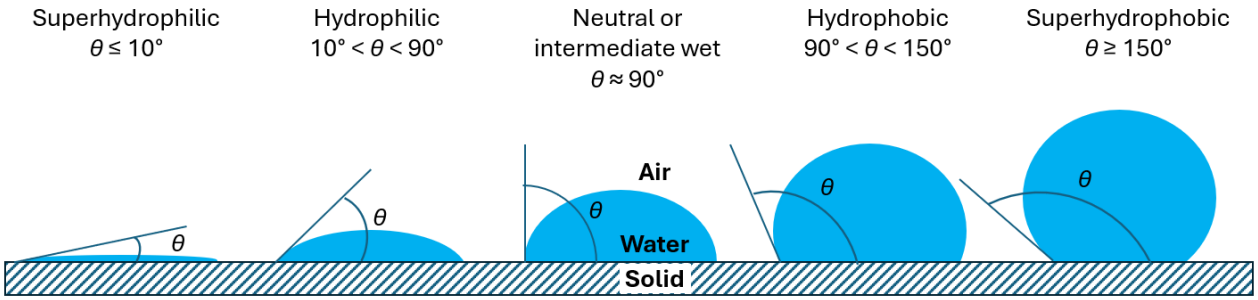

Figure 5 A classification of wettability characteristics in a water-air fluid system.

A foundation work by Young (1805), Wenzel (1936, 1949) and Cassie and Baxter (1944) established the dependency of wettability on both surface chemistry and surface topography of materials. Owing to them, today we distinguish between wettability measured on a smooth surface and surfaces that are considered rough. The wettability of a smooth flat surface is defined through a contact angle given by Young's equation (3):

$$\cos\theta_Y = \frac{\gamma_{sg} - \gamma_{sl}}{\gamma_{lg}}, \tag{3}$$

where θ_Y is Young's angle, γ stands for interfacial tension, while subscripts *s*, *l* and *g* denote solid, liquid and gas phase, respectively.

In cases where the surface is considered rough, two different models exist. Depending on whether the droplet placed on the surface is filling surface asperities or not, the condition may be described as either a Wenzel, Cassie-Baxter or in between wetting state (see Figure 6). Wenzel's wetting state is characterized by a complete adjustment of fluid to the surface topology. Contrary, in Cassie-Baxter's wetting state, the liquid drop does not fill the voids of surface roughness and instead stays on top of the surface.

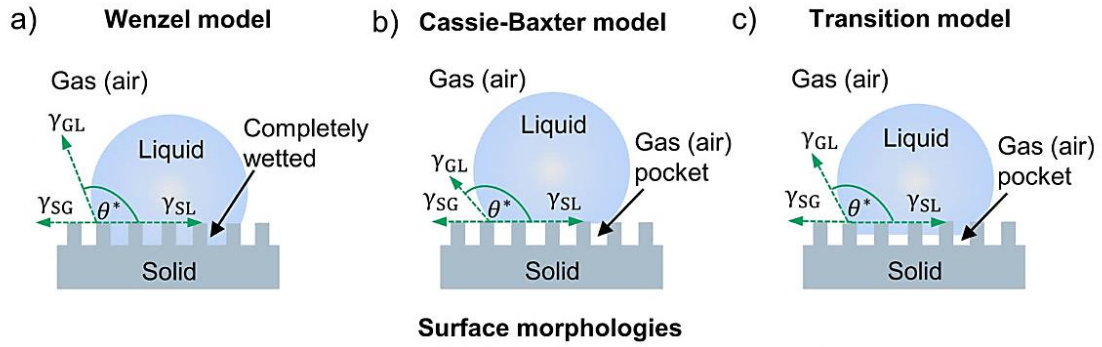

Figure 6 Base models to describe the wettability of a topologically rough surface. In the Wenzel model (a), a fluid fills the asperities of surface roughness. In the Cassie-Baxter model (b), a fluid floats on top of the topology, while in the transition model (c), fluid partially enters the voids. Taken from Ma et al. (2023).

It is generally accepted that the Cassie state is associated with higher phase mobility, while droplets in the Wenzel state are more "sticky" and pinned to the surface in contact, however, new discoveries are challenging this notion (Dai *et al.*, 2015). Important to note is also that in Wenzel state, increasing surface irregularities make already hydrophilic surfaces more hydrophilic and hydrophobic surfaces more hydrophobic (Zhu and Wang, 2022). Understanding how surface roughness influences wetting conditions within the same geological formation is thus crucial for assessing the performance of capillary and solubility trapping mechanisms. Rough surfaces in the Wenzel state can increase resistance to water flow, thereby promoting capillary trapping of CO_2. In contrast, rough surfaces in the Cassie wetting state may offer more surface area for CO_2 dissolution.

There are several terminology issues regarding contact angles that can be confusing. Different terms usually indicate different conditions or different notions of measurement. Apparent contact angles are the ones that are routinely measured on the macroscopic scale, and they can be different from the actual (local) ones which can be better seen on the micro and nanoscale (see Figure 7).

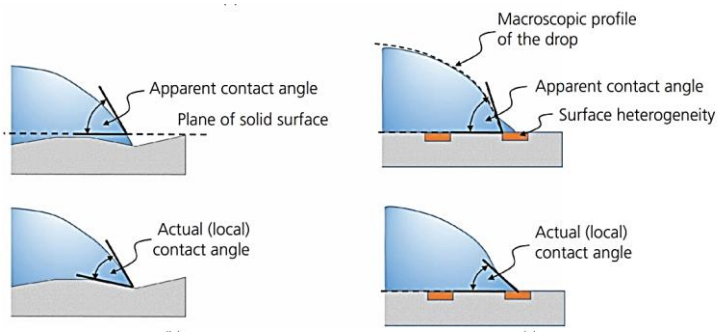

Figure 7 Apparent vs. actual (local) contact angle. Taken from Marmur et al. (2017).

The next misconception /confusion is related to contact angle hysteresis. Hysteresis is defined as the difference between advancing and receding contact angles (Kwok and Neumann, 1999). The advancing contact angle is produced during the wetting process, in contrast to the static contact angle, which is measured without altering the contact area between the liquid and solid. The receding contact angle occurs in the course of dewetting. Furthermore, advancing and receding contact angles are defined as the highest and the lowest metastable angles that can be measured. The most stable contact angle, usually referred to as the static contact angle, is located between the two, where Gibbs' potential energy (Morrow, 1970) is the lowest (see Figure 8). The most stable contact angle on a rough but chemically homogeneous surface is predicted by the Wenzel model. On the contrary, the most stable contact angle on a smooth but chemically heterogeneous surface is predicted by Cassie's model. The general model for chemically heterogeneous and rough surfaces is the Cassie-Baxter model.

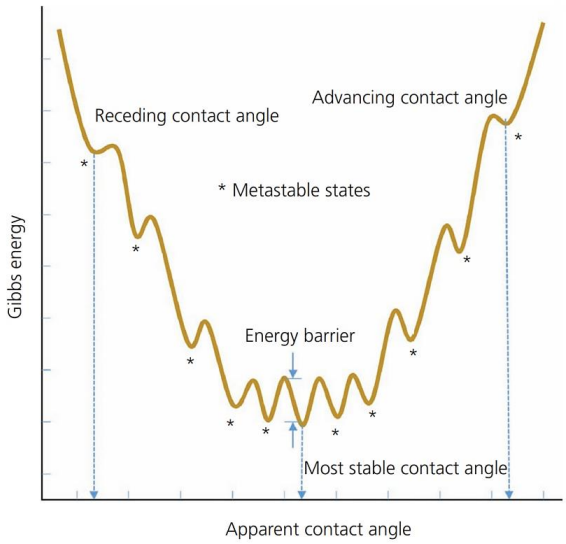

Figure 8 Contact angle dependency on Gibbs potential energy and the notion of contact angles that comes from different scenarios. Taken from Marmur et al. (2017).

According to Marmur *et al.* (2017), it is quite common to find advancing and receding contact angles encompassed under the term "dynamic" contact angle. Advancing and receding contact

angles are typically used terms for describing equilibrium wettability states under metastable conditions, differing from dynamic contact angles. Dynamic contact angles do not characterize equilibrium wettability as their value is affected by the velocity (Butt *et al.*, 2022) and therefore depends on the capillary number. To make a distinction between dynamic and metastable conditions, Chiquet *et al.* (2007), Hansen *et al.*, (2000), Huh and Scriven (1971) and many before them, started to differentiate between the terms "advancing" vs "advanced" and "receding" vs "receded" (see Figure 9). The terms "advanced" and "receded" are employed in literature to refer to what is commonly known as "advancing" and "receding". These alterations in terminology serve to emphasize that the angles being described and measured are static metastable contact angles, rather than dynamic contact angles, which may be erroneously suggested by the use of "advancing" and "receding". Advancing and receding contact angles then rightfully become dynamic contact angles. This terminology is however not widely accepted, and many studies still deviate from the notion.

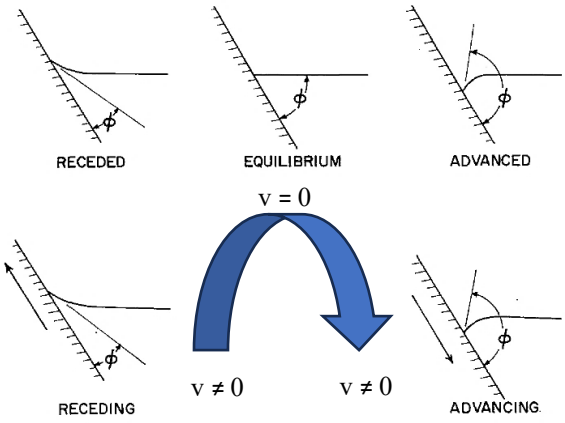

Figure 9 Distinction between "static" and "dynamic" contact angles. Adapted from Huh and Scriven (1971).

Chiquet *et al.* (2007) also reported two different scenarios of bubbles swelling. Figure 10a indicates bubble/drop expansion with a fixed contact point when swelling/growing occurs slowly, while Figure 10b depicts rapid swelling, which is characterized by a change of interfacial radius and movement of the contact point. Due to the planarity effect, Chiquet *et al.* (2007) emphasize that in both cases, the reference plane (frontier) for measuring the contact angle should be positioned slightly above the substrate plane with the actual triple contact point (line in 3D). While both cases a) and b) can occur during contact angle measurements on open surfaces, case a) is predominantly expected in confined spaces such as capillaries and microchannels. Regardless, these effects must be considered during measurement. Moreover, as evident from Figure 10, the contact angle also depends on the bubble/droplet size.

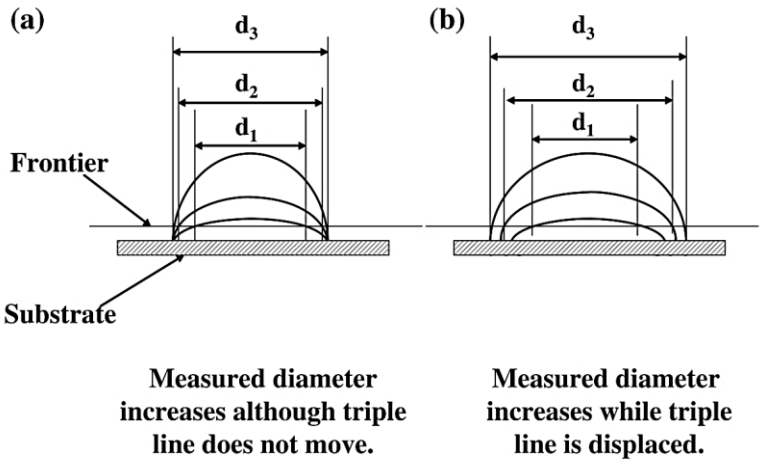

Figure 10 Interface behavior during swelling with fixed (a) and displaced triple line (b), where d is the diameter of the drop measured at the frontier. Taken from Chiquet et al. (2007).

Although surface roughness and heterogeneity are often cited as causes of contact angle hysteresis, recent research has shown that this phenomenon can also occur on smooth and chemically homogeneous surfaces. The most compelling evidence for this is the presence of contact angle hysteresis on free liquid films (not attached to a droplet), where there is no roughness or heterogeneity to explain the phenomenon (Kuchin and Starov, 2015). Norouzisadeh *et al*. (2024) state that for very thin films at the nanometer scale, the disjoining pressure, arising from the intermolecular interactions at the interfaces, significantly influences stability and spreading. Increasing film thickness beyond a critical point reduces the dominance of intermolecular forces, stabilizing the contact angle. The presence of a lubricating film minimizes interface pinning which results in a decrease of contact angle hysteresis. Consequently, measurements conducted on dry and prewetted surfaces may exhibit variations in contact angle hysteresis (van Rooijen *et al*., 2022).

Another very important observation is the dependency of the contact angle on the confinement. For example, in the paper of van Rooijen *et al.* (2022), they measured for hydrogen, nitrogen and carbon dioxide in the presence of water, advancing and receding contact angles reported in the paper indicate general inversely proportional behavior of contact angle with respect to channel width (see Figure 11). In natural porous media and microfluidic devices, fluid interfaces are confined within pores, where dimensions can vary widely across orders of magnitude. As a result, contact angles measured on free surfaces provide only a rough estimate and do not fully capture the *in situ* wettability conditions. Additionally, accounting for confinement is crucial to ensure valid comparisons between natural samples and synthetic environments, such as in microfluidic devices. In the case of CO_2, confinement beyond approximately 100 μm appears to have no significant effect on contact angle measurements.

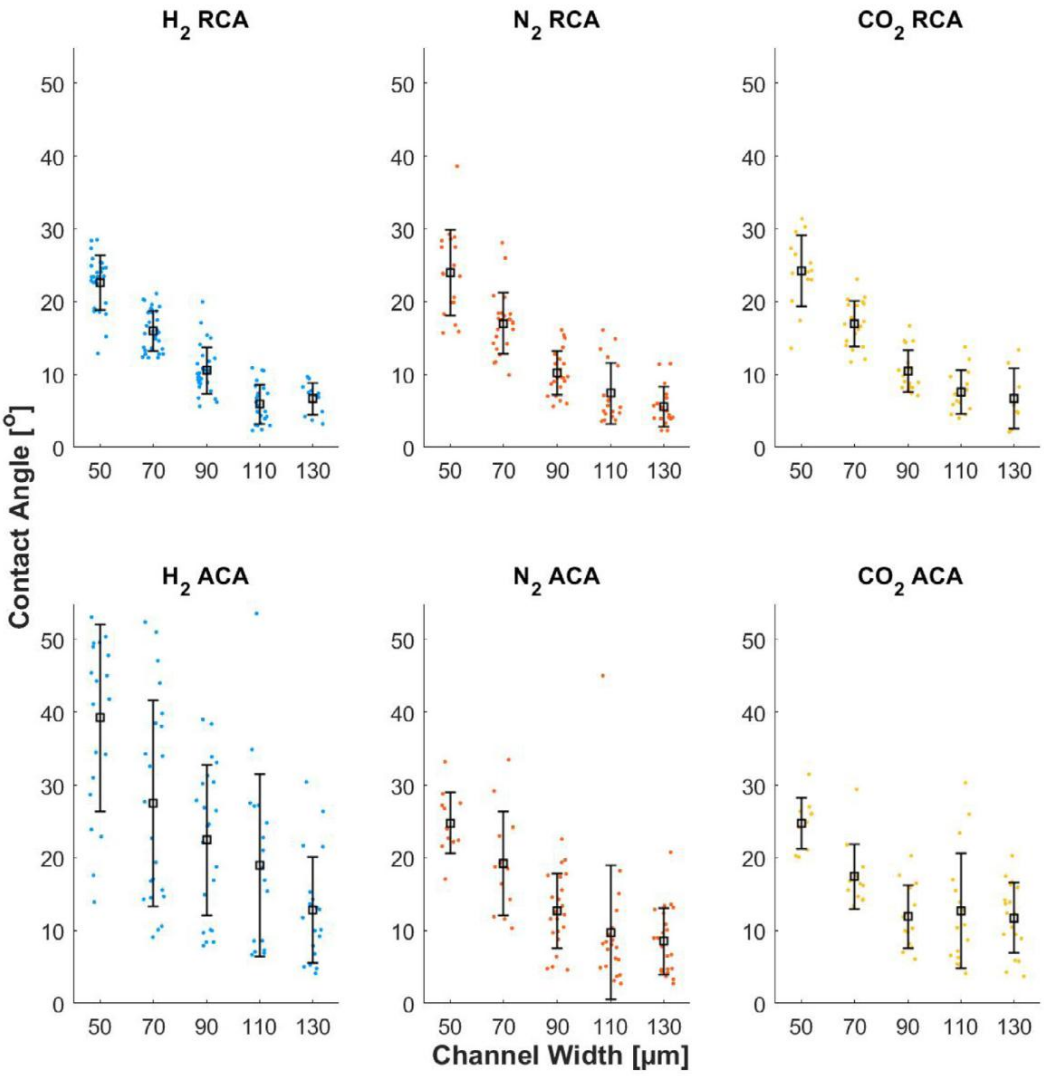

Figure 11 Dependency of in-situ measured advancing (ACA) and receding contact angles (RCA) on the confinement in microfluidic channels. Taken from van Rooijen et al. (2022).

b) *Wettability measurement methods and tools*

The nature of measuring contact angle and wettability in general is a far more complex task than what idealized models like Young's suggest. Numerous techniques for determining the wettability of porous media have been developed for various needs/applications. The list of some available methods with associated assets and liabilities is displayed in Table 1. Many available measurement methods are indirect and more suitable for engineering applications; therefore, this study focuses on contact angle-based methods, which offer a more direct approach.

Table 1 Wettability measurement methods. The acronyms AH and USBM refer to Amott-Harvey and U.S. Bureau of Mines wettability indices, respectively. Taken from Sagbana et al. (2022).

Method	Advantages	Limitations
Static contact angle	Simple Fast method (1–2 h) Accurate Surface wettability	Impurities between droplet and surface can affect readings Heterogeneity of surfaces can affect readings Cannot provide information regarding organic coatings Cannot relate results directly to core flooding performances
Dynamic contact angle	Measures transient variations in contact angles Accurate in relating to core flooding performance Fast method (1–2 h) Applicable for high-pressure high-temperature conditions	Speed of increasing or decreasing droplet volume is critical
AH	Reliable Core scale wettability investigation	Slow method (10days) Expensive Non-effective under neutral wettability
USBM	Reliable Core scale wettability Sensitive to neutral wetting systems	Expensive Slow method (1–2 days) Requires multiple procedures to produce quantitative results Expensive
NMR	Very fast method (10 min) High pressure and Temperature conditions Studies wettability at the macro, micro scale and fractional wettability Noninvasive	Complex and expensive
Micro-CT method	In situ wettability Pore-scale investigation	Expensive Uses a radioactive source for measurement
Microscopic	In situ wettability alteration can be examined Sub pore-scale investigation Surface morphology investigation using (AFM and SEM)	Expensive Image resolution competing with processing power
Thermogravimetric Methods	Infers surface wettability from physically and chemically adsorbed matter.	May Require further validation studies Destructive technique Expensive
Infrared (IR) Spectroscopy	Relatively fast method Sub pore-scale investigation Characterises desorption from calcite	Expensive
Flotation Test	Very Fast method (1 h) Low cost	The effect of strongly wetted systems is critical
Zeta Potential	Sub pore scale investigations	Destructive methods as samples are crushed Requires carbonate and the solvent to be in equilibrium for accurate reading
SCM	Low cost, Fast and effective	Model prediction errors Isotherms developed for many ambient conditions Requires validation from other standard methods

Contact angle measurements on substrates represent the sole category of methods capable of directly assessing wettability (see Table 2). These measurements are typically conducted using two techniques: the sessile drop method and the captive bubble method. Both approaches employ a telescopic goniometer setup (Bigelow *et al*., 1946), which can be integrated with a high-pressure, high-temperature cell (Iglauer *et al*., 2015). These techniques are widely regarded in the literature as the most effective for obtaining direct, quantitative evaluations of rock surface wettability across a broad range of operational conditions. These conditions include variations in pressure, temperature, brine chemistry, and surface roughness, all of which influence wettability. Both measurement approaches should give comparable but not necessarily identical values of contact angle.

The primary distinction between the sessile drop and captive bubble methods lies in the placement of the droplet or bubble. For systems involving water and CO_2, the sessile drop method positions a water droplet on the surface of a substrate surrounded by a CO_2 atmosphere. Conversely, the captive bubble method involves placing a CO_2 bubble beneath the substrate, surrounded by water (see Table 2). The specific configurations of these methods are dictated by the density differences between the fluids in the system. Following the selection of the experimental setup, the contact

angle is determined from image acquisition, either manually or automatically. Uncertainties arise from the need to identify the contact (triple) point and the reference plane.

A tilting plate configuration offers a valuable modification to these methods, enabling simultaneous measurement of advancing and receding contact angles. The advancing angle (θ_a) is measured at the leading edge of the droplet, while the receding angle (θ_r) is determined at the trailing edge.

Table 2 A summary of direct contact angle measuring techniques. Taken from Arif et al. (2019).

Method	Mode	Scientific/Analysis Mode	Analysis scale	Schematic
Sessile drop Measurement	Direct / quantitative	Experimental, manual/automatic analysis	Millimeter scale	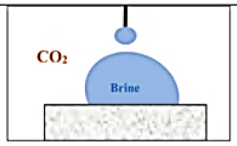
Captive bubble	Direct / quantitative	Experimental, manual/automatic image analysis	Millimeter scale	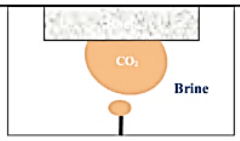
Sessile drop/Captive bubble on a titled plate	Direct / quantitative	Experimental, manual/automatic image analysis	Millimeter scale	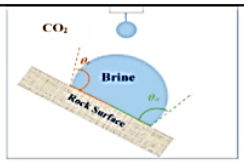
Capillary Meniscus analysis	Direct / quantitative	Experimental, image analysis	Millimeter scale	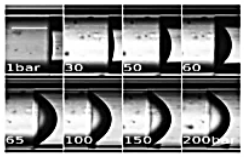
2D Micromodel	Direct / quantitative	Injected fluid imaged via microscope / Analyzed using ImageJ	Micrometer scale	
3D µ-CT imaging	Direct / quantitative	CT-scan under dynamic condition / Image analyzed using an algorithm	Micrometer scale	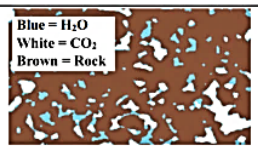

The current landscape of open-source investigations of contact angle measurements on images has been significantly shaped by advancements in camera technologies and the development of user-friendly software tools. Notable examples of software tools include CAMTIA, developed in Matlab by Nežerka *et al.* (2018); Dropen also in Matlab, by Akbari and Antonini (2021); DropToolKit in Python by Favier *et al.* (2017); SessileDropAnalysis tool in Python by Van Gorcum (2019); PyDSA in Python by Launay (2018); DropSnake and LBADSA as ImageJ plugins by Stalder and colleagues (2010, 2006), and some others.

Recommendations provided by Krüss, a leading company in contact angle measurement tools, are summarized in Table 3. For instance, the choice of algorithm depends on the range of contact angles being measured. Lamour *et al*. (2010) demonstrated that for contact angles greater than 40°, the drop profile is more accurately approximated using an ellipse, whereas for angles below this threshold, circular algorithms yield better results.

Table 3 Recommended range of applicability for different algorithms used for contact angle measurement. Taken from Williams et al. (2010).

	Circle	*Conic section*	*Polynomial*	*Young-Laplace*
Contact angle measuring range				
0–20°	✓			
10–100°		✓	✓	✓
100–180°			✓	✓
Drop weight (volume·density)				
Low	✓	✓	✓	✓
High		✓	✓	✓
Very high			✓	✓
Deposition				
Static (contour without needle)	✓	✓	✓	✓
Dynamic (contour with needle)		✓	✓	
Contour Shape				
Symmetrical	✓	✓	✓	✓
Slightly asymmetrical		✓	✓	
Very asymmetrical			✓	

For example, DropToolKit and LBADSA (Figure 12a) utilize the fitting of the Young-Laplace equation to image data, whereas DropSnake (Figure 12b) employs B-spline snakes (active contours) to define the droplet shape, subsequently fitting it with a polynomial function. Since droplet interfaces are seldom perfectly axisymmetric, global models such as LBADSA face inherent limitations in accurately determining contact angles. In contrast, local models using polynomial fitting are well-suited for handling non-axisymmetric droplets. However, the accuracy of contact angle measurements in these models is highly sensitive to the chosen polynomial degree and the number of fixed points. DropSnake addresses these challenges by applying an elasticity constraint to the active contours, enabling it to maintain a cohesive global shape while offering localized contact angle measurements influenced by finite-range forces.

a)

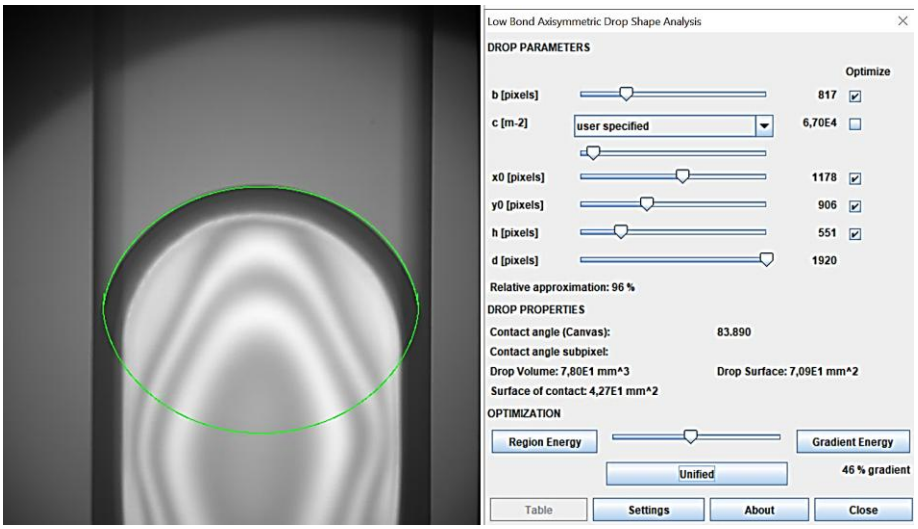

b)

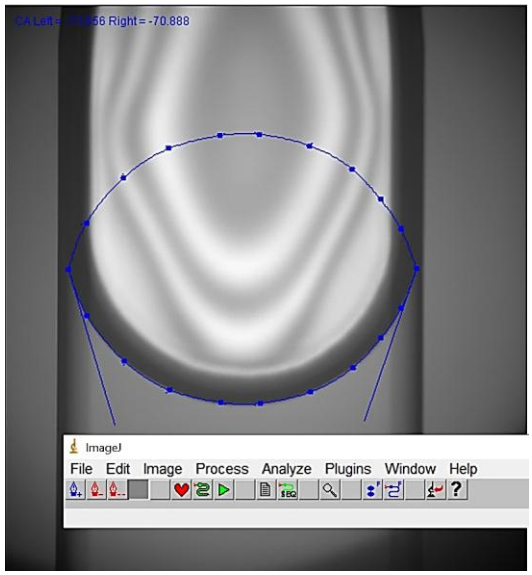

Figure 12 Contact angle tools: a) LBADSA, b) DropSnake. Measurements for both tools are taken on the same image, with the reference plane (0°/180°) being a horizontal line in contact points. Light gray represents the gaseous phase (CO_2) and the darker gray water phase.

The DropSnake tool can be operated in manual or semi-automatic mode. Both approaches leave room for subjective input of the points (knots) from the user, thus introducing uncertainty. The reported standard deviation can be as low as 0.2°, however, authors emphasize the importance of knot numbers and inter-knot distance. The number of knots and the inter-knot distance are two inverse factors. The recommendation from the authors is to have approximately 10 knots to have sufficient data to describe the interface in manual mode or 20 pixels as inter-knot distance (see

Figure 13). With very low inter-knot distance, the user runs into error due to discrete properties of images (e.g., due to contrast, subpixel interpolation, etc), while at too high inter-knot distance, an interfacial contour is not represented correctly.

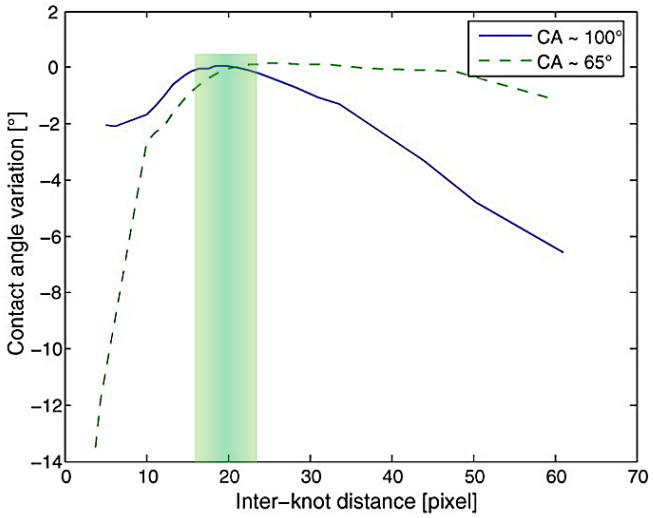

Figure 13 Dependency between contact angle variation and inter-knot distance. Adapted from Stalder et al. (2006).

The DropSnake tool was applied in a microfluidics study by Kovalev *et al.* (2020). They studied the influence of hydrodynamic conditions on dynamic contact angles in partially wet microchannels with a rectangular cross-section. To determine contact angles, three different algorithms were deployed. Out of the three, the DropSnake B-spline-based algorithm was selected as the most precise one, as it best described the interface contour near the triple point as visible from their analysis in Figure 14.

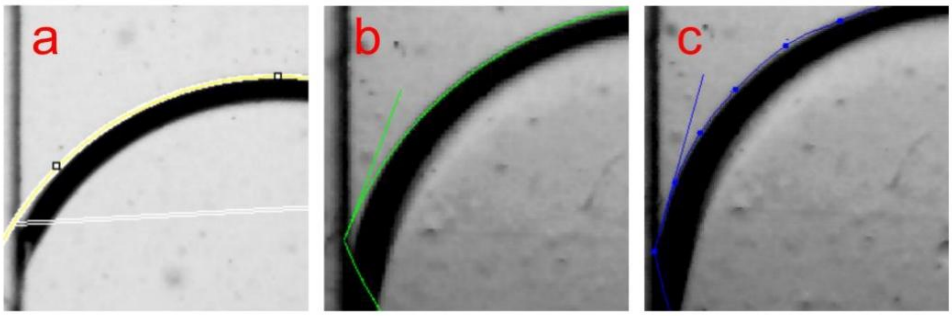

Figure 14 Testing of three different algorithms for meniscus approximation: a) circle/ellipse fitting, b) LBADSA with Young-Laplace solution and c) DropSnake B-spline fitting. Taken from Kovalev et al. (2020).

Despite the wide range of available methods for assessing wettability via contact angle measurements, each approach presents specific challenges and limitations. In microfluidic applications, *in situ* measurements are particularly complex, as they must be performed within confined geometries where surface curvature and channel dimensions can influence the results. In our study, contact angle measurements were performed through image-based analysis using the DropSnake tool, which calculates average apparent static contact angles from fluid interface profiles. This method proved well-suited for confined microfluidic environments, offering reliable and reproducible data under experimental conditions.

2. The role of wettability in carbon storage in geological reservoirs

The direct quantification of wettability in underground structures poses significant challenges due to the complex interplay of numerous parameters across multiple length scales. Nevertheless, heterogeneity in wettability within such structures is a well-documented phenomenon. The wettability of rocks is predominantly determined by the wettability characteristics of the mineral fractions comprising them. Since most mineral fractions exhibit water-wet (hydrophilic) behavior, the majority of rocks tend to be water-wet as well. However, beyond the intrinsic chemical properties of the material, surface topology, i.e., surface roughness, also plays a critical role in influencing wettability. Alterations of surface chemistry and topology can lead to wettability alteration.

With two soluble fluids coming into contact, mass transfer across the common interface is initiated, creating a concentration gradient in both fluid faces, resulting in dissolution trapping. The rate of dissolution trapping is influenced by factors such as fluid distribution, surface contact, fluid compositions, thermodynamic conditions, and potential chemical reactions at the interface. In the case of CO_2 dissolution in water, this process can alter the wettability of minerals, thereby modifying the system's dynamics. These changes can initiate a feedback loop, where altered wettability affects fluid distribution and trapping mechanisms, which in turn influence further dissolution and overall system behavior.

The following sections provide a detailed exploration of wettability alteration, fluid behavior in porous media, and implications of wettability for CO_2 storage mechanisms, with a particular focus on capillary and dissolution trapping.

a) Wettability alteration of reservoir rocks

As mentioned earlier, the wettability of rocks is primarily determined by their mineral composition, which dictates their affinity for water or oil. Rocks such as sandstones and carbonates, dominated by quartz or calcite, are generally water-wet due to their strong interactions with polar water molecules, making them common hosts for aquifers. In contrast, hydrophobic rocks - such as certain shales rich in organic matter, oil-wet carbonates coated with hydrocarbons, or coal beds - tend to attract non-polar fluids like oil and CO_2. The inherent wettability of rocks can also be influenced by factors such as surface roughness and the adsorption of substances like clay minerals or organic coatings. Additionally, natural rock wettability is not fixed and can change upon

exposure to different fluids. For instance, carbonate rocks are particularly susceptible to wettability alteration when interacting with various petroleum compounds, often becoming intermediate or oil-wet (Arif *et al.*, 2017; Deng *et al.*, 2020; Ivanova *et al.*, 2019; Sagbana *et al.*, 2022). Similarly, studies indicate that exposure to CO_2 can alter the natural wettability of rocks (Arif *et al.*, 2016; Chiquet *et al.*, 2007; Jafari and Jung, 2018; Wan *et al.*, 2014). Furthermore, efforts have also been made to understand and model the wettability and alteration processes numerically (Maes and Geiger, 2018; Norouzisadeh *et al.*, 2024).

The following paragraphs present experimental studies that investigate the wettability of various minerals under CO_2 exposure.

Chiquet *et al*. (2007) observed that the contact angle on mica increased from approximately 10 - 30° at 1 MPa to 60° at 11 MPa, and on quartz from 10 - 30° to 35°, suggesting a loss of hydrophilicity. The proposed mechanism involves CO_2 dissolution, reducing pH, which shifts interfacial forces and decreases electrostatic repulsion between phases.

Arif *et al*. (2017) further demonstrated that increasing CO_2 pressure up to 20 MPa and lowering temperature to 35 °C resulted in calcite becoming CO_2-wet, with advancing and receding contact angles reaching 122° and 108°, respectively. Salinity also plays a role: contact angles remain stable up to 5 wt% NaCl but increase significantly at 20 wt%. Additionally, surface roughness (RMS from 7.5 to 140 nm) was shown to decrease contact angles by about 10°, which may explain discrepancies in literature data.

While many studies confirm CO_2-induced wettability alteration (e.g., Broseta *et al*., 2012; Iglauer *et al*., 2014; Saraji *et al*., 2013), others report little or no change. Espinoza and Santamarina (2010) observed no significant variation on quartz and calcite surfaces transitioning from gaseous to liquid CO_2. Wang *et al*. (2013) similarly found stable contact angles across multiple minerals (e.g., quartz, calcite, kaolinite, illite) when changing pressure and temperature. They concluded that pH and ionic strength, rather than pressure alone, control wettability by influencing the surface charge of minerals relative to their point of zero charge.

Iglauer *et al*. (2015) reviewed contact angle behavior across diverse minerals and found inconsistencies, likely due to factors such as surface contamination, roughness, or mineralogical heterogeneity.

Beyond natural alteration, wettability can also be intentionally modified, often in enhanced oil recovery. Techniques include injecting surfactants, alkaline solutions, smart water, or nanoparticles (Delshad *et al.*, 2009; Deng *et al.*, 2020; Gong *et al.*, 2016; Kassa *et al.*, 2020; Vledder *et al.*, 2010).

In summary, wettability alteration is a frequent occurrence, influenced by the presence of CO_2, petroleum compounds, and various chemicals. These changes are not necessarily permanent (e.g., when caused by CO_2) and are highly dependent on factors such as pH, pressure, temperature, and salinity. However, the impact of these parameters can sometimes be ambiguous. Factors like surface roughness, contamination, and ionic strength - often overlooked in studies - warrant more

detailed investigation, as a more advanced approach is needed to fully understand their influence (Anderson, 1986; Liu *et al.*, 2018; Wan *et al.*, 2014).

b) *Implications of wettability on fluid-fluid displacement in porous media*

Wettability in geological porous media has traditionally been interpreted using representative elementary volume (REV) concepts such as relative permeability, capillary pressure, and residual saturation (Anderson, 1987a, 1987b; Iglauer, 2017; Kassa *et al.*, 2020; Masalmeh, 2003). This approach remains relevant and is still widely used in reservoir characterization as wettability is one of the most influential parameters governing these properties. The limitation of this characterization lies in the fact that such approaches inherently lump together the effects of multiple parameters, making it difficult to isolate and explicitly quantify the influence of wettability.

In two-phase flow through porous media, the injection process can be classified as either drainage or imbibition, depending on the order of fluid injection and the wetting characteristics of the solid surfaces (see Figure 15). Drainage refers to an invasion of non-wetting fluid into the porous media and displacement of wetting fluid. Imbibition refers to the invasion of wetting fluid that displaces the non-wetting fluid from the porous domain. In the context of CO_2 storage within water-wet geological formations, drainage corresponds to the injection of CO_2 into a water-saturated porous medium, leading to the displacement of water. Conversely, imbibition occurs when water is injected into a CO_2-saturated zone, displacing the CO_2 from the pore space.

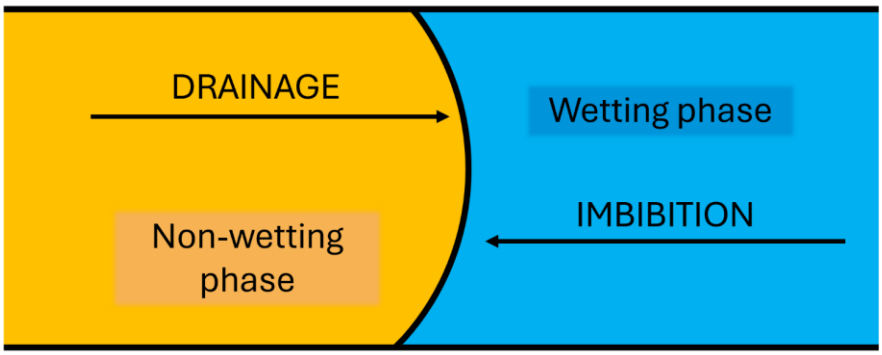

Figure 15 General schematics of the drainage and imbibition process.

Drainage and imbibition are however not perfectly reversible displacement processes. This leads to dissimilar behavior reflected in saturation differences between the two processes and their successive cycles. Hysteresis arises from factors such as pore size distribution and media anisotropy, wettability alteration, and trapping mechanisms. These complexities make capillary pressure and relative permeability insufficient for fully predicting fluid behavior in reservoirs with varying wettability conditions. A more comprehensive understanding requires incorporating dynamic wettability effects, pore-scale displacement mechanisms, and hysteresis-dependent modeling approaches.

In porous media research, fluid flow is often characterized in terms of the capillary number, the viscosity ratio and the Bond number. These parameters provide a generalized framework for analyzing multiphase flow behavior under different wettability conditions. The range of values for capillary number and viscosity ratio during CO_2 storage is dependent on the injection dynamics, distance from the well and reservoir properties. Two end-member scenarios can be identified: high-velocity viscosity-controlled flow (near injection wells) and quasi-static capillarity-controlled storage (far field and during long-term storage). A range of expected values is depicted in Figure 16.

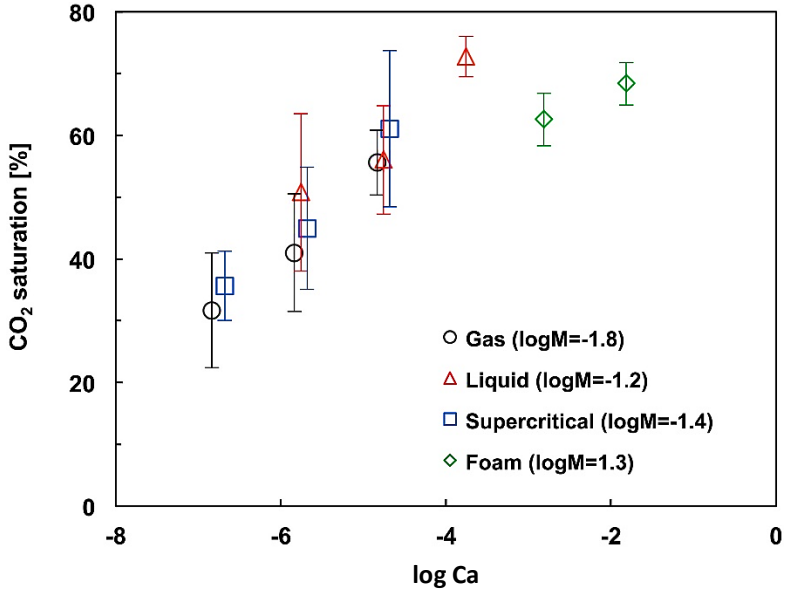

Figure 16 Range of capillary number (Ca) and viscosity ratio (M) during CO_2 storage. Taken from Zheng et al. (2017).

In that direction, a contribution was made by Primkulov and colleagues (2021). They have expanded Lenormand's diagram (Figure 4) where fluid behavior in porous media is governed by different hydrodynamic conditions (Ca), fluid properties (Ca, M) and now wettability of porous environment (θ). The produced graph (see Figure 17) is the result of 7560 fluid-fluid displacement simulations under dynamic and quasi-static conditions using a pore-network model reconstructed from a Hele-Shaw cell. Influenced by different magnitudes of capillary number, viscosity ratio and wettability conditions, 5 regions indicating different displacement patterns were identified. These include: stable displacement, viscous fingering, invasion-percolation regime, cooperative pore filling and corner flow regime. The significance of this study lies in its ability to visualize flow patterns as a function of dimensionless numbers during drainage and imbibition, providing insight into the regions where wettability exerts a notable influence. As illustrated in the graph, for a fixed viscosity ratio, wettability has a pronounced effect at lower capillary numbers. Under these conditions, capillary forces dominate fluid displacement, making interactions with the solid matrix particularly significant. Such conditions are generally considered more favorable for effective CO_2 trapping (Bandara *et al*., 2011).

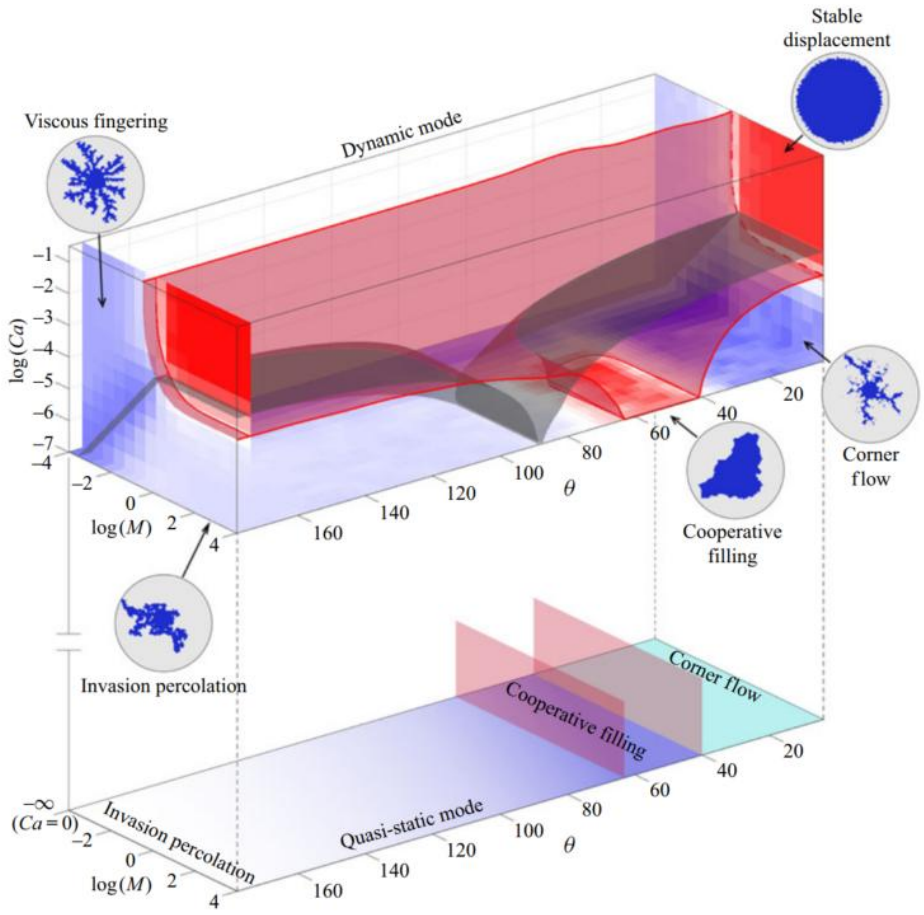

Figure 17 Extended Lenormand's diagram. The red surface is the border region between compact and non-compact displacement patterns while the gray surface separates capillary and viscous-dominated regions. Taken from Primkulov et al. (2021).

Understanding the natural or modified wettability and its spatial distribution within geological formations is essential for accurately predicting fluid behavior and localization (Sagbana *et al*., 2022). This knowledge facilitates the assessment of storage mechanisms by determining their overall potential and relative contributions. The total storage potential is governed by three key parameters: capacity (reflected in effective porosity, sweep and displacement efficiency, residual saturations), injectivity (reflected in relative permeability, capillary pressure), and long-term containment/safety (reflected in capillary entry pressure of the caprock, fracture stability, temporal scales of storage mechanisms) (Celia *et al*., 2015). Wettability plays a fundamental role in influencing these parameters. Specifically, it directly affects structural and capillary trapping while indirectly influencing dissolution and mineral trapping via interactions at liquid-liquid and liquid-mineral interfaces (Yekeen *et al.*, 2020). In this thesis, we will focus on the two mechanisms, capillary and dissolution trapping.

c) *Capillary trapping and impact of wettability*

Capillary trapping is characterized by the saturation of the immobilized phase. To clearly differentiate from structural trapping, where CO_2 remains a continuous phase capable of free flow, capillary-trapped CO_2 is confined within pore spaces and immobilized due to capillary forces, preventing its movement unless these forces are exceeded (Zhong *et al*., 2025). Capillary trapping in porous media occurs through two primary mechanisms (see Figure 18): (1) bypassing of bubbles or ganglia by the advancing fluid stream and (2) snap-off, which results from the formation of a wetting-phase capillary bridge between adjacent grains. Both mechanisms contribute to the sequestration of the non-wetting phase. Bypassing-induced entrapment is closely linked to invasion dynamics, whereas snap-off is governed by fluid film flow. Snap-off is the key mechanism that breaks continuous CO_2 into isolated droplets/ganglia within the pore space (Zhong *et al*., 2025). On a large scale, the effectiveness of both mechanisms is quantified by sweep efficiency and displacement efficiency, measuring residual saturation. Further details of capillary trapping at the pore scale will be given in Chapter 4.

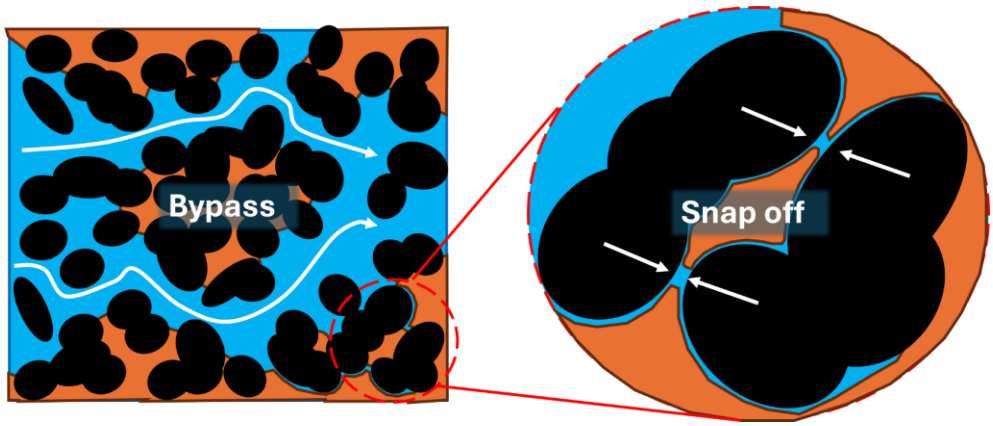

Figure 18 Schematics of bypass and snap-off mechanisms. Grains are depicted in black while two distinct fluid phases are in blue and orange.

The occurrence of both invasion patterns and film flow formation is highly sensitive to wettability. Thus, wettability alteration during the CO_2 sequestration process, as demonstrated in section a), could reduce capillary forces and facilitate the remobilization of the trapped phase. In addition to wettability, capillary trapping mechanisms are influenced by factors such as pore size distribution, flow intensity, and the viscosity ratio of the interacting fluids.

Namely, there are two groups of studies that are interested in determining the implications of wettability on capillary trapping of CO_2 in porous media (Hu *et al.*, 2017). The first group suggests that a medium that is more water-wet traps more CO_2 than an oil-wet or CO_2-wet medium (Chaudhary *et al.*, 2013; Herring *et al.*, 2016; Zhao *et al.*, 2016). This is because of the mechanism called corner flow. Domination of corner flow in largely water-wet media leads to encapsulation, i.e., entrapment of larger volumes of CO_2. The mechanism has been observed in both core-flooding and microfluidic experiments.

The second group of studies suggests that the dominant mechanism under strongly hydrophilic conditions is cooperative pore-filling, which leads to wider brine fingers resulting in less CO_2 bypassing (Holtzman and Segre, 2015; Jung *et al.*, 2016; Plug and Bruining, 2007; Tokunaga and Wan, 2013). Consequently, less CO_2 is trapped. Cooperative pore-filling mechanisms permit the fluid to advance as a flat front, i.e., multiple pores at once which leads to full displacement (Berg *et al.*, 2014; Blunt and Scher, 1995). The statements of this group are backed up both experimentally and numerically. To combine the two, the competition between corner flow and cooperative pore-filling mechanisms likely determines the overall amount of CO_2 trapping.

The following paragraphs provide summaries of selected studies that have investigated the potential effects of wettability on capillary trapping and consequently on key storage parameters.

In a microfluidic study by Chalbaud *et al.* (2009), the partial (i.e., intermediate) wetting behavior of CO_2 at reservoir conditions was investigated. The outcome of the study concluded that partially wetting conditions are expected to have a negative impact on the reservoir's capacity but improve displacement efficiency compared to strongly water-wet porous media. In an earlier study (Chalbaud *et al*., 2007), which also included core and reservoir scale pore network modeling, it was stated that different wettability scenarios could also affect the spatial extent of injected CO_2 and injectivity index. Namely, in lower permeability formations, less water-wet conditions facilitate lower injection pressure which can be interpreted as higher injection rates (each 0,1 MPa of injecting pressure can correspond to 75 tons per day of CO_2) or lower energy consumption of surface facilities (compressors). Spatial extent seems to be also positively affected by less water-wetting conditions. A greater area covered by a migrating plume within a reservoir may indicate a requirement for fewer injection wells. Fewer wells mean decreased overall expenses and a lower likelihood of CO_2 escaping to the surface through potential well integrity failures, which can act as a pathway for CO_2 escape.

Espinoza and Santamarina (2010) had a similar scope of the study, focusing on the implications of CO_2 injectability and sealing capacity of the geological formation. In theoretical discussion, they emphasized the importance of both interfacial tension and contact angle in the formulation of the capillary number. In conjunction with the viscosity ratio, they presented anticipated scenarios for the previously mentioned problems of CO_2 storage. In the vicinity of a well where the capillary number is high (i.e., higher fluid velocity) and the viscosity ratio is relatively low, liquid CO_2 is expected to take over larger pores with susceptibility of the front to instabilities like viscous fingering. Deeper in the reservoir, fluid velocity will drop (Ca is low), thus capillary forces will govern CO_2 propagation in the porous medium. This implies that capillary fingering might occur. Both mentioned scenarios suggest that formation fluid (brine) will stay in small pores, leading to a finite residual saturation of capillary-trapped CO_2. The favorable aspect of formation fluid trapped in small pores is in the cap rock, as the cap rock’s function is to keep fluids from escaping by means of high capillary entry pressure and low permeability.

Another interesting finding in a microfluidic study by Hu *et al.* (2017) indicates that when the flow rate is increased, the impact of wettability on capillary trapping is reduced. This is due to the increased influence of viscous forces at higher Ca values, which causes the displacement pattern to shift from capillary fingering to viscous-dominated stable displacement (Lenormand, 1990). This shift occurs regardless of whether the system is water-wet or intermediate-wet. Consequently, as Ca values increase, the contrast in capillary trapping between the two wettability conditions is lowered. In addition, it is generally observed that increasing flow rates lead to enhanced mobilization of the trapped phase (Datta *et al.*, 2014).

In summary, capillary trapping, reflected in the distribution of residual fluid saturation within porous media, is governed by the balance between trapping and mobilizing forces. Wettability is one of the key parameters influencing capillary forces, which are central to this balance. A stronger affinity between a fluid and the solid surface leads to stronger capillary forces and a greater likelihood of trapping that fluid phase. However, these processes are not well described in large-scale models.

d) Solubility trapping and impact of wettability

Solubility trapping is an interfacial mass transfer process (see Figure 19) in which a fluid phase gradually dissolves into a surrounding, more dominant phase, leading to immobilization of the dissolved compound. This mechanism enhances storage security by reducing the mobility of the trapped phase and promoting its dispersion within the host fluid. Dissolution trapping potential is usually expressed through the amount/concentration of the dissolved phase. It is however crucial to recognize that mass transfer in carbon storage is a bidirectional process, involving CO_2 dissolution into water and water evaporation into dry CO_2. Further details of solubility trapping at the pore scale evaluated through interfacial mass transfer will be given in Chapter 4.

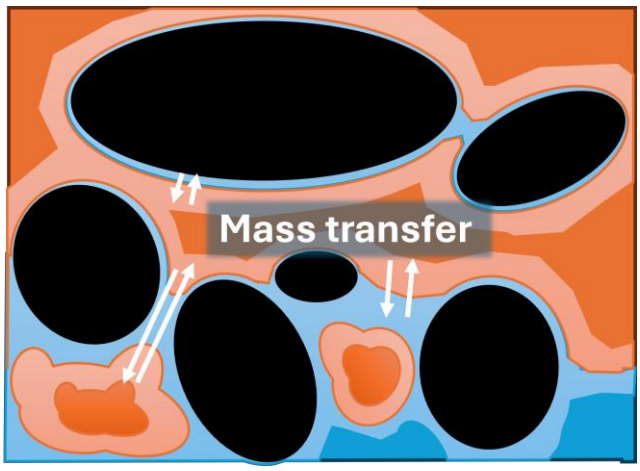

Figure 19 Schematics of mass transfer. Grains are depicted in black while two distinct fluid phases are in blue and orange. Variations in fluid phase colors reflect differences in species concentrations within respective phases.

Before proceeding with further discussion, it is essential to distinguish between solubility and miscibility. Concepts of solubility and miscibility both relate to the ability of one substance to dissolve in another, but they differ in scope and application. Solubility refers to the extent to which a solute (e.g., gas or liquid) can dissolve in a solvent under specific conditions of temperature and pressure. It is typically quantified as the maximum concentration of the solute that can be dissolved in the solvent before reaching saturation. Beyond this limit, the excess solute will form a separate phase. Miscibility describes the ability of two liquids to completely mix in all proportions without forming separate phases. If two liquids are fully miscible, they form a single homogeneous phase regardless of the mixing ratio. This is the case with chemically similar molecules (e.g., ethanol and water). If they are partially miscible, they mix only within certain composition limits, beyond which phase separation occurs (e.g., water and diethyl ether). Since CO_2 and water are chemically different molecules (water is polar and CO_2 non-polar), full miscibility cannot be achieved under typical geological conditions. Namely, at ambient pressure and temperature, CO_2 remains as a gas with relatively low solubility in pure water is expected to be below 0.1wt% (Lee and Lee, 2017; Perkins, 2003). At high pressures (e.g., in deep saline aquifers, >10 MPa) and moderate temperatures (30 - 60 °C), CO_2 solubility increases, but it still does not reach full miscibility. Supercritical CO_2 (> 7.4 MPa and > 31.1 °C) then forms a dense phase but remains immiscible with water, leading to two distinct phases (CO_2-rich and water-rich). However, in extreme conditions (e.g., > 300 °C and very high pressures on the order of 10^2 MPa), CO_2 can become highly soluble, approaching near-miscible behavior, but not full miscibility.

Dissolution is often studied under equilibrium conditions dictated by Henry's law, while the kinetics of the dissolution process receives less attention in research. According to Henry's law, dissolution continues until the fugacity of CO_2 is equilibrated between the gas and liquid phases. At equilibrium, the amount of dissolved gas in a liquid (x_i^{aq}) is directly proportional to its partial pressure in the gas phase (p_i^{sat}) related over the Henry constant (k_H, unit: Pa.m^3/mol) as given in the equation below,

$$x_i^{aq} = k_H \times p_i^{sat}. \quad (4)$$

Building on this principle, numerous semi-empirical thermodynamic models have been developed and optimized for various fluid pairs. Consequently, the effects of pressure, temperature, and salinity on CO_2 solubility in aqueous solutions at equilibrium are well-documented (Iglauer, 2011). One of the most influential models was proposed by Duan and Sun (2003) and (2006), which employs a modified Redlich-Kwong equation of state and refines Henry's law by incorporating activity coefficients to account for non-ideal behavior. Their model is applicable over a wide range of pressures (up to 200 MPa), temperatures (0 – 260 °C), and salinities (up to 4.5 salt molality with a variety of different ions), making it highly versatile for geochemical and engineering applications. Such models are particularly valuable for predicting pH variations and carbonate equilibria in geochemical simulators, aiding in the assessment of long-term CO_2 storage stability.

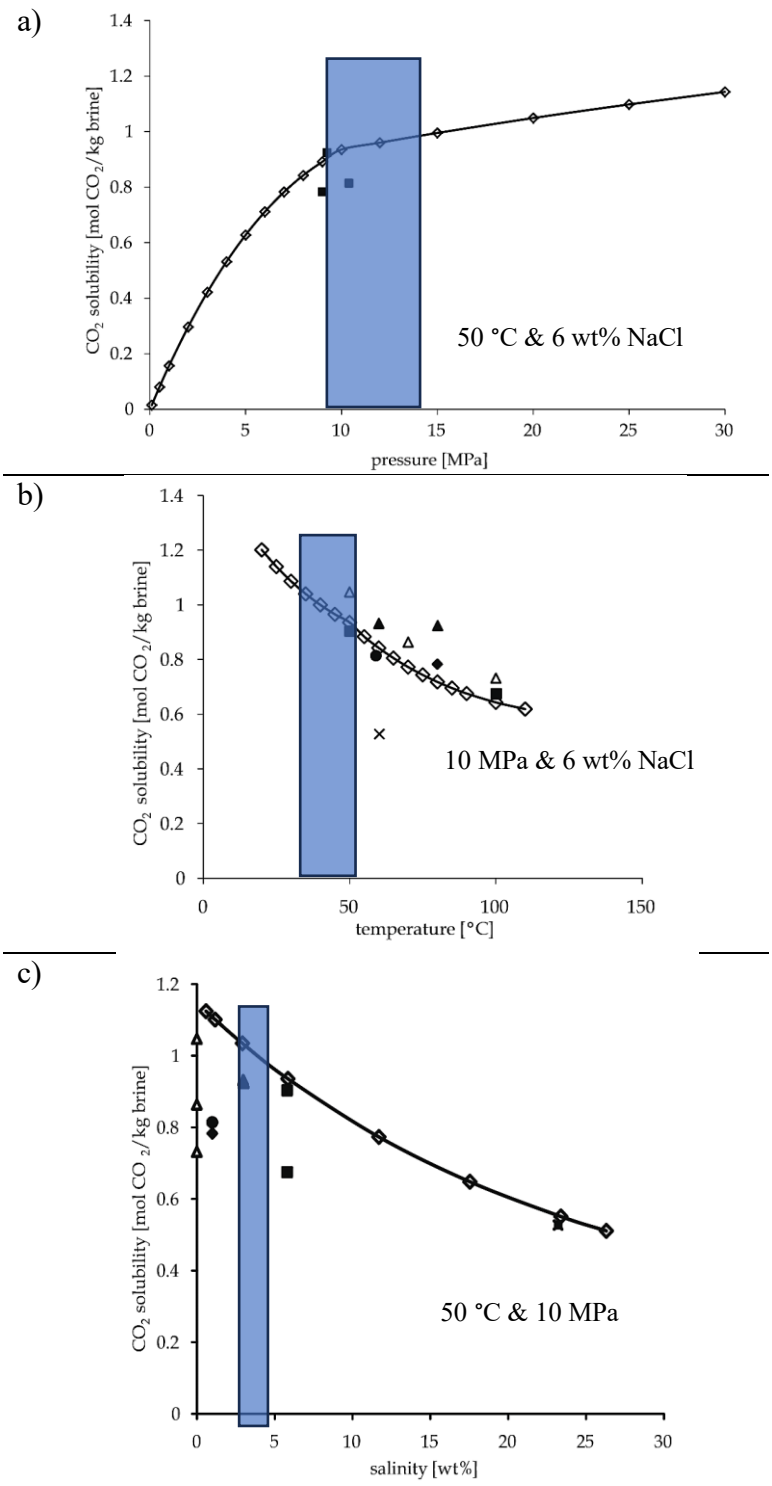

Figure 20 The CO_2 solubility with pressure (a), temperature (b) and NaCl salinity (c) according to Duan and Sun (2003) and (2006) model (solid line) and comparison to experimental data points. Blue rectangles represent conditions expected for the Sleipner project (Eiken, 2019). Adapted from Iglauer (2011).

In general (see Figure 20), increasing pressure enhances CO_2 solubility, while temperature and salinity scale inversely with CO_2 solubility. Above approximately 40 MPa and 65 °C, the solubility of CO_2 increases with temperature (Perkins, 2003). Based on the conditions from the Sleipner CCUS project (highlighted by blue rectangles in Figure 20), the expected CO_2 solubility is around 1 mol, equivalent to 44 g of CO_2 per kg of brine or around 4 wt%. Depending on the depth of injection projects (typically 1 – 3 km) and temperature gradient (25 – 45 °C/km), CO_2 solubility normally stays between 4 and 6 wt% (Celia *et al*., 2015; Dodds *et al*., 1956; Nordbotten *et al*., 2005).

CO_2 migration into the water phase leads to the formation of dissolved or *aqueous* CO_2 – $CO_{2\,(aq)}$ but also carbonic acid (H_2CO_3), resulting in a pH reduction (Figure 21). This decrease in pH augments mineral reactions, which can influence the storage safety either positively or negatively. The impact depends on whether the reactions promote mineral dissolution or precipitation and whether they occur within the reservoir or the caprock.

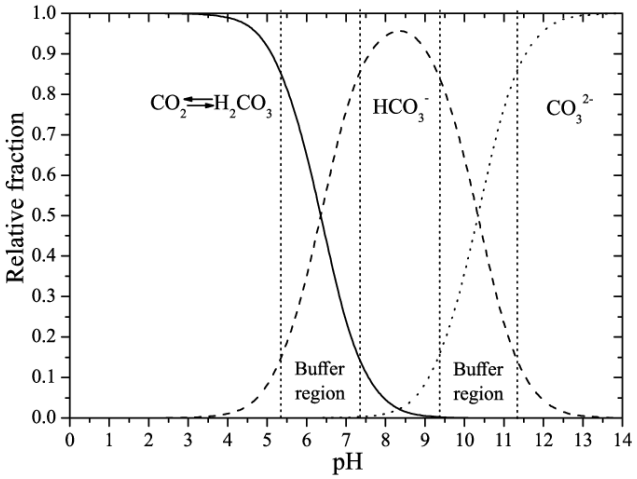

Figure 21 Carbonate species evolution as a function of pH during CO_2 dissolution in water. H_2CO_3 is carbonic acid, HCO_3^- is bicarbonate ion CO_3^{2-} is carbonate ion. Taken from Fioravante et al. (2019).

The Clausius–Clapeyron relation can be utilized to predict the vapor pressure of water under equilibrium conditions (Koutsoyiannis, 2012). Taking into consideration Raoult's Law, the dissolution of CO_2 in water lowers the water vapor pressure, decreasing evaporation. According to Sabirzyanov *et al.* (2002), the solubility of water in supercritical CO_2 is up to 1 mole percent, while Celia *et al*. (2015) similarly limit the amount of water in the CO_2 phase to less than 1 % by volume. A continuous injection of dry CO_2 can however lead to dry-out and salt precipitation in the near wellbore region, reducing the permeability and hence injectivity (Celia *et al*., 2015; Martynov, 2022; Zhong *et al*., 2025).

To achieve concentration equilibrium between the CO_2 and water phases, solute distribution is governed by steady or unsteady-state diffusive flux, described by Fick's laws. The equilibration process can be accelerated by advection, which enhances mass transfer by reducing concentration

gradients. The relative significance of diffusion and advection in mixing is typically quantified using the Péclet number, providing insight into the dominant transport mechanism.

If thermodynamic equilibrium conditions change (such as a pressure drop due to a reservoir leak), exsolution (the reverse of dissolution) of gas from the solution can occur (Xu *et al*., 2017). Ostwald ripening is one such phenomenon, where gas first dissolves in the liquid and then re-exsolves due to pressure differences between bubbles (De Chalendar *et al*., 2018). Smaller bubbles, having higher curvature, experience greater capillary pressure, causing gas to diffuse toward larger bubbles with lower pressure. As a result, larger bubbles grow while smaller ones shrink, eventually coalescing into a mobile gas phase that may enhance CO_2 migration and leakage risks.

Although very useful and significant, the thermodynamic approach disregards the influence of porous media. In fact, many experimental studies were conducted without considering the effects of porous media (see Table 4).

Table 4 A list of studies looking into the dissolution of CO_2. Taken from Amarasinghe et al. (2019).

Reference	Experimental Setup Description	Fluids	Porous Media	Conditions	Visualization method
(Vosper et al. 2014)	Hele-Shaw cell	CO_2 / Water	Glass beads	Ambient conditions	pH dye
(Teng et al. 2018)	Hele-Shaw cell	CO_2 / Brine	No porous media	150 bars / 80 °C	pH dye (Bromocresol Green - BG)
(Faisal et al. 2015)	Hele-Shaw cell	CO_2 / Water	No porous media	Ambient conditions	pH dye (Bromocresol Green - BG)
(Khosrokhavar et al. 2014)	Hele-Shaw cell	CO_2 / Water, CO_2 / Oil	No porous media	64-84 bars / 39 °C	Schlieren method
(Kneafsey and Pruess 2011) and (Kneafsey and Pruess 2010)	Hele-Shaw cell	CO_2 / Water and atmospheric air (380 ppm CO_2) / water	No porous media	40 bars / Ambient temperature	pH dye (Bromocresol Green)
(Lu et al. 2017)	Hele-Shaw cell	CO_2 / Brine	No porous media	Ambient pressure / 22 - 45 °C	pH dye (Bromocresol purple - BP) / Back luminance light/High speed Camera
(Mojtaba et al. 2014)	Hele-Shaw cell	CO_2 / Brine	No porous media	Ambient conditions	pH dye (litmus powder)
(Taheri et al. 2018)	Hele-Shaw cell	CO_2 / Water	No porous media	Ambient conditions	pH dye (Bromocresol Green - BG)
(Song et al. 2003)	High-pressure cell	CO_2 / Water	No porous media	50-125 bars / 0-15 °C	Mach-Zehnder Interferometry
(Thomas et al. 2015)	Hele-Shaw cell	CO_2 / Water	No porous media	Ambient conditions	pH dyes (BP and BG) / Schlieren method
(Fang and Babadagli 2016)	3D test tank	Oil / Solvent	Glass beads	Ambient conditions	Fluorescence dye / High speed Camera
(Lv et al. 2016) and (Lv et al. 2017)	3D high- pressure cell	CO_2 / Brine	Feldspar, Quartz, and Dolomite	8 bars / 40 °C	X-Ray CT scanning
(Zhao et al. 2011)	3D high- pressure cell	CO_2 / n-Decane	Glass beads	85 bars / 40 °C	MRI imaging

So far, we have established that wettability is affected by the dissolution but not the other way around (effects of wettability on the dissolution of CO_2). To our knowledge, the effects of wettability on dissolution in porous media are not extensively studied by experimental means, and

even less on a pore scale. The reasons for this scarcity are twofold. Firstly, $scCO_2$ dissolution has historically been considered at the equilibrium of the process. As a result, the researchers have mainly focused on multiphase flow processes without $scCO_2$ dissolution, that is, immiscible experiments where $scCO_2$ and water are equilibrated prior to injection. Secondly, $scCO_2$ dissolution entails several physicochemical processes such as phase interface evolution, fluid-fluid interfacial chemical reaction, multicomponent mass transport, and reactions at the fluid-solid interface. These processes are quite complex, and it is difficult for experimental techniques to capture all the physical fields involved, such as velocity, concentration, and phase interface, within the limited space of porous media.

Despite these challenges, some studies (predominantly numerical) have explored CO_2 dissolution under different wettability conditions. Al-Khdheeawi *et al*. (2017) and (2018) investigated the influence of wettability on CO_2 migration and trapping capacity at the reservoir scale. They employed the nonisothermal, multicomponent, multiphase flow simulator TOUGH2 and the ECO2M equation of state to model the thermodynamic and thermophysical properties of the system. In an earlier study (2017), they defined five uniform wettability scenarios (see Table 5) and simulated one year of CO_2 injection followed by 10 years of plume migration without injection. The effect of wettability was implemented in the simulation through adjusted relative permeability and capillary pressure curves. The results, visible in Table 5, demonstrate a significant impact of wettability on overall (solubility and residual) CO_2 trapping. Specifically, the strongly CO_2-wet case retained the highest proportion of the free CO_2 phase, as the injected gas remained continuous and was not effectively trapped by capillary forces. Conversely, dissolution trapping was most effective in strongly CO_2-wet rock, where 29% of the total injected CO_2 dissolved into the formation brine, compared to only 18% in strongly water-wet rock. This difference arises from the faster migration and broader spread of the CO_2 plume in CO_2-wet reservoirs, which increases the CO_2-brine contact area and enhances dissolution trapping. Overall, while CO_2-wet reservoirs promote dissolution trapping, this occurs at the expense of residual and total trapping efficiency, thus affecting the safety of short-term storage.

Table 5 Results of CO_2 plume migration simulation on a reservoir scale after 10 years without injection. Adapted from Al-Khdheeawi et al. (2017).

Wettability	Mobile CO_2 (%)	Dissolved CO_2 (%)	Residual CO_2 (%)
strongly water-wet (0°)	0.5	18.3	81.2
weakly water-wet (70°)	3.9	18.5	77.6
intermediate-wet (110°)	6.0	18.7	75.3
weakly CO_2-wet (130°)	13.8	23.2	63.0
strongly CO_2-wet (170°)	20.7	28.6	50.7

The following study, Al-Khdheeawi *et al*. (2018) aimed to simulate more realistic, non-uniform wettability conditions over an extended period of 500 years. A heterogeneous wettability model, comprised of 5% strongly water-wet, 30% weakly water-wet, 45% intermediate-wet, 15% weakly CO_2-wet, and 5% strongly CO_2-wet grid cells, was compared to an equivalent homogeneous intermediate-wet model. Simulation results indicate that wettability heterogeneity leads to a more pronounced upward migration of the CO_2 plume compared to the homogeneous wettability case. This effect arises due to variations in fluid flow dynamics and a more favorable pressure distribution, which facilitate plume migration along low-resistance wettability pathways. The increased mobility of the CO_2 plume enhances the contact area for dissolution into the fresh brine, leading to an increase in dissolution efficiency by approximately 2 -3 % in the heterogeneous reservoir. However, these same conditions appear to have a detrimental effect on residual trapping and thus overall trapping potential.

These findings highlight the inherent challenge of isolating the dynamics of solubility trapping from residual trapping when evaluating CO_2 storage efficiency. Since wettability directly influences fluid phase distribution, any change in wettability alters both capillary trapping and the amount of CO_2 available for dissolution. As a result, assessing solubility trapping efficiency in isolation remains difficult, as phase distribution and dissolution capacity are fundamentally interdependent.

An additional motivation to downscale to the pore scale is to experimentally isolate key porous media parameters such as wettability, while avoiding the complexities present at the reservoir scale that give rise to long timescales. These long timescales, spanning years to centuries or even more, are typically only accessible through numerical simulations, highlighting the need for simplified, representative experiments that can validate and inform such models. However, experimental studies are still relatively scarce, and numerical models require comparison with experimental and field data to ensure they accurately capture the full effects of wettability.

IV. Conclusion on the role of wettability for CO_2 storage

In summary, understanding the cause-and-effect relationship between wettability and fluid-fluid behavior is essential for the geological storage of CO_2. To achieve this, it is first necessary to comprehensively define wettability, identify the parameters influencing it, and quantify their effects. Over the past decades, significant efforts have been made to characterize the wettability of subsurface minerals in CO_2-brine systems. Available data indicate that most subsurface minerals and rocks exhibit water-wet behavior, with a few exceptions displaying intermediate-wet characteristics. However, substantial variability in reported data suggests that wettability is influenced by multiple factors, necessitating further research to reduce experimental uncertainties and improve our understanding of its role in CO_2 trapping mechanisms, particularly capillary and solubility trapping. While CO_2 solubility in water or brine under equilibrium thermodynamic conditions is well understood, the kinetics of mass transfer in wettability-influenced environments remains less explored. Notably, there exists a feedback loop wherein wettability affects CO_2 dissolution, while dissolved CO_2 can, in turn, alter mineral wettability. Additionally, the interplay between different trapping mechanisms and the inherent complexities across spatial and temporal scales in natural porous media further complicates the predictive capabilities for modeling CO_2 storage. The implications of wettability for CCUS are significant, as it directly influences rock sealing capacity, determines storage potential, and governs the distribution of stored CO_2 across different trapping mechanisms. Furthermore, wettability plays a critical role in optimizing injection strategies and ensuring long-term containment security. To improve the reliability of large-scale numerical simulations, fundamental pore-scale investigations, both experimental and computational, must be integrated to accurately incorporate key physico-chemical parameters like wettability. Experimental techniques like microfluidics offer a powerful tool to overcome these challenges by isolating specific effects that are difficult to distinguish in core-scale studies and not accounted for in simulations. However, to execute our research, we need a robust tool adapted to microfluidics to achieve reliable *in situ* wettability alteration.

V. Research objectives and thesis structure

The objective of this thesis is to address the existing gap in fundamental knowledge of mass transfer at the pore scale. Namely, this study aims to enhance the understanding of wettability-influenced fluid/fluid displacement and interfacial mass transfer processes within geological porous media. The findings will contribute to the calibration of both pore and reservoir-scale models, enabling more accurate predictive capabilities and facilitating the interpretation of field-scale phenomena in the context of carbon storage in geological reservoirs.

The specific scientific questions we will address are:

1. Can plasma be propagated and utilized for *in situ* wettability treatment of closed glass microfluidic devices?
2. How does wettability influence capillary trapping and interfacial mass transfer at the pore scale?
3. Can we follow the fluid-fluid interfacial mass transfer process by tracking chemical species evolution using Raman spectroscopy?

The research focuses on identifying patterns of mass transfer in porous media by observing the dissolution or evaporation of a trapped fluid within another. To isolate fundamental processes, the study employs:

1. Synthetic porous media - controlled geometries made in materials that ensure chemically inert fluid containment, enable tunable wettability, allow real-time visual observation, and replicate simplified natural porous media environments.
2. Analog fluids - pure CO_2 and water, to isolate the dissolution mechanism
3. Room pressure and temperature conditions - reduced thermodynamic conditions that facilitate straightforward identification of mass transfer patterns before extending findings to more realistic carbon storage environments.

By employing 2D glass microfluidic devices, we create a platform suitable for wettability alteration, thus capturing the effects of wettability diversity representative of natural porous media. To modify wettability, a novel atmospheric plasma-based technique is developed and specially adapted for *in situ* treatment of closed glass microfluidic devices. Various glass microfluidic devices were designed featuring rectangular trapping elements with various levels of geometrical complexity. Studying fluid trapping and interfacial mass transfer dynamics is achieved through advanced image acquisition and processing techniques. Visual observations are further complemented with micro-Raman spectroscopy, enabling *in situ* tracing of chemical species evolution during mass transfer, to achieve (semi-)quantitative process analysis.

In short, the research integrates a microfluidic platform with μRaman spectroscopy to track CO_2-water interfacial mass transfer and investigate the impact of wettability modifications that are generated by *in situ* atmospheric pressure plasma treatment.

The thesis is structured as a compilation of successive self-contained chapters, with each chapter addressing a key scientific question:

1. **Introduction**

The introductory chapter presents the foundational principles of CO_2 storage, highlighting the significance of wettability in governing interfacial mass transfer and CO_2 trapping mechanisms. It underscores the limitations arising from data variability and the scarcity of comprehensive datasets, which necessitate pore-scale experimental investigations. This gap in empirical research serves as the primary motivation for this thesis.

2. **Experimental Framework**

A subsequent chapter details the general experimental setup, common measurement techniques and tools used throughout the thesis, with a particular focus on the design of microfluidic devices.

3. **Development of a Novel Wettability Modification Method**

Key question: Can plasma be propagated and utilized for *in situ* wettability treatment of closed glass microfluidic devices?

Following an extensive state-of-the-art review, this chapter presents the technical advancements required to develop a robust wettability alteration technique based on atmospheric pressure plasma. We initiate by characterization of plasma propagation via light emission imaging under various electrode configurations, followed by analysis of plasma species by optical emission spectroscopy (OES) and measurements of plasma power and gas temperatures. The effects of treatment duration on wettability and aging behavior in different fluids (air and water) are systematically studied. A discussion on surface chemistry modifications is provided through X-ray photoelectron spectroscopy (XPS), unraveling the mechanisms underlying wettability alteration and its stability over time. Overall, we demonstrate that plasma can be successfully propagated in microfluidic devices, enabling appropriate wettability control for mass transfer experiments. The chapter is finished with a conclusive summary of the work, some preliminary results and perspectives.

4. **Effect of Wettability on Capillary Trapping and Interfacial Mass Transfer**

Key question: How does wettability influence capillary trapping and interfacial mass transfer at the pore scale?

Following a short introduction on scarce state-of-the-art data, we introduce our experimental procedures. Particle Image Velocimetry (PIV) is initially employed to extract fluid dynamics within different microfluidic geometries under single- and two-phase flow conditions. We determine a range of hydrodynamic conditions to be used in further experiments focusing on creeping flow. Then we briefly address the impact of wettability on capillary trapping potential which is a prerequisite for successful interfacial mass transfer experiments. Our results indicate that wettability is more important during drainage processes, influencing capillary trapping of water. Mass transfer experiments are conducted in microfluidic devices of increasing geometrical complexity, using both native and plasma-modified wettability surfaces under drainage and

imbibition injection modes. Acquired images of the mass transfer process are then analyzed and the results are presented with a comparative discussion of key parameters and their effects. Namely, we show that both CO_2 dissolution rates and water evaporation rates are increased on more hydrophilic surfaces, implying faster overall mass transfer and more rapid storage. Challenges, conclusions and perspectives are outlined at the end of the chapter.

5. *In situ* Raman Spectroscopy for Quantitative Dissolution Analysis

Key question: Can we follow the fluid-fluid interfacial mass transfer process by tracking chemical species evolution using Raman spectroscopy?

While the previous chapter is based on optical observation of mass transfer by following the fluid-fluid interface, no information is given about species transfer. To gain insight into the dissolution process, we propose to combine microfluidics experiments with Raman spectroscopy. Thus, this chapter initiates with a brief state-of-the-art on the CO_2 dissolution process and application of Raman spectroscopy to microfluidics. Next, we introduce the setup and optimization of parameters to acquire the signal of species in a microchannel. Experimental limitations and challenges encountered during the optimization are outlined. With the analysis of the *in situ*-acquired signal of dissolved CO_2 species, dissolution dynamics is examined both qualitatively and quantitatively. The mass transfer process is interpreted in conjunction with findings from PIV, capillary trapping, and previous dissolution experiments. Thus, we demonstrate a qualitative description of the process through species identification and a semiquantitative description of the dissolution process through analysis of Raman signal intensity.

6. Summary, Conclusion and Future Outlook

The final chapter presents a conclusive summary of the overall research findings. The practical spatio-temporal implications of wettability effects on mass transfer in the context of carbon storage are pointed out. Future research directions are proposed, emphasizing the need for further integration of microfluidic experiments with small and large-scale models to refine predictive capabilities for CO_2 storage.

Chapter 2 - Experimental microfluidic setup

The core technique of this study is glass microfluidics devices exploited over two laboratory platforms: (1) the main microfluidic platform coupled with a Raman spectrometer through a microscope depicted in Figure 22a, and (2) the atmospheric pressure kHz plasma station adapted for microfluidic applications depicted in Figure 22b). This chapter aims to introduce the basics of the microfluidic platforms with an emphasis on microfluidic devices, designed and utilized throughout this study on both platforms. Further specifics about each platform will be given in the designated chapters – plasma in Chapter 3, microfluidics in Chapter 4, and Raman spectroscopy in Chapter 5.

a)

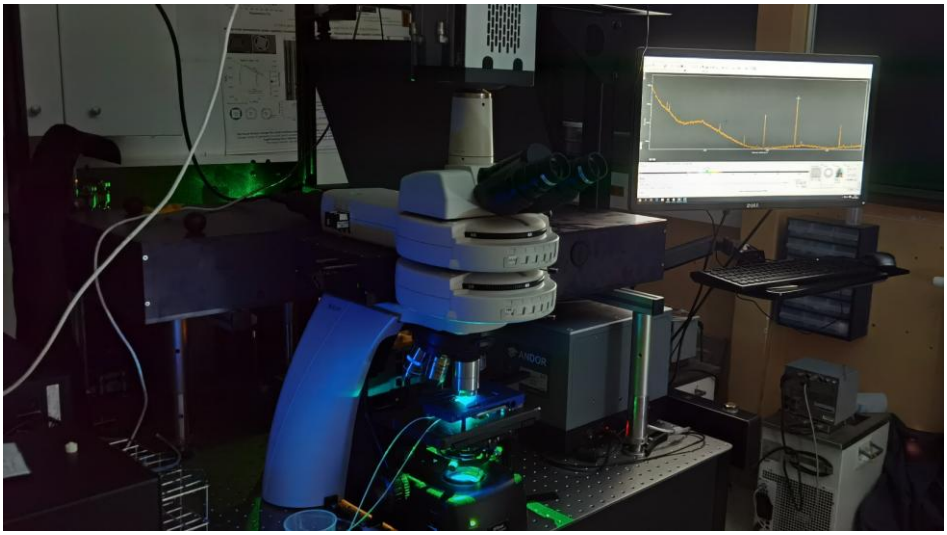

b)

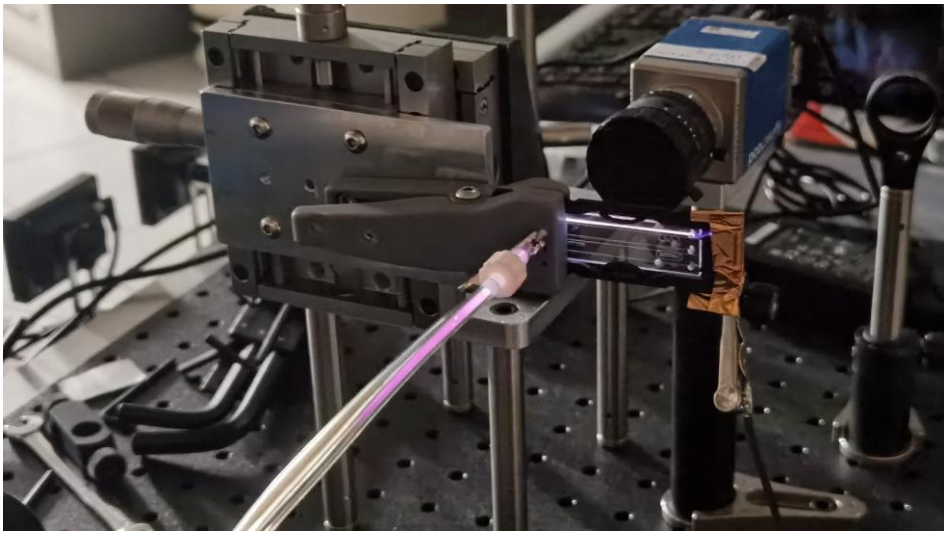

Figure 22 The main microfluidic platforms coupled with a Raman spectrometer through a microscope, featuring a green laser focused on the microfluidic device (a) and the atmospheric pressure plasma platform during plasma propagation in the microchannel (b).

I. Microfluidic platform

The microfluidic laboratory is comprised of two main microscopes providing a basis for optical investigations on microfluidic devices. An upright microscope (Nikon Eclipse Ni-U), equipped with a motorized stage (Prior Scientific PS3J100), is capable of operating in both transmission (utilizing internal light) and reflection mode (via mercury lamp Nikon Intensilight C-HGFI). To acquire high-resolution images, the microscope is paired with a camera (Andor Neo, sCMOS 5.50 Megapixel) operated by a designated Nikon software (NIS Elements). The upright microscope is coupled with a Raman spectrometer. The technical details of this μRaman setup will be presented in Chapter 5. The inverted microscope (Nikon Eclipse Ti2-U), equipped with a manually operated stage, is also well suited for investigations in both transmission and reflection modes. When paired with a high-speed Fastec camera (HS7), the setup can capture 2500 frames per second at 1080p resolution. This setup is primarily utilized to track rapid dynamic processes (e.g., fluid-fluid interface displacement, particle flow, etc). The microscope objectives are shared between the two stations and the list of their specifications is available in Table 6.

Table 6 A list of Nikon microscope objectives.

Configuration	Magnification	Numerical aperture (NA)	Working distance (mm)
Plan Apo	2x	0.1	8.5
LU Plan Fluor EPI P	5x	0.15	23.5
TU Plan Fluor	10x	0.3	17.5
CFI S Plan Fluor EL WD	20x	0.45	8.2 – 6.9
CFI S Plan Fluor EL WD	40x	0.6	3.6 – 2.8
CFI L Plan EPI CR	50x	0.7	3.9 – 3.0
CFI TU Plan EPI EL WD	100x	0.8	4.5

Details about pumps, tubing, and other auxiliary components are provided in Chapter 4. Image processing and procedures for contact angle determination are explained in Chapter 3, while image-based mass transfer analysis is covered in Chapter 4.

II. Microfluidic devices

To begin with, the terms “microfluidic device”, “micromodel”, and “microfluidic chip” are often used as synonyms. All our microfluidic devices are designed with the idea to trap one fluid and study interfacial mass transfer while continuous fluid flows. To that particular part of the microchannel, we refer to as the “main geometrical feature” or “trapping element”. The consumables for two-phase microfluidic experiments include ultrapure MilliQ water (resistivity = 18.2 Ωcm) and CO_2 gas (99,995 % purity). Different geometry designs are made to imitate a range of complexities found in natural porous systems. We designed two batches of microfluidic devices that were manufactured by specialized companies – one batch by Micronit from the Netherlands and the other by Klearia from France. Both batches are manufactured in borosilicate glass (D263) with the aim of having a rigid, inert and optically transparent porous media structure compatible with Raman spectroscopy and CO_2 utilization. Both companies manufactured devices of standardized dimensions (length × width × thickness = 45 × 15 × 1.8 or 2 mm) to fit in Micronit’s sample holder which is used to make the connection to tubing. Each device contains either 3 or 5 individual microchannels with particular geometry/ies. See the example in Figure 23.

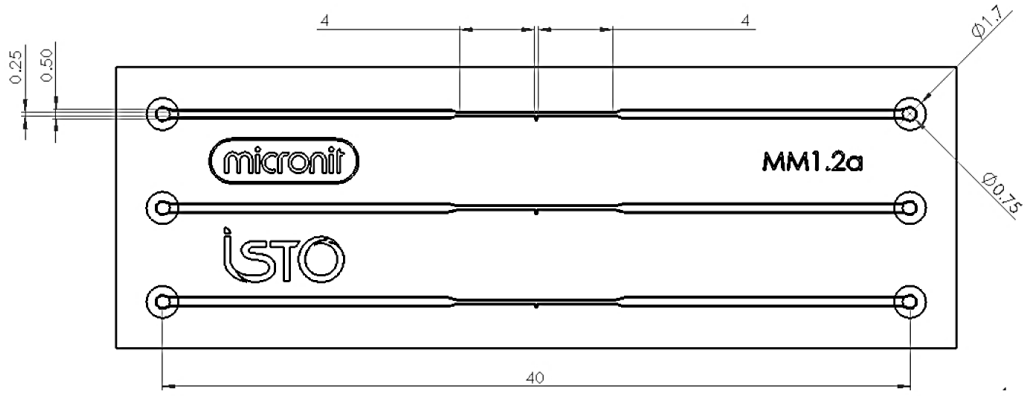

Figure 23 General dimensions of Micronit and Klearia devices. The dimensions are given in mm.

Rectangular microchannels are manufactured with a uniform nominal depth of 100 μm and a tolerance of up to 10%. Since the wet etching technique is applied in the production of both batches, microchannels have tapered walls with depth (see examples in Figure 24). Micronit devices are double etched, meaning that both top and bottom glass substrate have etched geometry with half depth (Figure 24a). On the contrary, Klearia’s devices are single-etched, meaning only one glass substrate is etched with a full-depth geometry (Figure 24b) and covered with a flat non-etched glass slab. The nominal width of the main channel starts at 500 μm, narrowing down to 250 μm before the main geometrical feature, just as shown in Figure 23.

a)

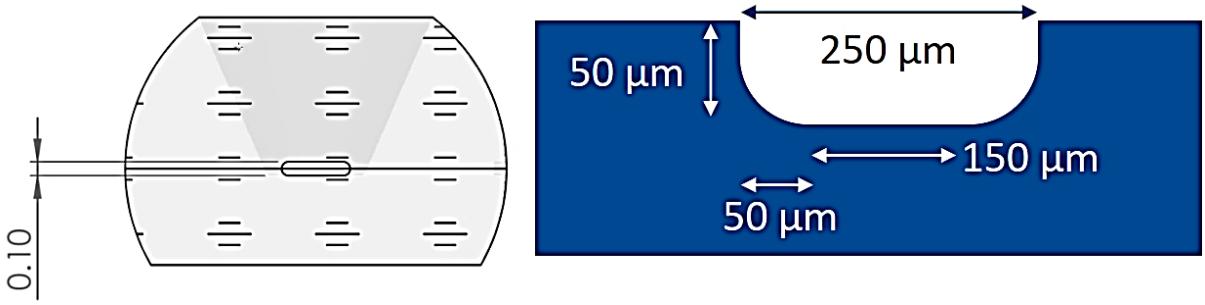

b)

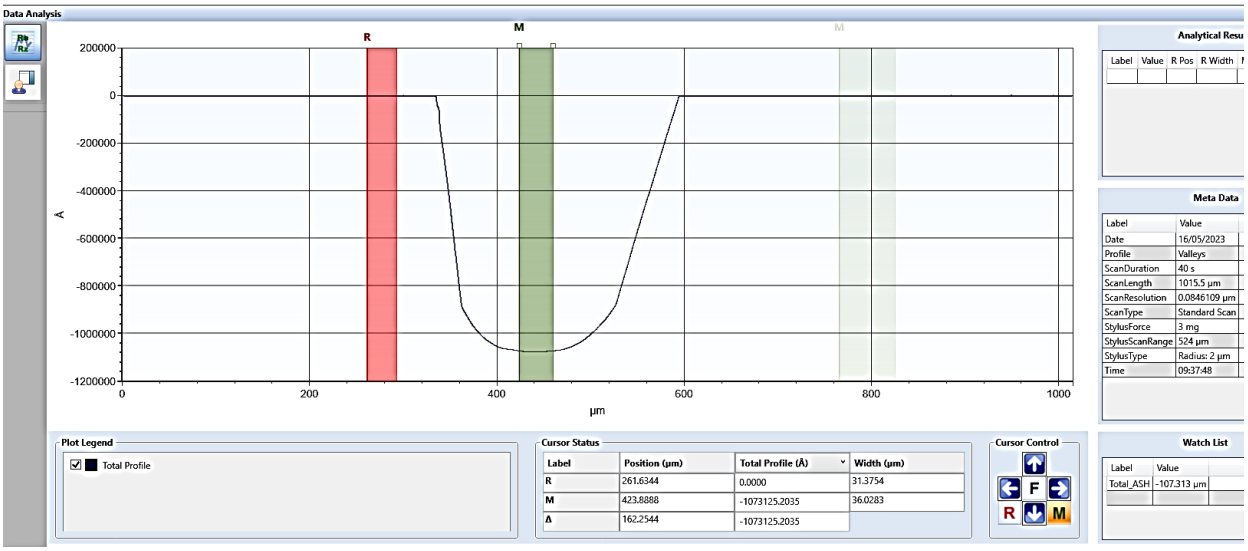

Figure 24 Schematics a) depicts a cross-section of Micronit's 250 µm wide channel made by utilizing double etched bonding. Graph b) depicts the measured depth profile from one 250 µm wide channel on Klearia's device. The maximum measured depth is 107.3 µm, within 10 % of tolerance. Both graphics are provided by the respective manufacturing companies.

To ensure redundancy for testing, especially in the case of plasma treatments, several devices with the same geometry are manufactured. The dimensions of each geometry are further elaborated in the following sections 1 and 2.

1. Micromodel geometries produced by Micronit

Nominal geometry designs produced in the first batch by Micronit, feature rectangular dead-end pores which will further be referred to as "pockets". The simplest geometry features just one single pocket (Figure 25a) which is also the most utilized geometry in the thesis. More complex designs feature two or six pockets attached in series, Figure 25b and Figure 25c, respectively. The nominal capacity of each 500 × 500 µm trapping element is 247 000 µm^2. Stacking multiple trapping elements in series aims to study their interaction during mass transfer and to better mimic parts of

complex natural systems. The round corners are common to all geometries, which comes down to the manufacturing process. The radius of curvature in corners is about 50 µm.

a) "Single pocket"

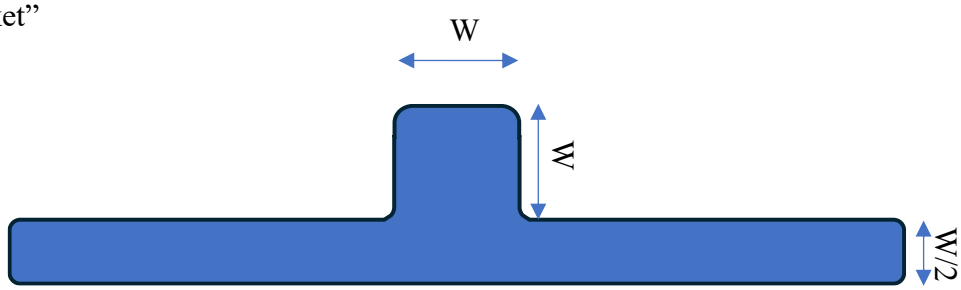

b) "Two pockets"

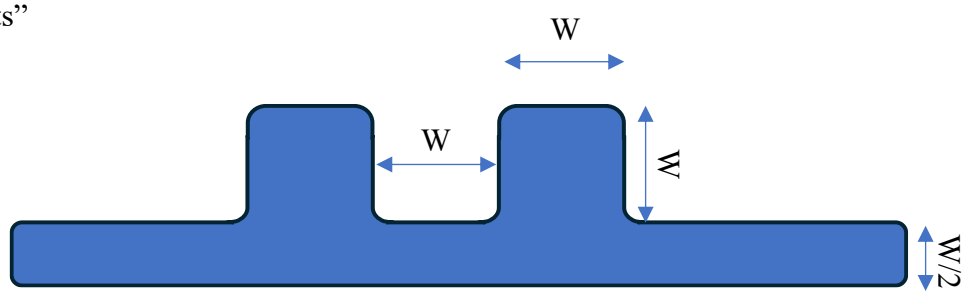

c) "Six pockets"

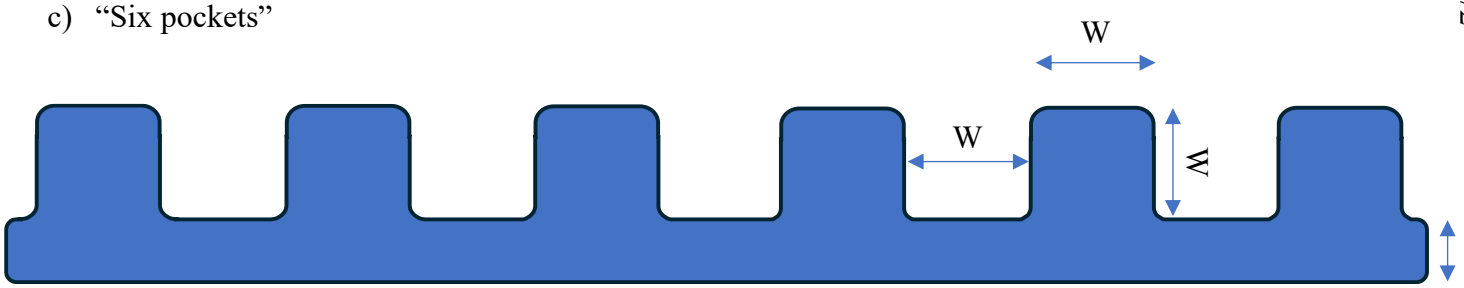

Figure 25 Nominal geometry designs produced by Micronit. Unit length W = 500 µm.

2. Micromodel geometries produced by Klearia

Microfluidic devices produced by Klearia feature another three trapping element designs with the aim of imitating more complex pore architecture. "Deep pocket" shown in Figure 26a, is equivalent to the "single pocket" in the previous figure with the goal of reducing the effects of advection from the main channel with the flowing fluid. The "L-pore" shown in Figure 26b features a bent dead-end pore and it is the most utilized geometry in the thesis from this batch. The nominal capacity of the L-pore trapping element (without underlying microchannel) is 572 000 µm^2. The "L-pore" geometry is designed to further increase the tortuosity of flowlines and create anisotropy depending on the flow direction. Lastly, the "pore doublet" shown in Figure 26c consists of two identical

simple rectangular pores connected in parallel. The goal of parallel geometry is to determine the influence of trapping elements on each other. The radius of curvature at the corners is larger compared to Micronit, measuring approximately 120 µm.

a) "Deep pocket"

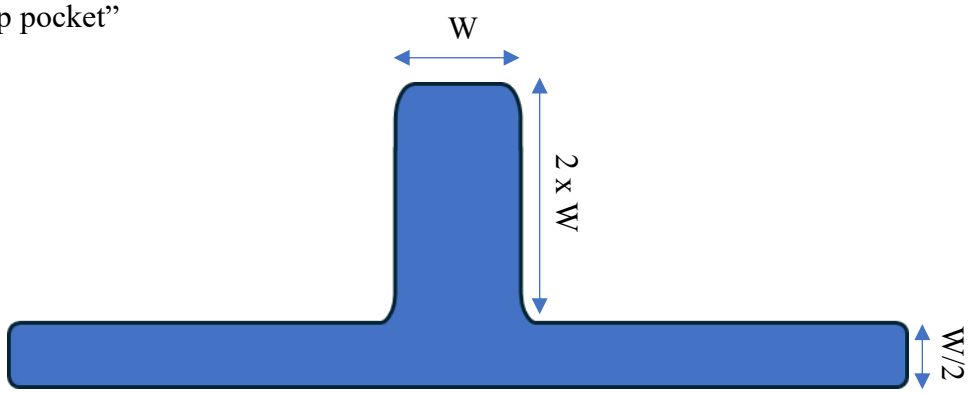

b) "L-pore"

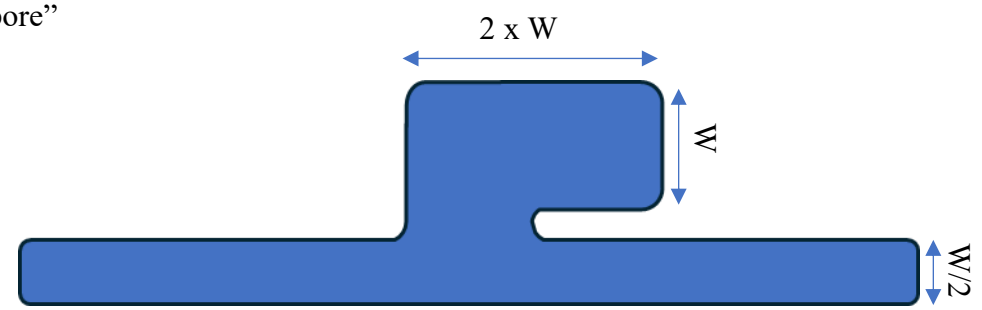

c) "Pore doublet"

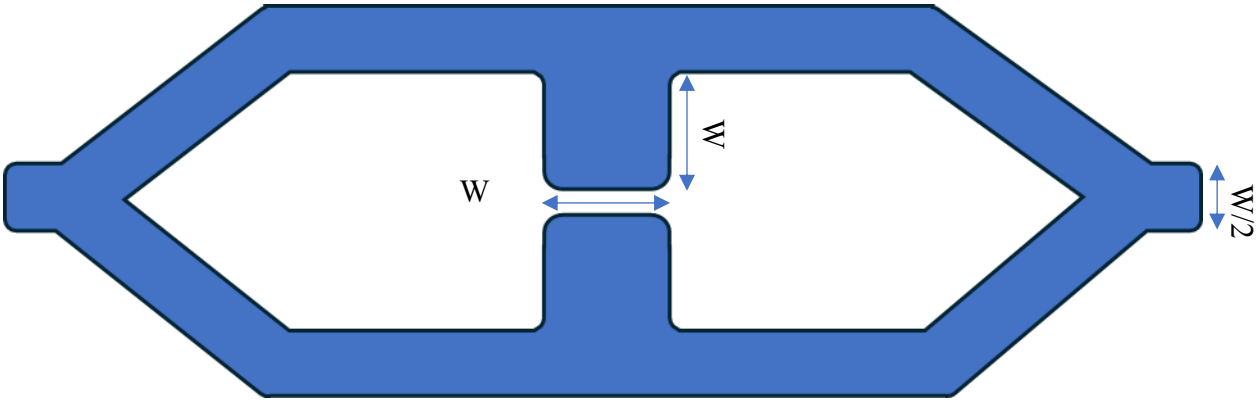

Figure 26 Nominal geometry designs produced by Klearia. Unit length W = 500 µm.

III. Conclusion

In this chapter, we introduced our research setup, composed of two platforms. A microfluidic platform coupled with a Raman spectrometer through a microscope is used for visual and chemical *in situ* analysis of mass transfer on a pore scale. An atmospheric pressure plasma platform is deployed with the objective of altering and controlling surface wettability by the injection of plasma into the closed microfluidic devices. The emphasis of the chapter is to define the design of glass microfluidic devices which are used throughout the thesis. The geometry of every microfluidic device is custom design by Sophie Roman and Viktor Gredicak. The idea behind our design was to generate simple pore representations and pore assemblies adapted to study processes of interest – interfacial mass transfer and capillary trapping. By designing devices with various geometrical complexities, we aimed to represent basic features of porous media like sharper or smoother edges, anisotropic pore geometry, parallel and serial connections between the pores, etc. The focus of this thesis are two geometries – single pocket and L-pore. The aim is to start with simple geometries, find the patterns of processes, and then gradually increase the complexity of pore structures to compare them and determine the effect of geometrical features, interference and upscaling as a part of future research.

Chapter 3 - Altering the wettability of closed glass microfluidic devices with *in situ* atmospheric pressure plasma

The objective of this chapter is to present our development that resulted in a novel, flexible and practical wettability alteration method for *in situ* treatment of closed glass microfluidic devices based on atmospheric pressure plasma. First, we will justify the need for a new wettability alteration of microfluidic devices. Then we present the state of the art concerning plasma propagation in confined spaces and its wettability alteration potential. Following is the methodological part of the development, characterization of plasma within glass microfluidic devices, wettability performance results, and finishing with a discussion about the mechanisms of alteration and aging supported by chemical analysis of surfaces.

I. Wettability alteration methods

In our context, customizable surface properties are essential. These properties are primarily influenced by the material, fabrication process, and additional treatments, but can also evolve during experiments. Among surface properties, wettability control has gained increasing attention, as it plays a crucial role in microfluidic studies (Zhu and Wang, 2022). To meet specific research requirements, the wettability of patterns engraved in micromodels must be carefully adjusted.

The most straightforward approach to adapt wettability is through the selection of manufacturing materials with inherent surface properties. For instance, microfluidic devices made in borosilicate glass (Nordin and Ahmad, 2015) and glass in general (Iglauer *et al*., 2014), exhibit strong to moderate water-wet behavior. The wetting properties of silicon depend on surface cleaning methods and storage conditions. Silicon with a native oxide layer exhibits strong water wettability, whereas hydrofluoric acid treatment removes the oxide layer, rendering the surface intermediately wet (Yang *et al*., 2014). Polymers such as PMMA (polymethyl methacrylate) tend to display weak water-wet characteristics (Bae *et al*., 2022). Interestingly, the polymer NOA 81 exhibits weak water wettability in terms of its static and advancing contact angles, while its receding contact angle indicates a moderate affinity for water (Wägli *et al*., 2010). SU-8 (Gao *et al*., 2008) and untreated PDMS (poly-dimethyl-siloxane) exhibit intermediate to non-water wetting properties(Chuah *et al*., 2015).

If the material choice is constrained due to experimental requirements or financial limitations, the wettability of microfluidic devices can be adjusted through surface treatments. In microfluidics, surface modifications are commonly achieved through chemical cleaning and coatings, pure plasma or plasma-assisted treatments, UV exposure, and other specialized methods (Glass *et al*., 2011; Shakeri *et al*., 2021).

Chemical coatings are usually accomplished through liquid chemical injection or by vapor deposition. Both approaches have their own perks and flaws which typically boil down to film thickness and uniformity, wear-resistance, temperature requirement and resistance, environmental friendliness/safety, equipment availability, cost, etc (Glass *et al*., 2011; Goncalves Canane, 2019; Holmberg and Matthews, 2009; Musbah *et al*., 2022). Chemical treatments can also be plasma-assisted or UV-aided which gives better control and speeds up the deposition process.

Silanization is arguably the most common chemical deposition process in microfluidics (Ansari and Imoukhuede, 2018; Glass *et al*., 2011; Vukovic *et al*., 2023). It is an inexpensive and efficient covalent coating method for the functionalization of material surfaces. For liquid chemical silanization, solvents like toluene, benzene, hexane, acetone and others can be incompatible with materials besides being flammable and toxic (Goncalves Canane, 2019). Some byproducts of reactions like methanol and hydrochloric acid can also be toxic and affect materials in their surroundings (Glass *et al*., 2011; Menawat *et al*., 1984). Silane reagents are predominantly used to turn surfaces hydrophobic, however, depending on the reagent, hydrophobic surfaces can be rendered hydrophilic as well (Arkles, 2011). For example, 3-aminopropyltriethoxysilane (APTES),

3-aminopropyltrimethoxysilane (APTMS) and 2-[methoxy(polyethyleneoxy)propyl]trimethoxysilane (PEG-silane) create hydrophilic surfaces (Kovach *et al*., 2014; Nguyen *et al*., 2014; Zeng *et al*., 2011), while hexamethyldisilazane (HMDS) silane, polytetrafluoroethylene organosilanes (PFS) and many other silane reagents make surfaces hydrophobic (Arkles, 2011; Glass *et al*., 2011; Goncalves Canane, 2019).

Besides silane compounds, other chemicals for surface treatments exist and are in use. For example, in a study by Yirijor *et al*. (2022), PDMS substrates were coated with sodium alginate, polyethylene-glycol (PEG) and poly(lactide-co-glycolic acid) (PLGA) after which measured water contact angles had values of 12, 25 and 42.2 ° respectively. Trantidou *et al*. (2017) measured the 25 - 37 ° water-air contact angle on PDMS after polyvinyl alcohol (PVA) treatment. An extensive overview of PDMS surface treatments and functionalization with chemicals is provided in a paper by Shakeri *et al*. (2021).

To avoid the challenges associated with using various microfluidic device materials and multiple chemical treatments; many of which can be toxic, expensive, or require specialized handling, equipment and protocols; we sought an alternative approach. Therefore, we opted for glass devices with inherent water-wetting properties imitating natural rocks, compatible with gas-phase applications (CO_2 injection), and resilient to significant mechanical and thermal stress.

Due to these challenges, we turn to plasma as a promising, straightforward yet robust method for tuning wettability, particularly well-suited for closed microfluidic systems. Plasma offers a clean, dry, and controllable alternative to chemical treatments, with fewer concerns regarding toxicity, solvent compatibility, and material degradation. Moreover, plasma treatments can be spatially selective, allowing fine control over wettability in patterned microenvironments. As a result of the material limitations, chemical handling constraints, and the need for precise surface modification, we explore the potential of plasma-based treatments as a versatile alternative. Compared to traditional methods, plasma offers the added benefit of compatibility with microfluidic geometries and experimental conditions relevant to subsurface studies, making it a compelling candidate for wettability control in porous media research. The fundamentals of plasma, its behavior in confined spaces, and its suitability for wettability modification will be presented and justified for our use in the following section (Section II).

II. State of the art: plasma and application to microfluidics as a wettability alteration method

This section is divided into several subsections with the aim of presenting basic characteristics of plasma in use, followed by the state of the art on plasma propagation in confined spaces like capillaries and finally presenting achievable wettability performance in terms of contact angle, treatment and aging time. All information is presented with the idea to make decision, support and justify the design of our setup to successfully propagate plasma in closed microfluidic devices and perform the wettability alteration on glass surfaces with improved performance.

1. Plasma basics

Plasma is usually referred to as the "fourth state of matter". Essentially, it is an ionized gas, electrically quasi-neutral, exhibiting collective behavior. Due to quasi-neutrality, fluctuations in charge densities occur over a characteristic distance known as the Debye length (λ_{Debye}), but the plasma remains neutral because the densities of ions and electrons are nearly equal (Goebel and Katz, 2008). This neutrality holds at larger scales, beyond the plasma length (λ_{plasma}), which is much greater than the Debye length ($\lambda_{plasma} >> \lambda_{Debye}$). Collective behavior in plasma means that the movement of charged particles creates disturbances in the local charge balance, generating an electromagnetic field that influences the plasma as a whole through long-range Coulomb forces.

Unlike thermal plasma found in the sun or lightning, plasma used for surface modification is a non-equilibrium plasma, where electrons are at high temperatures (in 10s of thousands of Kelvin) while the background gas particles, ions and neutral species, keep the overall plasma temperature low (typically below 500 K) (Turkoglu Sasmazel *et al*., 2021). Highly energetic electrons facilitate chemical reactions while relatively low overall temperature prevents thermal degradation. Hence, it is non-destructive to bulk materials and sometimes even safe to touch, finding its use in biotechnology, medicine, agriculture, clean energy and many other applications. For example, non-thermal plasma has been demonstrated to kill tumor cells, deactivate certain pathogens and promote wound healing without damaging healthy tissue (Choi *et al*., 2021; Chung *et al*., 2020; Maho *et al*., 2021). In the field of agriculture, researchers are investigating its potential for enhancing seed germination (Da Silva *et al*., 2017; Guragain *et al*., 2022). Again, here we want to explore the use of non-thermal plasma for surface modification of microfluidic devices without damaging them.

The most common way to ignite the plasma for the aforementioned purposes is to expose gas to a strong electric field as a source of energy. Hence, these plasma sources are classified according to the ascending frequency range in the following manner. At the lowest end, there is a single-shot, followed by the kHz region, then micro and radio waves going up to the GHz region, and finally, continuous emission (Laroussi and Akan, 2007; Mackie *et al*., 1997; Shao *et al*., 2018). The type of signal can be AC (sinus) or DC pulsed. Regardless of the source, three principal reactions that take place in plasma generation are excitation, dissociation and ionization (Turkoglu Sasmazel *et al*., 2021). In the beginning, electrons are being accelerated in the electric field, drifting between

the heavier gas particles (atoms/molecules) and causing mostly elastic collisions where energy losses are minimal. This process increases the energy of both free electrons and ionic particles. After sufficient energy is accumulated in the drifting process, electrons finally collide with atoms/molecules in an inelastic manner, transferring much of the gained energy. In the case of molecular gases, intermolecular bonds can absorb energy which can cause electronic, vibrational or rotational excitation but the molecules (M) can also ionize, dissociate or attach the electron and form a new bond (e.g., $O_2 + O + M \rightarrow O_3 + M$) depending on provided energy. Atoms have fewer interaction outcomes which include electronic excitation, ionization and electron attachment (the latter is not in the case of noble gases).

At a certain field strength, the applied voltage will exceed the threshold of a gas (dielectric material). If there are no pre-discharges, plasma will ignite, and the voltage will drop due to the existence of a lower resistance pathway created by electrons and ions. This moment is called ignition or breakdown voltage. The dependency of the breakdown voltage (V_B) on pressure (p) and distance between electrodes (d), i.e., pd characteristic, is very well known as Paschen's law (Figure 27). The shape of the Paschen curve and thus breakdown voltage is very much influenced by the atomic/molecular nature of a gas, characteristic ionization energy and different mean free paths (Encyclopedia Britannica, 2012; Yadav *et al*., 2008). The molecular nature of gas is responsible for energy dissipation through molecular vibrations. Higher characteristic ionization energy implies a stronger electric field required to strip an electron from the outer shell of an atom/molecule. A longer mean-free path enables free electrons to be more accelerated in the electric field, i.e., gain more energy. Despite high ionization energy, the breakdown voltage is lower in noble gases due to their atomic nature and a larger mean free path, allowing them to use energy more efficiently on ionization. Helium, argon, neon and their mixtures are thus frequently used noble gases in atmospheric pressure cold plasma, depending on the specific application. Helium's characteristic is particularly attractive near atmospheric pressure conditions (760 Torr), offering lower ignition voltages for the same electrode distance. In general, breakdown voltage is also dependent on a multitude of other parameters like shape, material and temperature of electrodes, frequency of the source, etc (Babich and Loiko, 2016; Radmilovic-Radjenovic *et al*., 2013; Yamasaki *et al*., 2013).

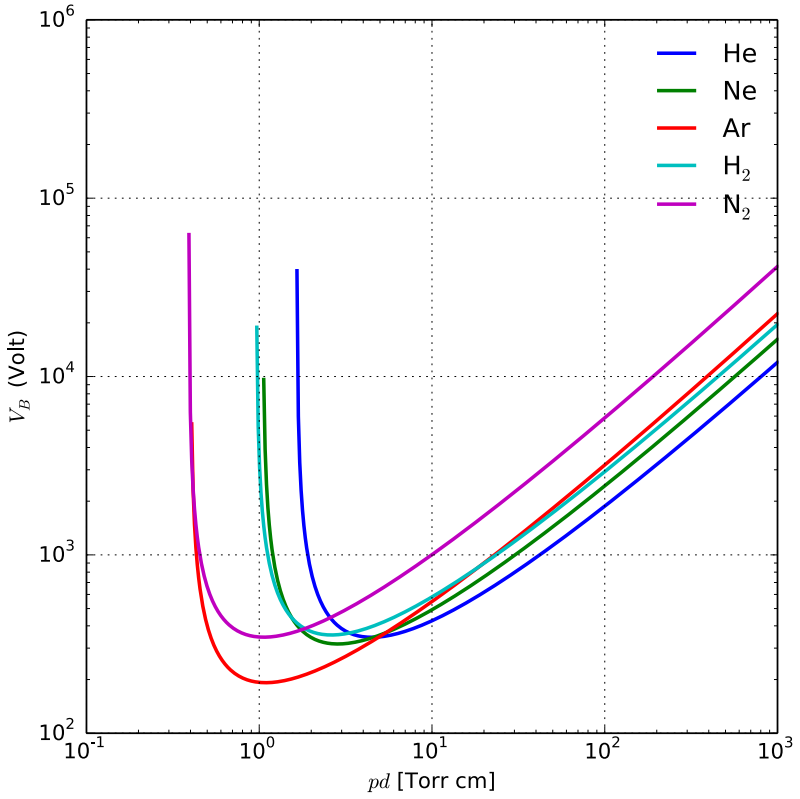

Figure 27 Paschen curves for He, Ne, Ar, H_2 and N_2 showing the dependency of breakdown voltage (V_B) on pd characteristic. Taken from Lieberman and Lichtenberg (2005).

At atmospheric pressure and higher, the breakdown behavior is better explained through the streamer mechanism. Streamers are defined as self-organized, ramified ionization fronts whose propagation in ambient air depends on the ratio of gas density (Nijdam *et al.*, 2020). The theory was first introduced by Loeb and Kip (1939), Meek (1940) and Raether (1939) to support experimental observations of the breakdown in these conditions. The theory predicts that when the impact ionization avalanche reaches a certain size (Meek's criterion), electrons which have higher mobility than ions, will propagate faster and accumulate at the spherical head, while slower ions will create a tail (Lehtinen, 2021). This charge separation increases local electric field strength, comparable to the external field. Due to the locally increased electric field strength and UV photons emitted in the de-excitation process, other atoms further away can be ionized and create new avalanches through photoionization and electron impact ionization (Lehtinen, 2021). The result is a very fast event with propagation speeds on the order of 10^5 - 10^6 m/s (Luque *et al.*, 2008; Raizer *et al.*, 2010). With the streamer breakdown, a highly conductive channel is created. Based on their polarity, streamers may be characterized as positive or negative. A positive streamer (illustrated in Figure 28a) has a region of net positive charge at its head due to charge distribution. As a result, it propagates toward the negatively charged cathode, moving against the electron drift but in the direction of the electric field (Lu *et al.*, 2014; Nijdam *et al.*, 2020). On the contrary, the negative streamer shown in Figure 28b) propagates in the direction of the electron drift, i.e., from the cathode

towards the positively charged anode (Lu *et al*., 2014; Nijdam *et al*., 2020). Although propagation in the direction of electron drift appears to be a more natural movement, positive streamers in the air are observed to initiate more readily and travel faster and farther (Luque *et al*., 2008; Nijdam *et al*., 2020).

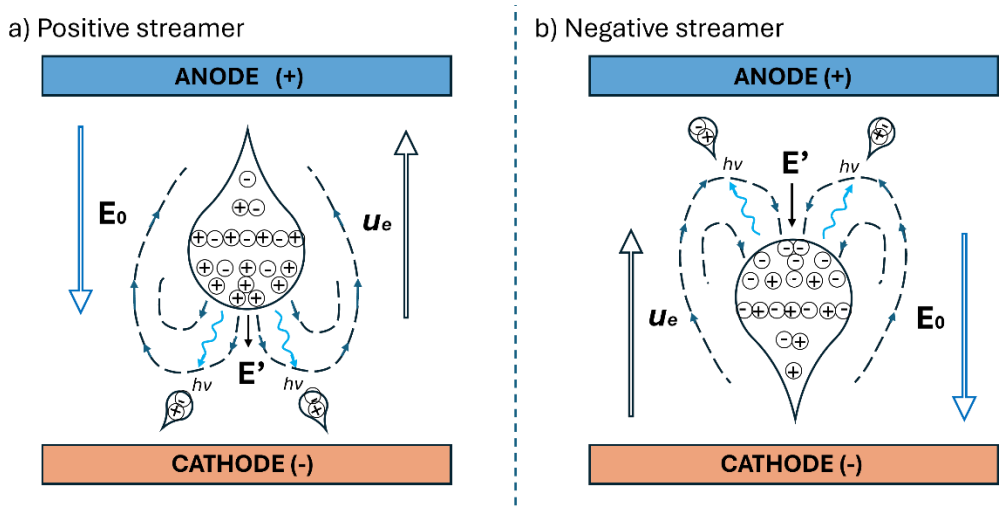

Figure 28 The mechanisms of streamer propagation. The direction of the electric field E_0 and electron drift with velocity u_e are denoted with an arrow, secondary electric field E' is depicted with dashed equipotential lines, while emitted plasma photons carrying certain energy (hv) are depicted with a wavy blue line.

To clarify, for plasma ignition, two electrodes are generally needed, although one may be ambient air or ground. Electrodes are typically called cathode (negative) and anode (positive) if their polarity is to be emphasized; or discharge (active) and ground (reference) electrode to describe their function. Several standard electrode configurations are relevant to surface treatment applications (Turkoglu Sasmazel *et al*., 2021; Yamasaki *et al*., 2013). The electrode configuration, together with applied voltage, defines the type of electrical discharge that can be attained.

Dielectric barrier discharge (DBD) is a type of plasma created between two electrodes separated by a dielectric, i.e., insulating material (see Figure 28a). The reason for introducing a dielectric barrier is to limit current and prevent arc formation, a type of thermal plasma. Countless variations of electrode configurations exist, but at least one is always covered with a dielectric material and thus not in direct contact with a gas. DBD-induced plasma produces filamentary or diffuse discharges which both appear uniform to the naked eye (Booth *et al*., 2022; Brandenburg, 2017). Compared to corona discharges, DBDs have lower operational costs due to lower energy consumption and more uniform discharge, yet they are dependent on the discharge gap and electrode polarity (Wu *et al*., 2018). DBDs are widely used in plasma-assisted chemical deposition for surface modification, as well as in applications such as biomedicine and biotechnology. The key advantage of the DBD configuration is its reduced risk of arcing, which is particularly crucial when working with living tissues to prevent damage or cell death. For a more in-depth review of DBD, the reader is advised to consult a paper by Brandenburg (2017).

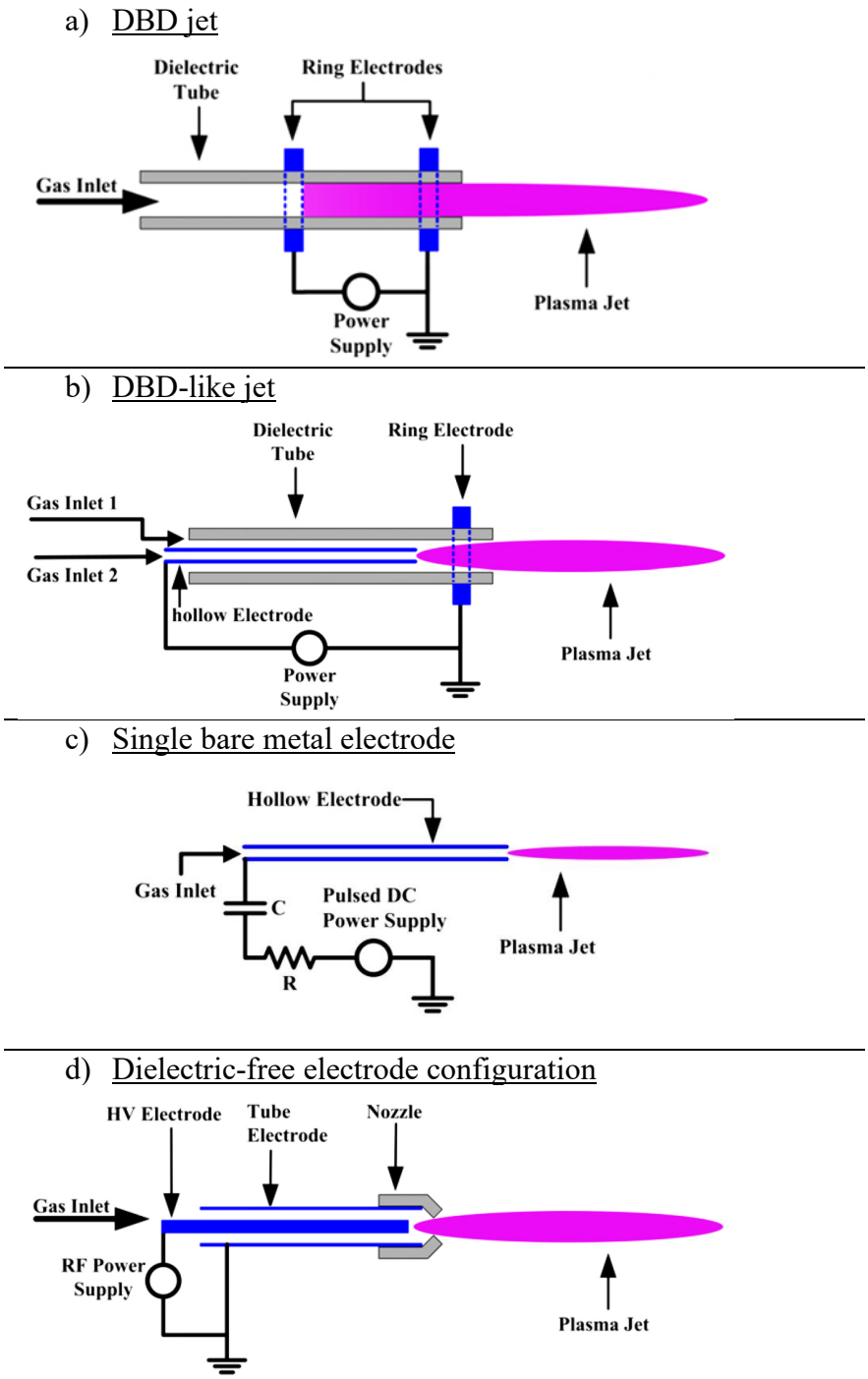

Figure 29 Four different APPJ electrode configurations are displayed as setup cross sections. Taken from Lu et al. (2012).

Atmospheric pressure plasma jet (APPJ) is a type of plasma that can propagate beyond electrode confinement (Winter *et al.*, 2015) which can be especially advantageous for microfluidic applications. Plasma jet discharges produced by kHz sources are often called "guided streamers" as their repeatable propagation is guided by the gas flow and not by itself, like in the case of classic

streamers. Streamers are also considered precursors to plasma jet (Jiang *et al*., 2009; Nijdam *et al*., 2020). The primary interest here is the plasma jet produced in the kHz frequency region.

According to Lu *et al*. (2012), there are four predominant electrode configuration groups for APPJ and these are (i) DBD jets, (ii) DBD-like jets and (iii) single bare metal electrode (SE) jets, (iv) dielectric-free electrode (DFE) jets, visible in Figure 29. Each configuration could be advantageous in certain applications, however single bare metal electrode propagates a plasma jet to comparable lengths as other configurations, yet under reduced applied voltage (Jiang *et al*., 2009). Therefore, the strengths of APPJ produced by a single bare metal electrode configuration are found in a flexible, reproducible and cost-effective generation of plasma, suitable for applications in microfluidic devices, just like ours.

In addition to the setup configuration, the choice of plasma gas is equally critical, as it governs both the fundamental plasma characteristics and its interactions with the surface. When the effects of gas on plasma are considered, observations can be made in breakdown voltage, plasma power, and propagation length of a jet inside and outside of the feeding tube. It is also common to look at optical emission spectra (OES) for detailed qualitative analysis of plasma species. The basis for plasma jets are noble gases which provide a low breakdown voltage. Molecular gas impurities are typically present and/or introduced in concentrations of less than a few percent for surface treatment to increase the production of reactive species (Lu *et al*., 2012; Schmidt-Bleker *et al*., 2015), while studies that look into plasma propagation look at all ratios. To achieve propagation of plasma plume beyond the electrode and tubing confinement, it is crucial to use noble gases with or without a minor amount of molecular gas impurities. Some commonly used gases for atmospheric pressure plasma are He, Ar and Ne, typically being the carrier gases, with the addition of O_2, N_2, H_2, Cl_2, CH_4, CO_2, CO, NH_3 and their mixtures as impurities (Ma *et al*., 2023).

The presence of impurities changes the behavior of the breakdown voltage in a nonlinear way. When two gases are mixed, a metastable state of one gas can assist the ionization of another gas by providing "seed" electrons. This process is called Penning ionization and it helps to initiate a breakdown at lower electric fields. The effect is only possible if the ionization energy of impurity molecules is lower than the excited levels of the noble gas. For example, metastable helium can ionize nitrogen atoms (N_2 to N_2^+) while argon cannot ($E(He^*) = 20.0$ eV $\geqslant$ E(ionization of N_2) = 15.5 eV > $E(Ar^*) = 11.9$-15 eV) (Jitsomboonmit *et al*., 2012; Kitsara *et al*., 2022). This phenomenon is particularly significant in the context of surface modification, as it can influence functionalization reactions.

Effects of gas composition on plasma jet propagation in ambient air have been researched as well. Wu *et al*. (2018) and Clement *et al*. (2011) observed that a small amount of impurities in the carrier noble gas can be beneficial, however, an increase beyond approximately 2% tends to hinder propagation.

Besides gas composition and earlier discussed electrode configuration; Xiong *et al*. (2009), Javanmard and Pouryoussefi (2023), and Jiang *et al*. (2009) report a positive influence of applied

voltage, gas flow rate, pulse width and the diameter of the nozzle on the length of plasma propagation; obviously to a certain degree. The effect of confinement will be further explained in the following section (2) as it represents a challenge for the application of microfluidic devices.

2. Plasma propagation in capillaries

One of the largest challenges to overcome for the successful application of plasma to microfluidics is the propagation in micrometer-sized channels. Covering all surfaces is a prerequisite for good wettability treatment with plasma. Hence, it is essential that the propagation of plasma is achieved through the desired length of a micromodel. Low-pressure plasmas are already utilized in microfluidics for the treatment of open flat surfaces of polymeric materials before bonding in the chamber/oven-type reactors. At low pressure however, the Debye length is commonly higher than 100 μm (Lieberman and Lichtenberg, 2005), posing a limiting factor for propagation in microchannels of similar dimensions and hindering its use as a wettability-alteration tool. The non-equilibrium atmospheric pressure plasma has the Debye length in the range of a couple of tens of μm (Brahme *et al.*, 2018; Wu *et al.*, 2023) and could potentially be used in microchannels. Propagation length could also be reduced as a consequence of the pressure buildup at high flow rates by reducing the mean free path of electrons. Therefore, a good balance in pressure needs to be found.

The second challenge is the manipulation of plasma propagation in complex microchannel geometry reflected in structural features like bends, branching, variations of cross-sectional dimensions, and elements (nearly) without flow, like dead-end channels. Thus, the uniformity of plasma propagation and variations of contact with surfaces might pose an issue if homogeneous treatment is needed. To gain a clearer understanding of plasma potential in microfluidic devices, we present a literature review, focusing primarily on work conducted on capillaries as the nearest analog and an initial feasibility reference.

Firstly, many researchers have realized the difference between plasma propagation in confined environments and free discharges in ambient air, which was mentioned in the previous subsection. Results of a comparative study by Xiong *et al*. (2009) indicate that the propagation length of atmospheric pressure helium plasma is reduced when propagated directly into the surrounding air compared to propagation in the tube, as illustrated in Figure 30. The reason for that is the diffusion of surrounding air into the helium gas stream compared to a controlled environment shielded by the glass tube. As the environment found in thin capillaries is the nearest analog to microfluidic systems, this result favors the idea of using plasma jets for surface treatment of microfluidic devices.

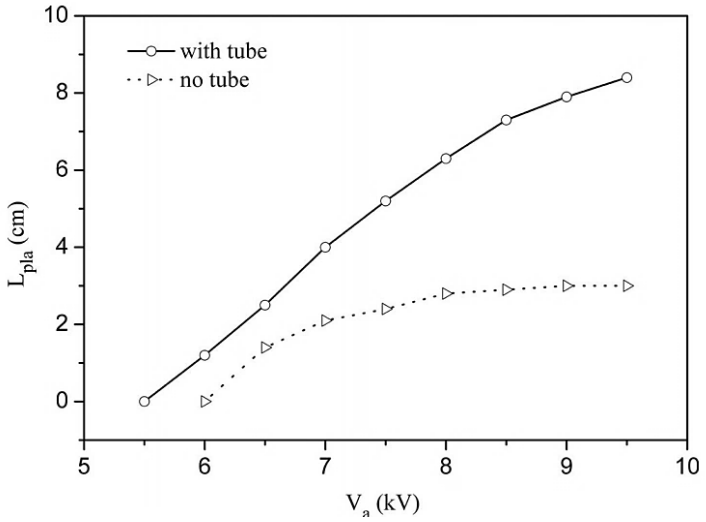

Figure 30 The propagation length of helium atmospheric plasma in confined and non-confined environment. The glass tube has an inner diameter of 800 µm. Taken from Xiong et al. (2009).

In the microfluidic study, Lepoetre *et al*. (2021) explored a new catalyst-free, atmospheric-pressure plasma-enhanced process of cyclohexane amination with ammonia. A gas-liquid microfluidic reactor was designed as a long winding channel, as illustrated in Figure 31a, with integrated electrodes placed above and below the channel, shown in Figure 31b. In the mentioned geometry, researchers successfully ignited plasma in ammonia and successfully performed an amination reaction. Therefore, this study reinforces the feasibility of igniting and propagating plasma in long micromodel channels with similar cross-section dimensions.

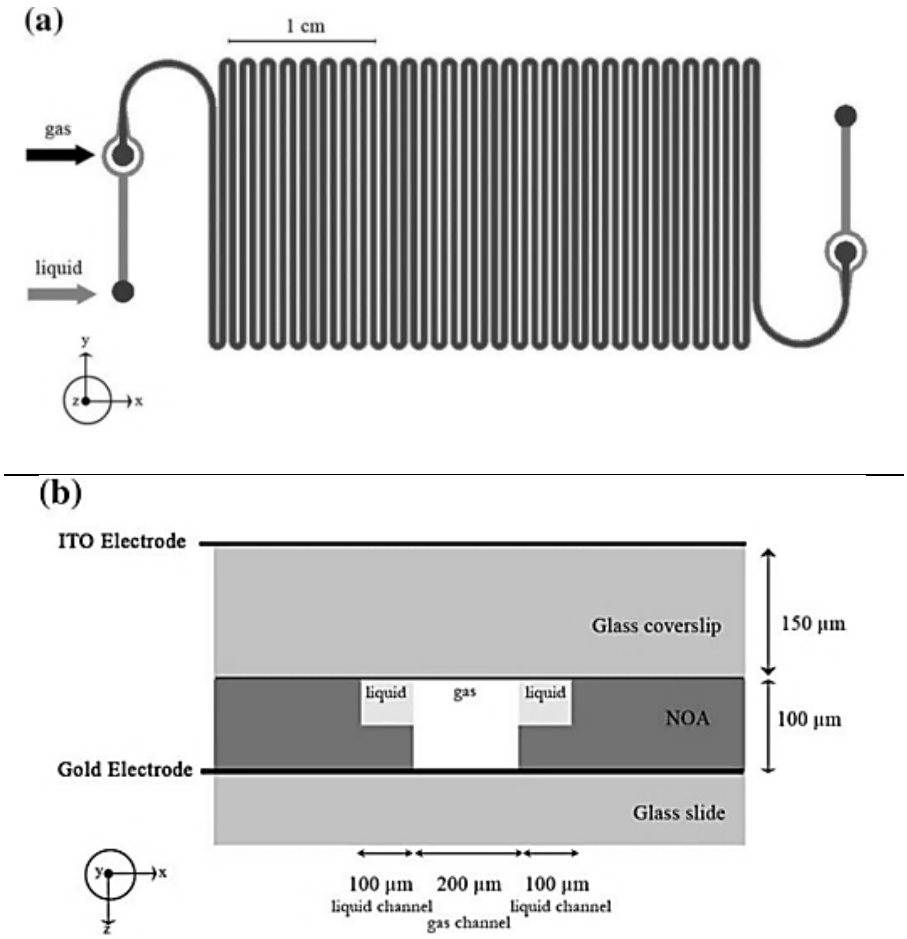

Figure 31 The top plane view of microreactor (a) and a cross-section of a channel (b). Taken from Lepoetre et al. (2021).

Wu *et al*. (2016) reported the dependency of atmospheric pressure plasma jet length on the diameter of a straight propagation tube. In the tested range of tube inner diameter (0.6 – 4.0 mm), helium plume propagation length indicates proportional behavior (see Figure 32). With a channel length of 4 cm and varying cross-section down to 250 × 100 µm, plasma propagation through the entire length of microfluidic devices might be challenging.

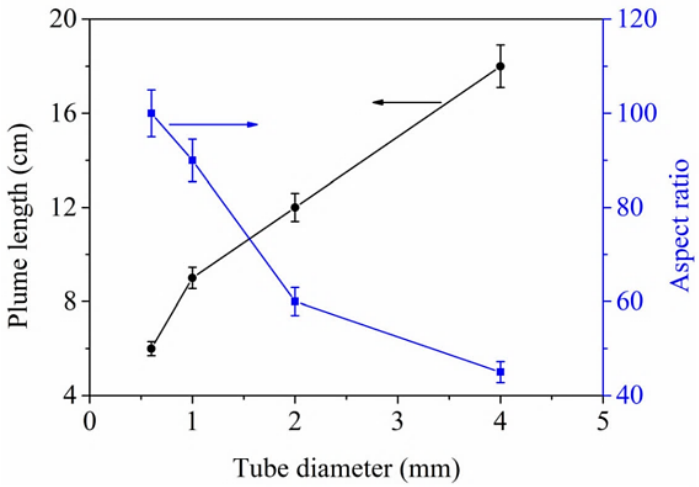

Figure 32 Scaling of plume length produced under constant electric conditions (pulsed DC voltage of 6 kV and 5 kHz) and gas flow rate (1 l/min). Aspect taken from Wu et al. (2016).

In an experimental study by Brahme *et al*. (2018), an atmospheric pressure plasma jet was ignited with a radio-frequency source with the aim of studying plasma propagation in Pyrex capillaries. The capillaries ranged in inner diameter between 100 µm and 1.5 mm. By utilizing helium and argon, they first calculated the Debye length from typical literature data relevant to their work. As seen from Table 7, both Debye lengths are smaller than the smallest inner diameter of a capillary, granting a possibility for both gases to propagate plasma in micrometer-sized capillaries. With slightly different input data, Jain and Bruggeman (2023) calculated the Debye length for a positive streamer made in helium to be between 1 and 2.5 µm, indicating the expected range. The propagation results from Brahme *et al*. (2018) indicate that both argon and helium jets can penetrate 500 µm diameter capillaries. With further adjustments of capillary position and utilization of ground electrode, the argon jet was able to penetrate a 250 µm diameter capillary while there was no penetration observed in the case of the helium jet. No plasma could propagate in a capillary with a diameter of 150 µm. Overall, the results show that the type of gas dictates the minimum confinement required for plasma propagation, with penetration typically occurring in dimensions one to two orders of magnitude larger than the Debye length.

Table 7 The Debye length in argon and helium atmospheric pressure plasma. Adapted from Brahme et al. (2018).

	Argon jet	**Helium jet**
Electron temperature (eV)	2	2
Electron density (m^{-3})	10^{19} - 10^{20}	$5x10^{17}$ – $5\text{-}10^{18}$
Debye length (µm)	**1 - 3**	**5 - 15**

A numerical study by Xiong and Kushner (2012) demonstrated that plasma can propagate even through very narrow tubes with multiple bends between the inlet and outlet. A capillary-bounded atmospheric pressure plasma jet was created in a 600 μm wide and 15 cm long channel filled with Ne/Xe = 99,9/0,1 mixture (see Figure 33). They concluded that streamer heads created by the high voltage (+/- 50 kV) can be propagated by tens of cm from the source to the target. Moreover, in the case of tortuous pathways, the streamer head tends to switch to the opposite side of the wall when the channel curvature changes (see selected time frames zoomed in the middle portion of Figure 33). This behavior is due to the relative orientation between the electric field in the wavefront and the local capillary channel. Overall, the results of this study indicate that propagation of plasma in complex tortuous geometries in microfluidic devices should not be an issue, although surfaces might not get uniform treatment.

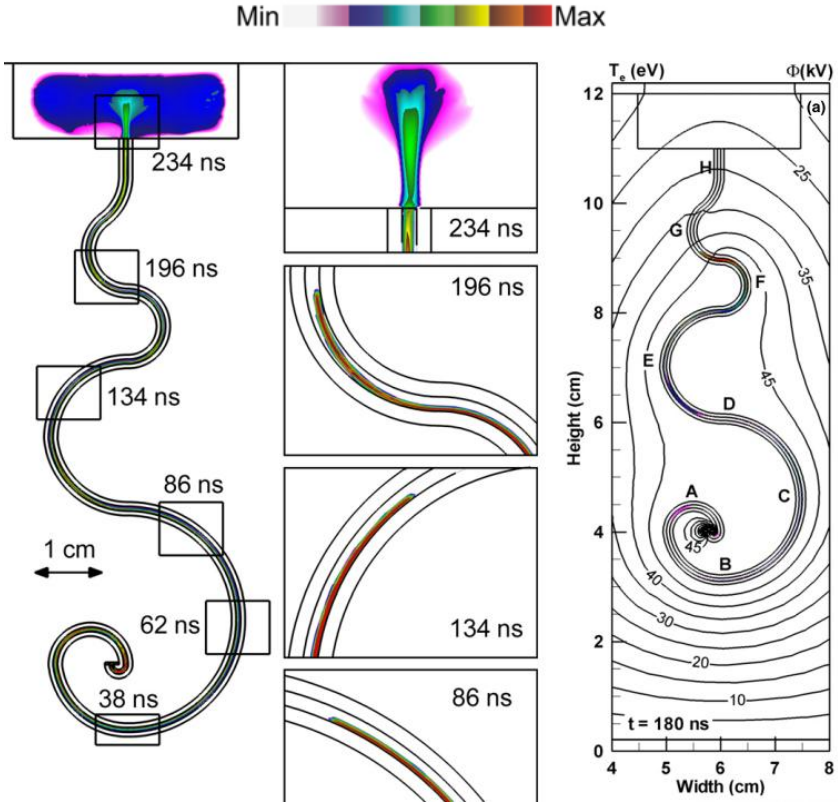

Figure 33 Plasma propagation in a tortuous capillary with certain timeframes showed zoomed-in and equipotent lines of electric field for 180 ns into the simulation. Taken from Xiong and Kushner (2012).

The last presented study, by Xiong *et al.* (2012), investigated splitting and merging of plasma (see Figure 34). A DBD-like generation setup was designed to produce atmospheric pressure fast streamer heads in neon. The generation setup was attached to the circular loop 5 cm in diameter, made of borosilicate glass tubes with a 4 mm of inner diameter. Experiments were backed up with a numerical model which provided additional information for the study. The results from both sources indicate that the propagation wave tends to be in wall-hugging mode, not necessarily the

same wall side (inner or outer) during the entire propagation. The splitting and merging ability of plasma may also be of great benefit for treatment in complex micromodel geometries like pore doublet.

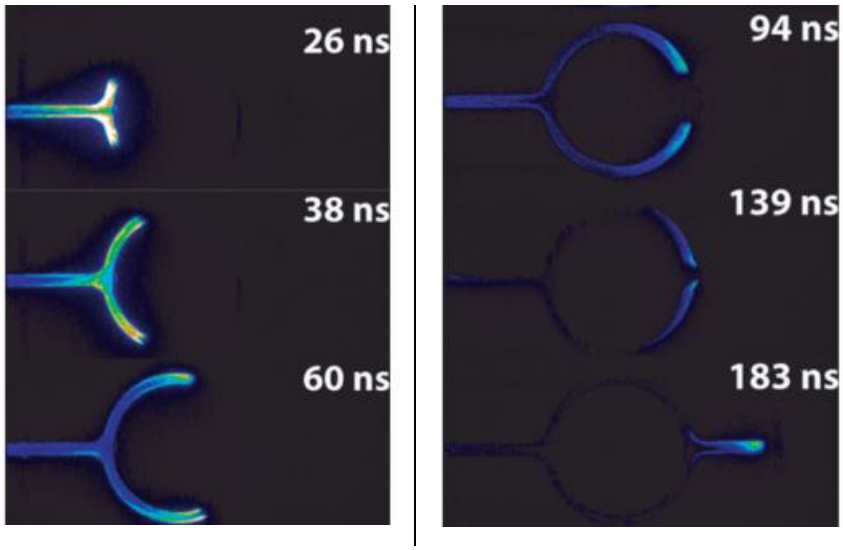

Figure 34 The splitting and merging of the fast streamer head. Taken from Xiong et al. (2012).

A summary of other relevant studies is presented in the table below. We included experimental and numerical studies utilizing different gases and capillary/tube materials, primarily targeting glass capillaries of micrometer size. Overall, studies show that plasma jets can achieve millimeter to centimeter length scales in which seems to be appropriate for our research.

Table 8 Review of plasma capabilities in capillaries. All reviewed plasmas are atmospheric pressure plasma jets sorted with increasing confinement. "Exp.", "Num.", "PTFE", "PE" and "ID" stand for "experimental", "numerical", "Teflon", "polyethylene" and "inner diameter", respectively.

Author	Approach and plasma gas	Confinement and material	Propagation length
Johnson *et al*. (2011)	Exp. He	1.6 - 9.5 mm PTFE tube	@ ID 4.8 mm -> 20 cm
Robert *et al*. (2013)	Exp. Ne	4 mm borosilicate capillary	1 m
Xu *et al*. (2015)	Exp. He/Ar + O_2	4 mm PVC tube	Not mentioned
Onyshchenko *et al*. (2015)	Exp. Ar	0.28 - 3 mm PE tubes	@ ID 0.28 mm -> 10 cm
Wang *et al*. (2020)	Exp. He + O_2	2 mm PTFE tube	30 cm
Jain and Bruggeman (2023)	Exp. He	75 - 500 µm Pyrex capillaries	Not mentioned
Wu *et al*. (2023)	Num. He	0.05 - 1 mm quartz tubes	Not mentioned
Wu *et al*. (2019)	Exp. Ar	4 - 100 µm quartz tubes	@ ID 100 µm -> 59 mm
Kakei *et al*. (2010)	Exp. He	0.1 - 5 µm glass capillaries	Not mentioned

All things considered, controlling plasma propagation in confined spaces like capillary tubes is a challenge, especially in complex geometries, but not an impossible task. The length of plasma jet propagation is dependent on confinement parameters like channel cross-section dimensions and tortuosity of a pathway, but also on setup and operational parameters like the type of gas used and its flow rate, applied voltage, electrode configuration, etc. Hence, the ability to influence plasma propagation means controlling the spatial extent and uniformity of wettability treatment, which is paramount within microfluidic devices.

3. Effect of plasma on surface wettability

To study the plasma effects on surfaces, several analytical techniques remain at our disposal. Since impact depth generally does not surpass 10 - 40 nm (Abou Rich *et al*., 2014; Gerhard *et al*., 2013; König *et al*., 2002) due to the constrained diffusion of radicals, plasma treatment does not affect the bulk properties of the materials. Thus, to characterize the material changes, several analysis techniques can be utilized depending on the desired penetration depth and nature of quantification. Wettability measurement through surface free energy or water contact angle (WCA) typically gives information about the very top layer i.e., to a depth of 1 nm or less. The same can be said for atomic force microscopy (AFM), which is used to detect changes in surface roughness (Wang *et al*., 2020; Xu *et al*., 2015). Film thickness can be measured by interferometry, confocal microscopy or ellipsometry/reflectometry (Park *et al*., 2019). Scanning electron microscopes (SEMs), usually equipped with X-ray microanalysis, can probe the elemental composition to a depth of about 1 µm (Wang *et al*., 2020). Arguably the most common technique for the evaluation of surface chemistry after plasma treatments is X-ray photoelectron spectroscopy (XPS) (Onyshchenko *et al*., 2015; Wang *et al*., 2020; Xu *et al*., 2015). Except for helium and hydrogen, all elements can be detected with a probing depth of up to 10 nm (Booth *et al*., 2022). To complement the detection of difficult-to-distinguish functional groups like amino, amido and imino, analysis can be supported with attenuated total reflectance Fourier transform infrared spectroscopy (ATR - FTIR) (Wang *et al*., 2020; Xu *et al*., 2015) or surface-enhanced Raman spectroscopy (Chevalier and Dwyer, 2021; Sabbatini and De Giglio, 2022).

The type and magnitude of plasma effect on the surface depends on the material, propagation uniformity, plasma power, gas type and treatment time which will all be covered in the following paragraphs. Note, here we refer to basic plasma treatments, not plasma-assisted depositions which require the utilization of specific chemicals.

The effect of different plasma gases on materials in the service of surface treatment is a result of different mechanisms. One of the mechanisms is the removal of surface contaminants by either chemical or physical interaction. Physical decontamination is also referred to as sputtering (Ma *et al*., 2023; Macgregor-Ramiasa and Vasilev, 2016). Physical decontamination is predominantly achieved with noble gases, while reactive molecular gases are largely responsible for chemical decontamination (Turkoglu Sasmazel *et al*., 2021). The schematics of both chemical and physical decontamination are depicted in Figure 35.

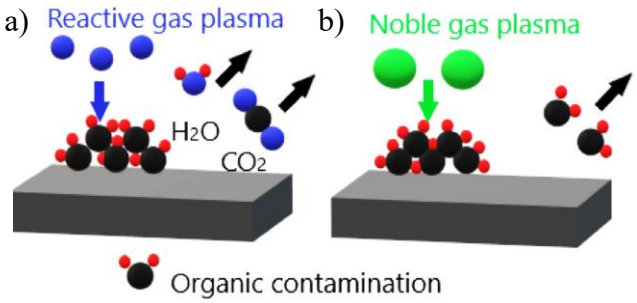

Figure 35 The mechanisms of chemical (a) and physical (b) removal of organic contaminants. Taken from Turkoglu Sasmazel et al. (2021).

Plasma etching is a mechanism where the surface of a material is changed by ablation and it encompasses both chemical and physical interaction with a surface (Ma *et al*., 2023). The effects of etching are typically seen in increased surface roughness. The final results are dependent on surface material, power and the duration of plasma treatment (Turkoglu Sasmazel *et al*., 2021). The last and most frequently discussed mechanism is the functionalization of surfaces with certain chemical groups. Functionalization reactions are dependent on the gas, ranging from oxidation, nitration, carbonation, and hydrogenation, to sulphuration, chlorination, polymerization, etc (Lin *et al*., 2022). Surface functionalization is generally used to (i) increase surface energy (activation), (ii) decrease surface energy (passivation), and/or (iii) functional group substitution (ketones, amines, alcohols, etc).

Surface activation by plasma (decrease of contact angle) is typically performed by inert gases like He, Ar, Ne, and Xe or with reactive gases like O_2, N_2, CO_2, and H_2O (Booth *et al*., 2022). For example, plasma treatment with the admixtures of carbon dioxide or oxygen will deposit hydroxyl, carbonyl and/or carboxylic groups while ammonia or mixtures of nitrogen and hydrogen will deposit amino, amido and/or imino functions (Booth *et al*., 2022; Ferreira *et al*., 2015; Li *et al*., 2023). The wettability effects of different activating gases on different surfaces are listed in Table 9. Overall, it is evident that a combination of treated material and plasma gas composition uniquely affects surface wettability.

Table 9 A review of plasma activation wettability treatments in a variety of gases on different materials. PE stands for polyethylene, PVDF for polyvinylidene fluoride and PCL for poly(ε-caprolactone).

Author	Plasma treatment	Duration	Gas	Surface material	WCA ° (before/after)
Lin *et al*. (2021)	Atmospheric DBD, 6.2 W	30 s	CO_2	PE	92 / 41
				PVDF	128 / 59
				plexiglass	74 / 28
			N_2	PE	92 / 51
				PVDF	128 / 79
				plexiglass	74 / 49
Kitsara *et al*. (2022)	Atmospheric DBD, 1.3 W	600 s	Ar	PVFD	132 / 116
			Ar + N_2		132 / 52
			He		132 / 44
			He + N_2		132 / 17
Lim and Lee (2004)	0.1 Torr, 100 W	180 s	O_2	glass	26 / 17
Yakimov *et al*. (2023)	DBD, 5 kPa (water boiling)	400 s	Humid air	PDMS	A: 120 /10 R: 70 / <1
		60 s	Humid air	glass	A: 80 / 10 R: 55 / <1
Bhattacharya *et al*. (2005)	600 mTorr	30 s	O_2	PDMS	109 / 5
				glass	20 / 5
Li *et al*. (2020)	Low pressure, 100 W	60 s	O_2	glass	21 / 3
Berndt *et al*. (2013)	0.3 mbar, 3 W	10 s	O_2	modified silicon	160 / 5
		60 s	Ar		
		220 s	N_2		
(Ozkan and Turkoglu Sasmazel, 2018)	Atmospheric DBD	360 s	Ar + O_2	PCL / chitosan	69 / 31
			Ar + N_2		69 / 59
Terpilowski and Rymuszka (2016)	0.2 mbar, 160 W	30s	Air	glass	A: 31 / 0
			O_2		
			N_2		
			Ar		

Surface passivation (increase of contact angle) is rather performed by using chlorinated and fluorinated hydrocarbons within carrier gas (see Table 10). Arguably the most famous hydrophobic coating using fluorinated hydrocarbons is Teflon, polytetrafluoroethylene (PTFE).

Table 10 A review of plasma passivation wettability treatments in a variety of gases on different materials. Abbreviations WCA, HDPE, PET, PA 6, PEEK and PMMA refer to water contact angle, high-density polyethylene, polyethylene terephthalate, polyamide 6, poly(ether-etherketone) and polymethyl-methacrylate, respectively.

Author	Plasma treatment	Duration	Gas	Surface material	WCA° (before/after)
Han and Moon (2015)	Atmospheric, 270 W	50 s	$He + CH_4$	glass	30 / 90
			$He + CH_4 + C_4F_8$		30 / 176
Berndt *et al*. (2013)	0.6 mbar, 5 W	200 cycles × (4 - 8) s	$Ar + C_2H_2$	silicon	70 / 160
Borcia and Brown (2007)	Atmospheric DBD, 400 W	1 s	$N_2 + CHCl_3$	PET	85 / 121
				HDPE	98 /126
			$N_2 + C_2HCl_3$	PA 6	69 / 109
				HDPE	98 / 111
			$N_2 + C_2Cl_3F_3$	PEEK	88 / 120
				PMMA	82 / 121
				HDPE	98 / 122

A significant advantage of plasma treatments lies in their ability to operate without solvents and other liquid chemicals, making them a more eco-friendly and cost-effective technique (Turkoglu Sasmazel *et al*., 2021). Nevertheless, further flexibility and improvements can undoubtedly be gained by adding solvents and other desired chemicals (Booth *et al*., 2022; Macgregor-Ramiasa and Vasilev, 2016). This primarily refers to the improvement of aging phenomena which will be discussed in an upcoming subsection. Overall, a range of wettability environments, from hydrophilic to hydrophobic, can easily be achieved by substituting one gas for another.

The following parameter to discuss is treatment (exposure) time. Treatment time can vary depending on the gas composition and flow, treated material, plasma type and wettability condition of interest (see also Table 9 andTable 10). Based on the study by Ozkan and Turkoglu Sasmazel (2018), treatment time and flow rate seem to be interchangeable – e.g., treatment of 60 s with a gas flow rate of 100 sccm closely matches wettability results achieved with 120 s treatment under a flow rate of 50 sccm. As already indicated in previously mentioned studies, plasma treatment time is usually in the order of minutes, some going up to an hour and some even under a second. The detailed behavior of the contact angle as a function of treatment time is given in the further text through example studies.

In a study by Li *et al*. (2020), low-pressure oxygen plasma was deployed on glass surfaces. As visible in Figure 36, after just 60 s (1 minute) of treatment with a gas flow of 40 sccm, surface wettability has reached its minimum of 2.6° from the initial 21.1° non-treated surface. The principle of wettability alteration was attributed to the formation of functional groups like carboxyl and hydroxyl, concluded through molecular dynamics simulations and XPS analysis of glass samples.

A slight increase in contact angle after 60 s was attributed to plasma etching which exposed fewer wetting layers. Similar behavior of the contact angle with treatment time was found by Aziz *et al.* (2017) who activated PE substrates with helium plasma and preceded the deposition of allylamine in a mixture with helium through a DBD setup.

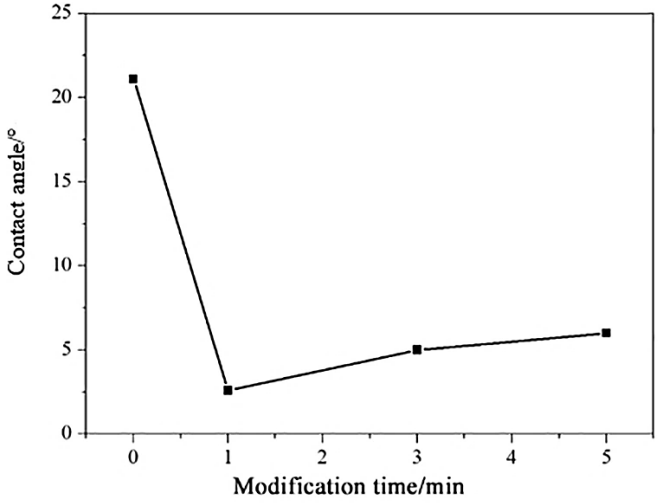

Figure 36 Contact angle as a function of treatment (modification) time. Taken from Li et al. (2020).

Lin *et al*. (2021) utilized atmospheric pressure CO_2 plasma in a DBD configuration to treat PTFE surfaces. After 60 s of treatment (see Figure 37), the water contact angle dropped to 48.6° from an initial 140.9°. Interestingly, further exposure time resulted in degradation of created surface properties, i.e., return of the contact angle to non-treated values at the 300-second mark. Reasons for surface degradation could potentially be attributed to etching due to ion bombardment (Vandenbossche and Hegemann, 2018) or due to polymer degradation towards monomeric compounds (Morent *et al*., 2010).

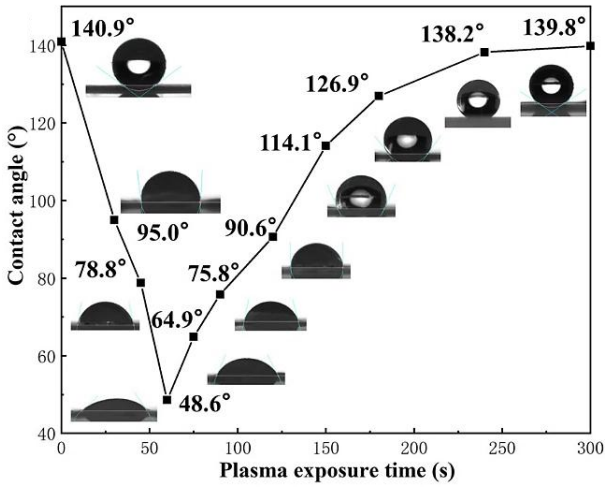

Figure 37 Tracking the evolution of the contact angle on PTFE surfaces after the treatment of pure CO_2 plasma for different exposure times. Taken from Lin et al. (2021).

The study by Zanini *et al*. (2014) primarily focused on the influence of plasma power in a low-pressure chamber reactor used to generate oxygen plasma for treating PTFE surfaces. Plasma power was shown to affect the contact angle, surface roughness, and elemental composition, as analyzed by XPS and ATR-FTIR. However, the study concluded that the contact angle behavior does not follow a monotonic relationship with plasma power. Additionally, the product of plasma power and treatment time (i.e., energy delivered) cannot reliably interpret wettability results, as energy is delivered differently.

A review in Table 9Table 10 reveals that the range of plasma power for wettability treatment is broad. It is adjusted based on the desired contact angle for a given material, optimized for an efficient treatment duration, and influenced by the specific plasma setup.

The influence of plasma type on wettability and treatment time is evident in the study by Wagner *et al*. (2003), which investigated the effects of various gases on polypropylene surfaces in a DBD configuration at atmospheric pressure. As shown in Figure 38, treatment times varied depending on the gas and plasma type. Glowing nitrogen plasma (data sets 3 and 5) achieved the lowest contact angle in the shortest time, whereas helium filamentary discharge (data set 1) had the weakest effect, even after 180 s. XPS surface analysis was conducted to explain these wettability differences, revealing that lower carbon content and a higher O/N ratio generally correspond to lower contact angles. A detailed analysis further showed that oxygen-containing plasmas generated carbonyl, carboxyl, and hydroxyl groups, while nitrogen and helium glow discharges primarily produced amine, amide, and nitrile groups. The study concluded that glow discharges were more effective due to their superior production of reactive species near the substrate compared to filamentary discharges. These findings highlight the need to carefully select plasma type based on the desired surface modifications, as different plasmas vary significantly in their effectiveness and required treatment time.

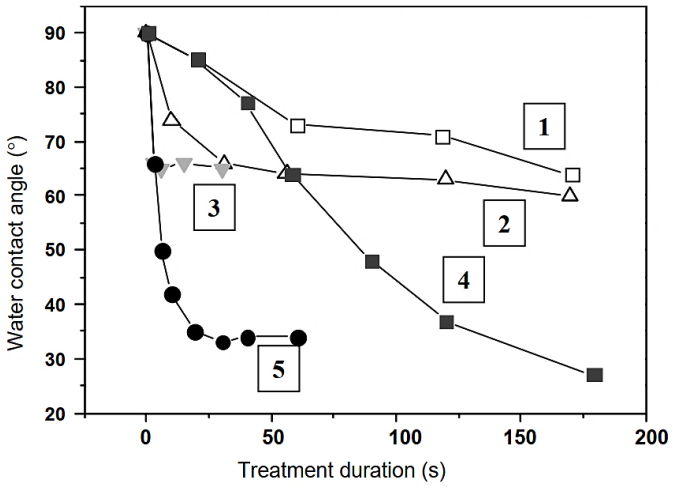

Case	Plasma type	(O/N) surface	C surface (%)
1	He, filamentary	8	90
2	air, filamentary	9	93
3	N_2 + 175 ppm O_2, glow	1.7	87
4	He, glow	0.45	87
5	N_2, glow	0.16	71

Figure 38 Contact angle evolution with treatment time for different plasma types and a legend table with results of XPS analyses. Taken and adapted from Wagner et al. (2003).

Overall, the unique plasma effect on wettability results from the interplay between material, gas, power, flow, duration, and plasma type. On average, a 1-minute treatment and flow rate in the order of tens or hundreds of sccm (DBD configurations), under relatively low plasma power, seems to be a good starting point for testing.

4. Aging performance of plasma altered surfaces and comparison with other wettability alteration methods

Once the plasma treatment is successfully performed, ensuring the comparability and reliability of experiments performed on treated surfaces becomes crucial. Additionally, researchers without access to plasma equipment might want to treat multiple surfaces at once and perform experiments after a period of waiting. Hence, the stability of newly created wettability conditions needs to be evaluated beforehand. Basic plasma treatments (not in service of assisting other methods like chemical coatings) are especially known to be prone to aging (Ma *et al.*, 2023). Aging, i.e., wettability deterioration, hydrophobic or hydrophilic recovery, is a loss of wettability properties created after plasma treatment. The effects of plasma treatment are not permanent as a high concentration of polar functional groups is against the rules of thermodynamics - the entropy of all systems tends to increase until equilibrium is reached (Primc and Mozetič, 2022; Vandenbossche

and Hegemann, 2018). It is known that aging mechanisms are dependent on material, plasma treatment operational parameters (already mentioned before), storage conditions (storage medium, light exposure, temperature, humidity), reactants in the experiments to which the surface is exposed (pH, mechanical abrasion) and many other factors, yet limited research has been conducted at the atomic or molecular level to understand them. The proposed mechanisms of aging, mostly described on polymer surfaces, are summarized by Primc and Mozetič (2022). These include (1) segmental mobility of various sequences, (2) oxidation and desorption of the low-molecular-weight fragments, (3) reorientation and migration of polymer chains, (4) hydrolysis and dissolution of oligomeric fragments, (5) surface contamination with adsorbed organic molecules, and (6) neutralization of trapped charges; amongst others. To get a sense of stability time frame, we present several research examples featuring different treated materials, different plasma gases and other contrasted parameters. However, it is essential to recognize that the criteria for stable or acceptable wettability oscillations can differ widely between applications, driven by the unique demands of each research context.

Tan *et al*. (2010) performed treatment on PDMS in a low-pressure oven-type plasma reactor with oxygen gas. For treatments longer than 300s, the surfaces remained hydrophilic for more than 6 hours if left in ambient air (Figure 39). However, notable deterioration of wettability conditions can be observed, somewhat less for longer treatment times. When stored in deionized water, the authors stated that contact angles between 50 and 60° could be prolonged up to several weeks, providing sufficient stability for microfluidic experiments. A similar evolution of wettability on PDMS surfaces was observed by Mansouri-Boroujeni (2022). The treatment was performed in the same type of reactor utilizing air as gas instead. His results indicate that for 5 and 7-minute treatments contact angle drops to around 20° and then rises to around 45° after 4 h of aging in air at room conditions. The results on PDMS are particularly significant, as it is one of the most commonly used materials for microfluidic devices, which is the case in the previously mentioned studies.

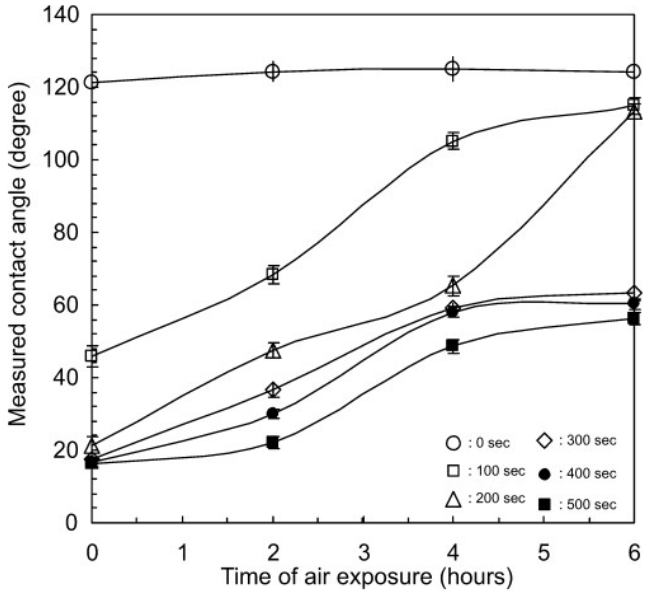

Figure 39 Evolution of contact angle inside of PDMS microfluidic channel that has a width of 150 μm and a height of 100 μm. The oxygen plasma treatment was performed at various exposure times indicated in the legend of the chart. Taken from Tan et al. (2010).

Furthermore, Massey *et al*. (2012) also analyzed the wetting behavior of PDMS with applications to microfluidics. PDMS slabs were exposed to low-pressure oxygen plasma for 45 s under 30 W of power in the chamber-type reactor. The contact angle dropped from an initial 115° to only 4° immediately after treatment, which was even better than PPAA chemical coatings. When left in ambient air (Figure 40a), a parabolic increase of contact angle was observed, resulting in a final contact angle of 95° at the end of the 14-day test. When stored in distilled water (Figure 40b), the contact angle increased linearly for the first 5 days and then stabilized around 65°. The decay of wettability in both cases was attributed to the reorientation of created hydrophilic groups on top of polymer chains and was greater than in the case of chemical coating.

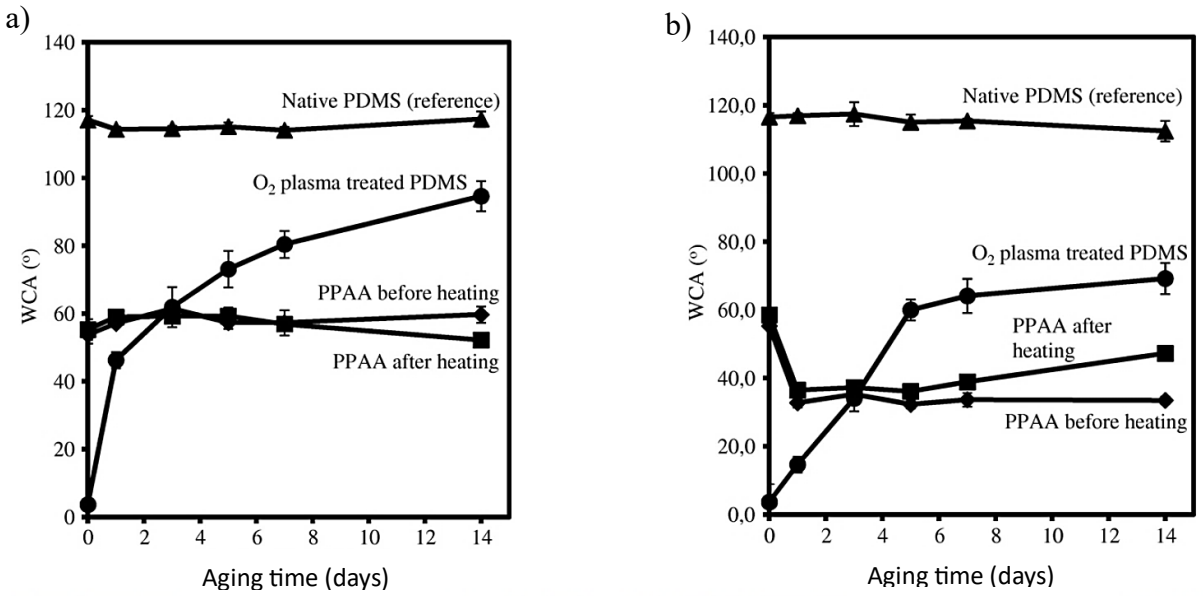

Figure 40 Aging performance of plasma-treated PDMS in air (a) and water (b). The results are shown in comparison to the non-treated (native) PDMS wettability and PPAA chemical coating. Taken from Massey et al. (2012).

Morent *et al*. (2010) looked at the aging behavior of polylactic acid surfaces after treatment with different gases in a DBD plasma setup. By varying treatment time between different gases, the goal was to ensure constant deposited energy density. Note that the type of plasma produced is not equal between the treatments (see Figure 41a), yet the authors argue that it should not cause the difference since the same energy is delivered. Unfortunately, this had been disputed in the study of Zanini *et al*. (2014), presented in the previous subsection. As visible in Figure 41b, wettability degradation in the air is rapid on the first day for helium, nitrogen and air, but not for argon plasma treatment. Looking at longer storage times, the contact angle increases less rapidly and tends to stabilize, yet the values do not return to levels prior to the treatment of the tested time frame. Looking at the relative loss of wettability, nitrogen plasma treatment lost 76 %, air 64,1 %, argon 35.8 % and helium 35 % of its wettability potential. The cause of this loss was attributed to different levels of cross-linking in the polymer surface. Less cross-linked polymer surfaces leave a higher proportion of mobile groups which can then diffuse and reorient themselves, resulting in less stable surfaces prone to aging. As air and nitrogen plasma induce low-level cross-linking, the stability of these treatments is not as good as in the case of argon and helium. Namely, most of the power in air and nitrogen plasma is used for ionizing nitrogen and oxygen species which then get incorporated into the polymer. Conversely, argon and helium plasma tend to utilize more energy in interaction with polymer bonds which leads to firmly cross-linked polymer.

a)

Operating mode	Air Filamentary	Nitrogen Filamentary	Helium Glow	Argon Glow
Amplitude of the applied voltage (kV)	1.22	1.22	0.54	0.69
Discharge power (W)	4.5	4.8	0.8	1.1
Treatment time (s)	12.0	11.2	67	49
Energy density (J/cm^2)	4.7	4.7	4.7	4.7

b)

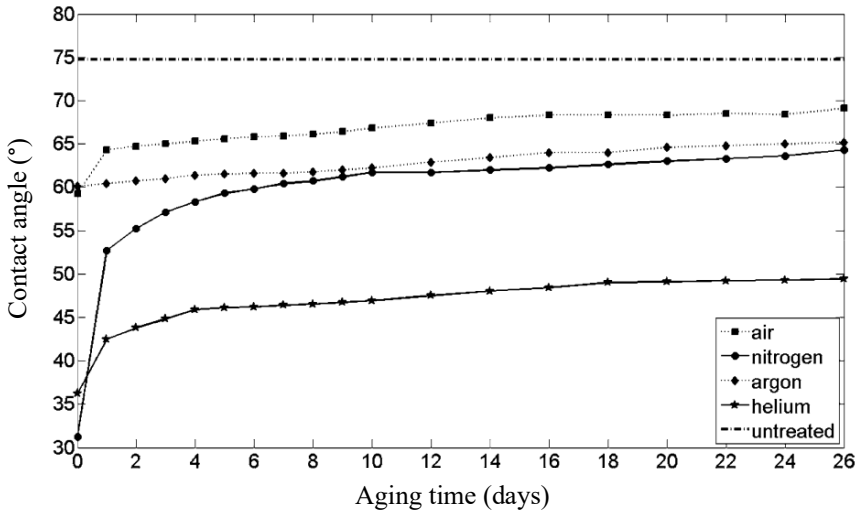

Figure 41 Effects of different gases and plasma characteristics (a) on aging performance of polylactic acid surfaces (b). Taken from Morent et al. (2010).

The effect of the storage medium on plasma-treated acrylic resin photoresist was researched in a study by Dou *et al*. (2021). Although not explicitly mentioned in the study, a low-pressure chamber-type reactor with oxygen as a gas was utilized for plasma generation. This conclusion was presumed since the application was mentioned to be in microfluidics. In addition to oxygen plasma, aging results for UV/O_3 treatment are presented, indicating a weaker wettability effect and will not be discussed in greater detail. In the case of air storage (Figure 42a), mostly linear decay in hydrophilicity was observed over the tested time. On the contrary, surfaces stored in water (see Figure 42b) had stable contact angles after the initial increase that was observed on the second day after the treatment. Interestingly, with increasing treatment time, both storage media exhibited milder aging effects. The behavior of aging was also tracked through XPS analysis indicating the increase of carbon content with the onset of aging. Preserving effects of water on wettability compared to air were therefore explained through the formation of hydrogen bonds which prevented reorientation and migration of species between the surface and the bulk of the material.

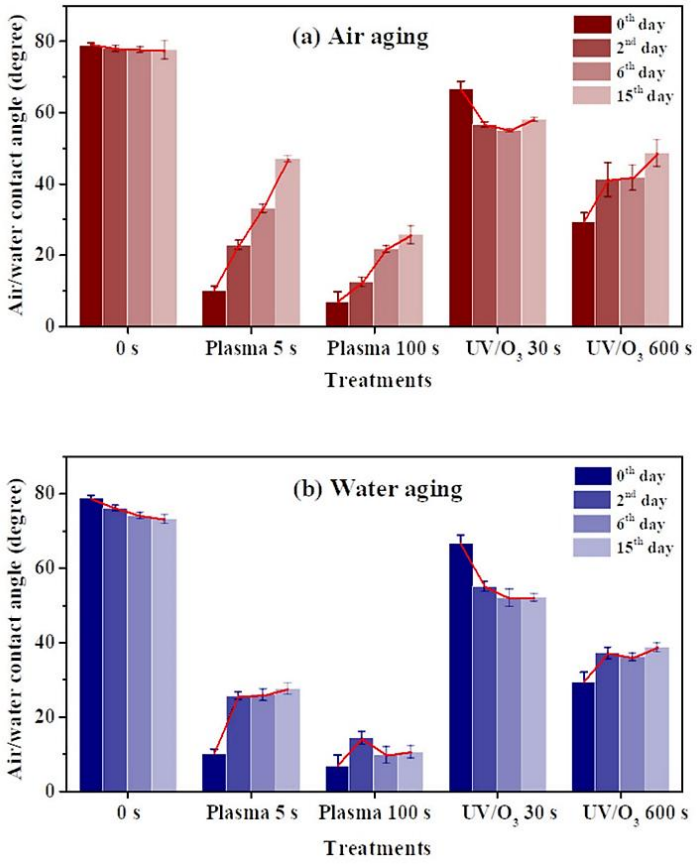

Figure 42 Aging behavior of acrylic resin over the course of 15 days when stored in air (a) and water (b). Taken from Dou et al. (2021).

The pH is also a factor to consider, especially where surfaces are used in experiments that create far from neutral conditions. This primarily affects the deposited functional group which may be more or less stable at certain pH conditions (Vandenbossche and Hegemann, 2018). Thus, the acidic environment coming from CO_2 dissolution in our experiments may also be somewhat detrimental.

As seen from previous studies, aging is a challenge that needs to be addressed. So, is there a way to prevent aging? – The simple answer is no, however, there are ways to reduce the rate of decay, i.e., slow it down. Vandenbossche and Hegemann (2018) claim that plasma-assisted chemical depositions (2) are more stable than basic plasma treatments (1), yet still far from the ideal case (3). All cases are schematically shown in Figure 43. The reason for that is the high level of cross-linking which provides stability of deposited layers.

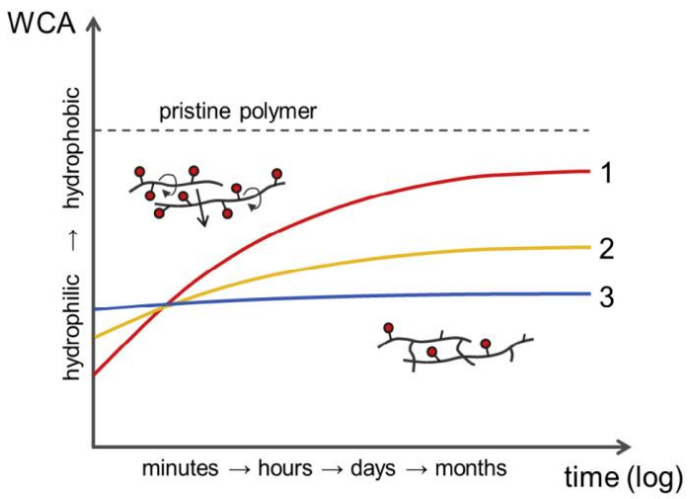

Figure 43 Aging behavior for different versions of plasma treatments on polymers. (1) plasma-activated polymer surfaces, (2) plasma-assisted polymer deposition with desired functional groups, and (3) ideal plasma-assisted polymer coating with reduced aging. Taken from Vandenbossche and Hegemann (2018).

To conclude, plasma treatment is a promising method for modifying wettability in microfluidic devices, but its effectiveness and stability depend on multiple factors, including material type, plasma power, gas composition, and treatment configuration. While low-pressure plasma is commonly used, especially for treating open PDMS slabs before bonding, achieving uniform and stable wettability inside closed glass-based devices remains challenging due to limited penetration and complex geometries. Although plasma can propagate into confined spaces, its reach and consistency are still limited, making the optimization of treatment conditions and long-term stability an important area for continued research.

III. Experimental setup for *in situ* plasma treatment

Based on the literature review of state-of-the-art plasma systems, we adapted a DBD-like electrode configuration for microfluidic devices. Our design features a bare metallic tube electrode in direct contact with the gas and a second electrode placed outside a dielectric glass barrier. This configuration (see Figure 29c) aims to generate homogeneous, arc-free plasma and enhance its propagation.

We selected kHz plasma jets due to their unique ability to produce self-sustained ionization waves, which can propagate several centimeters beyond the electrode confinement. These jets can be ignited at atmospheric pressure in various gases, producing cold plasma with low gas temperatures - a crucial factor for modifying surface properties without damaging the bulk material. Despite the borosilicate glass transition temperature being above 500 °C (Avramov *et al*., 2005), we prefer to stay below 200 °C to be able to extend the work to polymers like PDMS (Al-Harbi *et al*., 2018). Additionally, kHz jets offer high energy efficiency, as their microsecond-pulsed operation reduces overall power consumption.

Helium was chosen as the working gas due to its low breakdown voltage, which facilitates plasma ignition and sustains propagation in confined spaces. Moreover, helium produces a uniform glowing discharge, ensuring better coverage compared to the filamentary discharges typically observed in air. Since wettability alterations often rely on reactive impurities (e.g., functionalization processes), helium is particularly advantageous due to its ability to induce Penning ionization of such impurities. To establish a fundamental understanding of plasma-induced wettability changes, the idea is to use pure helium initially before introducing other gases and gas mixtures in future experiments, further expanding the flexibility and potential of our setup.

The plasma propagation within microfluidic channels is highly sensitive to gas flow rate, requiring an optimal balance. Excessively high flow rates can cause pressure buildup and shorten the mean free path, hindering plasma sustainment. Based on literature and previous laboratory experience, we identified a flow rate of several dozen sccm as an appropriate starting point.

Using these design principles, we constructed the experimental setup, which is detailed in the following section. The setup's performance was evaluated through various parameters, and the corresponding results are presented in the next section (0).

Further text and graphics are based on our article Gredicak *et al*. (2025) published in the Microfluidics and Nanofluidics journal.

1. Materials and equipment

Our in-house-developed setup, shown in Figure 44, is based on a kHz power source unit with tunable voltage and frequency. The power source unit creates voltage pulses up to 20 kV and a frequency from 0 to 30 kHz. The unit is also equipped with two electric probes (Tektronix P6015A probe: 75 MHz with 1000:1 division ratio and Elditest GE3121 probe: 150 MHz and 100:1

division ratio). One probe is used to measure the applied voltage on the high voltage electrode while the other serves to measure voltage across the resistor and evaluate the current. Both probes are connected to a 200 MHz bandwidth digital oscilloscope (LeCroy WaveRunner 6050) to record the electrical measurements. The produced voltage is supplied via cables to a stainless-steel needle (gauge 20 from Nordson) serving both as a power electrode (anode) and a gas conduit to the microfluidic device.

Helium gas of 99.999 % purity is flown through this high-voltage electrode in a 10 - 50 standard cubic centimeters per minute (sccm) range regulated by a calibrated mass flow controller (EL-FLOW Prestige from Bronkhorst). A gas-tight connection from Teflon tubing is established by using rubber/plastic fitters typically used in microfluidics. The connection between the stainless-steel needle and the microfluidic device is secured via a custom-made 3D-printed plastic clamp which also serves as a device holder, just as shown in the image above schematics (Figure 44). A clamp is mounted on a x-y-z linear translation stage, allowing position adjustments for imaging over a length of 25 mm and with a precision of 2 μm. Close to the outlet of a microchannel, a grounded copper foil electrode (cathode) is glued to enhance the plasma propagation. The setup is thus assembled as a dielectric barrier discharge-like jet creating a positive streamer plasma. Note that the electrode position described in the text and shown in Figure 44 is of an illustrative nature, as various electrode positions were tested in this thesis to optimize plasma propagation within the specific microchannel geometry. As a safety measure, the core part of a setup is located within an insulating box with transparent doors to provide visual observations.

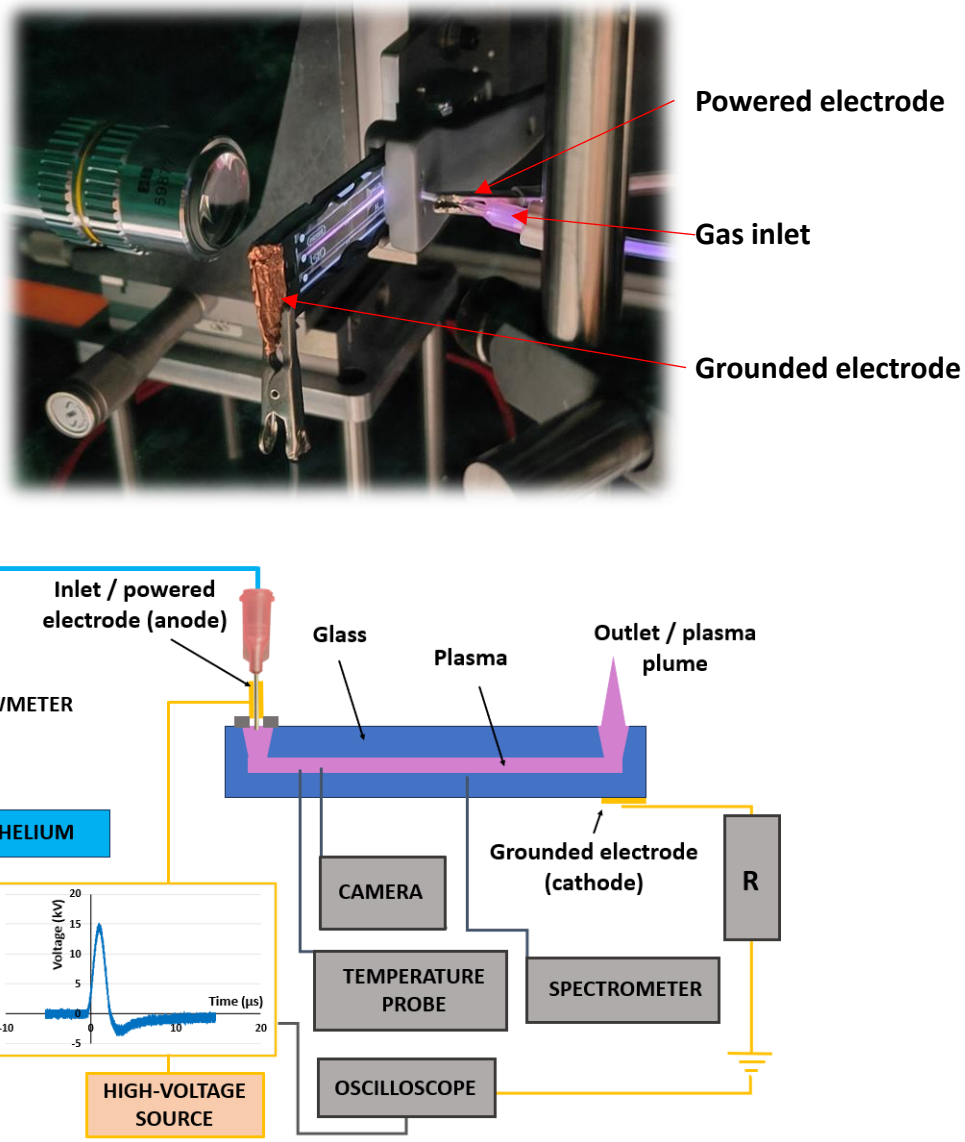

Figure 44 The setup for the generation and analysis of atmospheric pressure plasma.

Optical analysis of plasma propagation inside the microfluidics devices during treatment is performed with a fast CCD camera (pco.pixelfly usb) and an objective 10x with NA of 0.28 (Edmund optics). To acquire information about created plasma species, an optical fiber is deployed to collect the light from the plasma coming through the glass of a microfluidic device. The signal is analyzed by a spectrometer AvaSpec-ULS4096CL. To measure plasma power a resistor (R = 1 kΩ) is added to the ground and connected to the ground and back to the oscilloscope. Measurements of the glass outer temperature are performed with the help of a temperature sensor (GaAs Optocon).

The storage of microfluidic devices after plasma treatments is achieved in either air or water. In an AC-equipped microfluidic laboratory, air storage implies room temperature ranging from 19 to 22 °C and relative humidity typically ranging from 50 to 70 %. MilliQ water is used both as a storage fluid, but also, for contact angle determination together with CO_2 gas. The images of the

contact angle are acquired on the upright microscope in reflection mode with a 20x objective (further details are in Table 6). Image processing is performed with Image J software and a contact angle measurement tool DropSnake (Stalder *et al.*, 2006).

Due to the inability to effectively open glass microfluidic devices without damaging them, the treatment for chemical surface analysis with XPS is performed in a modified plasma setup configuration as shown in Figure 45. Namely, plasma is ignited with the same stainless-steel electrode connected to a glass tube which serves as a conduit for plasma to the top surface of the microfluidic device. The glass tube creates a circular treatment spot 5 mm in diameter. Underneath the microfluidic device, a copper foil electrode connected to the ground is placed to help with plasma propagation and thus enhance the glass surface treatment.

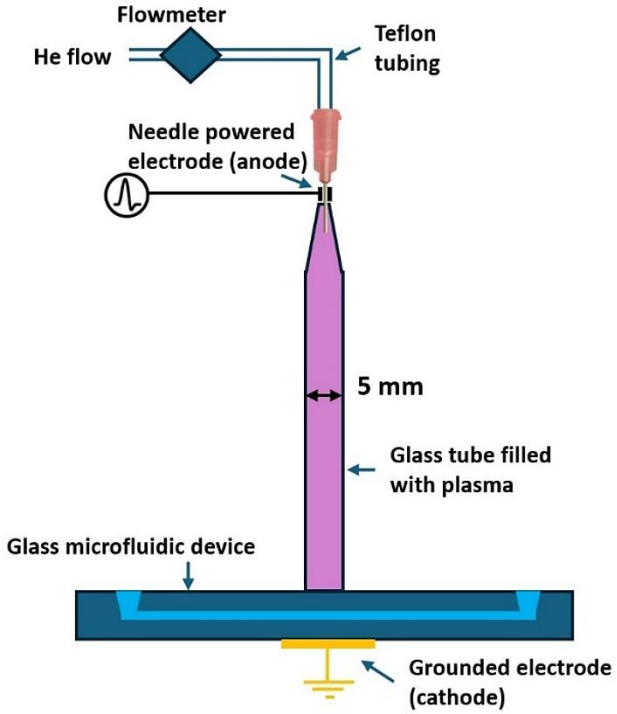

Figure 45 Modified plasma setup for XPS analysis.

To characterize chemical changes to the surface of microfluidic devices made by the plasma, XPS analysis was performed in the ICMN laboratory (France) (Figure 46). XPS measurements are performed using an ESCALAB Xi+ X-ray photoelectron spectrometer (Thermo Fisher Scientific) employing a monochromated Al Kα X-ray source (hv = 1486.6 eV). The carbon C(1s) level (284.8 eV) is used as the reference binding energy. All spectra are collected using an analysis area of 650 × 650 µm and a 20 eV pass energy. The charge neutralizer is used for data collection, being monitored using the C(1s) signal corresponding to adventitious carbon (Biesinger, 2021). All spectra are collected and fitted using the Avantage software (Thermo Fischer Scientific).

The optical tensiometer Theta Flex (Biolin Scientific) is utilized for the measurement of the contact angle on the top surface of microfluidic devices.

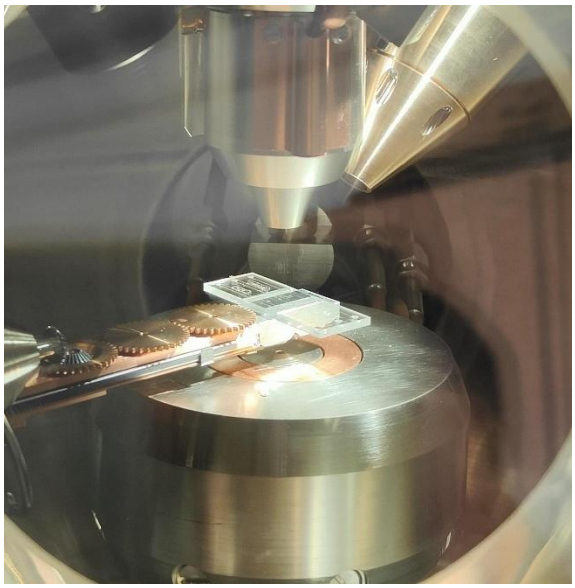

Figure 46 Microfluidic device loaded in the vacuum chamber for the XPS analysis.

2. Procedures

a) Plasma treatment in microchannels and on a top glass surface

To minimize impurity levels by tubing outgassing and ensure reproducible conditions, helium is flowed at 50 sccm for at least 30 minutes prior to any plasma treatment. The plasma is then ignited, and its propagation length increases with the applied voltage magnitude. The high voltage is adjusted to fill the entire length of a microchannel with plasma, typically requiring a voltage between 10 and 15 kV. After a brief testing of the frequency range (1-30 kHz), it was observed that changing frequency doesn't significantly affect plasma propagation, therefore frequency of 8 kHz was chosen from previous experience as a good value. Since the microchannel outlet is open to the atmosphere, the plasma propagates further into the air along the helium channel, occasionally forming a short, faint plasma plume (see the schema of Figure 44). For the XPS analysis, the procedure is similar, ensuring that the plasma fills the glass tube and makes contact with the top surface of the microfluidic device. After the treatment, which lasts between 30 seconds and 10 minutes, the plasma is turned off. The devices intended for air storage are kept in a small plastic box, while those intended for water storage are first saturated with water and then stored in a container filled with MilliQ water. The day of plasma treatment is designated as day 0.

b) Plasma properties measurement

While the plasma is on, real-time data is collected, including images of plasma propagation, optical emission spectra (OES), plasma power measurements, and temperature readings. Plasma propagation images captured using a 10x objective to balance resolution and field of view, illustrate only representative sections of the microchannel geometry, as shown in Figure 47. Depending on the size of the principal geometrical feature located in the middle of a microchannel, several images

may be stitched together. The stitching is performed with the ImageJ plugins (Preibisch *et al.*, 2009). Helium flow is always kept from left to right in images to make further analysis easier.

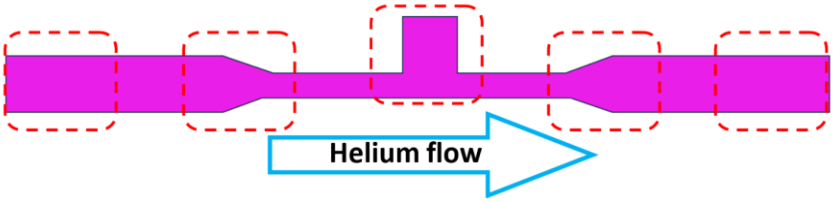

Figure 47 Schematics of representative locations shown on plasma propagation images.

Optical emission spectra are collected by positioning an optical fiber directly against the glass at the desired location along the microchannel. Optimal acquisition times are selected to balance the maximum visibility of all species at a given voltage, yet avoid detector saturation. Furthermore, all spectra are normalized to the intensity of the helium line at 706.5 nm.

c) Power measurement

Plasma power is determined by measuring the voltage at the power electrode and the current at the ground electrode after a resistor (Mestre *et al.*, 2024). Initially, a voltage (V_a) is applied to microchannels filled with air to prevent plasma ignition and measure the capacitive current (I_{capa}) which serves as the background signal. When the same voltage is applied to microchannels filled with helium, plasma is ignited, and a total current (I_{tot}) is recorded. The discharge current (I_{disch}), which originates solely from the plasma is then obtained by subtracting the capacitive current from the total current. The energy delivered to the plasma during a single pulse (E_p) is thus calculated using the following equation:

$$E_p = \int_0^T P(t)dt = \int_0^T V_a\,(t) I_{disch}(t)dt \qquad (5)$$

Since the frequency (f) is kept constant, the average power input can be easily obtained by multiplying energy per pulse and frequency, as seen in equation *(6)*.

$$P = E_p \times f \qquad (6)$$

d) Temperature measurement

To estimate the thermal load on the material, an optical fiber temperature sensor is pressed against the outer glass surface of the microfluidic device, directly above a 500 µm-wide microchannel. Temperature measurements are performed at two distinct locations: Location 1, situated near the inlet, i.e., powered electrode, and Location 2, near the outlet, i.e., grounded electrode. Temperature acquisition is performed over a period of several minutes, waiting for the stabilization period to start. The goal is to get an estimation of the temperature range.

The plasma gas temperatures are then back-calculated from the thermal Ohm's law with two assumptions. The first assumption states that all discharged energy is converted to heat without any

losses to other mechanisms. The second assumption refers to the calculation of thermal resistivity. Thermal resistivity is calculated based on heat conduction from the microchannel (thermal source) to the external glass surface (sink to the environment). For the calculation to remain valid, the microchannel's width and length must always exceed the thickness of the glass through which heat conduction occurs. While these assumptions are not entirely applicable in our case, they provide a first-level estimation of thermal behavior. With these assumptions in mind, thermal resistivity (R) is obtained using the following equation:

$$R = \frac{e}{\lambda \times S} \tag{7}$$

where e is the thickness of the glass (700 µm), λ is the thermal conductivity (1.2 W/m K) and S is the plain conduction area of the glass (approximated as a straight channel with a width of 500 µm and a length of 40 mm). To estimate the temperature loss through the glass (ΔT) we utilized the following equation:

$$\Delta T = R \times \Phi \tag{8}$$

where thermal flow (Φ) is equal to the dissipated plasma power. By summing the measured temperature (T_{glass}) and the calculated temperature loss (ΔT), the plasma gas temperature at the walls of the microchannel can be determined.

e) Contact angle measurement

The wettability of microchannels is checked before and periodically after plasma treatment by measuring the contact angle. Utilizing an upright microscope setup with an objective of 20x, the procedure for image acquisition is performed as follows (see Figure 48). Using a ⊥-junction to ensure a closed system at the inlet side, water and CO_2 are injected into the tubing one at a time, forming a small volume of CO_2 sandwiched between two larger slugs of water. By delicate manual injection of water from a syringe, the CO_2-water interface is brought from the tubing to the inlet side of the 500 µm channel. When the interface between CO_2 and water is made quasi-static within the camera window, image acquisitions are made. Stabilizing the interface after plasma treatment was a tedious task due to the existence of lubricating water films over which the interface is easily sliding.

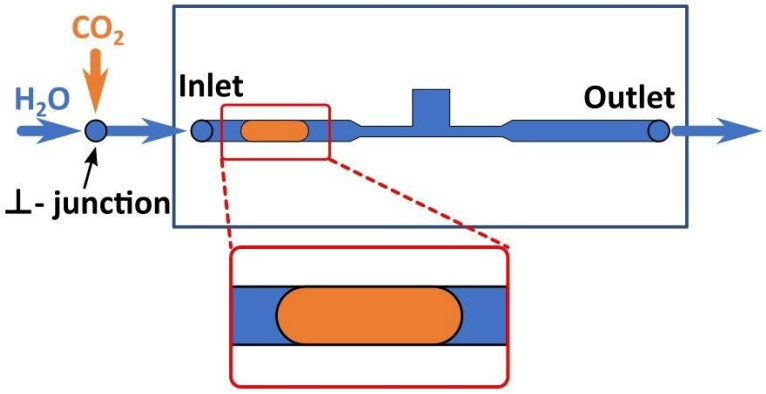

Figure 48 Fluid injection sequence for in situ contact angle measurement. A small amount of CO_2, stabilized and sandwiched between two water sections, creates a fluid-fluid interface in a wider part of the microchannel.

Acquired images are first pre-processed with ImageJ software. To enhance the visibility of the interface and contact points, images are first converted to an 8-bit grayscale format and basic adjustments of brightness and contrast are performed. The DropSnake plugin, developed by Stalder *et al*. (2006) and based on the snake algorithm, is chosen as the optimal tool to measure the contact angle. The principle of the DropSnake plugin is to fit points around the interface which are then interpolated by the algorithm (see Figure 49). The first and the last points are considered the triple contact points. On average, 12 points have been manually placed to describe the outer edge of the interface which is above 10 recommended by the creators of the tool. Two contact angle readings (θ1 and θ2) are obtained for each image (see Figure 49). For statistical significance, no fewer than 5 images are utilized to determine one wettability condition. The dispersion of measured values is expressed through standard deviation (error bars graphically) and it is attributed to the contact angle hysteresis (Hansen *et al*., 2000; Huh and Scriven, 1971; Marmur *et al*., 2017b), manual input of points affected by the visibility of interface and contact points, and to the accuracy of the tool itself. Overall, readings typically oscillate ± 5° which is in agreement with the accuracy of contact angle measurements in microfluidic devices (van Rooijen *et al*., 2022).

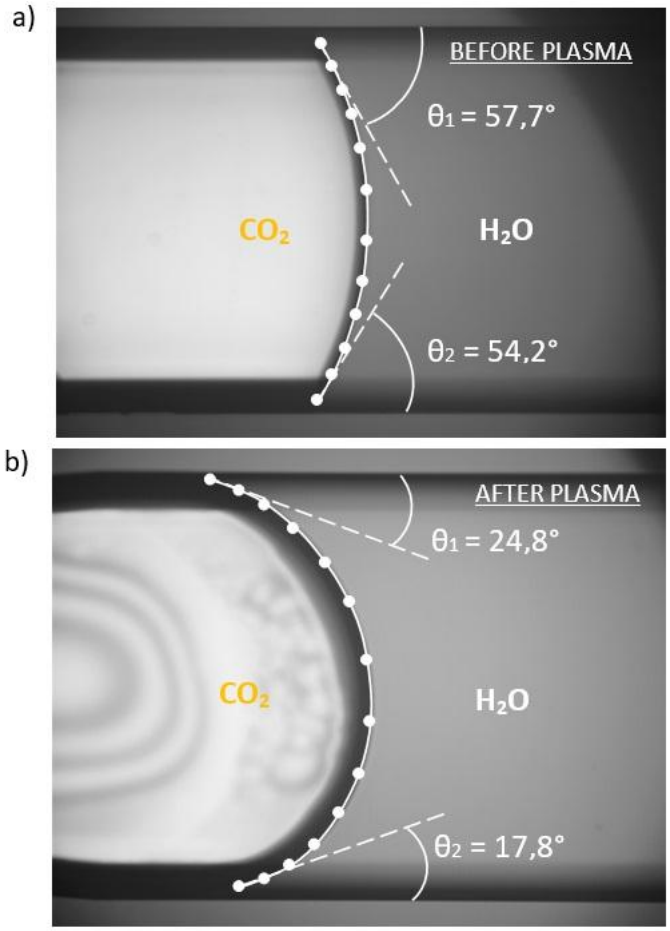

Figure 49 The principle of the contact angle measurement with the DropSnake plugin. Image a) depicts the CO_2-water interface before plasma treatment and image b) after plasma treatment. Two contact angle readings θ_1 and θ_2 are acquired for every picture.

IV. Results and discussion

This section introduces firstly plasma propagation in different microfluidic devices, followed by the identification of plasma species and measurements of plasma temperature and power. The principal part then focused on evaluating wettability through contact angle for different treatment times and compares the aging performance of new and reused devices stored in air and water. Finally, we discuss the mechanisms of alteration and aging through chemical surface analysis.

1. Analysis of plasma properties

a) Plasma propagation

By optimizing the voltage to prevent arcing between the electrodes, plasma is successfully ignited and propagated through the entire length of the microchannel. Unlike many previous studies that focus on plasma propagation in simple tubes, our microchannels highlight specific geometrical features with varying rectangular cross-sections, presenting greater geometric complexity and thus a greater challenge for plasma propagation. With stable plasma propagation from the inlet to the outlet, close-up images are captured to provide detailed insights at the microscale. In addition to the primary electrode configuration, where the power electrode is positioned at the inlet and the ground electrode near the outlet (shown in Figure 44 & Figure 50a), alternative configurations are tested to enhance the homogeneity of plasma propagation. The initial analysis focuses on the simplest geometry, a single pocket, to establish a baseline understanding.

Single pocket geometry

A simple electrode position along the axis of the microchannel, just as shown in Figure 50a) and b), produces a plasma light distribution that is generally brighter along the central axis and decreases towards the walls of the microchannel. This contrasts with previous studies (Douat *et al*., 2016; Leiweke *et al*., 2011; Mericam-Bourdet *et al*., 2009), where the light distribution in plasma plumes typically exhibits a ring shape, with more intense emission at the edges. Numerical models (Boeuf *et al*., 2013; Breden *et al*., 2012) have explained this annular structure as a result of charge accumulation on the dielectric surface, forming a surface discharge. Wu *et al*. (2023) noted that central column plasma propagation, similar to our observations, vanishes below 100 µm due to strong shielding effects, transitioning to a ring-shaped configuration. At atmospheric pressure, the width of the streamer head is on the order of a few hundred micrometers (Xiong and Kushner, 2012). To form a ring structure, the confinement radius must exceed the streamer's width. In our setup, the channel has a rectangular cross-section of 100 × 500 µm, where the width is smaller than the streamer width, preventing observation of surface discharge.

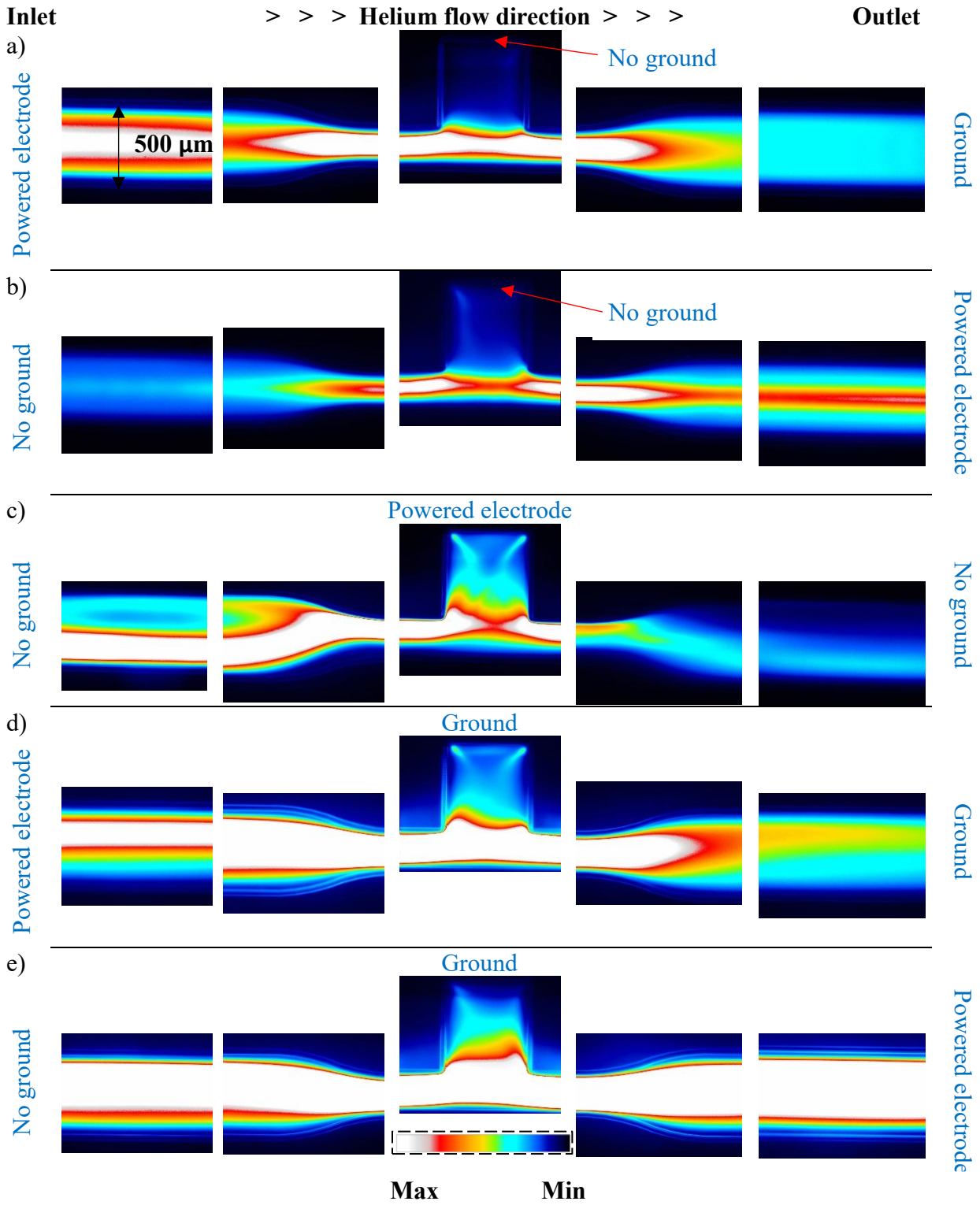

Figure 50 Plasma propagation followed through light intensity in single pocket geometry for various electrode configurations: a) "simple normal", b) "simple reverse", c) "pocket powered electrode", d) "normal + pocket ground", and e) "reverse + pocket ground". Images captured with 100 ms exposure. Voltage is 12 kV for all except c), where 15 kV is used.

Between the two electrode configurations, the overall light intensity is higher in the simple normal (Figure 50a) compared to the simple reverse configuration (Figure 50b). In the simple reverse electrode configuration, the absence of a grounded electrode on the opposite side of the microchannel results in a diminished electric field enhancement, which directly affects the light intensity.

Additionally, we observed a decrease in light intensity with increasing distance from the power electrode and an increase with greater confinement. The statement is true not only for a) and b), but for all electrode configurations. These findings align with Wu *et al*. (2023), who recently demonstrated in their 2D numerical model that the electric field and electron density decrease due to continuous charge losses to the sidewalls but increase with a reduced tube diameter.

Examining the impact of gas flow relative to electrode positioning reveals that plasma consistently propagates from the powered electrode toward the opposite side of the channel, regardless of the flow direction (see Figure 50). Given that the characteristic plasma propagation time is on the order of hundreds of nanoseconds (Xiong and Kushner, 2012), while the gas flow time through the length of the microfluidic device is in the millisecond range, the gas can be considered static during plasma propagation. This explains why the direction of plasma propagation is unaffected by the gas flow direction.

Within the pocket, the plasma light intensity is weaker than in the underlying channel and forms irregular shapes depending on the electrode configuration. For simple normal and reverse configurations (Figure 50 a) and b)), plasma seems to be anchored to one side near the wall opposite the powered electrode. As previously noted, plasma propagation is independent of the gas flow direction. Studies have shown that the electron distribution of the streamer head tends to cling to the wall, typically on the side with a smaller radius of curvature, and is influenced by the local instantaneous electric field (Xiong and Kushner, 2012). In our case, this suggests that the electric field parallel to the channel axis is stronger than the perpendicular electric field.

When a ground electrode is placed close to the pocket (Figure 50 d and e), the plasma light distribution changes. Compared to the previous two configurations (a and b), plasma propagates further into the pocket. This observation is consistent with the behavior in microchannels where the emitted light is more intense, closer to the wall where the ground electrode is located. Consequently, placing a ground electrode near the geometric feature of particular interest, enhances plasma propagation, suggesting a better wettability treatment.

A single powered electrode located above the pocket, as shown in Figure 50c, results likewise in increased light intensity, indicating enhanced plasma propagation within the pocket. With no designated ground placed in this configuration, plasma within the microchannels is located away from the powered electrode, closer to the opposite wall. This is consistent with the observations in the pocket in simple normal and reverse electrode configurations, where the light intensity tends to be stronger on the wall opposite the power electrode. Among all the electrode configurations, this

is the only one with a complete dielectric barrier to the powered electrode, necessitating a higher voltage,15 kV or more, to ignite the plasma.

Taking all the information into account, the simple normal and reverse electrode configurations are the most suitable for treating straight channels, as the plasma extends symmetrically along the main (long) channel axis. Normal and reverse electrode configurations with the ground placed close to the pocket, demonstrate enhanced propagation within the pocket thus being perspective for good surface treatment of the main geometric feature. Additionally, all reverse configurations had lower ignition voltages and achieved full propagation at lower applied voltages. This difference is attributed to the positioning of the powered electrode. Namely, in reverse configurations, the powered electrode is located within the outlet of the microfluidic device, whereas in normal configurations, it is positioned just outside the inlet. In contrast, the pocket-powered electrode configuration is the least suitable due to high ignition voltage and risk of arcing with nearby metal components. Overall, this highlights an important implication: by strategic electrode positioning in targeted areas, we can manipulate plasma propagation, enabling spatial control of wettability alteration. This approach proves particularly useful for treating more complex geometries. Since the propagation within the microchannel is thoroughly covered, further analysis in more complex geometries will focus solely on the main geometrical feature of the microfluidic device.

Deep pocket geometry

Here we present three other geometries that gradually add geometrical complexity, further challenging plasma propagation. Compared to the “single pocket”, “deep pocket” geometry offers more pore volume extending laterally from the underlying channel. In Figure 51, we observe that plasma enters well in the first part of the pore, while further away it tends to stick more to the wall opposite the power electrode. The observation that plasma propagates to the end of the deep pore suggests its potential for treating geometries with substantial volumes distant from the main channel. While further improvements in plasma propagation through alternative electrode arrangements are possible, propagation patterns in this specific microfluidic geometry will not be explored further within the scope of this thesis.

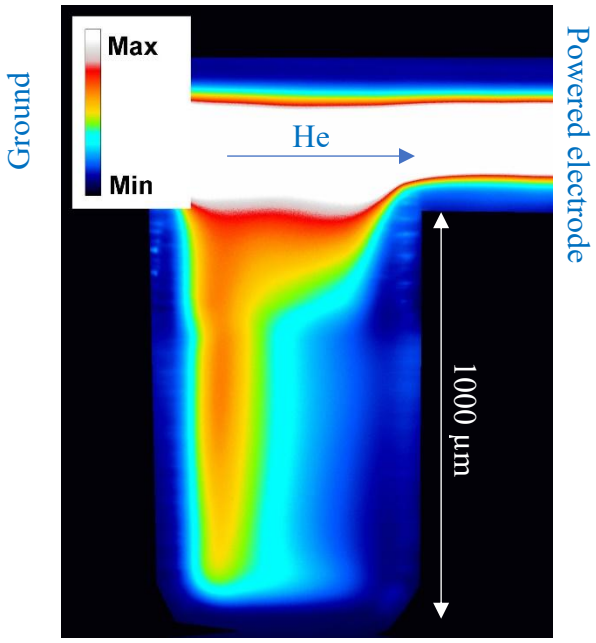

Figure 51 Plasma propagation in deep pore geometry. Plasma is ignited in the simple reverse electrode configuration (Figure 50b) under 11 kV. The image is captured with a 500 ms acquisition time.

The next element of complexity examined is branching/splitting. It is a frequent element in natural porous media (e.g., blood vessels, soil and rock structure, etc) which microfluidic devices are trying to replicate. Compared to the study by Xiong *et al*. (2012) presented before, the channel size is significantly smaller (250 × 100 µm vs 4 mm tube inner diameter), implying more challenging conditions for plasma propagation. As visible from Figure 52, plasma propagates symmetrically in both channels after branching with almost identical light distribution in both pockets. Again, with different electrode configurations, the spatial extent of the treatment could be diverse. For instance, plasma could potentially be steered to propagate exclusively in one branch, enabling the creation of heterogeneous wettability conditions that are frequent in geological porous media. This presents a promising avenue for advancing plasma-based wettability treatments on microfluidic devices.

Pore doublet geometry

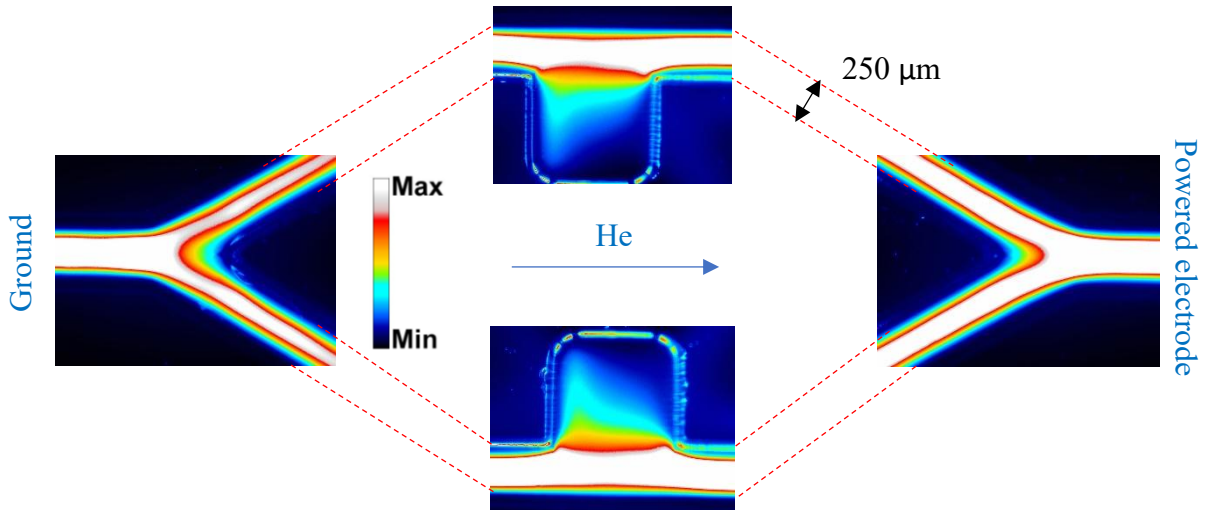

Figure 52 Plasma propagation in pore doublet geometry. Plasma is ignited in the simple reverse electrode configuration (Figure 50b) under 11 kV. All images are captured with a 500 ms acquisition time. Red dashed lines approximate the part of the geometry that is not captured in schematics.

L-pore geometry

The last considered feature is anisotropy of geometrical structure, also a frequent element in porous media (e.g., Tesla valve). To investigate this, we utilized our L-pore geometry. Two strategies are available to study the differences in plasma propagation within anisotropic geometries: rotating the micromodel or reversing the electrode positions. We opted to modify the electrode positions but also examined the effects of altering the orientation of the microfluidic device. The modified electrode configurations for this geometry are shown in Figure 53. In configuration (a), plasma penetration into the geometric feature is minimal and primarily occurs along the wall opposite the powered electrode. This behavior is consistent with observations from other geometries and aligns with expectations. Conversely, configuration (b) exhibits significantly stronger light emission across the entire volume. This occurs because the L-feature extends away from the powered electrode, aligning with the direction of plasma propagation, while the plasma is further attracted to the nearby ground electrode. Comparing these propagation patterns reinforces the critical importance of electrode positioning for achieving optimal plasma propagation. To counteract the effects of anisotropy during treatments in microfluidic devices, we suggest double-side treatments as an effective solution.

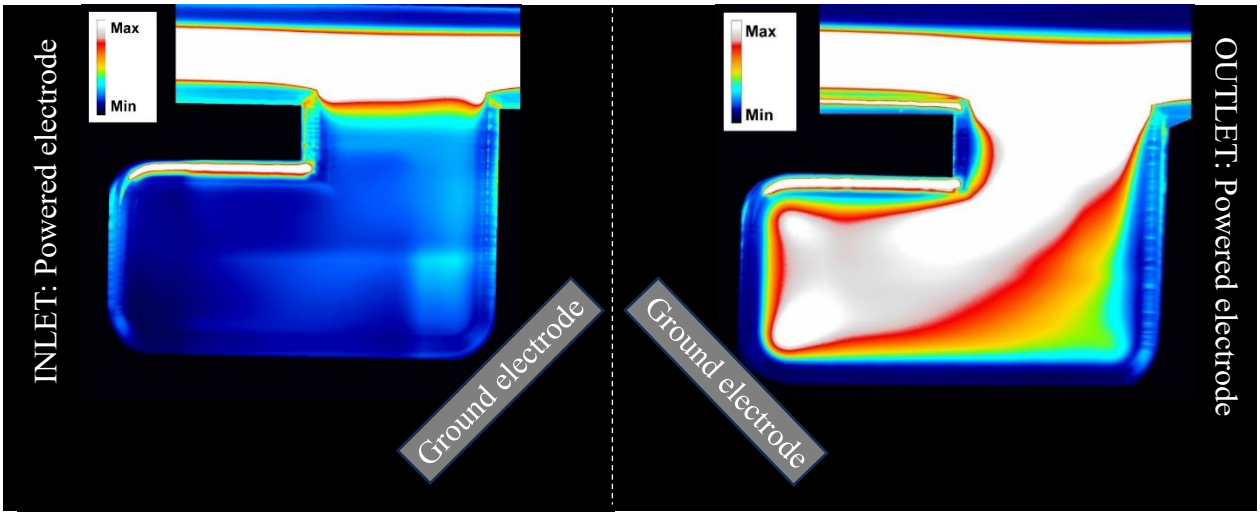

Figure 53 Plasma propagation in L-pore geometry. Plasma is ignited with the two similar electrode configurations depicted in the schematics (a & b). A ground electrode (metal clamp) is placed at roughly 45° with respect to the main channel and a few mm from the geometry. The applied voltage in configuration a) is 12 kV and 10 kV in configuration b). Both images are captured with a 500 ms acquisition time. Note: square features or straight lines in image a) are artifacts from image stitching.

In summary, we demonstrated plasma propagation in microfluidic devices with various geometric features treated using different electrode configurations. Features such as deeper sections, branching structures, and anisotropic geometries provide a fundamental structural basis for many microfluidic devices. Our findings highlight the critical importance of electrode positioning in manipulating plasma propagation, enabling effective plasma-based wettability treatments.

Looking ahead, we aim to adapt our setup to treat complex microfluidic devices that mimic the realistic pore structures of rocks, such as the Enhanced Oil Recovery chip commercially available from Micronit, a complex porous media pattern with various pore sizes.

b) Analysis of plasma species

The first visual observation of our helium plasma propagating within the microchannel is its bright purple-pink-whitish color which serves as a preliminary indicator of the gas composition (Figure 54a). For comparison, low-pressure air plasma created in the chamber-type reactor in our lab has a distinct pink color (Figure 54b). Jitsomboonmit *et al*. (2012) describe the color of helium and air plasmas as "violet-blue" and nitrogen plasma as "blue." Other sources may offer different descriptions, as the perception of color can be subjective and may also vary objectively due to factors such as composition, pressure, temperature, applied power, camera color profile, and other conditions.

a) b)

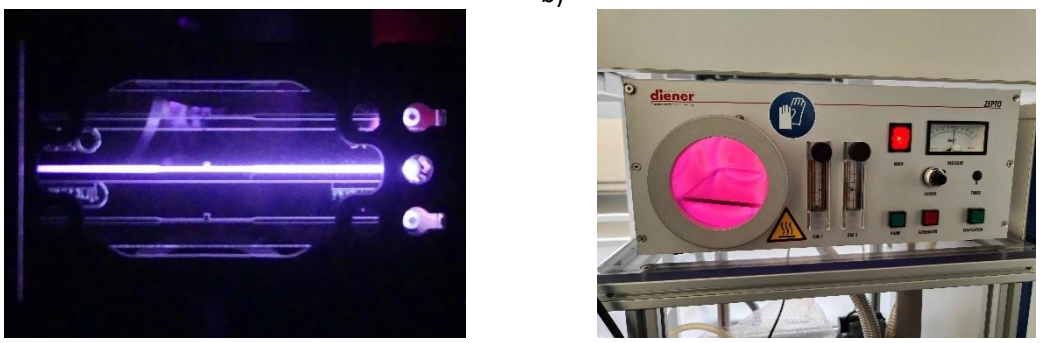

Figure 54 Plasma color appearance for atmospheric pressure helium plasma propagating within a glass microchannel (a) and low-pressure air plasma within a chamber reactor.

To get a better insight into plasma composition, we ran a spectral analysis of plasma species with optical emission spectroscopy (see Figure 55). The lines at 587.6 nm and 706.5 nm are attributed to helium, the primary gas in the system. To facilitate comparison, the entire spectrum is normalized to the intensity of the most intense helium line, which is at 706.5 nm. In addition to helium, the spectrum prominently features the second positive system of nitrogen, N_2 (C-B), ranging from 315 to 486 nm (Pearse and Gaydon, 1976). Within this range, the presence of N_2^+ (B-X) species is indicated by the line at 391.4 nm, while the cyano radical or nitrile group (CN (B-A)) is identified by bands with heads at 386.1 and 388.3 nm (Nemes *et al*., 2000; Pearse and Gaydon, 1976).

The CN band is observed only when the applied voltage exceeds 10 kV, regardless of whether the needle power electrode is positioned at the inlet or the outlet. This suggests that energetic electrons are necessary for CN molecule formation. When the microfluidic device is removed, the needle power electrode produces a thin plasma jet propagating in air, and no CN bands are detected in the emission spectrum. This indicates that CN formation is not due to the presence of CO_2 in the air. Since the CN band appears exclusively with the microfluidic device, it can be concluded that the carbon originates from the interaction of plasma with the borosilicate glass. Furthermore, the Raman spectrum of plasma-treated microfluidic devices also reveals the presence of a new band around 2260 cm^{-1} that is attributed to a nitrile group (-C≡N) (Mojica *et al*., 2018; Quinet *et al*., 2006). This implies that CN bands are created in plasma and then deposited on the surfaces.

The presence of N_2^+ (B-X) and CN (B-A) species suggests Penning ionization involving metastable helium atoms and potential plasma-enhanced chemical reactions, respectively. Strong lines attributed to hydrogen (H_α at 656.3 nm) and an oxygen triplet (777.2 - 777.5 nm) are also observed. Raman spectrum on ignited plasma in gas-feeding Teflon tube further indicates the presence of hydroxyl ions (-OH) at 3563, 3635 and 3826 cm^{-1} and C=O bond at 1783 cm^{-1}. These were difficult to observe inside the microfluidic device with OES due to the opaqueness of glass in the region around 300 nm. The presence of nitrogen, oxygen, hydrogen, C=O and -OH bonds is likely due to trace impurities from air introduced by tubing outgassing, minor leaks, or bottle impurities.

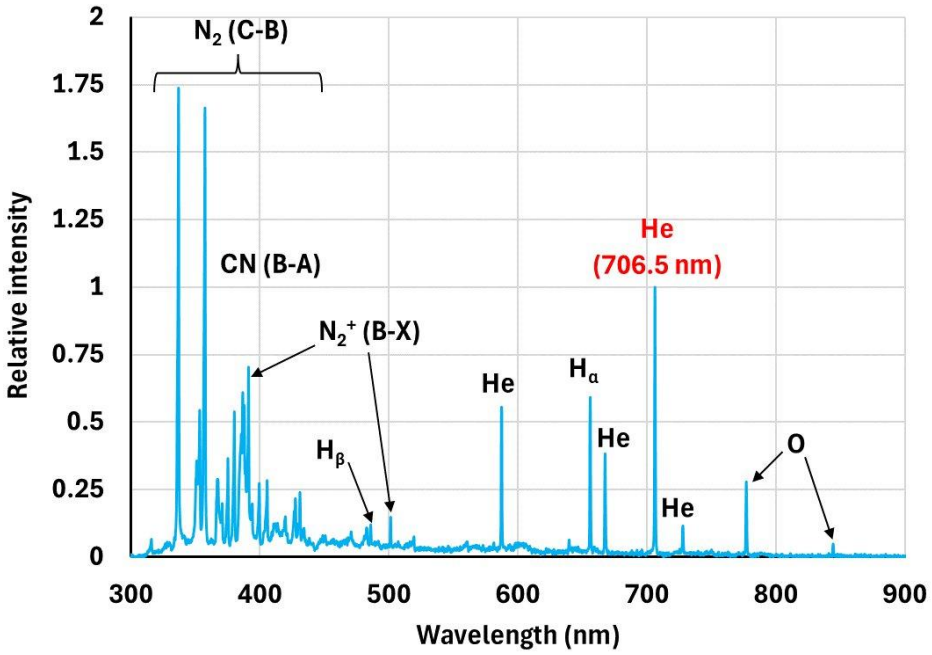

Figure 55 The optical emission spectrum is recorded at the inlet of a 500-µm channel of a microfluidic device produced by Micronit. Plasma is ignited with a 14 kV voltage, using the electrode configuration shown in Figure 20. The spectrum is obtained with an acquisition time of 500 ms and it is normalized to the intensity of the helium line at 706.5 nm, highlighted in red on the graph. The notations "C-B," "B-A," and "B-X" represent de-excitation processes occurring between specific molecular energy states.

The intensity of spectral lines and bands decreases with distance and increases with the confinement of the microchannel which is consistent with the plasma imaging results shown in Figure 50. Overall, in terms of plasma propagation, the treatments are expected to achieve uniform wettability alteration within the channel and main geometric feature with an appropriate electrode position. Based on the plasma composition revealed by the OES and Raman analysis, we expect rich plasma chemistry to be the driver of wettability alteration. In-depth chemical surface analysis is discussed in subsection 3.

c) Estimation of plasma power and temperature distribution

To estimate the impact of plasma on the material, we ran power and temperature measurements.

Plasma power

To measure plasma power, we first acquired the applied voltage (V_a) and current waveforms as shown in Figure 56. The initial measurement was conducted in an air-saturated microchannel to prevent plasma ignition, allowing us to measure capacitive current (I_{capa}), shown as a blue curve. As expected, the dielectric properties of air limited current flow. In contrast, when the microchannel was filled with helium and plasma ignited, a conductive pathway formed, enabling higher current flow (I_{tot}) (red curve). Subtracting the background capacitive current yielded the pure plasma

discharge current (I_{disch}) (green curve). The discharge current waveform exhibited a strong positive amplitude followed by a ≈ 50 % weaker negative amplitude, suggesting bidirectional plasma pulse propagation within the microchannel.

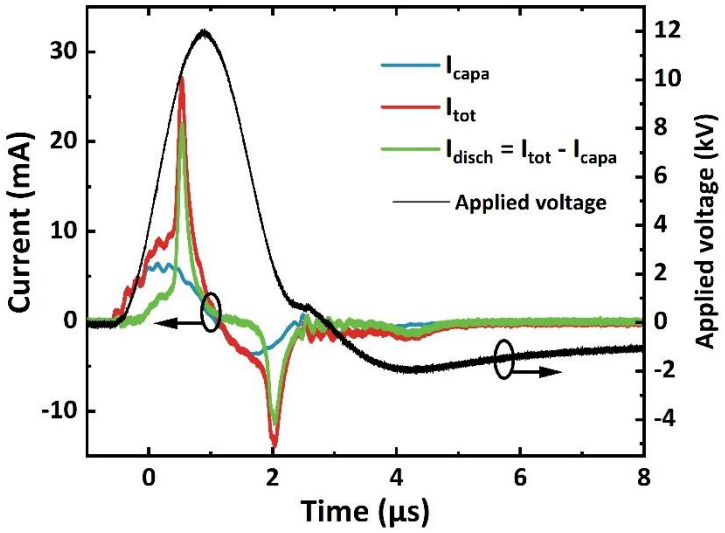

Figure 56 Waveforms of applied voltage (V_a), capacitive current (I_{capa}), total current (I_{tot}) and discharge current (I_{disch}). The measurements are acquired at 12 kV and 8 kHz as representative of typical plasma treatment.

Across the range of applied voltages and corresponding discharge currents, we determined the energy per pulse. Given the constant frequency of 8 kHz, the average plasma power was readily calculated. As shown in Figure 57, both energy per pulse and average plasma power increase with applied voltage, though the relationship is not strictly linear. For typical wettability treatment, plasma power reaches the order of hundreds of milliwatts.

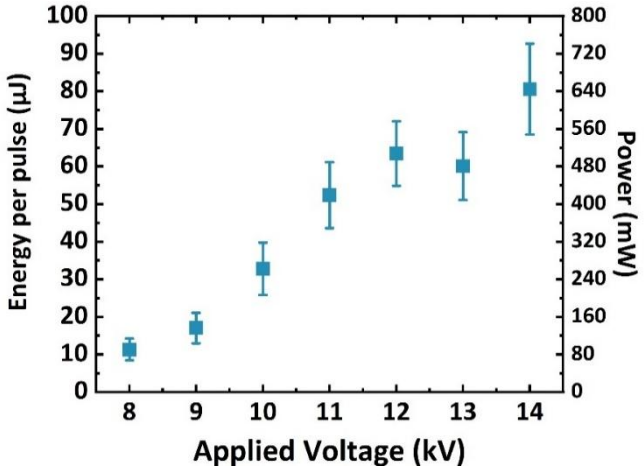

Figure 57 Energy per pulse and discharge power over the range of applied voltages.

Glass and gas temperature

As earlier described in the Procedures, temperature measurements are conducted on the external surface of the microfluidic device by placing the measurement probe directly onto the glass surface. The measurements are taken at two distinct locations: Location 1, near the inlet and powered electrode, and Location 2, near the outlet and grounded electrode, along a 500 µm-wide microchannel.

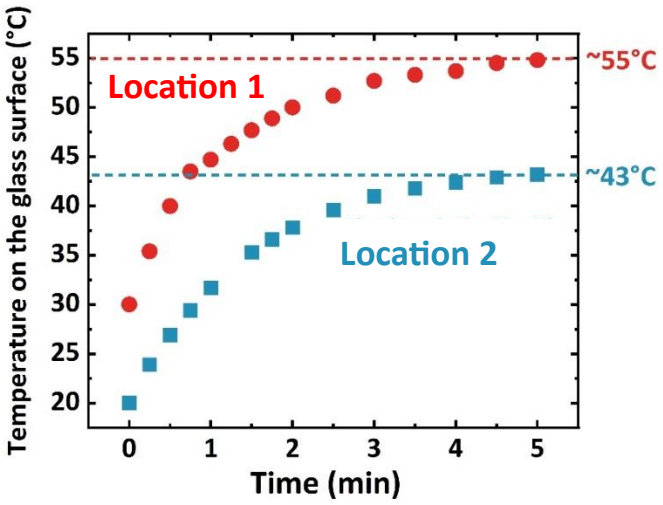

Figure 58 The temperature evolution of the microfluidic device during plasma treatment on two distinct locations. The measurements are performed under 12 kV of applied voltage.

The results of typical treatment performed at 12 kV, presented in Figure 58, indicate that temperature reaches a constant value after 5 minutes, with distinct values depending on the measurement location. At Location 1 (near the powered electrode), the temperature stabilized at approximately 55 °C, while at Location 2 (near the grounded electrode), it stabilized at around 43 °C.

With the measurement of glass temperature, we estimated gas temperatures at respective locations (1 and 2) within the microchannels to be around 70 and 60 °C. These values align well with those reported in the literature for helium atmospheric pressure jets, further validating the accuracy of the measurement and estimation methods (Chang *et al*., 2012; Douat *et al*., 2016; Jõgi *et al*., 2014; Mestre *et al*., 2024).

Overall, these findings highlight the extent and rate of material heating during plasma wettability treatment. With the maximum temperature remaining well below 100 °C, we can conclude that our plasma treatment is suitable for microfluidic devices fabricated from polymeric materials such as PDMS. Moreover, given the short treatment duration (approximately 1 minute – see Figure 59), the thermal load on the device can be further minimized.

2. Wettability performance

a) Treatment time

After achieving successful plasma propagation, the next objective is to evaluate its impact on surface wettability. Several single-pocket microchannels (Micronit) are treated with varying plasma exposure times, and the contact angle is measured shortly after treatment (within 2 hours). The electrode configuration for this treatment is just as depicted in Figure 44 and Figure 25a, with the powered electrode at the inlet and the ground at the outlet. The CO_2-water contact angle is measured at the inlet side of the 500 µm channel, just as shown in Figure 48.

As shown in Figure 59, the contact angle decreased from 53 ± 7° to 23 ± 5° within the first 60 seconds of treatment, resulting in an average reduction of 30°. Beyond 60 seconds of exposure, even with extended treatment times of up to 600 seconds, the contact angle remained stable. The maximum effect of the treatment is thus achieved within the initial 60 seconds. Based on these findings, an optimized treatment time of at least 120 seconds is selected.

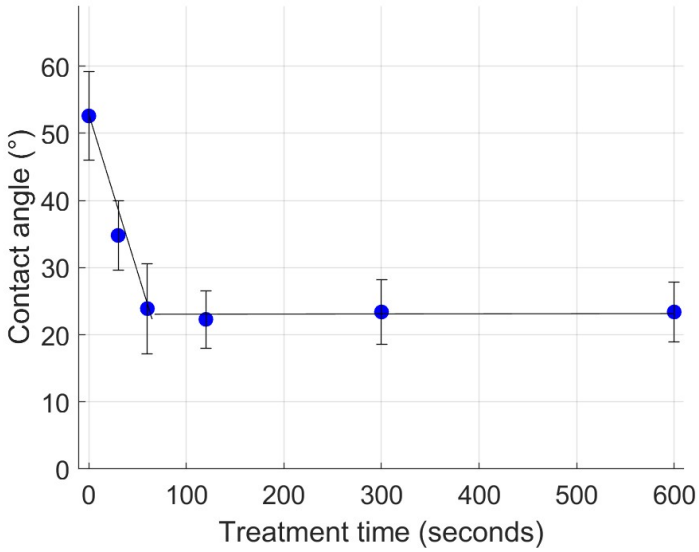

Figure 59 The dependency of in situ measured contact angle on plasma treatment time with illustrated with hand-drawn guide lines to emphasize the trend. Measurement on never-before-used Micronit devices.

To ensure the validity of further analysis, contact angles are also measured on the L-pore geometry, representing a batch of microfluidic devices manufactured by Klearia. *In situ* measurements of contact angles at the same location on untreated devices yielded a wettability of 59 ± 12°. While this result is comparable to previous findings, it has a larger error margin, likely due to more pronounced surface morphology and roughness variations in Klearia devices (see Figure 60) compared to Micronit devices (see Figure 49).

A single plasma treatment was conducted on the Klearia device for 120 seconds using the same electrode configuration as for the Micronit devices. As shown in Figure 60, the contact angle could not be measured, as a continuous water film formed along the microchannel walls, preventing the formation of a contact point at the channel edge between all three phases (glass, water and CO_2). This observation indicates that a perfectly hydrophilic condition, equivalent to a 0° contact angle, is achieved.

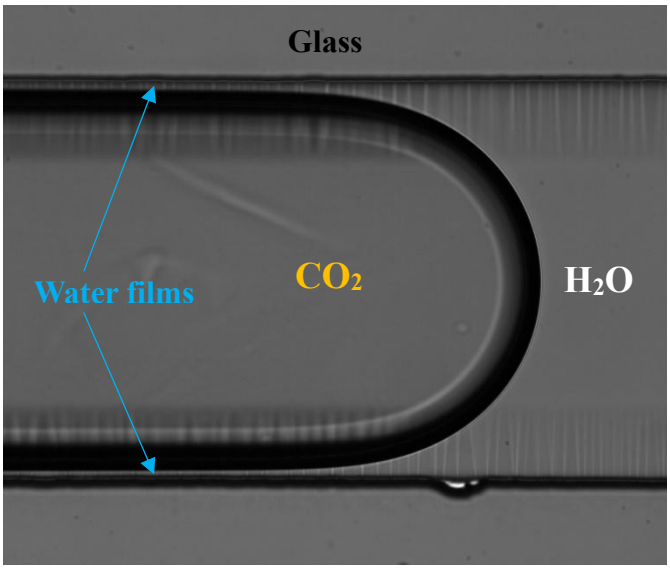

Figure 60 The interface between CO_2 and water in the Klearia device after plasma treatment.

To compare the wettability of confined and free surfaces, contact angle measurements were performed using the sessile drop method, a standard approach in the literature. Plasma treatment is applied to the top glass surface of the microfluidic devices using the XPS setup configuration shown in Figure 45. The setup was modified by incorporating a larger-diameter glass tube to accommodate droplet spreading. Measurements were conducted on both untreated and plasma-treated surfaces, with two replicates for each condition.

As depicted in Figure 61a, the air-water contact angle measure on the untreated surface is 52°, with a subsequent measurement at a nearby location yielding 55°. These values are consistent with the *in situ* CO_2-water contact angles observed in both microfluidic device batches. Following a 90-second plasma treatment, the first measurement recorded a contact angle of approximately 3°, while the second measurement at a different treated location exhibited rapid droplet spreading, precluding accurate contact angle determination. The observed reduction in contact angle, from approximately 50° to a superhydrophilic state, underscores the efficacy of plasma treatments as a robust method for inducing significant wettability alterations on glass surfaces.

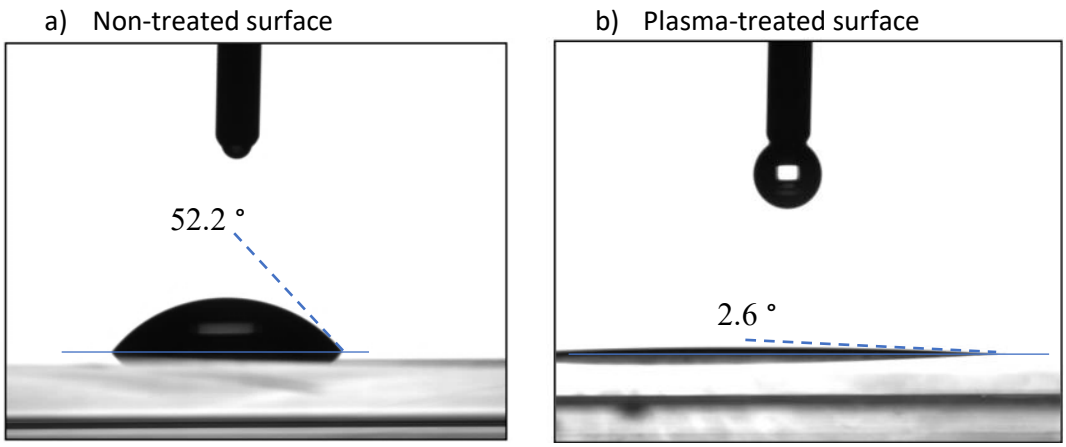

Figure 61 Sessile drop measurement results. Note, the contact angle measured here is between air and water on the Micronit device.

To summarize, atmospheric pressure plasma demonstrates major potential as a rapid and effective method for altering wettability on glass surfaces. Wettability values are influenced not only by the material's intrinsic properties but also by surface characteristics, including confinement and morphology. Overall, atmospheric pressure plasmas represent a promising tool for *in situ* wettability modification in enclosed glass microfluidic devices.

The potential for microfluidics extends well beyond the scope of this thesis, offering remarkable versatility. This includes compatibility with various materials, the use of different working gases, adjustable treatment durations for precise wettability control, and applicability to complex geometries, including three-dimensional microfluidic systems. In the next section, we evaluate the aging performance of the treated devices.

b) Aging performance

Given that wettability treatments are not permanent (Mansouri-Boroujeni, 2022; Primc and Mozetič, 2022; Tan *et al*., 2010), we chose to monitor the evolution of contact angles over time when microfluidic devices are stored in air and water. Additionally, we investigated the potential for re-treating previously used microfluidic devices.

The hypothesis is that longer treatment times may enhance the durability of surface modifications, resulting in more stable wetting conditions. Additionally, storing devices in water rather than ambient air is proposed as a more effective storage method. Ultra-pure MilliQ water is chosen as the storage medium to minimize potential reactions and thus protect against wettability degradation. All our tests are performed on Micronit devices.

Air storage

For air storage, three brand new microchannels are treated by plasma during 2, 5 and 10 minutes and comparison is made with one previously plasma-treated device. The contact angle is measured at the inlet side of the 500 µm channel where the plasma indicates a stronger light intensity. The evolution of the contact angle is evaluated for 23 days. As illustrated in Figure 62, the variations

between different treatment durations (2-, 5- and 10-min treatments on new microchannels) all fall within the margin of error. Consequently, the hypothesis that treatment time affects the aging performance of wettability is disproven and a 2-minute treatment appears more than sufficient for proper plasma treatment.

To maximize the utility of costly glass microfluidic devices (300 - 600 € per device), the feasibility of re-treatment is investigated. As shown in Figure 62, the initial contact angle after retreatment exhibits slightly lower and less dispersed average values; however, well within the range observed in new microfluidic devices. Full hydrophobic recovery is also consistently achieved within approximately two weeks. These findings indicate that retreating previously treated devices after their hydrophobic recovery does not significantly alter their wetting behavior. To date, up to five retreatments have been successfully applied to a single microchannel. Given the robust and inert nature of glass, combined with the fact that plasma treatments do not affect the bulk properties of the material, it is reasonable to assume that many additional retreatments are feasible. This durability offers a distinct advantage over certain polymer materials which are typically intended for single use; as such, retreatments are unnecessary and could potentially degrade the material.

Since the results obtained on new and retreated surfaces closely match (Figure 62), we can confidently state that strongly hydrophilic conditions with our plasma treatment within microchannel glass surfaces stay stable for at least 1 day in air storage.

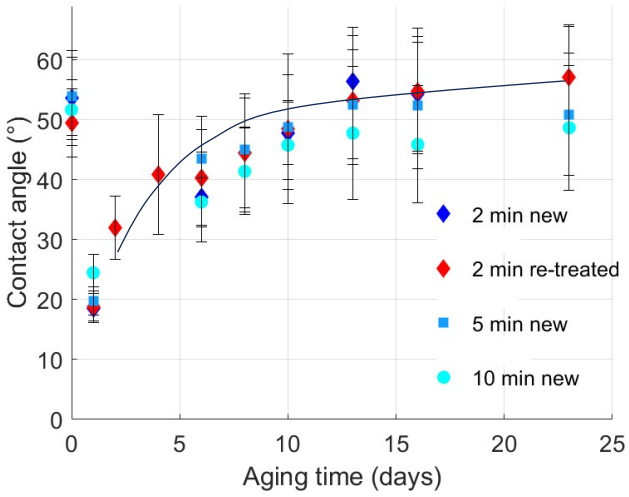

Figure 62 The evolution of contact angle in air storage after treatment with a simple normal electrode configuration (Figure 50a) for 2, 5 and 10 minutes. A hand-drawn guideline is used to emphasize the trend. Note: day "0" represents the contact angle just before plasma treatment.

To assess the uniformity of plasma treatment, contact angles were further measured near the outlet of a 500 µm channel. As shown in Figure 63, the average values between the inlet and outlet differ by approximately 3 to 4°. Slightly lower average values are consistently observed near the inlet, where the plasma intensity is higher. However, given the fact that all measurements fall within the margin of error, the treatment can be deemed uniform overall.

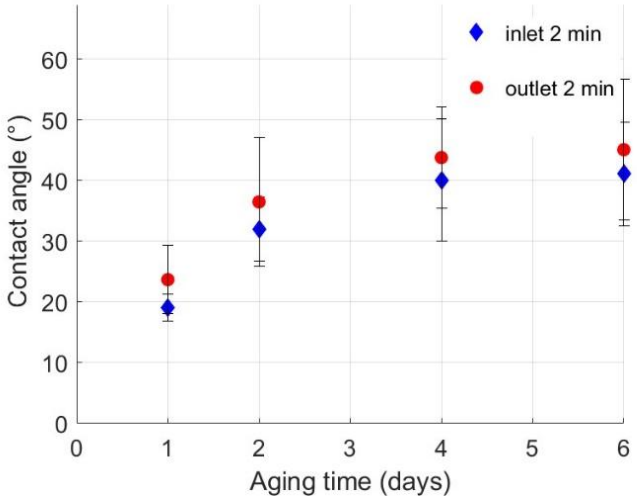

Figure 63 The uniformity of plasma treatment, checked by comparing the wettability of the inlet and outlet 500 µm channel in air storage.

Water storage

The same plasma treatment methodology and wettability measurements were extended to samples stored in water. As depicted in Figure 64, highly hydrophilic conditions remained stable for at least three days post-treatment. During this period, up to 17 contact angle measurements were conducted, wherein CO_2 was introduced for each measurement (approximately 5 minutes to fully saturate the microchannel with CO_2 and evaporate water). These results demonstrate good overall stability of the induced wettability, making it suitable for two-phase microfluidic experiments involving these consumables.

Beyond three days, the wettability gradually increased, reaching 31 ± 8° by day four. Long-term observations revealed that the wettability remained stable for at least 70 days, regardless of the initial plasma treatment duration. This behavior contrasts sharply with that observed under air storage conditions.

The evolution of wettability aligns with the initial hypothesis and corroborates findings from the literature on plasma treatment effects on other materials (Dou *et al*., 2021; Vizireanu *et al*., 2017). Consequently, water storage presents a promising solution for long-term storage or experiments conducted in pure water, provided that a moderate increase in contact angle is acceptable.

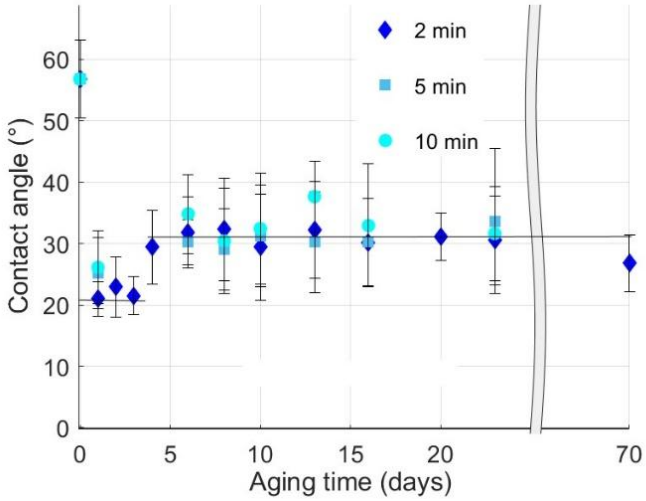

Figure 64 The evolution of contact angle in water storage after treatment with a simple normal electrode configuration (Figure 50a) for 2, 5 and 10 minutes. Hand-drawn guidelines are used to emphasize the trend. Note: day "0" represents the contact angle just before plasma treatment.

3. Surface chemical characterization with XPS

To investigate the mechanisms behind wettability alteration and aging, we performed chemical analysis on the glass surfaces of microfluidic devices using XPS. In addition to analyzing a non-treated reference sample, four other conditions were evaluated. To validate the immediate effect of plasma on surface wettability without aging influences (day 0) and to assess potential differences in applied voltages during plasma treatment (10 kV and 15 kV), two samples were prepared for comparison. The remaining two samples were prepared to explore the distinct aging mechanisms in air and water storage. Our findings are presented as (1) a comparison of elemental composition based on normalized areas under the curve for oxygen, carbon, and nitrogen, as summarized in Table 11 and (2) processed XPS general survey and high-resolution spectra shown in Figure 65.

Table 11 Elemental composition of glass surfaces for five samples, with corresponding treatment parameters and wettability. Values are based on the area under high-resolution XPS peaks, normalized to a reference for each element. These areas reflect the surface elemental quantities.

Sample	1	2	3	4	5
Plasma (Yes/No)	**No**	**Yes**	**Yes**	**Yes**	**Yes**
Voltage (kV)	**/**	**10**	**15**	**15**	**15**
Aging (Yes/No)	**/**	**No**	**No**	**Yes**	**Yes**
Storage medium	**/**	**/**	**/**	**Air**	**Water**
Contact angle (°)	**53**	**23**	**23**	**42**	**31**
Carbon	**1.00**	**0.53**	**0.53**	**0.59**	**0.61**
Oxygen	**1.00**	**1.39**	**1.37**	**1.32**	**1.28**
Nitrogen	**1.00**	**0.65**	**1.26**	**0.74**	**0.39**

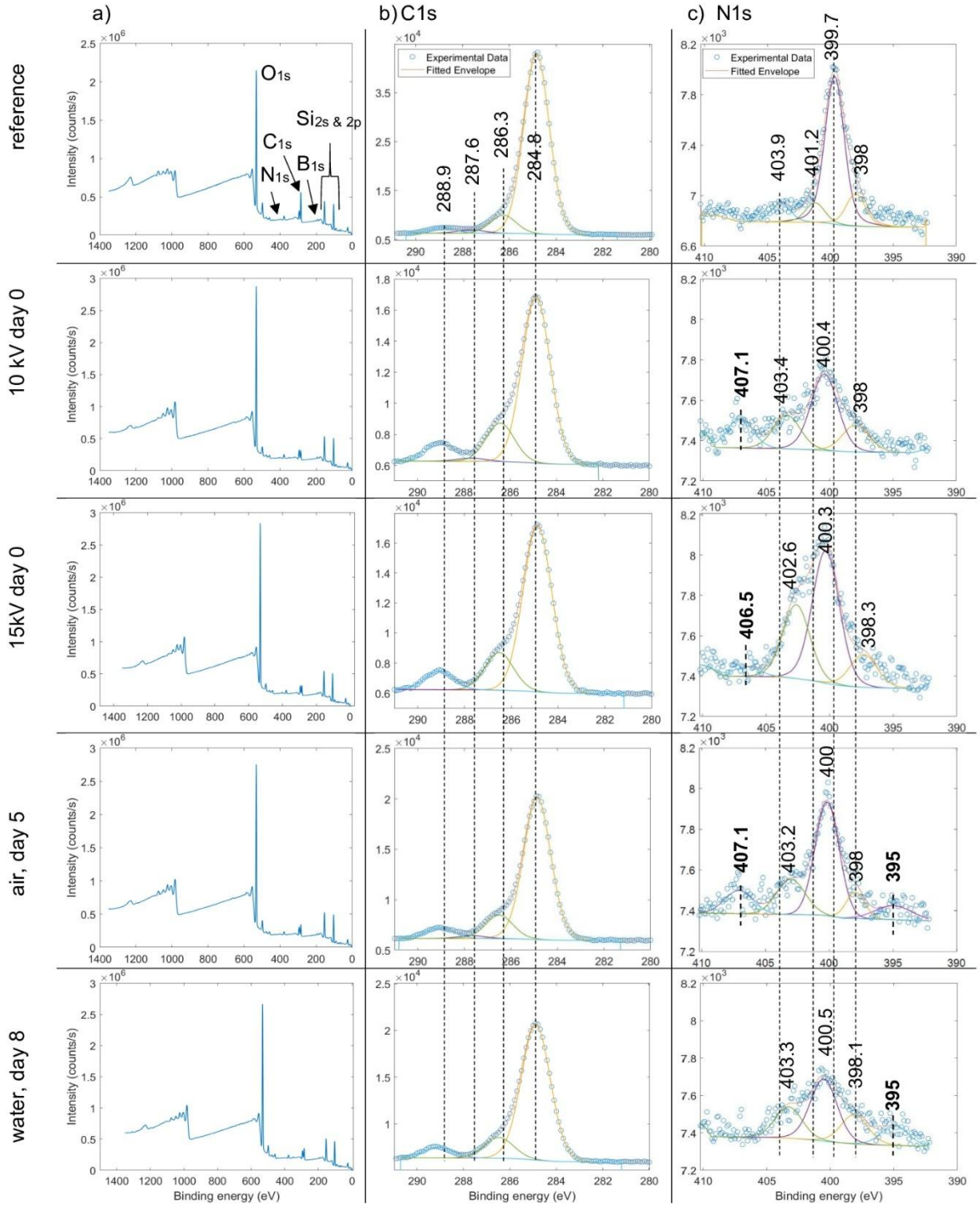

Figure 65 The XPS spectra for five tested samples: Column a) shows general survey spectra (5 scans/sample, 1 eV resolution), while b) and c) display high-resolution carbon and nitrogen spectra (50 scans/sample, 0.1 eV resolution). Dashed lines mark reference sub-bands, highlighting binding energy shifts in plasma-treated samples.

a) Mechanisms of wettability alteration

In the general survey spectrum of the reference (non-treated) sample (Figure 65a), the presence of principal and minor glass elements is evident. These include silicon (103 eV), oxygen (532 eV), carbon (285 eV), boron (192 eV), zinc (1022 and 1045 eV), aluminum (74 eV), sodium (1073 eV), and nitrogen (399 eV). Notably, hydrogen and helium remain undetectable by XPS analysis. Comparing the reference spectrum to any plasma-treated sample (Figure 65a) reveals predominantly quantitative changes in the elemental composition of the glass surface.

As oxygen, carbon, and nitrogen were previously identified by OES as components of plasma (see Figure 55) and drivers of wettability alteration (Vandenbossche and Hegemann, 2018), further analysis focuses on these elements using high-resolution spectra. The untreated sample surface consists primarily of oxygen (84.2%), with some carbon (14.9%) and a small amount of nitrogen (0.9%). Referring to Table 11, the initial XPS analysis indicates an increase in oxygen and a decrease in carbon and nitrogen content on all plasma-treated surfaces, irrespective of treatment or aging conditions. High-resolution spectra decomposition confirms oxygen's presence in the bulk glass structure (Si-O and B-O bonds), while most carbon and nitrogen appear as removable surface contaminants (see Figures 9b and 9c). This observation suggests that plasma cleaning exposes a fresh, uncontaminated glass surface rich in oxygen while physically and chemically removing carbon and nitrogen contaminants. Consequently, the exposure of oxygen groups increases the surface's hydrophilicity. Since oxygen and carbon dominate the surface's elemental composition, plasma cleaning is considered to be a key driver of wettability alteration. The treatment's effectiveness appears independent of applied voltage, as oxygen and carbon levels between 10 kV and 15 kV treatments show minimal differences (Table 11).

Nitrogen levels in all plasma-treated samples are lower than in the reference (Table 11), indicating nitrogen's association with surface contaminants removed by plasma. For day 0 samples, the 15 kV treatment results in slightly higher nitrogen levels than the 10 kV treatment, consistent with OES findings that show increased nitrile/cyanogen groups due to interactions between ionized nitrogen and surface carbon. As earlier mentioned, following the plasma treatment, the nitrile group was also identified in the Raman spectrum. Overall, it appears that surface nitrogen and carbon contaminants are transformed into functionalized groups under plasma exposure.

High-resolution spectral analysis (Figure 65b and Figure 65c) further investigates potential binding energy shifts indicative of new chemical bond formation. Carbon peak analysis (Figure 65b) reveals a small increase in the O-C=O bonding sub-band at 288.9 eV after plasma treatment, with a stronger effect at 15 kV. This sub-band corresponds to carboxyl group (COOH) formation (Egghe *et al*., 2022), suggesting a functionalization mechanism contributing to wettability alteration. Other sub-bands show a significant decrease, confirming their role as surface carbon contamination and warranting no further analysis.

Nitrogen peak analysis (Figure 65c) demonstrates qualitative (binding energy shifts) and quantitative (intensity/area-under-the-curve changes) alterations across conditions. The sub-band

at 398 eV, associated with strong nitrogen bonding to silicon and/or boron in the glass, is present in all spectra with minimal binding energy shifts (up to 0.3 eV). The reference spectrum's sub-band at 401.2 eV disappears in plasma-treated samples, while the 403.9 eV sub-band shifts to lower binding energies with changes in the area under the curve. The entire region between 392 and 405 eV, linked to organic nitrile, amino, or similar groups (Aziz *et al*., 2017; Egghe *et al*., 2022; Jansen and Van Bekkum, 1995), shows shifts and area changes. This suggests a dual plasma effect: some organic compounds are transformed into functionalized groups (evidenced by broader nitrogen bands in treated samples), while others are etched away, reducing less hydrophilic surface contaminants.

b) Mechanisms of aging in air and water

Further analysis of the nitrogen spectra (Figure 65c) reveals that the highest energy sub-band, around 407 eV, is present exclusively in plasma-treated samples, except for those stored in water. According to Thermo Fisher and other XPS databases, this sub-band is associated with the formation of nitrates. Its absence in water-stored samples is attributed to the solubilization of nitrates in water.

The reduced aging effects observed in water storage compared to air storage can be explained by a synergistic interplay of several mechanisms. As noted, the hydrolysis of certain nitrogen compounds by water is the primary cause of partial wettability loss. However, the presence of ultra-pure MilliQ water covering the glass surfaces prevents the reintroduction of hydrophobic contaminants from the surrounding environment (air). Additionally, hydroxyl groups, essential components of carboxyl groups, are present in water but absent in air. This results in a preserving effect on the carboxyl groups, contributing to sustained wettability after the initial increase in contact angle.

These XPS findings align with the observed wettability behavior, supporting the initial decrease in contact angle following plasma treatment and the subsequent increase over time during aging in both storage fluids.

V. Conclusion

Based on the literature review, we opted for atmospheric pressure plasma as a promising tool for wettability alteration and developed a setup tailored for closed glass microfluidic devices. We selected a kHz helium atmospheric pressure plasma in a DBD-like configuration due to its ability to penetrate and propagate within microchannels, its cold, non-thermal nature, and its reactive plasma chemistry, enabling *in situ* surface modification while preserving the bulk material.

We demonstrated that our setup indeed produces cold plasma (< 100 °C) with a power of several hundred mW that successfully propagates through 4 cm long microchannels of variable width. Analysis of plasma propagation indicates that electrode configuration plays a major role in the manipulation of plasma propagation, which is especially in more complex geometrical patterns. A quick overview of plasma species by OES indicates rich plasma chemistry extending far beyond helium, which is the dominant gas.

The core section of this chapter focuses on wettability performance. We achieved rapid surface treatment in approximately one minute, with aging performance dependent on the storage medium. Devices stored in air exhibited one day of the lowest contact angle stability, extended to approximately three days when stored in water. Microfluidic devices stored in the air experienced complete hydrophobic recovery to their initial state prior to plasma treatment. Re-treatment demonstrated consistent wettability results, highlighting the possibility of reusing precision-engineered, difficult-to-manufacture glass microfluidic devices, which is advantageous given their high production cost.

Initial insights into the mechanisms underlying wettability alteration were derived from OES and preliminary Raman spectroscopy analyses. Further investigation using XPS attributed wettability changes to surface cleaning and functionalization of the glass surfaces. Namely, plasma treatment reduces carbon surface contamination by exposing a natively hydrophilic glass layer and attaches various hydrophilic functional groups (carboxyl, amino, etc) whose stability depends on the storage medium.

This *in situ* wettability treatment facilitates the processing of pre-bonded microfluidic devices commonly purchased from manufacturers, enabling the treatment of all microchannel walls while minimizing wettability degradation that may occur during bonding. Overall, the application of atmospheric pressure plasma as an *in situ*, post-bonding treatment represents a novel and effective method for wettability alteration, particularly suitable for closed microfluidic systems.

VI. Preliminary work/perspectives

Here are some of the preliminary results and perspectives to continue work on our plasma platform.

1. Improving stability by optimizing plasma composition

For some of our experiments, the gas tubing was not adequately flushed with helium, resulting in increased concentrations of air impurities within the gas. We observed that the presence of these impurities extended the stability of wetting conditions for up to 85 days in air storage (refer to Figure 66). This is a massive improvement compared to the previous 1-day stability. Therefore, it would be interesting to further investigate the influence of air as a composite mixture, as well as the individual effects of its components - nitrogen, oxygen, carbon dioxide, and water vapor. The concentration of these admixtures should be kept low. According to the literature, higher impurity concentrations could lead to issues such as ignition difficulties, hindered plume propagation, and the generation of arc discharges, resulting in less uniform surface effects, which are undesirable.

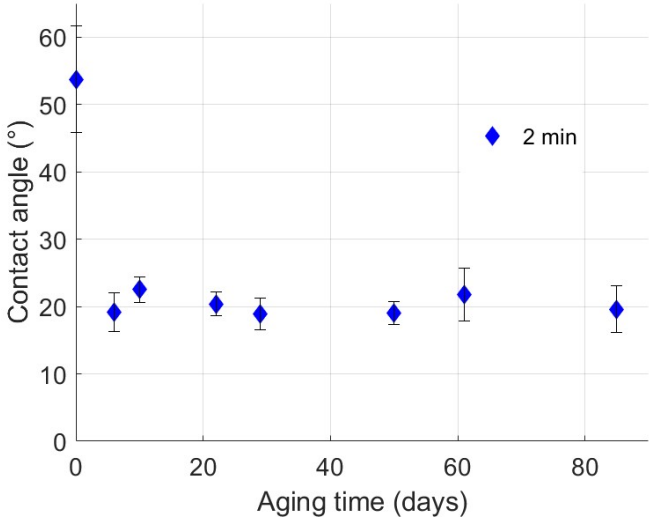

Figure 66 The in situ contact angle evolution with aging time in air storage. Plasma is ignited in helium with an unknown amount of impurities.

2. The addition of CO_2 impurities

In addition to "pure" helium plasma, CO_2 was introduced into the helium stream to investigate its potential effect on the wettability of glass surfaces. CO_2 was selected due to its known ability to deposit hydrophilic functional groups, such as carboxyl groups, which could enhance the stability of treated surfaces. This choice is particularly relevant given the presence of CO_2 in microfluidic experiments. To the best of our knowledge, no prior studies have examined the influence of CO_2 admixture in helium plasma or pure CO_2 plasma on the wettability of borosilicate glass. The most comparable study, conducted by Lin *et al.* (2021), utilized up to 100% CO_2 in atmospheric-pressure dielectric barrier discharge (DBD) plasma for the treatment of PTFE surfaces. They found that

increasing the CO_2 to N_2 ratio in favor of CO_2 results in lower contact angle values due to functionalization with carboxyl groups.

In our experiments (Figure 67), CO_2 was added to helium plasma as an admixture ranging from 0.1 to 10.7 vol%. The treatment duration was fixed at 2 minutes, while all other plasma parameters remained constant (50 sccm helium flow rate, voltage sufficient for full propagation, and an operating frequency of 8 kHz). At a CO_2 flow rate of 0.3 sccm (0.6 vol%), the plasma treatment achieved a minimum average contact angle of 21.3°, comparable to that obtained with pure helium plasma. Contact angles remained stable across higher CO_2 concentrations, showing no significant variation. However, at CO_2 flow rates exceeding 1 sccm (2 vol%), the voltage required for plasma ignition and propagation across the entire microchannel increased. This higher voltage occasionally caused arc discharges, which are undesirable due to their adverse effects on surface treatment uniformity.

From the perspective of altering wettability, the addition of CO_2 did not produce notable differences. Nevertheless, its potential effects on treatment duration and stability warrant further investigation. Similar experiments could be extended to molecular gases such as oxygen and nitrogen, given prior observations that higher air content in plasma treatments enhances the stability of hydrophilic surfaces stored in air.

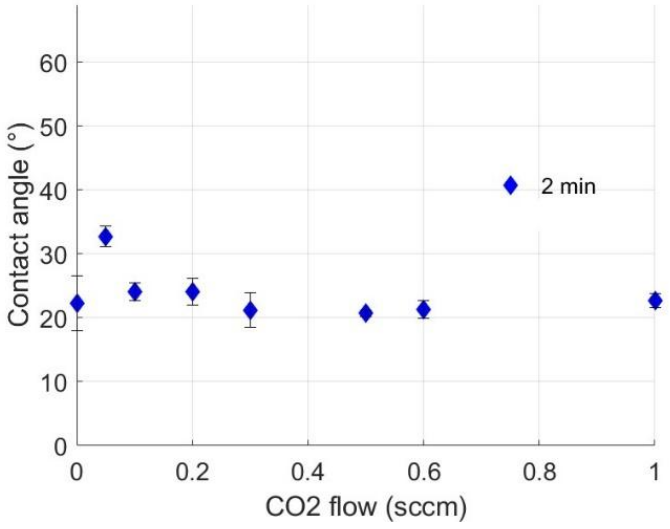

Figure 67 The impact of CO_2 impurities into helium plasma on the in situ contact angle.

Our plasma treatments so far have focused primarily on enhancing surface hydrophilicity, as most unaltered rocks are typically water-wet. However, as suggested in the literature review (Table 10), exploring chloro-fluoro-hydrocarbons may offer a pathway for achieving hydrophobic wettability characteristics on glass microfluidic devices.

3. Propagation in a complex porous system

The final set of preliminary results focuses on plasma propagation within highly complex microfluidic designs, such as those found in the enhanced oil recovery (EOR) device from Micronit. This device features a uniform depth of only 20 µm and various grain and pore sizes ranging in width from 50 to 130 µm.

At a helium flow rate of 50 sccm, a notable pressure buildup was observed. Elevated pressure conditions presented significant challenges for plasma ignition, as the reduced mean free path between gas molecules at higher pressures hindered the process.

Despite these obstacles, plasma propagation was successfully achieved in a portion of the geometry (see Figure 68). Thus, to enhance the propagation, a vacuum pump at the outlet could be used to partially offset the pressure buildup.

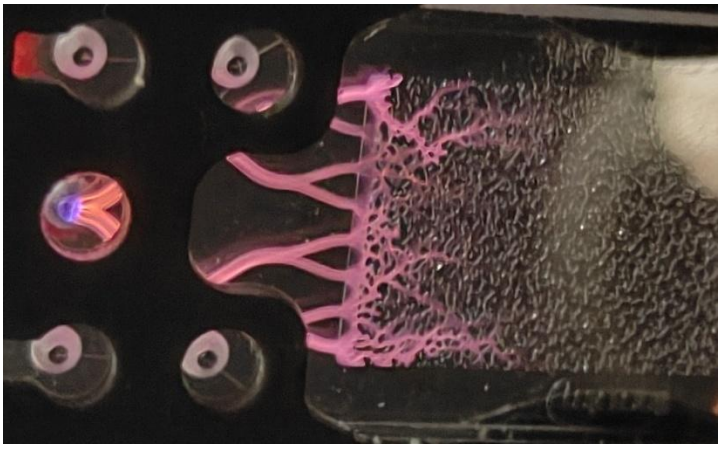

Figure 68 Plasma propagation in the EOR microfluidic device. The plasma is ignited with 16 kV by placing a power electrode at the outlet and a ground copper foil at the inlet of the geometry.

4. PDMS and other typical microfluidic systems

Extending the application of atmospheric pressure plasma treatments to polymeric materials like PDMS, a widely used material in microfluidics, offers significant potential for advancing device functionality. PDMS is valued for its flexibility, transparency, and ease of fabrication, but its inherent hydrophobicity presents challenges in applications requiring enhanced wettability or specific surface properties. Thus, our powerful yet non-destructive atmospheric pressure plasma treatment could effectively modify PDMS surfaces by introducing polar functional groups, improving wettability, and enabling better adhesion for biofunctionalization or bonding. The versatility of this treatment could address challenges related to hydrophobic recovery, as plasma-induced modifications can be tuned for durability through storage medium optimization and/or supplementary coating strategies. Furthermore, the ability to process fully assembled PDMS devices using atmospheric plasma allows for to treatment of all the inner walls of the device and ensures a uniform wettability alteration. In that direction, some preliminary work was performed in GREMI (France) on PDMS-glass microfluidic devices. Neon plasma was successfully

propagated in rectangular straight channels with 200 × 200 μm. Following the treatment, the increase in interface curvature between air and water indicated that the microchannel became more hydrophilic, however, further research is needed to systematically evaluate treatment time and aging performance.

Chapter 4 - Influence of wettability on residual and solubility trapping

The aim of this chapter is to utilize microfluidic devices to evaluate the effect of porous media wettability on interfacial mass transfer in the CO_2-water system, emulating a solubility storage mechanism within the scope of CCUS. Following the state-of-the-art research overview on capillary trapping and fluid/fluid interfacial mass transfer, we introduce our setup and procedures. Glass microfluidic devices with various geometries are deployed with the purpose of trapping one fluid phase at a time while the other is flowing, thus performing drainage or imbibition. At first, basic flow properties are determined and adjusted to be representative of CO_2 underground processes. The wettability of microfluidic devices is controlled by plasma treatments as described in Chapter 3 and it is kept within a hydrophilic range which is representative of most underground rocks. The core of the results and discussion is focused on evaluating capillary trapping and mass transfer for two distinctive geometries and two wettability conditions. The main results are outlined in the conclusion, together with perspectives for future research.

I. Introduction

In this section, we introduce the current pore-scale state of the art on wettability-influenced capillary trapping and fluid-fluid interfacial mass transfer.

1. Capillary trapping at the pore scale

Percolation theory provides a statistical framework for understanding capillary trapping by modeling fluid invasion in porous media as a network of connected pathways (Larson *et al*., 1977). During fluid displacement within a porous structure, the invading phase can either percolate through continuous flow channels or become immobilized in isolated clusters due to capillary barriers. At low capillary numbers, displacement follows an invasion percolation regime, where the movement of the non-wetting phase is governed by the largest pore-throat capillary entry pressures. However, significant discrepancies in numerous experimental data (Figure 69) suggest that capillary trapping in natural porous media is influenced by additional parameters beyond those accounted for in traditional percolation models.

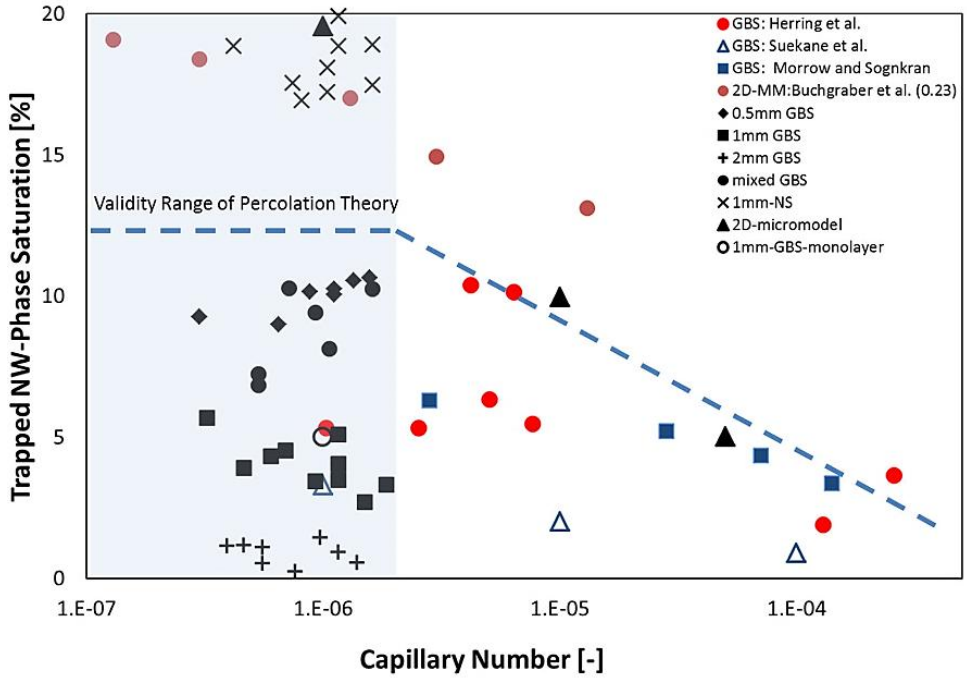

Figure 69 Experimental data on trapping efficiency of non-wetting (NW) phase over a range of capillary numbers. Taken from Geistlinger et al. (2015).

A more comprehensive description of capillary trapping requires incorporating pore-scale mechanisms that directly influence fluid retention or displacement. Snap-off and bypassing are critical processes that control the distribution of trapped non-wetting fluids across the porous medium during displacement. Capillary storage of wetting fluids during drainage is typically measured in volumes present in thin films and corners adhering to the solid fraction of porous media. All these mechanisms are strongly dependent on fluid properties, flow conditions, and

porous media characteristics, which collectively govern the balance between capillary and mobilizing forces (Chatzis *et al*., 1983; Geistlinger *et al*., 2015; Mansouri-Boroujeni *et al*., 2023; Primkulov *et al*., 2021). The lack of a complete physics description of the process in large-scale models limits the accuracy of macroscopic flow predictions, underscoring the need for a multiscale approach to capillary trapping.

Key factors governing capillary trapping mechanisms have been extensively investigated through experimental studies. Niu *et al*. (2015) demonstrated that CO_2 capillary trapping is governed by key dimensionless parameters such as the viscosity ratio and capillary number, rather than directly by reservoir pressure and temperature. This allows for the use of analog fluids, such as air, to reproduce the relevant flow conditions and study capillary trapping mechanisms under ambient experimental settings. This finding endorses the use of controlled laboratory platforms, such as microfluidic experiments, to systematically isolate and analyze pore-scale trapping mechanisms under well-defined and reproducible conditions.

The influence of flow conditions on capillary trapping is largely governed by the capillary number, which dictates the balance between viscous and capillary forces. At higher capillary numbers (i.e., higher flow velocities), viscous forces typically dominate, leaving a lower saturation of non-wetting fluid (see Figure 69). At lower capillary numbers (i.e., lower flow velocities), the variability of fluid (e.g., viscosity ratio) and porous media properties (e.g., wettability) becomes important and creating discrepancies in capillary trapping (Mansouri-Boroujeni *et al*., 2023; Primkulov *et al*., 2021). For example, Mansouri-Boroujeni *et al*. (2023) demonstrated in a pore doublet microfluidic experiments that a fast-moving interface in the viscous flow regime improves sweep efficiency by penetrating both branches but reduces displacement efficiency, leaving a significant amount of wetting phase behind. Conversely, a slower-moving front in the cross-over and especially capillary flow regime, enhances displacement efficiency, but leads to higher overall residual saturation of the wetting phase.

Surface roughness is another less accounted parameter, especially at large scale, that plays a role in capillary trapping by promoting wetting film and corner flow, which enhances snap-off events ahead of bulk fluid displacement. In smoother pore structures, displacement tends to follow a piston-like filling pattern, resulting in a more uniform gas-liquid distribution. In contrast, rougher surfaces facilitate the formation of pendular rings and capillary pinning, where liquid becomes immobilized at pore throats or edges, restricting its movement. These surface irregularities create anchoring sites and increase surface area, enhancing the retention of the wetting fluid and promoting the formation of suspended structures that facilitate the trapping of the non-wetting fluid. Mehmani *et al*. (2019) and Sun *et al*. (2021) demonstrated in microfluidic experiments that when the hillock height to pore depth ratio approaches 0.1, capillary trapping becomes highly sensitive to surface roughness.

Wettability inherently implies surface roughness; however, surface roughness can create irregular interfaces that cannot be described by a single contact angle due to contact line pinning at random

surface asperities. In rough channels, the interface advances dynamically and unstably, whereas in smooth channels, it moves in a piston-like manner (Sun *et al.*, 2021). Wettability influences phase distribution across different pore sizes, determining flow patterns and fluid-fluid displacement, which can occur as either drainage or imbibition depending on the solid surface properties.

A significant experimental contribution to wettability studies on microfluidics during two-phase flow was made by Zhao *et al*. (2016). They saturated microfluidic devices with silicone oil and injected water at varying flow rates. For a fixed fluid injection order, they modified the wettability of the porous media, characterizing injections as either drainage or imbibition. The resulting observations of fluid distribution and flow pattern are shown in Figure 70. Regardless of wettability conditions, a decrease in the capillary number was found to increase the displacement efficiency of the defending fluid (silicone oil) and the saturation of the invading fluid (water). This highlights the growing significance of porous media surface properties as flow forces diminish. Furthermore, they found that the effect of porous media wettability is not linear due to variations in governing displacement mechanisms. Transitioning from strong drainage (150°) to weak imbibition (60°) increases the invading fluid saturation and enhances displacement efficiency via cooperative pore-filling. At strongly wetting conditions (7°), spontaneous imbibition directs invading fluid flow along solid surfaces, leading to corner flow in microfluidic devices with rectangular cross-sections. The onset of corner flow in right-angle microfluidic channels occurs at approximately 45° of contact angle, as described by the relation $\theta < (180 - \alpha) / 2$, where α is the corner angle (Concus and Finn, 1969). For CCUS applications, this suggests that the displacement during CO_2 injection should be most efficient under weak imbibition conditions, implying slightly CO_2-wet reservoir rocks. However, efficient displacement in a CO_2-wet environment implies that the phase is still connected and mobile possibly favoring structural trapping on a large scale. In contrast, significant capillary trapping is more likely in water-wet environments, where spontaneous imbibition into CO_2-saturated zones can occur when injection ceases and/or in regions further from the injection point, where the capillary number remains low.

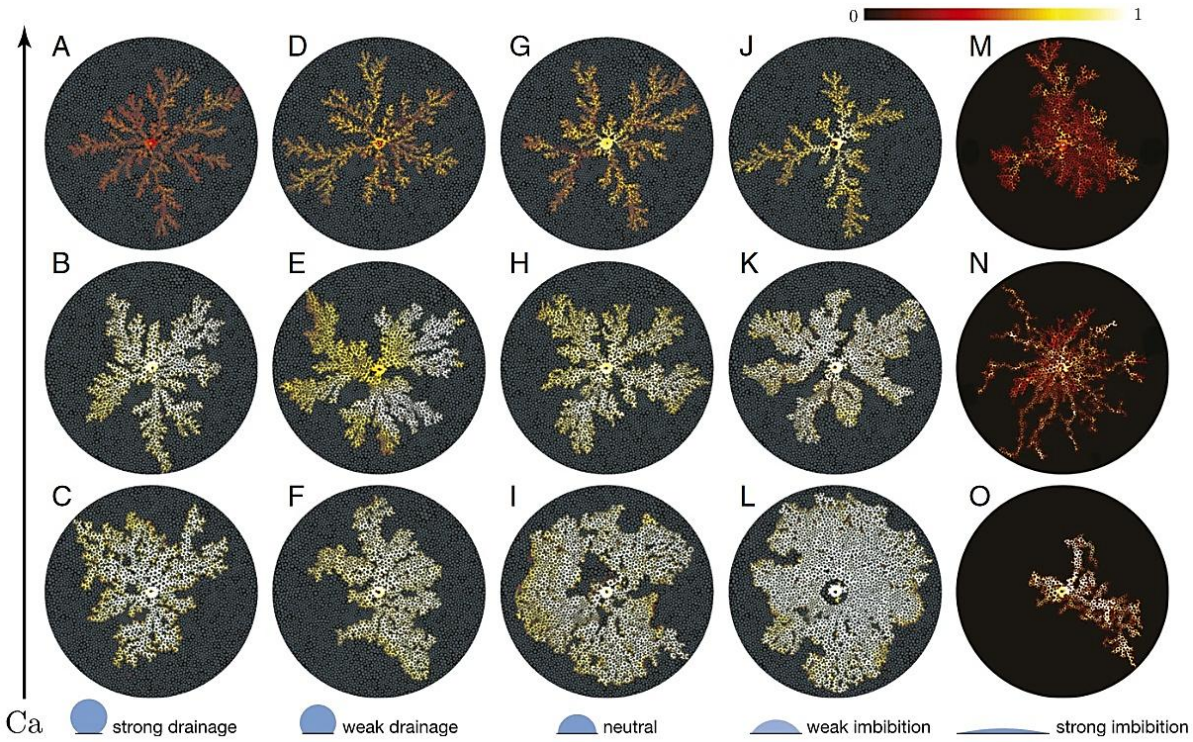

Figure 70 The displacement patterns in microfluidic devices using silicon oil and deionized water (M = 340). Respective contact angles going from left to right are: 150°, 120°, 90°, 60 and 7°. Capillary numbers going from the bottom to the top are 3×10^{-3}, 3×10^{-2}, 3×10^{-1}. The color bar shows the average saturation of the invading water. Taken from Zhao et al. (2016).

Pore geometry, wettability, and surface roughness collectively dictate two-phase flow behavior and fluid trapping through well-established displacement mechanisms. Furthermore, increased system disorder - characterized by broader grain size distributions, heterogeneous coordination numbers (the number of throats connected to a single pore), and wettability variations - has been generally associated with enhanced fluid trapping.

Once capillary-bound to the solid and isolated by a continuous fluid phase, the trapped fluid is not necessarily fully immobilized. Microfluidic PIV experiments by Roman *et al*. (2016 and 2020) reveal four distinct viscous dissipation mechanisms, observed through the recirculation of trapped wetting fluid during drainage. These dissipation mechanisms are influenced by capillary number, viscosity ratio, trapped fluid geometry, and lubrication effects. Since these mechanisms depend on the attraction of fluid to solid surfaces and the fluid-fluid interfacial area, the wettability of solid surfaces is expected to directly influence the occurrence and distribution of different dissipating regimes across porous media.

These pore-scale phenomena underscore the critical role of experimental pore-scale research in addressing discrepancies in understanding capillary trapping at larger scales that deviate from the standard multiphase Darcy model. Furthermore, such observations enhance the understanding of

other trapping mechanisms, including dissolution trapping, i.e., interfacial mass transfer in porous media.

2. Fluid-fluid interfacial mass transfer at a pore scale

Despite the recognized importance of wettability in multiphase flow and mass transfer (Agaoglu *et al*., 2015), most models describing mass transfer at fluid-fluid interfaces in porous media neglect its effects due to the lack of reliable quantitative data. High-resolution experimental studies under controlled conditions remain scarce, limiting our ability to quantify the role of wettability in key sequestration processes. As emphasized by Aminu *et al*. (2017), CO_2 sequestration is inherently dynamic, yet existing research still lacks quantitative pore-scale investigations that capture the temporal evolution of individual trapping mechanisms. Solubility trapping is the crucial link between capillary trapping on one side and mineral trapping on the other side, bridging time and safety scales of CO_2 storage. Capillary trapping immobilizes CO_2 within the pore structure, while dissolution facilitates its transfer into the aqueous phase, reducing mobility and minimizing leakage risks. Wettability strongly affects capillary trapping behavior and consequently, the extent and efficiency of CO_2 dissolution. However, the coupling mechanisms between these processes remain poorly understood, necessitating further experimental research to improve predictive models and optimize sequestration strategies. Pore architecture, together with capillary trapping, can alter preferential pathways and create stagnation zones, making the dynamics of mass transfer more affected by advection or diffusion (Gao *et al*., 2023). Given that different phase entrapment arrangements lead to distinct mass transfer scenarios, a better understanding of their influence on storage dynamics and capacity is critical (Agaoglu *et al*., 2015). Adapted to the CO_2 storage in saline aquifers, 4 base mass transfer scenarios for different phase entrapment arrangements can be identified (see Table 12).

Table 12 Interfacial mass transfer in systems with different mobile and trapped phases.

Trapping situation	**Interface mass transfer direction**	
	Water to CO_2 (evaporation)	**CO_2 to water (dissolution)**
Mobile water / trapped CO_2	**(1)** CO_2 has a limited volume, limiting the capacity for the evaporation of water	**(2)** Trapped CO_2 could be completely dissolved by an incoming stream of fresh water
Mobile CO_2 / trapped water	**(3)** Trapped water could completely evaporate into the stream of dry CO_2	**(4)** Water has limited volume, limiting the capacity for CO_2 dissolution

During the injection of CO_2 into the reservoir filled with water (usually drainage), besides pure advection transport (displacement), the moving plume of CO_2 promotes both dissolution of CO_2 in water and water evaporation in the dry stream of CO_2. This happens at the main front, where both phases can be considered mobile, and in the sweep zone, where water tends to remain trapped (cases 3 and 4). Further away from the injection wells and especially after the injection has finished,

buoyancy-driven segregation will force brine recirculation within the reservoir (usually imbibition). This redistribution of fluid phases promotes mixing and dissolution between the phases. Over the decades, potentially centuries, significant portions of CO_2 will be bypassed and capillary trapped by snap-off. Following the redistribution of fluids, the ongoing mass transfer (cases 1 and 2) will be a function of concentration potential between the two phases until thermodynamic equilibrium is achieved or either fluid phase is consumed. If, however, thermodynamic conditions change, the dynamics of the process can also include liquid (water) condensation and or gas (CO_2) exsolution. A change in local thermodynamic conditions can lead to a phenomenon named Ostwald ripening, where the mass transfer first facilitates the dissolution of gas in a liquid phase and then the exsolution of the gas from supersaturated liquid back into a gaseous phase. In all scenarios, the velocity of the mobile phase dictates the magnitude of interphase mass transfer until the onset of diffusive conditions. It is worth noting that not all configurations from Table 12 have been (extensively) studied (Agaoglu *et al*., 2015).

On a pore scale, interfacial mass transfer investigations are generally divided between three domains of investigation: meniscus, fluid film, and grain surface roughness (see Figure 71). The meniscus is the region where two bulk volumes of fluid phases meet while fluid films and surface roughness are investigated when saturation of the wetting phase is at residual values. Here, we will primarily focus on the main meniscus, keeping in mind that fluid films and surface roughness also contribute to the overall mass transfer.

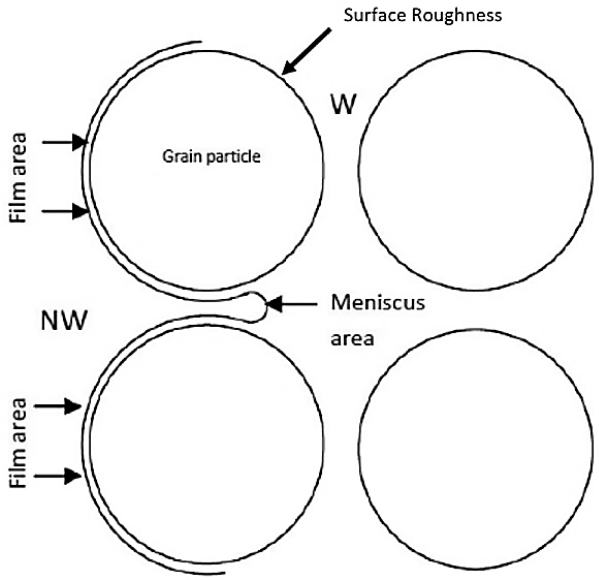

Figure 71 The three investigation domains, depicted in schematics of porous media. Taken from Agaoglu et al. (2015).

The solubility, diffusivity, and mass transfer coefficient are fundamental parameters governing the transport and dissolution of CO_2 in brine. Solubility defines the equilibrium concentration of CO_2 in brine at saturation, while diffusivity (D, unit: m^2/s) characterizes the rate at which CO_2 molecules

migrate through the liquid phase. The mass transfer coefficient quantifies the rate at which CO_2 is transferred across phase boundaries, particularly from the gas phase into brine. There are two common mass transfer coefficient formulations, i.e., the liquid-side (k_L, unit: m/s) and volumetric or lumped (k_La, unit: s^{-1}), related through normalized interfacial area (a, unit: m^{-1}). The lumped mass transfer coefficient arose due to the complex nature of multiphase flow in porous media and the difficulty of measuring the interfacial area on a pore scale (Agaoglu *et al*., 2015). The values of diffusivity found in literature for the CO_2-water system are around 10^{-7} - 10^{-9} m^2/s (Farajzadeh *et al*., 2009; Lefortier *et al*., 2012; Zarghami *et al*., 2017), k_L oscillates between 10^{-8} and 10^{-4} m/s (Han *et al*., 2013; Patmonoaji and Suekane, 2017; Teng and Yamasaki, 1998) while k_La values are typically between 10^{-6} and 10^{-1} s^{-1} (Ndiaye *et al*., 2018; Patmonoaji and Suekane, 2017; Vandu *et al*., 2005). Traditionally, these values are derived from PVT cell measurements, which emulate macro-scale environmental conditions such as pressure, temperature, and brine composition between the bulk fluid phases (Sell *et al*., 2013). However, more and more research is nowadays performed on natural (core experiments) and synthetic porous media (e.g., microfluidics) which makes the results applicable across the scales (Chang *et al*., 2017). The important difference between fluids contained in porous media vs in bulk is a high fluid-fluid interfacial surface-to-volume ratio which has been shown to deviate from bulk-phase behavior due to altered fluid properties near interfaces (Mozhdehei *et al*., 2024). Moreover, the dissolution kinetics assessment through mass transfer coefficient at the pore scale is particularly complex due to its dependence on multiple factors, including thermodynamic, flow and physicochemical properties but also the magnitude of concentration of already dissolved species, porous media properties governing interfacial geometry, etc (Agaoglu *et al*., 2015; Chang *et al*., 2017; Patmonoaji and Suekane, 2017; Sell *et al*., 2013; Seo *et al*., 2019; Vandu *et al*., 2005; Xu *et al*., 2017; Yang and Tsai, 2024; Zhong *et al*., 2025).

The theoretical foundation for modeling mass transfer processes is rooted in the Maxwell-Stefan equations, which describe multi-component diffusion based on the interactions between species (Taylor and Krishna, 1993). Nowadays, the prediction of mass transfer coefficients is based on various theoretical models that describe mass transfer at the gas-liquid interface. Some of these include: the two-film theory by Lewis and Whitman (1924), Higbie's penetration theory (1935), Danckwerts (1951) proposed the surface renewal theory, Levich (1962) developed boundary layer theory, etc (Lefortier *et al*., 2012; Vandu *et al*., 2005).

Overall, accurate prediction of mass transfer coefficients in CO_2-brine systems is crucial for understanding CO_2 dissolution in subsurface environments. Classical models, including the two-film, penetration, and surface renewal theories, offer fundamental insights but vary in applicability based on flow regime, turbulence, and chemical interactions. These models often neglect the influence of porous media, and recent research lacks explicit consideration of wettability (Zhong *et al*., 2025). Experimental studies remain essential to identify porous media effects, develop new or calibrate existing numerical models for accurate prediction of dissolution and storage dynamics (Maes and Soulaine, 2018). Available experimental approaches utilized for pore scale mass transfer

research include tracking of saturation, i.e., volume (e.g., microfluidic imaging (Yang and Tsai, 2024) and X-ray μCT core imaging), pressure response evaluation, pH evolution assessment (Chang *et al*., 2017) or *in situ* methods for concentration estimation (e.g., Raman spectroscopy (Liu *et al*., 2012)).

There are very few examples in literature addressing pore-scale wettability effects on fluid-fluid interfacial mass transfer, particularly from an experimental perspective. To provide some insight into the problematics, we present two numerical studies.

In a 2D numerical study by Chen *et al*. (2018), pore-scale dissolution of $scCO_2$ in water was investigated. The study examined the impact of different initial $scCO_2$ saturations in porous media and the role of wettability conditions on mass transfer between the two phases. The process was monitored through the evolution of saturation, dissolved CO_2 concentration, pH, and interfacial area.

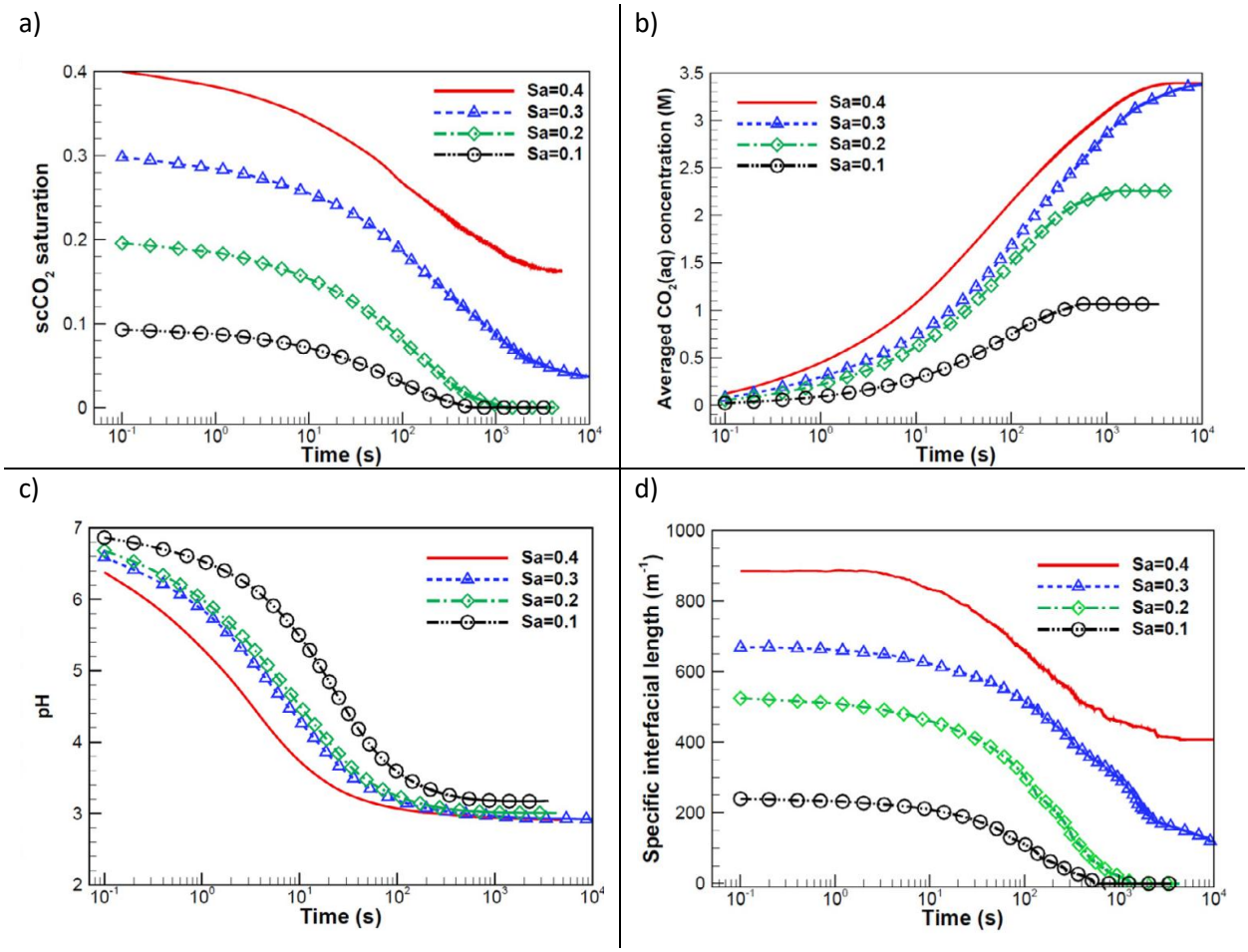

Figure 72 Numerical results of $scCO_2$ dissolution tracked through saturation (a), concentration (b), pH (c) and specific interfacial area evolution (d). Taken from Chen et al. (2018).

As expected (see Figure 72), in an enclosed system without imposed flow, the concentration of $CO_{2\,(aq)}$ in water increased over time (b), leading to a corresponding decrease in $scCO_2$ saturation

(a). As a consequence of dissolution, pH expectedly dropped due to the dissociation of carbonic acid (c). Based on the data from Figure 72, the effective mass transfer/dissolution rate was found to slow down (note - time is in log scale) as the solution becomes more saturated. The dissolution process terminates when there is no more volume to dissolve (cases with Sa = 0.1 and 0.2) or the aqueous solution reaches saturation (cases with Sa = 0.3 and 0.4). Additionally, the specific interfacial area (d) evolved as a function of dissolution in time. The authors also found two distinct power-law slopes as a function of saturation, possibly coming from the position of the interface within the pore (body vs throat). Chang *et al*. (2017) also experimentally confirmed the connection between dissolution dynamics and the morphology of the capillary trapped phase through the interfacial area.

Besides being a function of porous media morphology and dissolution process itself, interfacial area is also directly linked to wettability (see Figure 73). In a sensitivity analysis of wettability, interfacial length was found to render a parabolic "U" shape with respect to contact angle (see Figure 73). The minimum of the function is around 90° (intermediate wetting), whereas going to either end of the spectrum (0° or 180°) interfacial area increases.

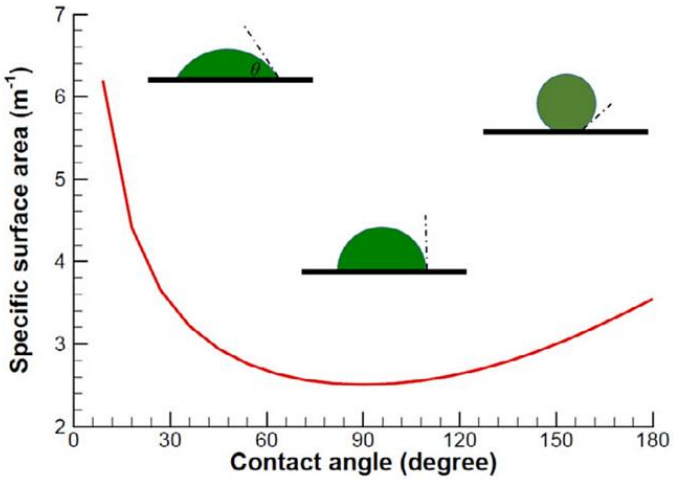

Figure 73 The specific $scCO_2$-water interfacial area as a function of $scCO_2$ contact angle (note: it is the inverse of the contact angle measure through the water phase). Taken from Chen et al. (2018).

If analyzing the cause-effect relationship of the system, wettability has a direct influence on the interfacial area, which in turn positively scales with the dissolution dynamics as mentioned before. Going by the logic of Figure 73, the most efficient trapping of CO_2 by the dissolution mechanism is expected to happen in a strongly water-wet or strongly CO_2-wet system which has been confirmed in the aforementioned study.

Sun *et al*. (2024) utilized the lattice Boltzmann method to simulate $scCO_2$ dissolution in 3D natural porous media (Berea sandstone) and examine wettability effects in greater detail. Initially, they analyzed the dependence of capillary-trapped $scCO_2$ morphology on wettability and found results

consistent with those of Chang *et al*. (2017) and Chen *et al*. (2018). The study further revealed a strong linear relationship between $scCO_2$ saturation and overall specific interfacial area (Figure 74). Specifically, in strongly water-wet media (low contact angle), the contact area between the two fluid phases was greater despite less dispersed phase (fewer bubbles and clusters), whereas in weakly water-wet or neutrally wet conditions, $scCO_2$ bubbles also had significant contact with the rock matrix. These observations highlight the influence of wettability on phase morphology and, consequently, on the interfacial area between fluids, which is essential for predicting the magnitude of interfacial mass transfer.

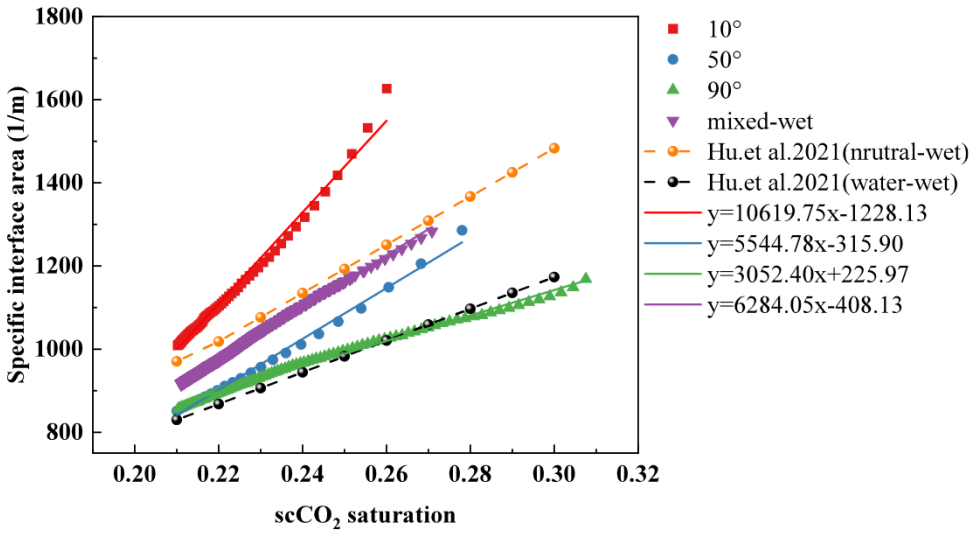

Figure 74 The dependency of specific interfacial area on $scCO_2$ saturation. Taken from Sun et al. (2024).

Upon initial contact between the two phases, the concentration of dissolved CO_2 at the interface rapidly reaches saturation (3.4 M). However, the overall dissolution process, governed by the diffusion of dissolved CO_2, proceeds relatively slowly, indicating a nonequilibrium process (Figure 75a). Although the averaged pH and averaged $CO_{2\,(aq)}$ concentration exhibit an inverse relationship, their dependence is nonlinear (compare function shapes in Figure 75) (Clingerman *et al*., 2007). This nonlinearity arises from the logarithmic pH scale and the rapid dissociation of carbonic acid, which causes a sharp initial pH drop, followed by a slower decline due to buffering from bicarbonate and carbonate species. Thus, pH does not directly reflect the mass transfer dynamics in the system.

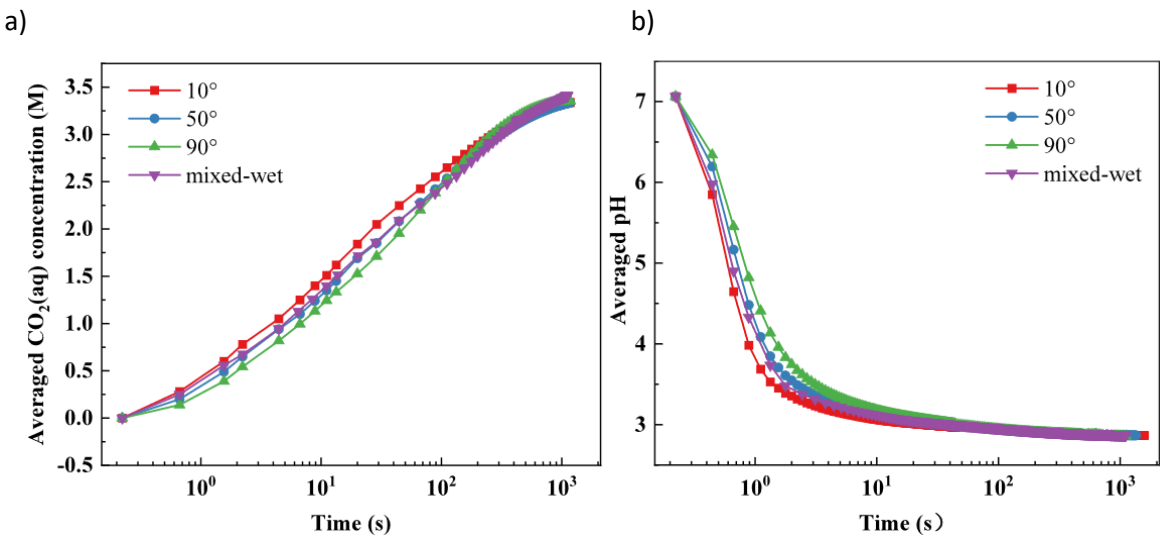

Figure 75 The evolution of average $CO_{2\,(aq)}$ (a) and pH (b) in aqueous solution over time for different wettability conditions. Taken from Sun et al. (2024).

Finally, it has been shown that the mass transfer coefficient evolves over time as a function of wettability conditions. During the initial dissolution period (see Figure 76), it is highly sensitive to wettability, but this effect diminishes later and even reverses. As saturation is reached in the near-interfacial region, the concentration gradient decreases, and dissolution becomes governed by the slow diffusion of $CO_{2\,(aq)}$ in water. Moreover, Sun *et al*. (2024) confirmed that dissolution rates are influenced not only by wettability but also by pore structure heterogeneity, pore space interconnectivity (coordination number), the shape of $scCO_2$ bubbles, and changes in fluid properties during dissolution (e.g., interfacial tension). These factors significantly impact the interfacial area, which is strongly reflected in the lumped mass transfer coefficient.

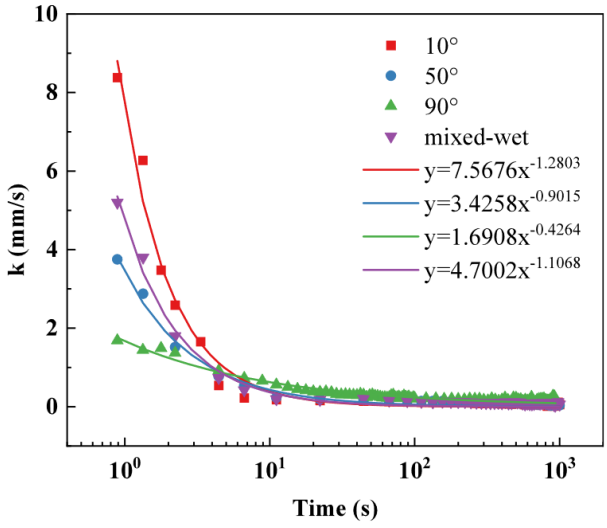

Figure 76 The evolution of lumped mass transfer coefficient over time for different wettability conditions. Taken from Sun et al. (2024).

Both simulation studies offer valuable insight into the mechanisms of interfacial mass transfer, particularly emphasizing the critical role of wettability in controlling interfacial area. However, there is a lack of benchmarking against experimental data or real-world observations. This underscores the ongoing need for experimental studies to validate and complement numerical models.

II. Setup and procedures

1. Setup, consumables and conditions

In addition to the microfluidic devices discussed in Chapter 2, the experimental microfluidic setup used in this study consists of pressure pumps (Fluigent, model: LineUp Push-Pull), fluid reservoirs (Fisherbrand glass bottles, 100 mL), chip holder (Micronit), tubing (ETFE, 1/16”), ferules for sealing the connections, various valves and connectors, etc. Optical visualization and image acquisition are achieved through microscope platforms equipped with high-resolution cameras (for further details, refer to Chapter 2). The essential part of our setup is shown in Figure 77. For the observation of the physical phenomena during the trapping and dissolution processes, a microscope objective with 10x magnification and a numerical aperture of 0.3 is selected as the best fit to the dimensions of the dead-end pore of the micromodel. The upright microscope's transmission and reflection mode are used for microfluidics experiments. Transmission mode offers better sharpness and visibility and it is thus prevalently used. Reflection mode offers better contrast, enhancing the detail clarity.

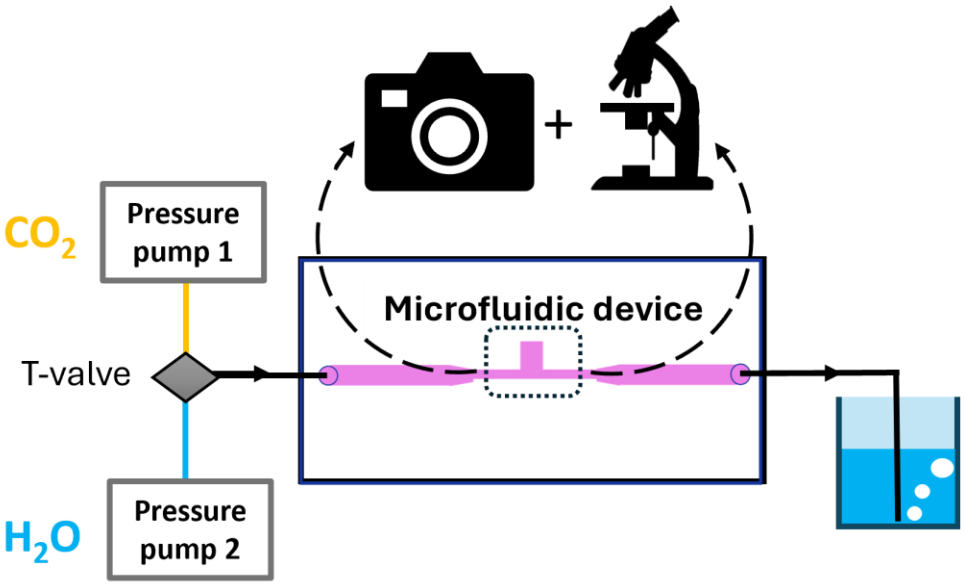

Figure 77 Microfluidic setup for research of capillary trapping and fluid-fluid interfacial mass transfer.

All the microfluidic experiments are performed using ultrapure MilliQ water with a resistivity of 18.2 MΩ-cm and 99.995 % pure CO_2 from Air Liquide. Ultrapure water is selected to prevent any unwanted mineral reactions. All experiments and storage of devices are performed under ambient conditions. The temperature is kept around 293 K (20 °C) with an air conditioning unit, while humidity is not controlled (typically around 60 %). The imposed relative pressure and the

maximum pressure difference across the microchannels remain below 0.1 MPa (1 bar) in all experiments, as this is the upper limit achievable by the pumps used.

2. Trapping and mass transfer experimental procedure

To study pore-scale mass transfer, we performed classic two-phase drainage and imbibition microfluidic experiments. In imbibition, we track the dissolution of a CO_2 bubble in water, while in drainage, the evaporation of a water droplet into the stream of CO_2. Unlike the plasma-based wettability measurements discussed in Chapter 3, the primary focus here is on the main geometrical feature of the microfluidic device, which is specifically designed to trap one fluid at a time. This configuration provides a stable and well-defined location for imaging and monitoring interfacial mass transfer.

The preparation of a typical experiment begins by saturating the dry microchannel with a stream of CO_2 for a few minutes to displace any air. The T-valve is then switched to water injection until all gas phase is dissolved and/or displaced, thereby making the microchannel fully saturated in water. Note, water is being pushed out of its reservoir by injecting air to avoid pre-saturation with a significant amount of CO_2. Once the microchannel is saturated, the CO_2 pump pressure is set, waiting for the T-valve opening to initiate the first drainage experiment. The outlet of the microchannel is directed towards a collection cup, which is controlled by the ambient pressure. Image recording begins at the moment the T-valve is switched to CO_2 injection. Upon complete water evaporation in the system at the end of the experiment, the setup is simply switched for the injection of water in the CO_2-saturated microchannel and the recording of the imbibition process is started. Drainage and imbibition are alternated over the range of the imposed pressure differences until all water is used up. Alongside the dynamic experiments, a prolonged static experiment looking at CO_2 dissolution was also conducted. In the anisotropic L-pore geometry, flow reversal is achieved by rotating the microfluidic device by 180°, thereby switching the inlet and outlet positions. This approach produces images with a flipped geometry orientation while maintaining the flow direction consistently from left to right.

Before each experiment, the camera speed is adjusted depending on the injection type (drainage/imbibition), wettability conditions, imposed pressure and forecasted experiment duration. In imbibition experiments, the interval between images is set between 0.2 and 2 seconds, while in drainage, due to a slower process, it is between 10 and 30 seconds, defining the resolution of the recorded data. The average experiment duration is typically less than 30 minutes.

Following the experiments, the recorded gray-scale image sequences undergo processing to extract valuable data. The image-processing software, developed in MATLAB by Sophie Roman, forms the foundation of this analysis. The software employs binary image analysis to track the volume and interfacial area of the trapped phase (see Figure 78). In 2D image analysis, the volume of a bubble or droplet is roughly associated with the top-view area (white), whereas the fluid-fluid interfacial area is represented as length, i.e. perimeter (red). A fluid-fluid interfacial area is assumed

to be uniform in the z-direction following the top plane view. In reality, the interface also exhibits curvature in the z-direction.

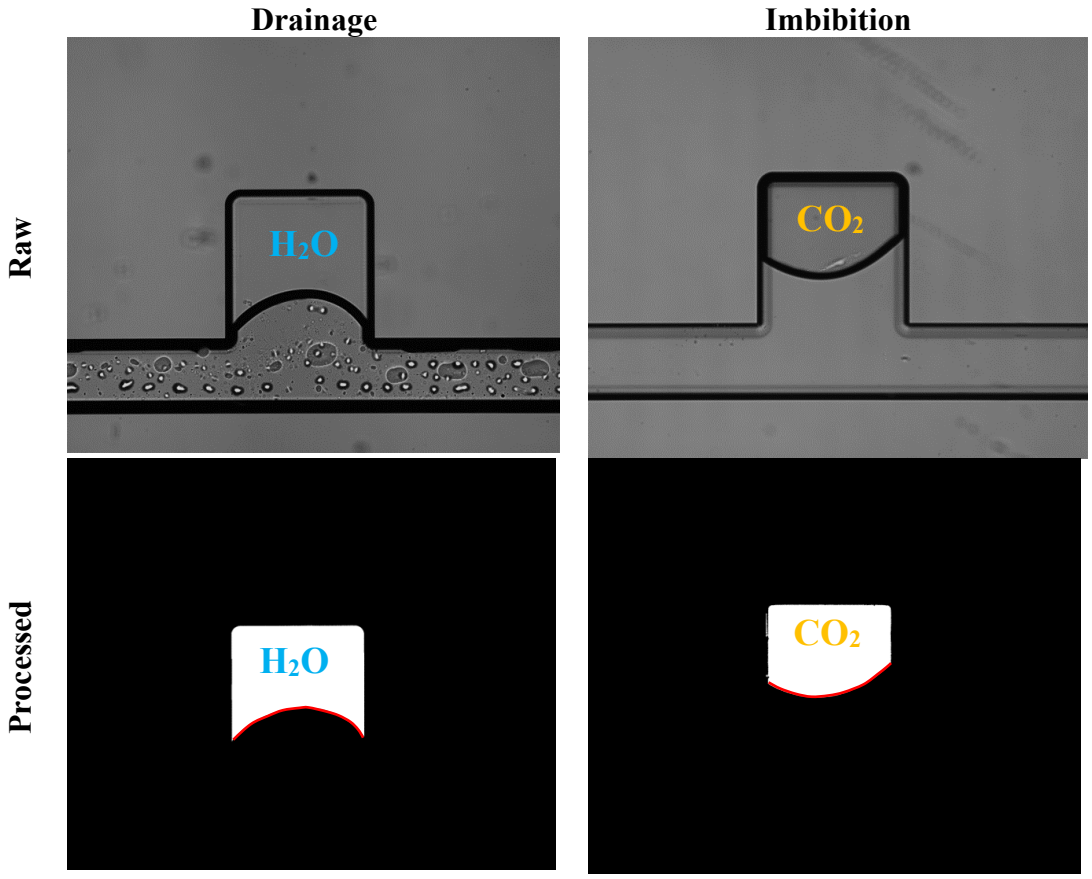

Figure 78 The processing of the raw gray-scale images recorded in transmission mode into a binary format.

Capillary trapping potential is thus assessed only through the initial volume of trapped phase, i.e., the initial top-view area (A_1). Interfacial mass transfer analysis based on the top-view area (A) and perimeter (P) evolution in time which are further normalized to their respective initial values (A_1 and P_1). To facilitate comparative analysis of mass transfer process over the unit of interfacial length (perimeter) and eliminate the influence of varying capillary trapping potentials, the top-view area is normalized to the perimeter (A_p) and further to the initial conditions (A_p/A_{p1}). To obtain the interval mass transfer rate (dA_p/dt) evolution in time, we utilized the difference in perimeter normalized top-view area (dA_p) over one time interval (dt). In graphical depictions where time is not the primary analyzed variable, time is normalized to the end time (t_{END}) that corresponds with the end of the mass transfer process (A = 0, i.e., below the detection limit). For simplicity in the result section, the "top-view area" will be referred to as just the "area".

3. PIV procedure

Micro-PIV is a complementary technique to microfluidics used to assess fluid dynamics. Namely, small interrogation windows are employed to track particle displacement between two time-steps, as illustrated in Figure 79. Since particles are designed to closely follow fluid motion, these measurements enable the determination of fluid velocity profiles and fluid streamlines (fluid pathways). This information provides valuable insight for the interpretation of capillary trapping and interfacial mass transfer dynamics.

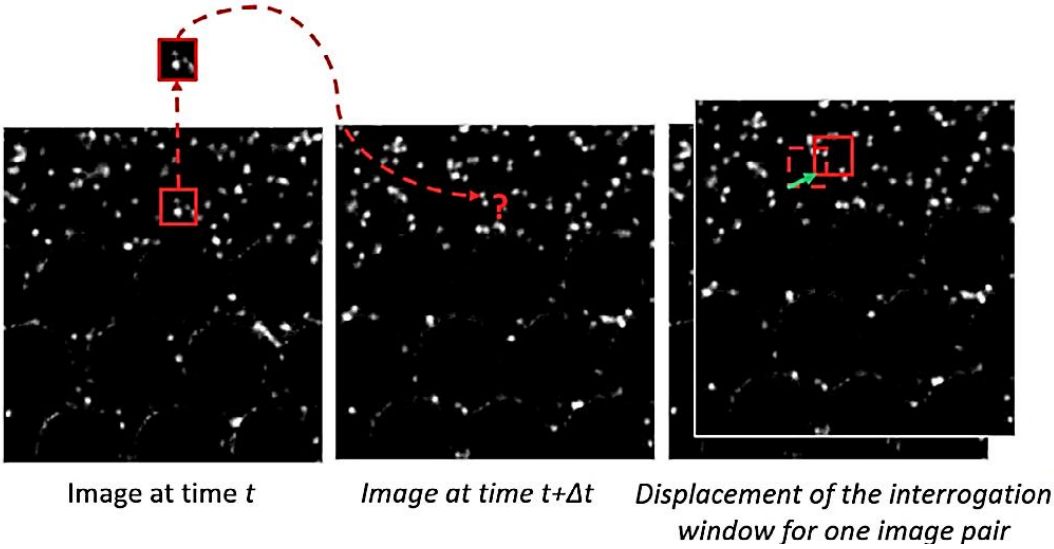

Figure 79 The principle of PIV. Taken from Roman et al. (2016).

Our PIV experiments are performed by creating a diluted solution of particles in water and injecting it into a microchannel with constant pressure imposed by the pressure pump. The diluted solution with 0.12% vol concentration of particle is prepared by mixing 0.55 g of commercially available concentrated solution (Polysciences) and 10 g of water. Polystyrene particles with carboxylate cover, 1 µm in diameter, were chosen as they fit the fluid properties and therefore do not affect the flow behavior.

The experiment preparation closely follows the mass transfer procedure, beginning with the injection of CO_2. The microchannel is then manually saturated with MilliQ water using a syringe to dissolve and/or displace any remaining gas phase. Subsequently, the water injection is replaced with a particle solution until it fully saturates the microchannel and becomes visible at the outlet. To reduce interface moving due to dissolution, the CO_2 in the two-phase flow particle experiments is replaced with compressed air.

To establish the initial pressure difference with no-flow conditions in the microchannel, the pump pressure is carefully adjusted and the stabilized pressure reading is recorded. It can be noted that even minor pressure differences arising from variations in fluid levels within the reservoir (due to gravitational potential) can induce significant flow velocities within the microchannel without any

pressure applied from the pressure pump. The desired pressure differences (5-100 mbar) are then applied, and image acquisition is performed at an appropriate frame rate (fps) and shutter speed to ensure sharp images with well-resolved particles. In the narrow sections of the microchannel, capturing high-velocity flow may require frame rates of up to 5 000 fps at a maximum imposed pressure difference of 50 mbar (the upper limit of our measurement range). To achieve optimal particle visibility relative to the size of geometric features, all particle experiments are conducted using a 20x magnification objective with a numerical aperture of 0.45.

After a successful acquisition of image sequence with a high-speed camera attached to the inverted microscope, sets of 100 images are binarized in a way that makes the background black and the particles white. Binarization preprocessing is performed with ImageJ after which images are exported to PIVlab software (Thielicke and Stamhuis, 2014). A mask is first applied to block all the areas of an image where particles are not actually present and therefore speed up the analysis. We use three passes with progressively smaller interrogation windows (128, 64 and 32 pixels). These are chosen to optimize between performance (analysis time) and spatial resolution of results based on Roman *et al*. (2016). After images have been analyzed, calibration is performed by inputting the timestep between images and setting up the reference distance.

III. Results

The results section is divided into three parts. First, we present the characterization of flow properties in selected microchannel geometries using PIV on single and two-phase flow experimental data. Next, we assess the CO_2 and water capillary trapping potential under varying pressure differences for two wettability conditions, defined by static contact angles in Chapter 3 (see also Table 13). Finally, we look into the interfacial mass transfer on the very same selected microchannel geometries. For each geometry, CO_2 dissolution and water evaporation potential are separately analyzed. The discussion in each section is based on evaluating mass transfer behavior across the range of pressure differences for the two aforementioned wettability conditions. To enhance clarity and consistency in result interpretation, the flow direction in all images is consistently presented from left to right.

The varying geometrical complexity of microfluidic devices is designed to replicate the diverse pore shapes and sizes found in natural porous media. Adjusting the imposed pressure difference simulates different regions within the reservoir, where pressure gradients and consequently flow rates may vary. Higher pressure gradients are typically found near the injection well during CO_2 injection, whereas lower gradients occur farther from the well and after injection ceases. Spatially and temporally, low-pressure gradients and low-flow conditions dominate during CO_2 storage, making them a relevant focus for our microfluidic experiments. Our experiments are specifically designed to evaluate capillary trapping and track mass transfer mechanisms separately. Capillary trapping and evaporation of water are considered during drainage, while CO_2 trapping and dissolution potential are the primary focus during imbibition. While the two mass transfer processes occur simultaneously in porous media, in our experiments, we assume Stefan diffusion, meaning that only one fluid at a time diffuses through the interface (Taylor and Krishna, 1993). This assumption simplifies the investigation by neglecting counter-diffusion effects, making it more applicable to our experimental approach. While dissolution and evaporation are the dominant mass transfer processes, we acknowledge that other mechanisms also contribute to long-term CO_2 storage behavior. Finally, modifying the contact angle, which represents wettability conditions, aims to mimic the diversity of mineral compositions and their associated surface properties. Since our focus is on CO_2 storage in aquifers, where most rocks are hydrophilic, our experiments replicate this environment using glass microfluidic surfaces and altering them using plasma treatment presented in Chapter 3. Table 13 is given as a reminder of the wettability conditions analyzed in this study.

Table 13 An overview of wettability conditions on microfluidic devices.

Wettability condition/Device	**Single pocket (Micronit)**	**L-pore (Klearia)**
Native	53 ± 7°	59 ± 12°
Plasma altered	23 ± 5°	≈ 0°

1. Characterization of flow properties

Characterizing flow patterns, capillary (Ca) and Reynolds number (Re) is of the essence for fluid flow analysis in porous media as they determine which forces have a prevalent influence in the system. The microchannel geometry features a variable width, and the presence or absence of a trapped phase can alter the effective flow cross-section. Additionally, fluid properties such as viscosity and the imposed pressure difference, which influence velocity, depend on the imposed experimental conditions. The dimensionless numbers in this study are calculated on a large channel (cross-section of 500×100 µm) and the implications will be extrapolated to the key geometric features relevant to this study. Additionally, pore-scale analysis provides valuable insight into flow patterns and velocity distributions, contributing to a deeper understanding of dynamic phenomena.

a) Single-phase flow

Following the earlier described PIV procedure, we injected particles in a microfluidic device with a single pocket geometry and acquired an image sequence. After processing the data in PIVlab software, we extracted velocity distribution maps and corresponding velocity profiles. One representative case acquired at 20 mbar of pressure difference is visible in Figure 80. Both the map and profile representations clearly show that the velocity profile is flat in the central region of the microchannel, where the maximum values occur. As visible from the streamlines, the velocity layers stay parallel to each other at all times, indicating a laminar flow even at pressure differences in excess of 100 mbar.

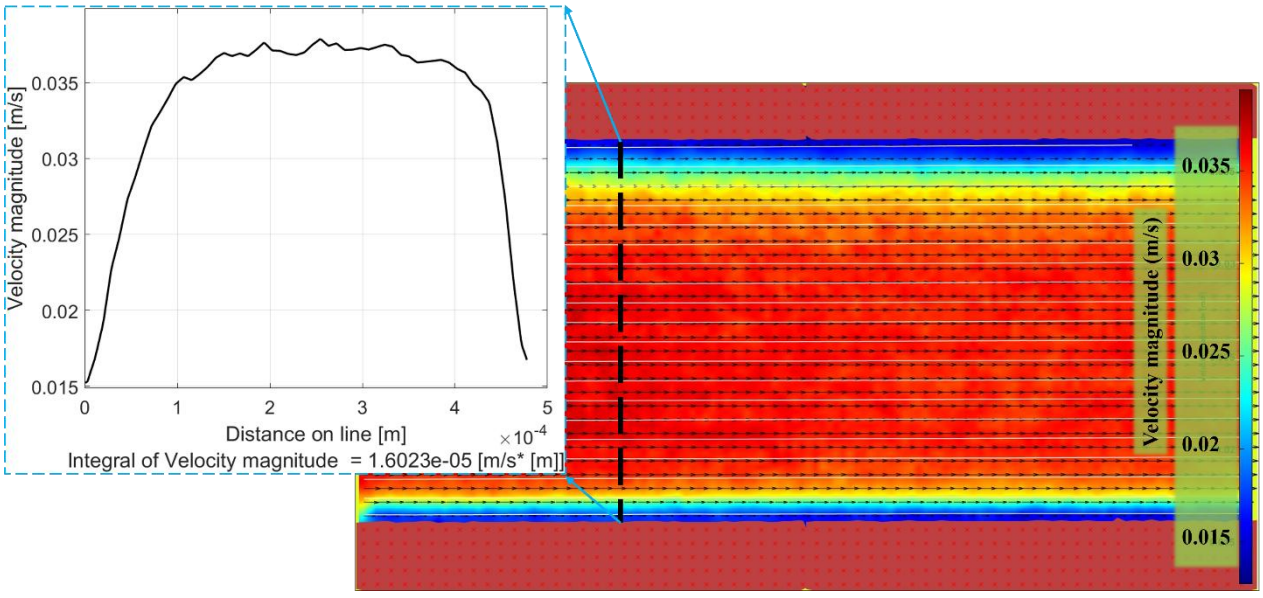

Figure 80 Velocity distribution in a 500 µm-wide channel for a single-phase water particle experiment under 20 mbar of pressure difference. White lines are streamlines.

From integrals of the velocity magnitude (indicated on flow profiles, see Figure 80) and taking into account the constant depth of 100 µm, we obtained the average volumetric flow rate. The range of

volumetric flow rates obtained on a 5 to 50 mbar pressure difference is between 0.5 and 3.8 µL/s. The average fluid velocity in this microchannel is obtained by multiplying the integrals of the velocity magnitude by its width (500 µm). The scaling of average fluid velocity with imposed pressure difference is depicted in Figure 81. As expected for the laminar flow, velocity scales linearly with the imposed pressure difference which is in accordance with Darcy's law. Thus, the permeability of the 4 cm microchannel saturated with water (1 mPas) is estimated to be on the order of 6×10^{-8} m^2.

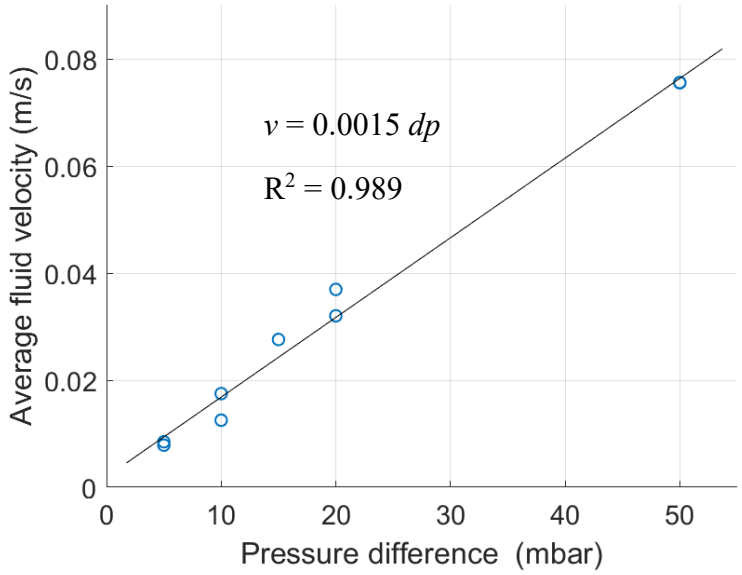

Figure 81 Scaling of average fluid velocity (v) with the imposed pressure difference (dp).

Now, with the acquired pressure-velocity relationship (see the equation in Figure 81), one can calculate the capillary and Reynolds numbers using the following equations (9 and (10, respectively):

$$Ca = \frac{\mu v}{\sigma} \tag{9}$$

$$Re = \frac{\rho v l}{\mu} \tag{10}$$

where μ, v, σ, θ, ρ, and l are viscosity, velocity, interfacial tension, contact angle, density and characteristic length, respectively. Taken from Espinoza and Santamarina (2010), the CO_2-water interfacial tension at 295 K and 0.1 MPa is around 72 mN/m. Since dimensionless numbers are determined in water, the density used in the calculation is 1000 kg/m^3 and the viscosity 1 mPas. The characteristic length is the microchannel depth, i.e., 100 µm.

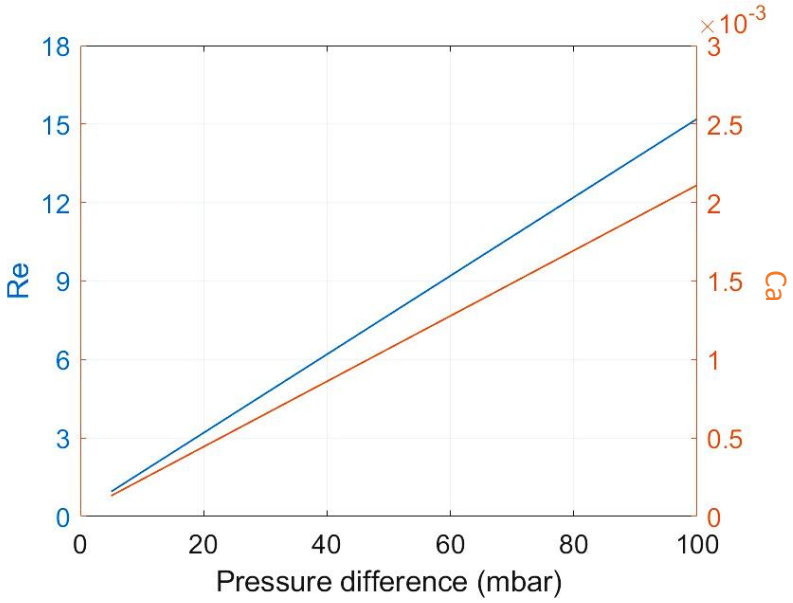

Figure 82 Scaling of Reynolds and capillary number with imposed pressure difference.

As shown in Figure 82, capillary number is on the order of 10^{-3} while the Reynolds number remains below 20. These dimensionless numbers characterize the expected flow conditions in the reservoir during the CO_2 injection process. Although the Reynolds number is always above unity, it remains well below the turbulence transition threshold (Lienhard *et al*., 1966). Since there are no obstacles in the straight channel, the flow remains streamlined and unseparated. To confirm this behavior across the microchannel, we shift our focus from the 500 µm channel to the key geometric features. Specifically, we analyze single pocket and L-pore geometry.

By looking at the results in Figure 83, at low pressure differences (e.g., 20 mbar), the streamlines coming from the channel are parallel and follow the geometry. At higher pressure differences (see 100 mbar example) we start noticing the occurrence of a recirculation vortex. It first appears near the inlet wall of the pocket and starts transitioning towards the middle (300 mbar) and the outlet side of the pocket at higher values (500 mbar) of imposed pressure difference. The pressure difference at which the first recirculation is noticed is 65 mbar. Hence, to stay in creeping flow, our experiments will mostly be performed under this value.

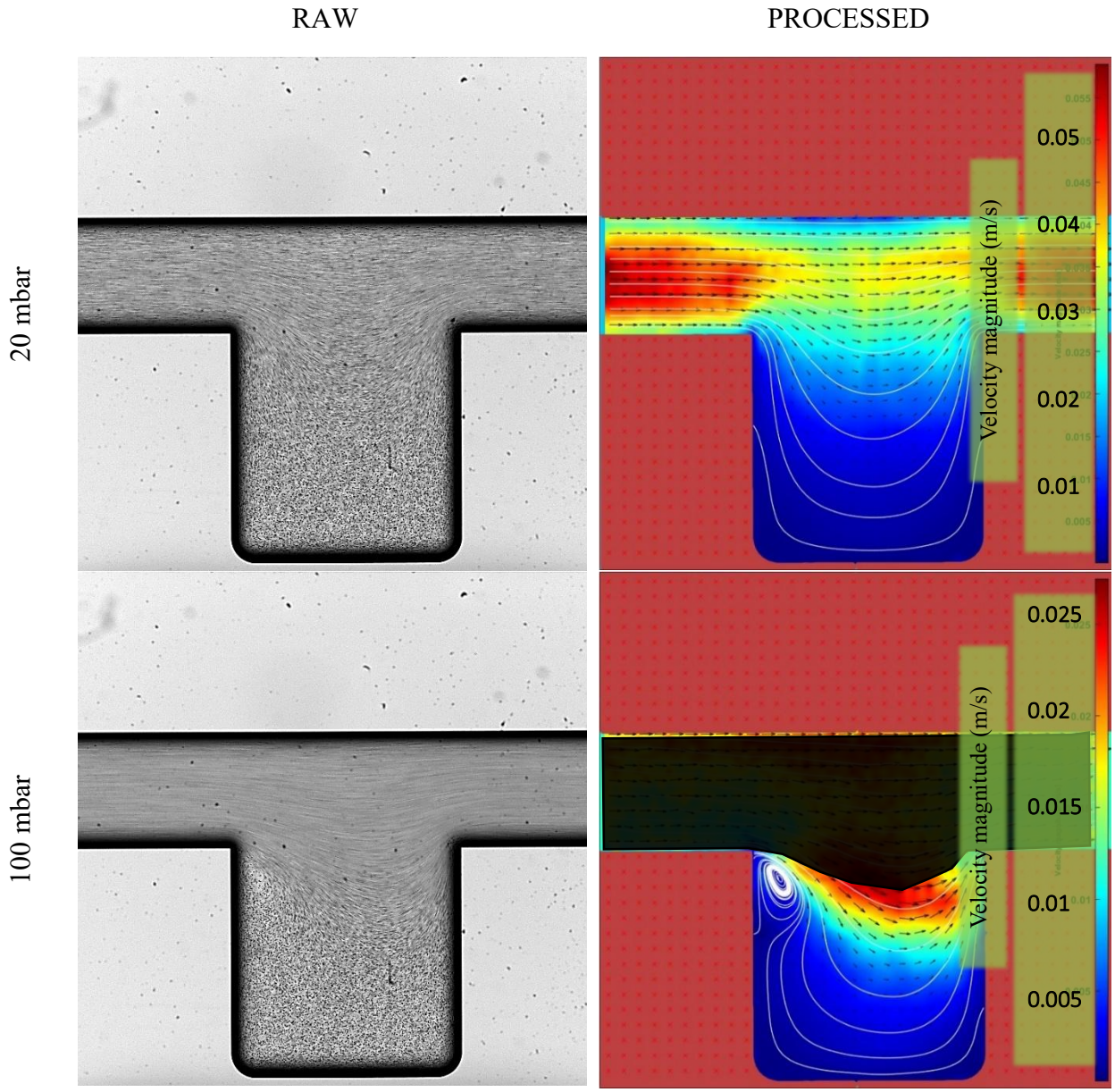

Figure 83 Fluid velocity patterns for single pocket geometry. Flow direction is indicated with black arrows, while streamlines are colored in white. Note: the results of velocity magnitude in the overlaying microchannel and around the entrance are not correct at higher imposed pressure differences (e.g., 100 mbar) due to imaging limitations.

The same experiments are performed on the L-pore geometry with similar results since the L-pore geometry is built on top of the single pocket design. As visible in Figure 84, velocities near the feeding underlying channel are higher and rapidly decrease towards the dead-end part of it. At lower imposed pressure differences (e.g., 20 mbar), streamline analysis once more indicates a creeping flow. At higher pressure differences (e.g., 100 mbar), there is a fully developed vortex and separation of the flow in two opposite directions.

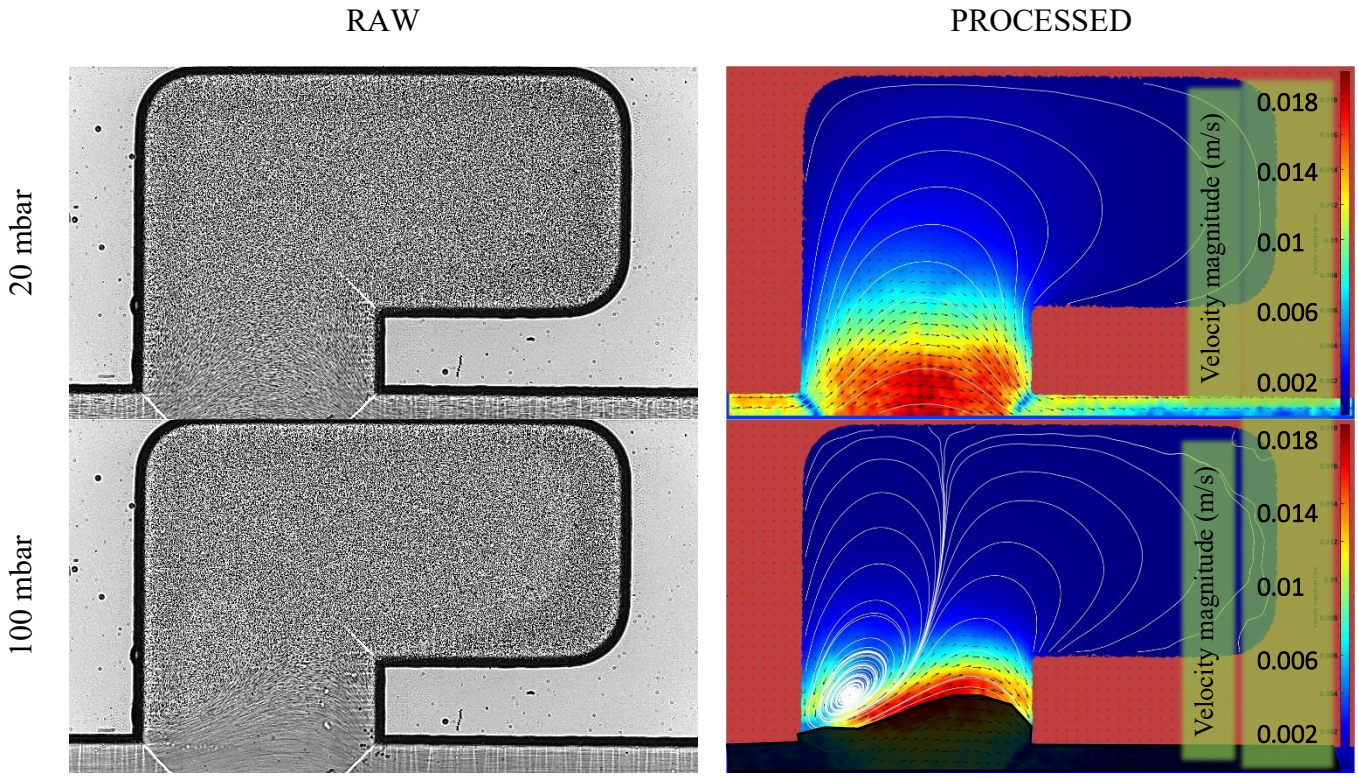

Figure 84 Fluid velocity patterns for L-pore geometry. Flow direction is indicated with black arrows, while streamlines are colored in white. Note: the results of velocity magnitude in the overlaying microchannel and around the entrance are not correct at higher imposed pressure differences (e.g., 100 mbar) due to imaging limitations.

Overall, for the upcoming two-phase dissolution experiments, it is important to note that velocity magnitude decreases significantly further from the feeding channel, with streamlines indicating stagnation zones near the end corners, especially in the deeper L-pore geometry. These findings are crucial for interpreting dissolution dynamics, as the interface progressively shifts away from the main channel due to dissolution.

b) Two-phase

In our two-phase flow particle experiments, we focused on the behavior of the trapped phase. To investigate this, we trapped a particle suspension droplet and observed its response across a range of imposed pressure differences.

Native surfaces

The results for a single pocket in drainage injection mode on native surfaces (53°) are presented in Figure 85.

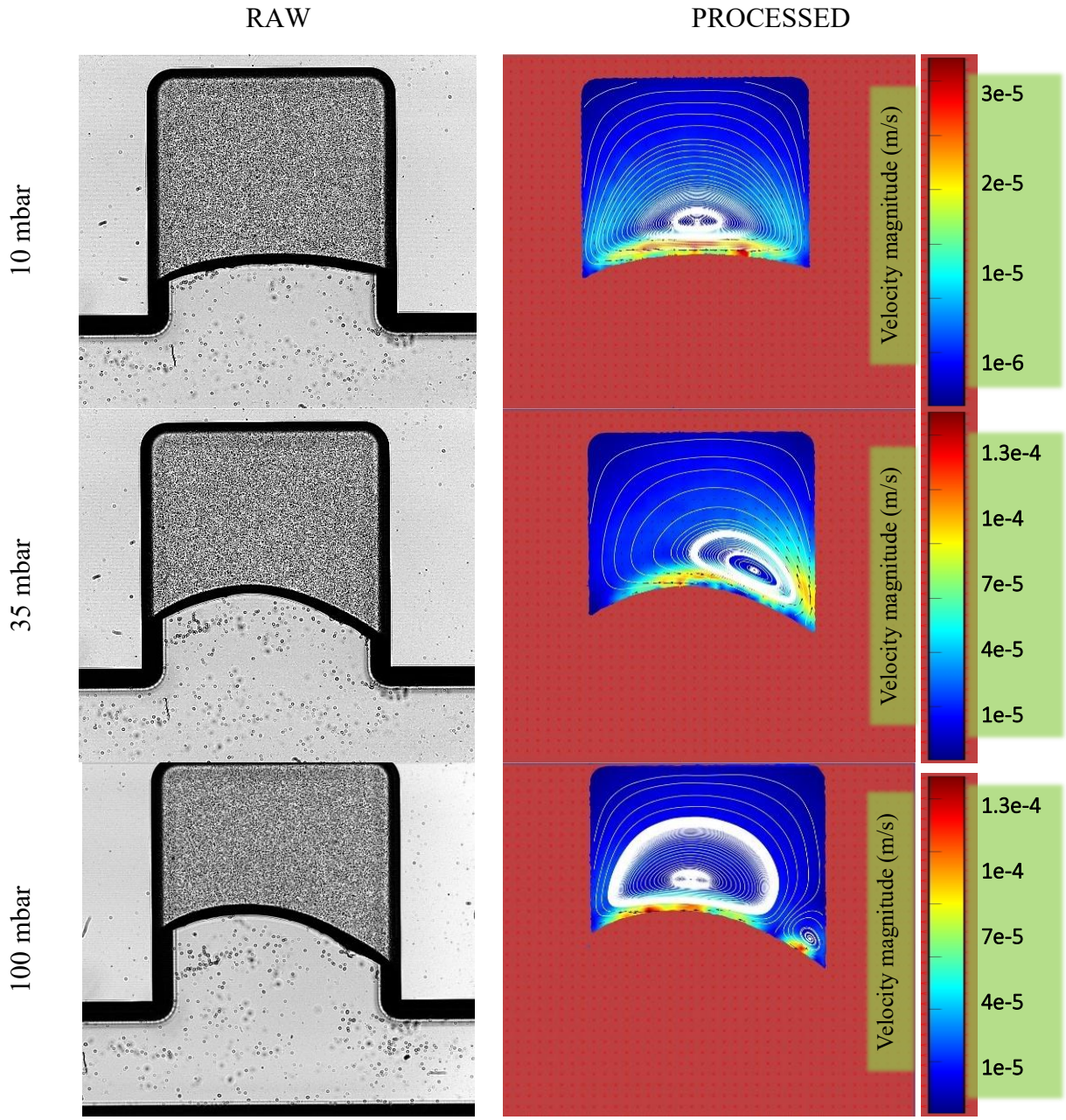

Figure 85 Fluid velocity patterns in drainage mode for single pocket geometry. Flow direction in the main underlying microchannel is from left to right to be consistent with single-phase flow experiments. Streamlines are depicted in white.

At first, it is visible that velocity values are 2-3 orders of magnitude lower compared to single-phase experiments as only a part of the kinetic flow energy is transferred from the interface onto the trapped phase. However, even at very low imposed pressure differences (e.g., 10 mbar), the gas phase provides sufficient momentum across the interface to initiate a detectable recirculation process. The center of the resulting recirculating vortex is located near the middle of the single pocket geometry, closer to the interface. Based on the earlier-presented classification by Roman *et*

al. (2020), this flow regime corresponds to a lid-cavity-driven mechanism. As the imposed pressure difference increases (e.g., 35 mbar), the vortex center shifts in the direction of the underlying gas flow, moving toward the outlet pocket wall. This shift occurs because the higher gas velocity in the microchannel enhances momentum transfer from the interface to the trapped liquid phase. The increased momentum transfer also affects the volume distribution inside the pocket, leading to an asymmetric shape where more liquid accumulates along the outlet wall (see 20 and 100 mbar examples). For imposed pressure differences of 50 mbar and above (see 100 mbar example), the recirculation vortex splits into two distinct vortices, indicating a more complex flow structure at higher driving pressures. Since the wettability is comparable and the opening to the trapping element is identical, similar results with even lower overall velocity are expected in L-pore geometry.

Plasma treated surfaces

During the drainage experiments in microfluidic devices with more hydrophilic surfaces (plasma treated), particle fluid films are found to be flowing all along the microchannel corners, going in and out of the main particle volume (Figure 86). Due to differences in surface properties, films are much thinner in single pore geometry (not shown here) compared to L-pore geometry (see Figure 86). The recirculation patterns in L-pore geometry are not present, instead particle fluid steadily drains from the microchannels and trapping element towards the outlet. This is contrary to single pore geometry, where fluid patterns of plasma altered surfaces nearly resemble native ones. Depending on the wettability (23° or ≈ 0°) and applied pressure difference, the magnitude of the outflow of wetting (particle + water) fluid from the trapping element can lead to displacement occurring within seconds or even instantaneously. Due to highly hydrophilic surfaces in this case, near instantaneous fluid displacement of non-wetting fluid (air) is observed during imbibition (particle fluid injection into air-saturated device), resulting in 100 % displacement efficiency.

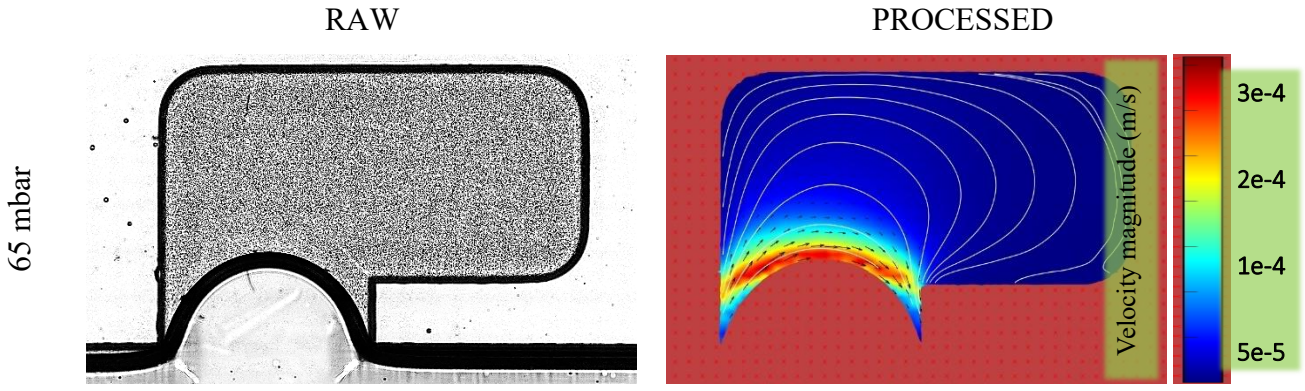

Figure 86 Fluid velocity patterns in drainage mode for a plasma-treated single pocket geometry. Flow direction in the main underlying microchannel is from left to right to be consistent with single phase flow experiments. Streamlines are depicted in white.

All in all, understanding the fluid advection patterns in two-phase flow experiments is essential to explain the capillary trapping phenomena and dissolution dynamics. In our single-phase liquid

experiments, we found creeping flow without recirculation patterns until 65 mbar of imposed pressure difference, which corresponds to Re number of 10. The recirculation of trapped water in two-phase drainage experiments occurs due to viscous force transfer from the underlying flow to the trapped fluid via the common interface. Detectable recirculation is observed from the very lowest applied pressures (5 mbar in our case) and the recirculation pattern evolves with the increasing pressure difference. Overall, the recirculation enhances advective species transport within the trapped volume. Thus, recirculation is expected to facilitate rapid CO_2 concentration equilibration in water leading to uniform concentration for the pores near the main CO_2 flow pathways. Finally, we show that wettability has a significant impact on fluid flow patterns in trapped volumes through film and corner flows. While the implication of wettability for capillary trapping may depend on pore geometry and the scale of investigation, solubility trapping is expected to benefit from more hydrophilic conditions due to increased surface area found in fluid films.

2. Capillary trapping and mass transfer

This section presents the results of capillary trapping and mass transfer experiments in the following manner. The two microfluidic geometries introduced in the previous section, the single pocket and L-pore, are individually analyzed. For each geometry, results are separately examined under imbibition and drainage conditions.

- In imbibition, the focus is on evaluating the capillary trapping potential of the CO_2 bubble, followed by an analysis of the dissolution-driven mass transfer.
- In drainage, the capillary trapping potential is assessed for the water droplet, along with its evaporation dynamics.

The results are tracked across the pressure difference range established in the previous section to ensure purely laminar flow conditions. The discussion emphasizes the role of wettability in capillary trapping and interfacial mass transfer, highlighting its impact on fluid retention and transport.

a) Imbibition - water injection experiments

As a reminder, within hydrophilic surfaces, as is the case here, imbibition refers to injecting water into a CO_2-saturated microchannel. The goal is to trap CO_2 in the trapping element while allowing water to continue flowing through the microchannel, thus enabling the study of CO_2 dissolution dynamics.

Capillary trapping potential of CO_2

Results on "single pocket" geometry

Owing to the water-wet nature of the glass, water injection results in a complete CO_2 displacement from the microchannel, encapsulating a small CO_2 bubble in the pocket. The CO_2-water interface during imbibition is expected to take on a convex shape, by observing from the water to the CO_2 phase. However, after conducting multiple experiments, it has become evident that the interface does not always form a perfectly smooth, circular shape as one might expect (see Figure 87). Instead, various deviations from the ideal convex shape are commonly observed. These interface distortions are particularly noticeable on native microchannel surfaces, though they are not exclusive to them. Interestingly, interface distortions remain stable across experiments, consistently appearing in the same locations unless the surface is modified. After the plasma treatment, interfaces seem to glide on freshly cleaned surfaces being guided by interfacial tension to minimize their potential energy. This suggests that physical and chemical surface heterogeneity influences local wettability, leading to variations in interface curvature. On more hydrophilic surfaces (contact angle 23°), the initial CO_2 bubble is often observed to be positioned in one of the corners of the trapping element, as demonstrated in the 25-mbar example (Figure 87). Having a CO_2 bubble shape covering the full width of the trapping element (e.g., at 50 mbar & 23°) or just being attached to one corner appears to be random, i.e., independent of imposed pressure difference.

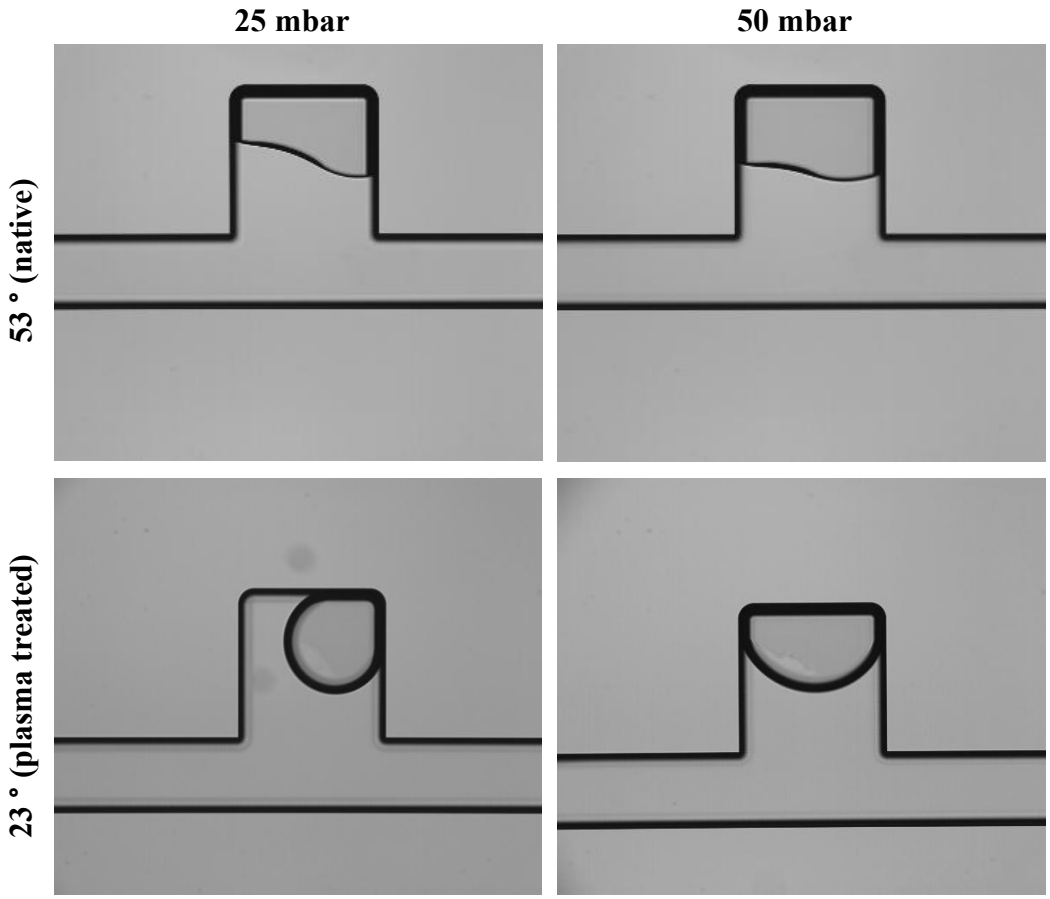

Figure 87 Variations of initial CO_2 bubble shape and size for two pressure differences and wettability conditions.

When looking at the size of trapped volume (refer to Figure 88), CO_2 bubbles vary considerably in their initial size between experiments under the same experimental conditions. This possibly occurs due to small perturbations in the flow patterns which are beyond experimental control. Moreover, the bubble size data analysis (Figure 88) indicates a positive correlation between the initial bubble size and the imposed pressure difference, independent of surface wettability. The proportional relationship can be attributed to fundamental fluid dynamics. At higher fluid velocities, the increased inertia of water in the underlying channel limits its penetration into the pocket, thereby reducing the extent of CO_2 gas displacement. On average, a more hydrophilic environment (contact angle of 23°) appears to slightly enhance the CO_2 capillary trapping potential.

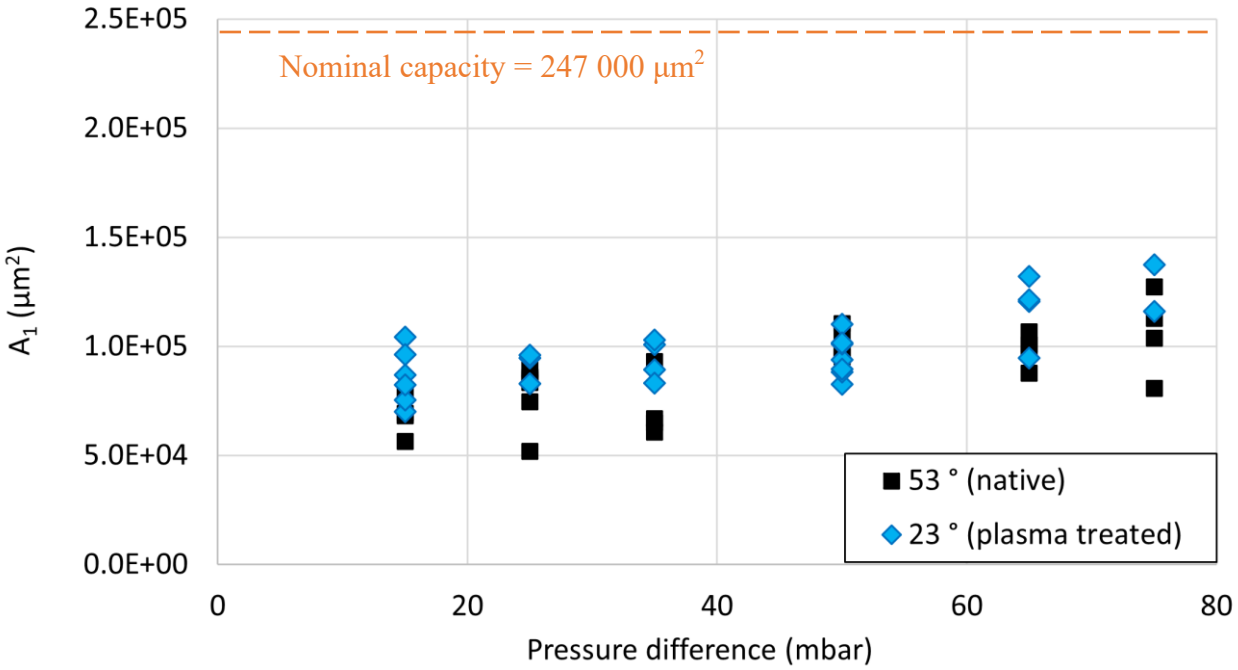

Figure 88 The initial CO_2 bubble size (A_1) scaling with the imposed pressure differences for the two wettability conditions. Nominal capacity denotes the measured area of a 500 × 500 µm trapping element.

Results on "L-pore" geometry

Similar to the single pocket geometry, the L-pore configuration in imbibition mode traps a CO_2 bubble. The bubble interface exhibits variations in convexity influenced by the microchannel surface properties and flow conditions (see Figure 89). A major distinction from the single-pocket geometry arises after plasma treatment, which reduces the contact angle to approximately 0°, rendering the surfaces superhydrophilic. As evident from the images, the CO_2 bubble remains suspended between the water-covered surfaces, with no significant adhesion to the solid surface. Bubble displacement is thus frequently observed as its size decreases during the dissolution process. Additionally, when the pressure difference exceeds 35 mbar, viscous forces become sufficiently strong to displace the bubble immediately from the trapping element. Due to the anisotropic nature of the trapping element geometry, this observation is present only in the normal direction of the flow compared to the geometry direction (refer to Figure 89). In the native moderately water-wet surfaces, no significant change in initial bubble shape or size was observed. This is likely because the bubble is in contact with the trapping element surface while the entrance to the L-pore is essentially the same, maintaining a uniform width of 500 µm and at a substantial depth of 140 µm.

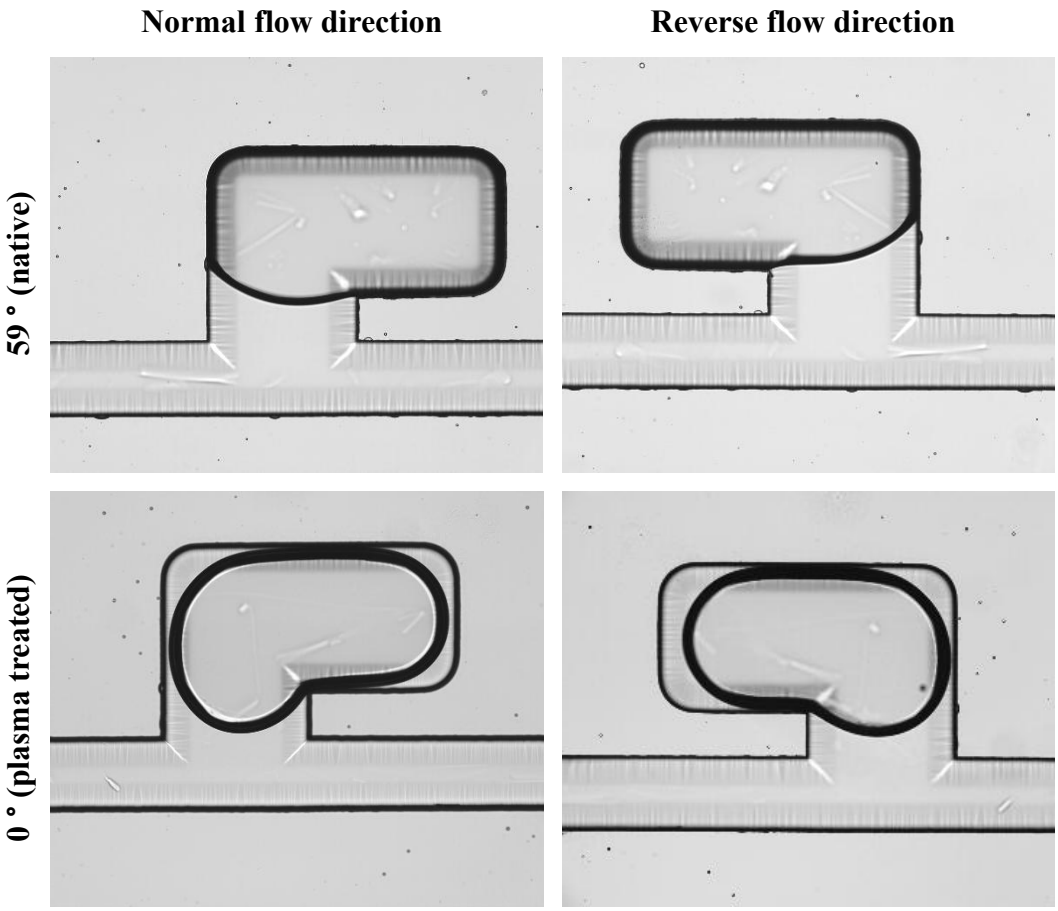

Figure 89 Variations of initial CO_2 bubble shape and size at 25 mbar of pressure difference for the two wettability conditions and the two flow directions (achieved by re-orienting the microfluidic device for consistent flow direction from left to right).

The variation of initial bubble size over the range of pressure differences for two flow directions to account for anisotropy and two wettability conditions is featured in Figure 90. As previously discussed, despite the anisotropic geometry, altering the flow direction does not significantly affect the initial bubble size under moderately water-wet conditions within the reference pressure difference range (compare fully black squares with black squares marked with orange x). In highly water-wet conditions (represented by diamond-shaped data points), the capillary trapping potential of CO_2 decreases progressively. For the normal flow direction, capillary trapping remains effective up to a pressure difference of 35 mbar (blue diamonds), whereas in the reverse flow direction, trapping persists across the entire tested pressure difference range. This behavior is likely attributed to the preferential water flow patterns in the normal direction, which penetrate the L-pore geometry more effectively. In contrast, under reverse flow conditions, the flow from the underlying channel does not reach the terminal region of the L-pore, thereby maintaining capillary trapping. Overall, there is no clear difference in initial bubble size between the tested wettability conditions.

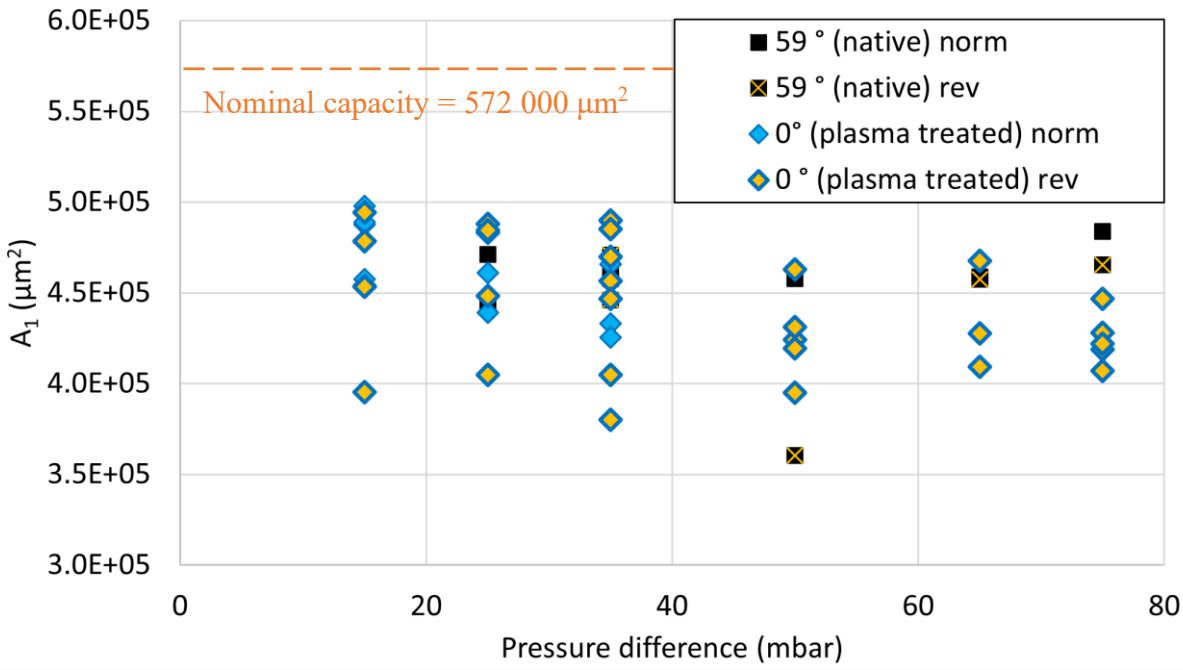

Figure 90 Initial CO_2 bubble size (A_1) scaling with the imposed pressure differences for the two wettability conditions and the two flow directions. "Norm" and "rev" stand for normal and reverse flow directions, respectively. Nominal capacity denotes the measured area of the L-pore trapping element.

Discussion on the capillary trapping potential of CO_2 during imbibition

When comparing the overall performance of two geometries in terms of saturation, we find that single pocket traps up to 60 % of CO_2 while L-pore up to 85 %, relative to their respective nominal capacities. This suggests that more complex dead-end geometries tend to trap more non-wetting fluid. Such geometries isolate the non-wetting fluid from the main advection zones, thus shielding it from viscous forces that could otherwise displace it.

It is however important to note that our observations are based on a single dead-end trapping element in the referenced geometries. This differs significantly from previous studies such as Mansouri-Boroujeni (2022) and Zhao *et al*. (2016), where geometries consisted of multiple trapping elements in which the fluid was capable of flowing through the middle of the trapping element. In such complex porous media, capillary trapping (i.e., the saturation of the defending phase) is reflected in both displacement and sweep efficiency. In contrast, our study focuses on a scale of one pore, i.e., single trapping element, where only displacement efficiency is relevant. Our findings show that increasing the pressure difference, corresponding to a higher capillary number, leads to greater CO_2 trapping. This aligns with observations by Mansouri-Boroujeni (2022), where displacement efficiency decreases, and Zhao *et al*. (2016), where overall saturation of the defending phase increases.

Regarding the effect of anisotropy, the L-pore geometry did not show a substantial change in capillary trapping capacity under most explored conditions. However, under high pressure differences and superhydrophilic surface conditions, displacement increased to the extent where the capillary trapping is no longer effective, thus compromising the security of CO_2 storage. Notably, the referenced studies did not address the influence of anisotropy.

Additionally, previous studies highlighted that porous media characteristics such as wettability have a more pronounced effect at lower capillary numbers, which correspond to lower imposed pressure differences. In our experiments, the range of applied pressure differences, and therefore capillary numbers, may have been insufficiently broad or the overall values may have been too high. This could explain the limited observable effect of wettability in most cases. However, in the earlier-mentioned exception, a synergistic effect of low contact angles, specific trapping element orientation and elevated pressure differences may have led to complete elimination of capillary trapping.

Finally, while differences in mobility ratio may also contribute to discrepancies between our results and those in other studies, the influence of mobility ratio was not explored here and remains outside the scope of this thesis.

CO_2 dissolution dynamics

Results on "single pocket" geometry

During imbibition, we track interfacial mass transfer through the dissolution of trapped CO_2 volume. The onset of mass transfer is as soon as two fluids are in contact (T-valve) however we track it only following the initial displacement in the microchannel leading to the entrapment of a CO_2 bubble in the pocket. This part of the process following initial displacement and entrapment (t_0) is visually depicted in Figure 91, showcasing representative examples for native and plasma treated surfaces at 25 mbar.

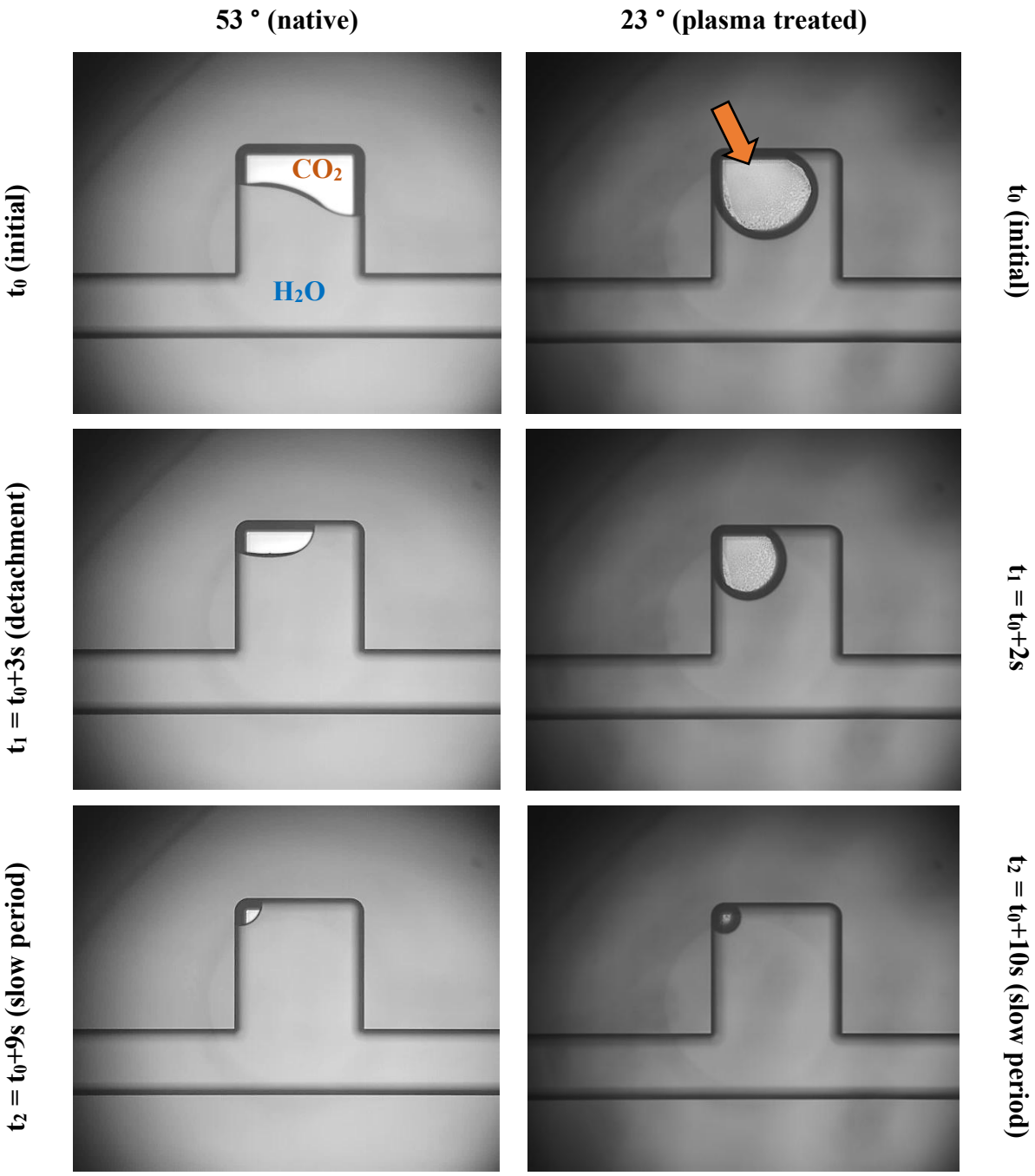

Figure 91 CO_2 dissolution evolution during imbibition under 25 mbar acquired in reflection mode. The arrow points to water droplets.

At time t_0, the initial entrapment phase is characterized, serving as a reference for evaluating capillary trapping potential, as discussed in the previous section. Since the bubble often spans the entire width of the pocket (see example on native surfaces at t_0), a key event in the mass transfer process is its detachment to one of the pocket's end corners (t_1). As the bubble undergoes dissolution, interfacial tension forces act to minimize its surface potential energy by reshaping it into a more spherical form. Once detachment occurs, the bubble remains in the corner until

complete dissolution. As dissolution progresses, the bubble continues to shrink to a fraction of its initial volume, reducing its interfacial area and gradually migrating away from the primary advection regions into more stagnant, diffusion-dominated zones. Time t_2 marks the onset of a significantly slower dissolution phase.

An intriguing observation is spotted during the mass transfer process on plasma-altered glass surfaces (see time t_1). Within the bubble, a tightly packed cluster of micrometer-sized water droplets occurs immediately following the displacement. These droplets are hypothesized to form due to condensation, indicating that during displacement within the tubing, water evaporates into the CO_2.

Mass transfer dynamics

In addition to purely visual observations, patterns of bubble dissolution behavior are also tracked and analyzed through normalized perimeter (P/P_1), normalized area (A/A_1), normalized perimeter area (A_p/A_{p1}) and normalized dissolution rate ($\left(\frac{dA_p}{dt}\right) / \left(\frac{dA_p}{dt}\right)_{MAX}$). These metrics of the representative case are shown in Figure 92 and evaluated for both wettability conditions (53° and 23°). Note, the perimeter-area parameter represents the bubble volume-to-interfacial area ratio (in 3D), normalized to its initial state.

The initial period of the mass transfer process is characterized by a rapid CO_2 dissolution, showcased in all 4 parameters. In cases where a CO_2 bubble covers the full pocket width (see the example with native surfaces at 53°), the progress of dissolution will eventually result in bubble detachment to one of the end pocket corners. During the detachment, the redistribution of the bubble volume in 3D results in an alteration of its shape. In 2D, this may be observed as a small temporary apparent increase in bubble size, or more often, a comparably smaller apparent decrease in bubble size deviating from the existing trend. Most pronounced changes are visible in the perimeter and dissolution rate behavior. The perimeter (see Figure 92a) stays constant during the translatory movement of the interface and only starts dropping when the bubble detaches (marked with an orange arrow). The dissolution rate (see Figure 92d) will experience a sudden, significant drop (marked with an orange arrow) that may even produce negative values if the bubble increases in size (not shown here). In cases where a bubble is attached to one of the corners from the beginning (see the example with plasma-treated surfaces at 23°), all 4 parameters decrease smoothly as the bubble gradually shrinks during dissolution.

When the bubble size decreases to less than 5 % of its initial volume (see A/A_1 ratio in Figure 92b), the average bubble volume-to-interfacial area ratio (A_p) falls below 32 µm at 53° and 38 µm at 23°. At this stage, dissolution rates significantly decrease (refer to Figure 92d and the dashed lines), marking the onset of the slow diffusion-dominated period. In addition to the bubble position shifting away from the primary flow pathways, the reduced interfacial area leads to a lower mass transfer rate, prolonging the dissolution process.

No significant difference in mass transfer patterns is observed between the two wettability states. Both exhibit a rapid dissolution phase during the initial period, followed by a prolonged phase of slow dissolution.

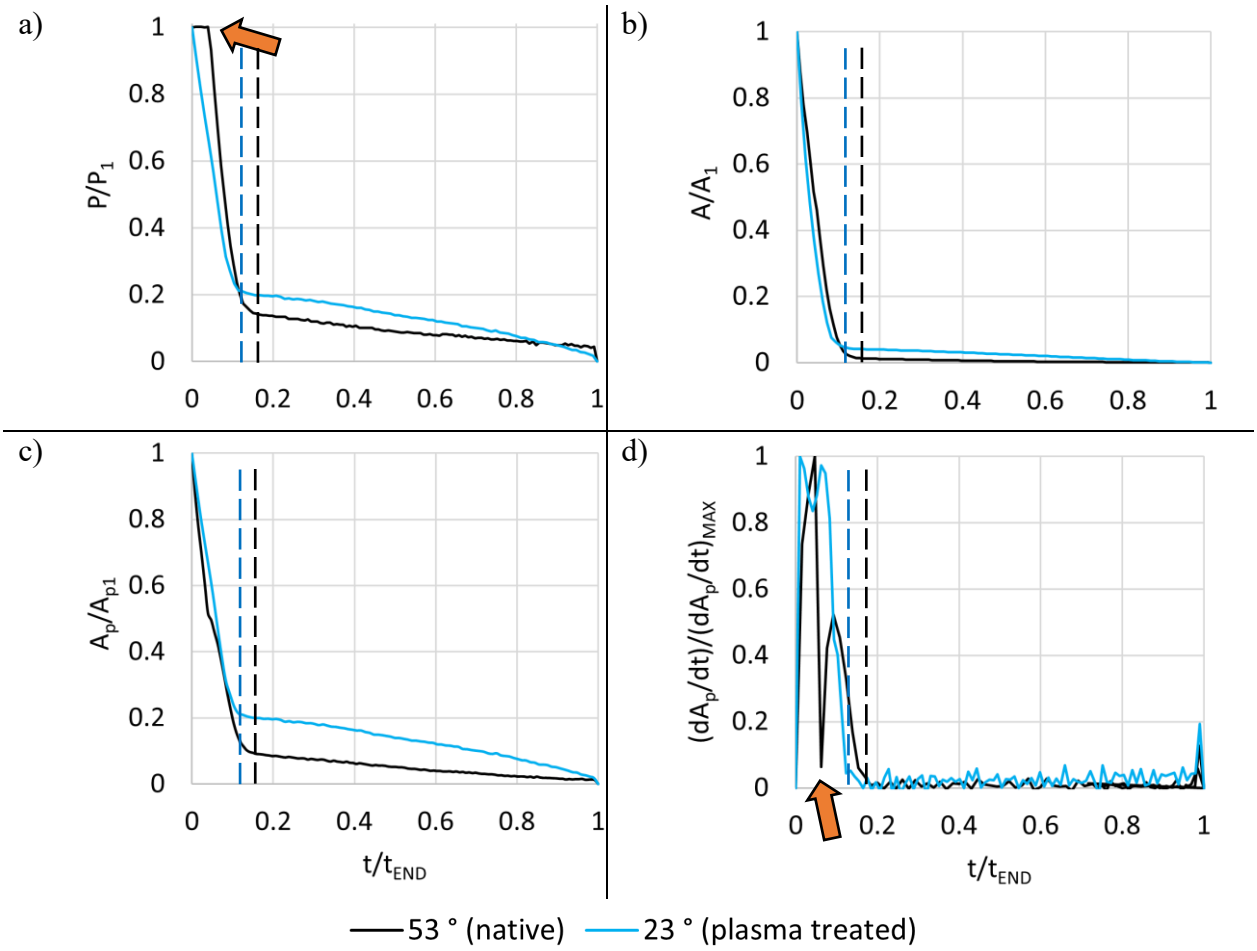

Figure 92 The representative example of the bubble dissolution process, given for a 25 mbar of pressure difference. The process is tracked through the normalized perimeter – P/P_1 (a), normalized area - A/A_1 (b), normalized perimeter area – A_p/A_{p1} (c) and normalized interval dissolution rate - $(dA_p/dt) / (dA_p/dt)_{MAX}$ (d). Dashed lines indicate the separation between fast and slow period for respective wettability conditions. Orange arrows mark the moment of bubble detachment.

Mass transfer rates

Each period can be approximated using a linear function, allowing for the extraction of average mass transfer rates specific to the respective periods. Overall and period-dependent CO_2 dissolution mass transfer rates are shown in Figure 93.

Since the first period (Figure 93a) is advection dependent, the magnitude of dissolution scales proportionally with imposed pressure difference. Specifically, the increase is observed up to 65 mbar while a further increase (up to 75 mbar) had no effect. The reason for this is likely the appearance of a vortex that dissipates kinetic energy through circular motion, limiting the

concentration potential. The second period (Figure 93b) is diffusion-dependent, hence, the imposed pressure difference does not have a significant effect on mass transfer rates. The values are thus also two orders of magnitude lower compared to the first period. When comparing performance in different wettability conditions, the results indicate no significant wettability effect on mass transfer rates in the first period. Namely, the dominant factor governing dissolution in this period is advection while wettability is only a secondary factor. On the contrary, in the second period, there is a clear distinction between the two wettability states. Namely, wettability greatly influences the slower diffusion-governed period. A discussion on the observed behavior is provided in the following section.

Overall mass transfer rates (Figure 93c) are thus a superposition of the two separate periods, proportionate to their respective magnitude and duration. The first period is very short, thus its impact compared to the significantly longer, slower period is minor. Therefore, in overall behavior there is only a minor dependency of the imposed pressure differences and a clear distinction between the two wettability states. Namely, mass transfer rates are meaningfully higher at a contact angle of 23° compared to 53°. Since the effect of the interfacial area is accounted for by perimeter normalization, the mechanism by which wettability impacts mass transfer rates remains to be answered. The average mass transfer values are on the order of a few μm/s ($=10^{-6}$ m/s) which is comparable and consistent with other research findings presented in the Introduction section (Han *et al*., 2013; Patmonoaji and Suekane, 2017; Teng and Yamasaki, 1998).

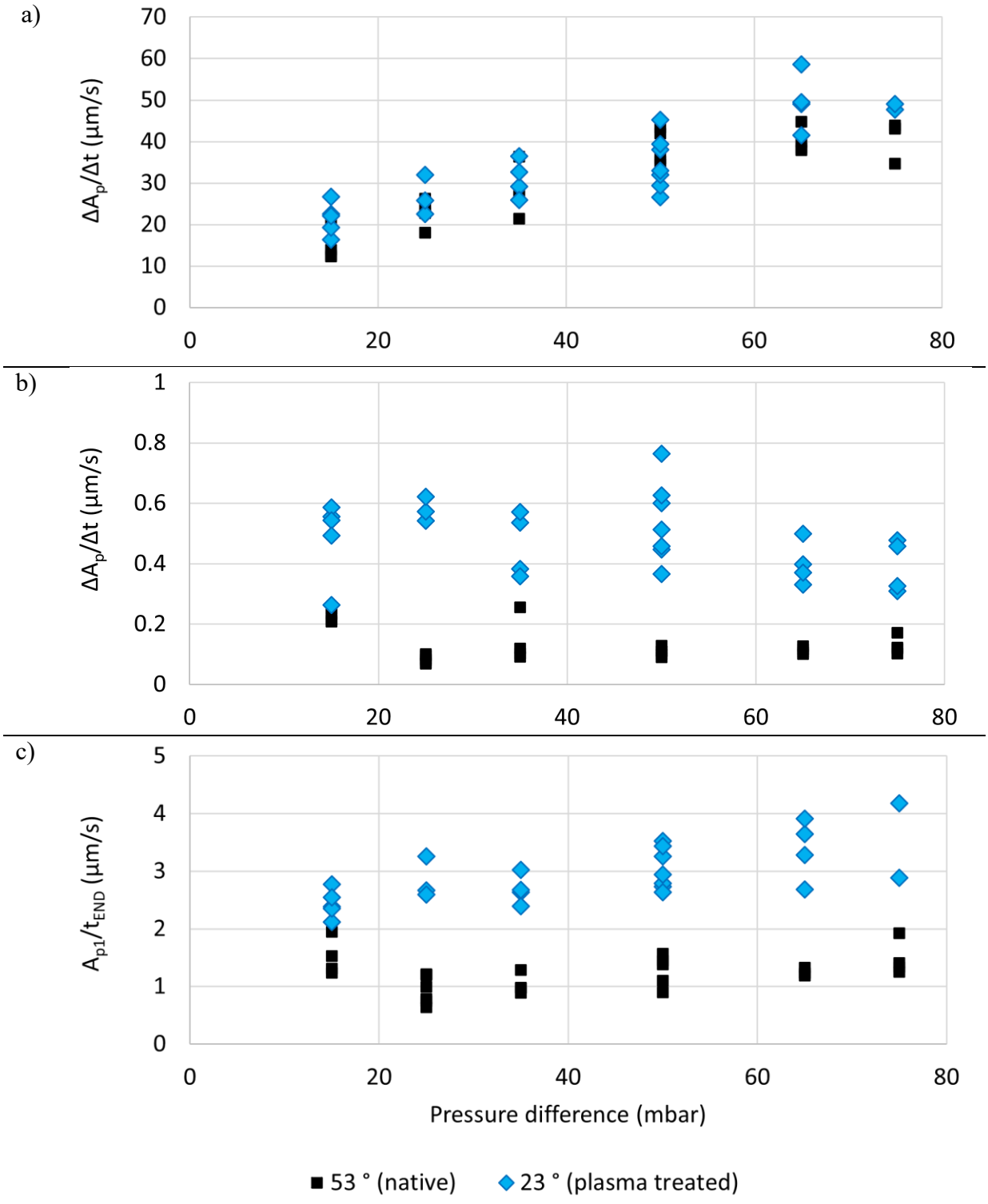

Figure 93 The average perimeter-normalized dissolution rates ($\Delta A_p/\Delta t$) during fast period (a), slow period (b) and for the entire duration of the experiment (c) presented as a function of an imposed pressure difference for two wettability conditions.

To investigate the mechanisms by which wettability influences mass transfer, in Figure 94 we present the overall mass transfer coefficient lumped with the perimeter (interfacial area in 3D). This mass transfer formulation complements the previous one (Figure 93c), where the interfacial area was excluded from the analysis by normalizing to the perimeter. By comparing both mass transfer formulations, we observe that the effect of wettability persists regardless of interfacial area. While existing literature suggests that variations in the interfacial area under different wettability conditions are the primary mechanism influencing mass transfer (Agaoglu *et al*., 2015), our comparison indicates the presence of an additional unaccounted mechanism. We hypothesize that differences in curvature (1/r) between wettability states lead to variations in capillary pressure, which in turn affects the mass transfer driving force at the interface. The increased curvature at a lower contact angle increases capillary pressure and thus overall pressure inside the bubble resulting in increased mass transfer rates. Another possibility are film and corner flows which would also increase the interfacial area available to facilitate mass transfer.

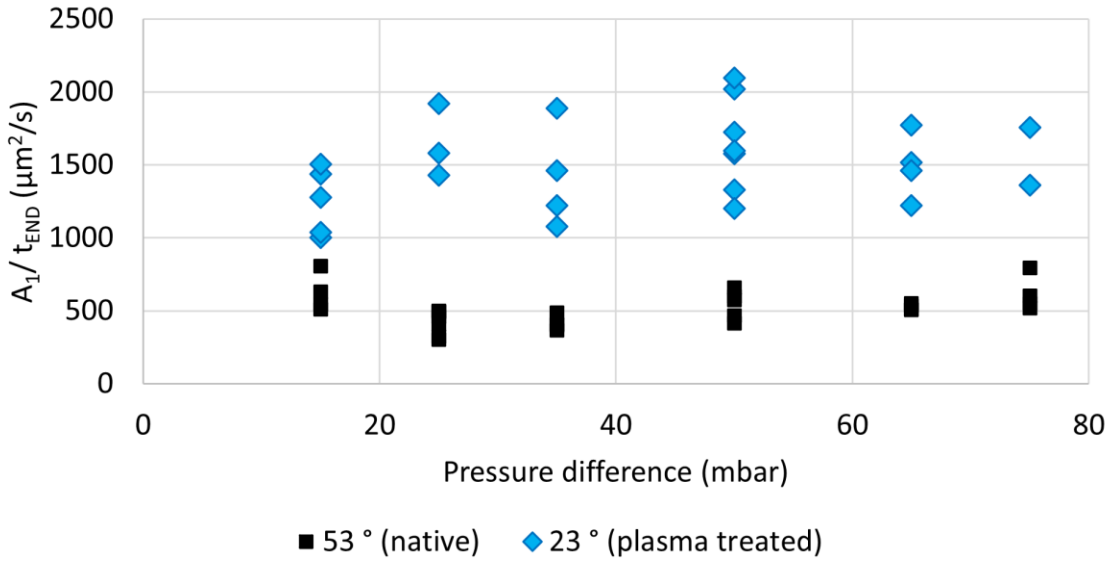

Figure 94 The overall non-normalized dissolution rate (A_1/t_{END}) presented as a function of an imposed pressure difference for two wettability conditions.

To summarize, we identified two regimes of dissolution – the fast mass transfer in the initial period is governed by advection, while the slower period mass transfer in the second period is governed by diffusion. Overall, we demonstrated that wettability plays a critical role in governing dissolution dynamics, which is a key mass transfer process during CO_2 storage. While the influence of wettability is secondary in high-advection zones, it becomes significant in low-advection environments, aligning with numerical findings by Primkulov *et al.* (2021) (discussed in Chapter 1). Within the tested wettability range (23 - 53°), more hydrophilic surfaces are found to facilitate faster CO_2 dissolution. We hypothesize that, in addition to the increased interfacial area,

differences in curvature and the resulting capillary pressure may contribute to variations in wettability-influenced mass transfer rates.

Since capillary trapping does not differ significantly between the two wettability conditions, the shorter overall dissolution time observed on more hydrophilic surfaces (not shown) can be attributed to enhanced mass transfer rates. This promotes more effective solubility trapping, contributing to safer long-term CO_2 storage.

This highlights the importance of comprehensive wettability characterization when selecting reservoir rocks and suggests the potential for surface engineering strategies to optimize long-term CO_2 sequestration efficiency.

Static CO_2 dissolution

Before moving to drainage experiments, one static experiment was conducted to characterize what happens to capillary-trapped CO_2 bubbles located far away from advection zones. In large-scale projects, near-static conditions are assumed to occur in the reservoir after stopping the injection and after the gravity-induced segregation processes have diminished. The bubble dissolution would thus be governed by (Fickian) diffusion-dominated conditions where the concentration gradient decreases with time, slowing down the interfacial mass transfer.

By starting the static experiment as an imbibition process, a small quantity of CO_2 is trapped in the pocket. The main idea behind static conditions is to determine the possible time scale for full bubble dissolution when there is no advection to supply fresh water. The results of our single static experiment on native surfaces are shown in Figure 95. During the 3.5-day-long experiment, the CO_2 bubble did not manage to dissolve entirely into the surrounding water. To determine the possible time scale needed for complete dissolution in static conditions, we fitted the experimental points and extrapolated the behavior. The extrapolation is performed assuming an infinite reservoir and results indicate that a bubble would nearly dissolve (less than 1 % of the initial size) after 117 days. Such a timescale is more representative of actual subsurface CO_2 dissolution processes compared to the rapid dissolution within minutes observed in our laboratory experiments.

Looking at the overall dissolution process, the pattern follows previously shown imbibition experiments, however, the behavior seems to be stretched over a longer time frame. The dissolution is significantly higher at early times which is in accordance with expected behavior due to contact with unsaturated water. As the water in the vicinity of a bubble becomes more and more saturated in CO_2 with time, dissolution rates are being retarded. Since the spreading of dissolved CO_2 within the liquid (water) phase is governed by a concentration gradient (Fick's law), bubble dissolution continues in later periods as a lot of liquid volume remains in the microchannels and connecting tubes. With time, unsaturated water is located further and further away making the system enter a quasi-static dissolution regime.

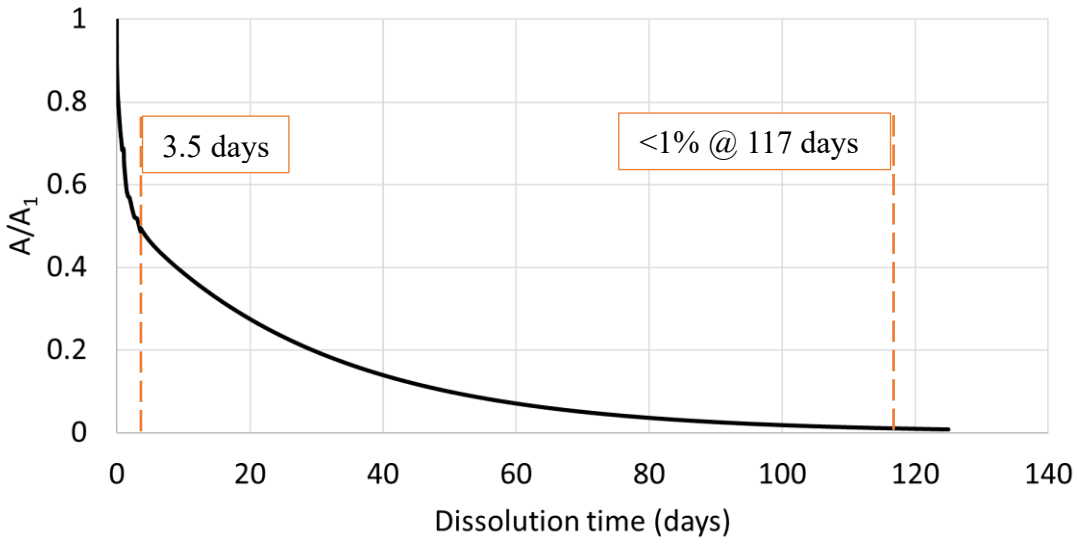

Figure 95 A static experiment showing the evolution of a CO_2 bubble under no-flow conditions. The 3.5 days of experimental data are fitted with a two-parameter exponential function, corrected for basic artifacts and extrapolated to 125 days.

Results on "L-pore" geometry

The dissolution process in L-pore geometry is visually depicted in Figure 96. The initial displacement in the presented cases resulted in bubble entrapment (t_0). In the native wettability with the average static contact angle of 59°, the interface is initially pinned in the convex corner (see orange arrow mark at t_0). As the dissolution starts, the interface moves by adjusting itself to the geometry contours revolving around the convex corner as shown in t_1. When the bubble reduces its size significantly (t_2), it detaches to one of the concave corners where it stays until it completely dissolves. Similar to the single pocket geometry, the bubble remains in contact with the glass surfaces throughout the process.

For plasma-altered surfaces, where the contact angle is nearly 0°, the bubble is never in direct contact with the glass. Instead, it is surrounded by a continuous water film, contrasting with the behavior observed in single-pocket geometries, where the bubble is still attached to the glass surfaces due to a significantly higher contact angle (23°). Despite the absence of direct solid contact, the bubble remains geometrically constrained near the same convex corner. As dissolution progresses, the bubble settles within the widest section of the L-pore (see dashed orange double arrow line at t_1) where it adopts a circular shape as interfacial tension minimizes surface energy. Under highly water-wet conditions (0°), the bubble is positioned significantly closer to the underlying microchannel and primary fluid pathways compared to the moderately water-wet case (59°). Thus, wettability and pore structure geometry conjointly influence dissolution kinetics and mass transfer efficiency.

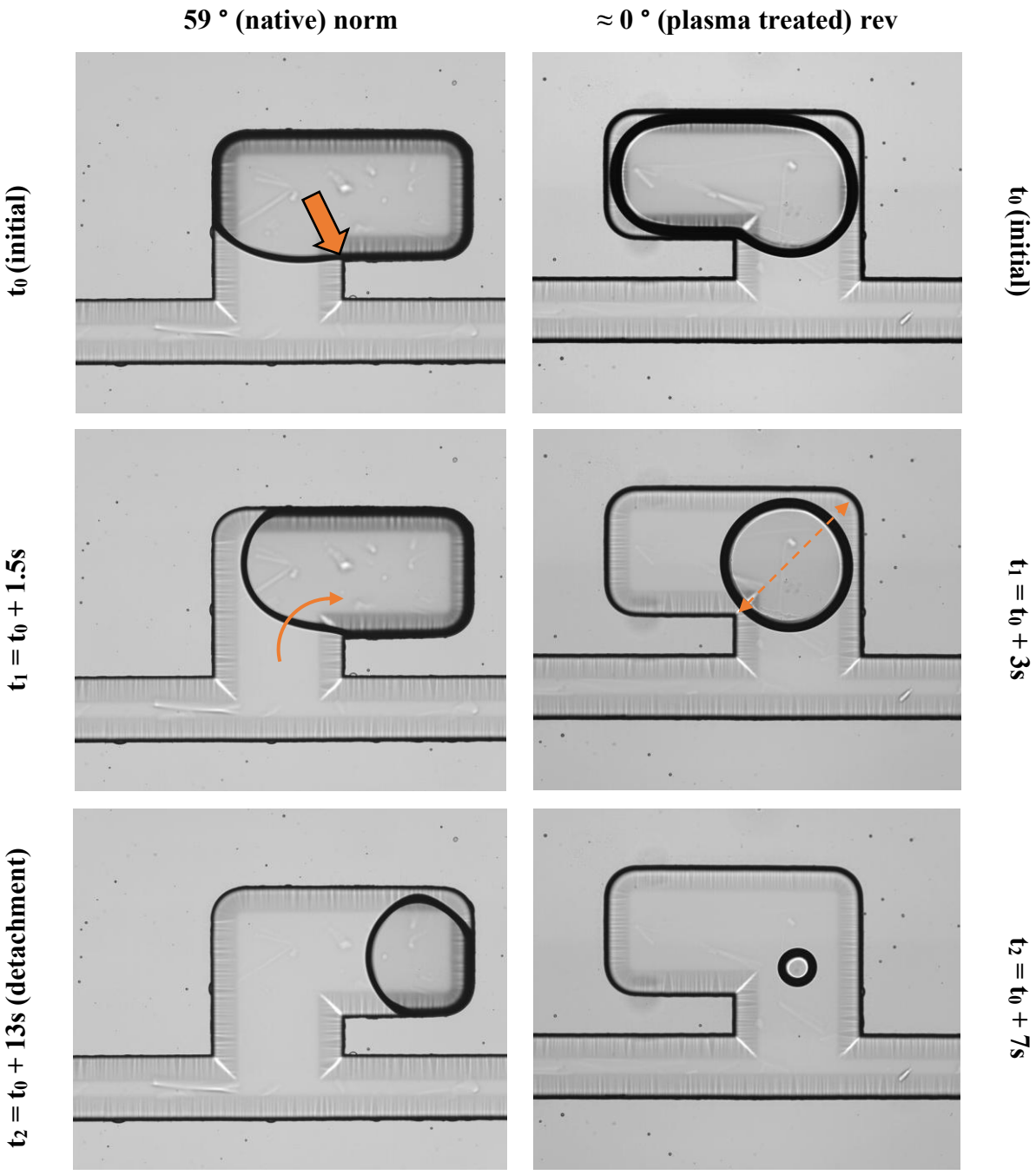

Figure 96 CO_2 dissolution evolution during imbibition under 50 mbar. "Norm" and "rev" stand for normal and reverse flow directions, respectively. The thick arrow points to the location of pinning in the corner, the curved arrow shows the direction of interface movement in geometry and the double arrow indicates the widest part of the geometry.

A more detailed analysis of the dissolution process is provided through the previously defined parameters (P/P_1, A/A_1, A_p/A_{p1} and $\left(\frac{dA_p}{dt}\right) / \left(\frac{dA_p}{dt}\right)_{MAX}$). Unlike single pocket geometry, identifying a representative dissolution pattern in the L-pore configuration presents greater challenges. Multiple displacement events occurring at the initial stages of the process complicate the analysis of mass transfer dynamics with greater statistical significance. Out of all tested conditions and with current experimental data availability, we chose only two with representative behavior for the whole pressure difference range.

Thus, in Figure 97, we showcase dissolution patterns at 50 mbar of imposed pressure difference. Since L-pore geometry is more complex having the potential to trap more volume, the experiments on native surfaces lasted significantly longer compared to single pocket geometry. Therefore, to highlight important events featured at the beginning of the dissolution process we configured these graphs to a log scale. Looking at the P/P_1 graph (Figure 97a), we observe two major increases in the interfacial area compared to initial conditions (marked by orange arrows). The first corresponds to the interface passing through the widest part of the L-pore geometry (t_1 in Figure 96) while the second marks bubble detachment (t_2 in Figure 96). Due to proximity to the underlying microchannel, the first increase in interfacial area corresponds to a maximum observed dissolution rate (see orange arrow mark in Figure 97d). Following another increase during the detachment, the dissolution rate decreases to minimum values, marking the onset of a slow diffusion-dominated period (marked by the dashed line in all graphs). Up to this point, the behavior observed in the normal flow direction has also been representative of the reverse injection direction. However, shortly after the onset of the slow dissolution period, bubble growth was observed in the case of reverse flow, persisting for several hours.

A hypothesis is that this process could potentially refill the trapping element with exsolved gas, returning the bubble to its initial size or even exceeding it. When the entire system was subjected to an additional 100 mbar of confining pressure while maintaining the same pressure difference, the exsolution phenomenon was no longer observed. This suggests that the water in the inlet reservoir became saturated with air, while the remaining trapped bubble acted as a nucleation site, initiating the exsolution process. However, the reason this phenomenon occurs exclusively on native surfaces in one flow direction remains an open question. A hypothesis is that a particular mixing occurs, leading to an increase in concentration gradient and consequently exsolution. With fluid recirculation and pressure oscillations, this phenomenon is also likely to occur on a large scale, reducing the potential for solubility trapping and potentially mobilizing the capillary-trapped CO_2 phase.

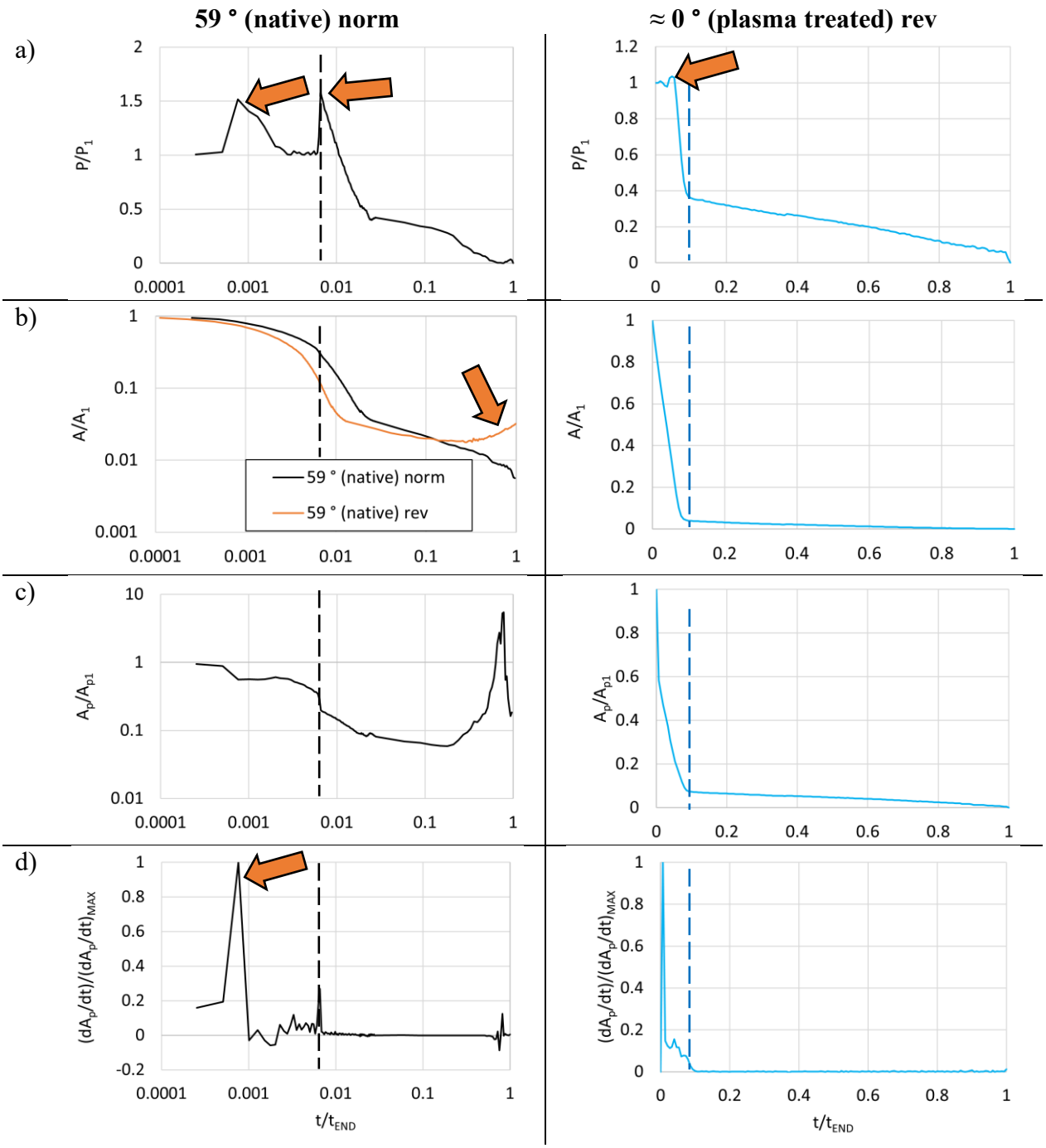

Figure 97 The representative example of the bubble dissolution process, given for a 50 mbar of pressure difference. The process is tracked through the normalized perimeter – P/P_1 (a), area - A/A_1 (b), perimeter area – A_p/A_{p1} (c) and interval dissolution rate - $(dA_p/dt) / (dA_p/dt)_{MAX}$ (d). Dashed lines indicate the separation between fast and slow period for respective wettability conditions. Orange arrows in a) and d) point to bubble detachment, while in b) it indicates a period of bubble size increase during reverse flow. Note, a logarithmic scale is used to make crucial events more visible, particularly in the case of native wettability conditions.

On superhydrophilic surfaces with 0° contact angle, dissolution patterns are simplified and closely resemble those observed in the single pocket geometry results. By observing the interfacial area evolution in the P/P_1 graph (Figure 97a) stays relatively constant for a few seconds while the bubble rapidly shrinks down (Figure 97b). With a round bubble confined to the widest part of the L-pore (time t_1 in Figure 96 corresponding to a moment denoted with an orange arrow mark in Figure 97b), the interfacial area gradually decreases over time as dissolution progresses, maintaining a relatively high dissolution rate (Figure 97d). The reach of the critical A_p value of around 43 μm marks the onset of a long and slow diffusion-dominated indicated with blue dashed lines in all graphs of Figure 97. The corresponding critical A_p value on the native (59°) surface at the moment of detachment is rather high, averaging 188 μm. Compared to the values obtained in the single-pocket geometry (32 and 38 μm), the measurements of A_p in the L-pore geometry are consistently higher. No significant oscillations in the critical A_p values were observed with imposed pressure differences or changes in flow direction within either geometry or wettability state. Therefore, these differences primarily arise from the bubble's exposure to advective conditions, which are influenced by the interplay between geometrical features and wettability.

Overall, it can be concluded that both wettability and the complexity and anisotropy of geometrical features play a crucial role in influencing the dissolution patterns.

Mass transfer rates

Given the significantly different dissolution patterns indicating exsolution and the limited availability of complete experimental data on native surfaces, together with the occurrence of bubble displacements at higher imposed pressure differences on plasma-altered surfaces, we present the period-dependent and overall dissolution rates in Figure 98. On the whole, the dissolution patterns are consistent with those observed in the single-pocket geometry, where dissolution occurs rapidly in the initial period, followed by a significantly slower second phase.

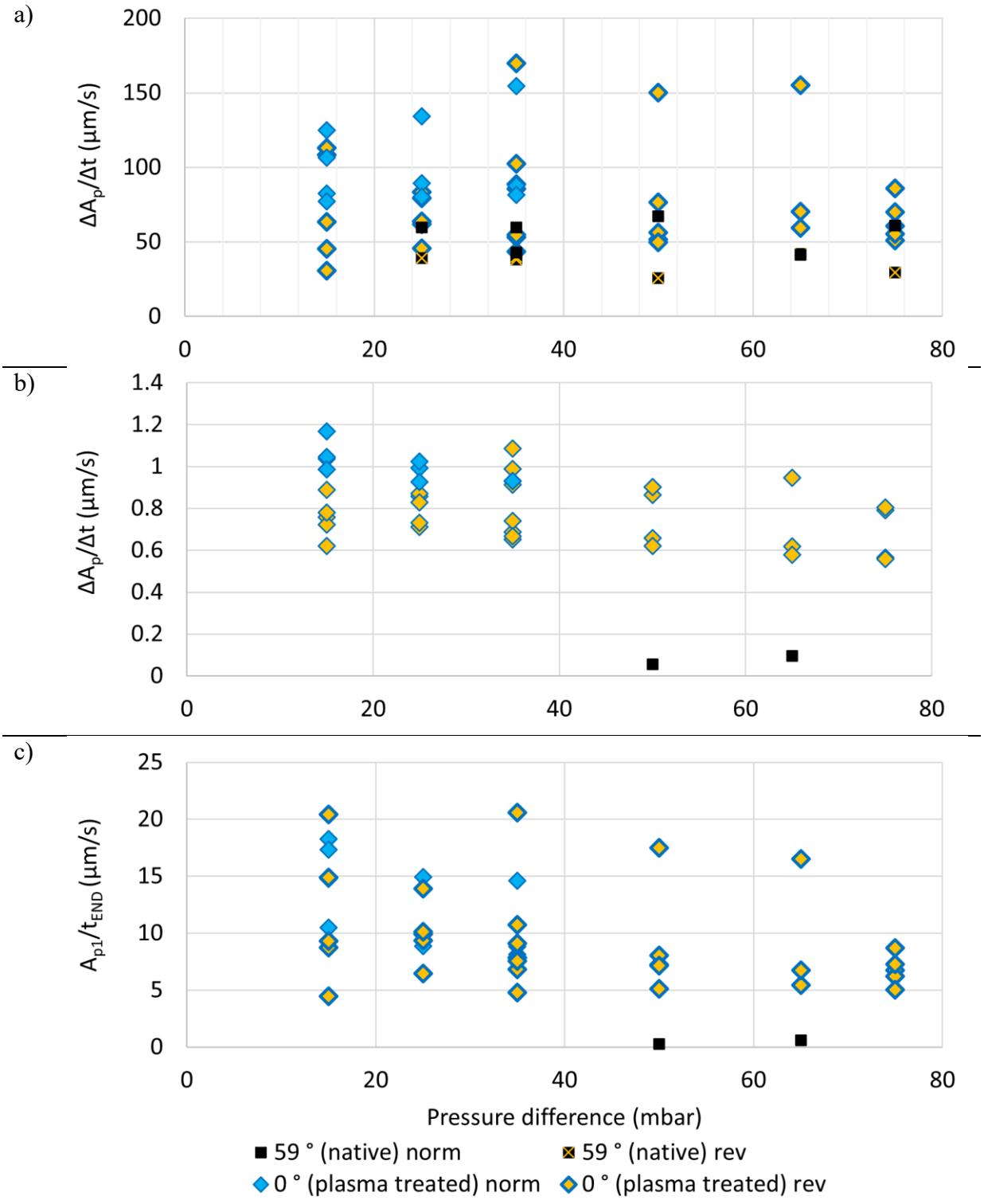

Figure 98 Average dissolution rates (ΔAp/Δt) during fast period (a), slow period (b) and for the entire duration of the experiment (c) presented as a function of pressure for two wettability conditions.

During the first period (Figure 98a), the dissolution rates range from 10^1 to 10^2 μm/s, with only the results produced on 0° contact angle surfaces in normal flow direction exhibiting a clear dependence on the imposed pressure difference. The 0° and normal flow direction is also the only case where we systematically observe bubble displacement from the trapping element right from the beginning of the process, occurring for pressure differences exceeding 35 mbar. Generally, higher average dissolution rates and bubble displacements at higher pressure differences stem from the bubble's exposure to the advection zones which is a synergic effect of trapping element geometry, flow direction and surface wettability. When comparing the two wettability conditions, the lower contact angle data points are on average associated with higher dissolution rates. However, the limited experimental data on native surfaces prevents drawing strong conclusions, restricting further analysis.

In the second, diffusion-governed period (Figure 98b), dissolution rates are two to three orders of magnitude lower compared to the initial advection-governed period as the interface shrinks and moves further away from the primary advection zones reducing concentration potential. The available data suggest that native surfaces (59°) exhibit dissolution rates on the order of 10^{-2} μm/s, approximately one order of magnitude lower than their superhydrophilic counterparts (0°).

The overall dissolution rates are once again the superposition of the distinctive periods, weighted by their respective magnitudes and durations. On moderately hydrophilic surfaces (59°), overall dissolution rates are on the order of 10^{-1} μm/s, whereas on superhydrophilic surfaces (0°) they range from 10^0 to 10^1 μm/s.

Discussion and conclusion

In L-pore geometry, two dissolution regimes are identified with dissolution rates being higher on more hydrophilic surfaces (0°) which is consistent with observations on single pocket geometry. Though some tendencies are visible in the first period, the wettability effect on mass transfer rates is dominant in the second period. This contrasts with the observations by Sun *et al*. (2024) presented in section I.2., where they numerically acquired results suggesting that wettability plays a more important role in the initial period of dissolution.

When comparing the performance between geometries, the CO_2 dissolution mass transfer rates on native surfaces are higher in the single pocket geometry, whereas plasma-altered surfaces exhibit higher rates in the L-pore geometry. While the difference in geometric complexity between the two microfluidic designs explains the performance on native surfaces, favoring more simplistic single pocket geometry, the difference in performance observed on plasma-altered surfaces can be attributed to a meaningful contrast in contact angle, favoring the lower contact angle found on L-pore geometry. Although geometric anisotropy strongly affects capillary trapping, its influence on mass transfer rates appears to be minimal as the diffusion regime prevails. Thus, it can be concluded that geometric complexity and the wettability conditions together play a role in governing pass transfer rates related to CO_2 dissolution.

b) *Drainage - CO_2 injection experiments*

To remind the reader, drainage in our hydrophilic microfluidic devices refers to the injection of CO_2 in the water-saturated microchannels. The objective is to achieve water entrapment and investigate water evaporation dynamics. Large-scale operations such as natural gas storage, injection of CO_2 for enhanced oil recovery (EOR) and improved oil recovery (IOR), CO_2-based geothermal projects, and underground CO_2 injection and storage in water-wet porous media are all inherently drainage processes.

Capillary trapping potential of water

Results on "single pocket" geometry

Following the water displacement in our hydrophilic microfluidic devices, the CO_2 flows in the middle of the microchannels while water remains attached all along the walls. Depending on the surface wettability, water is present in the form of dispersed droplets (see Figure 78 and Figure 100) when the contact angle is high, or in the form of fluid films and corner flow (see Figure 99) when the contact angle is low.

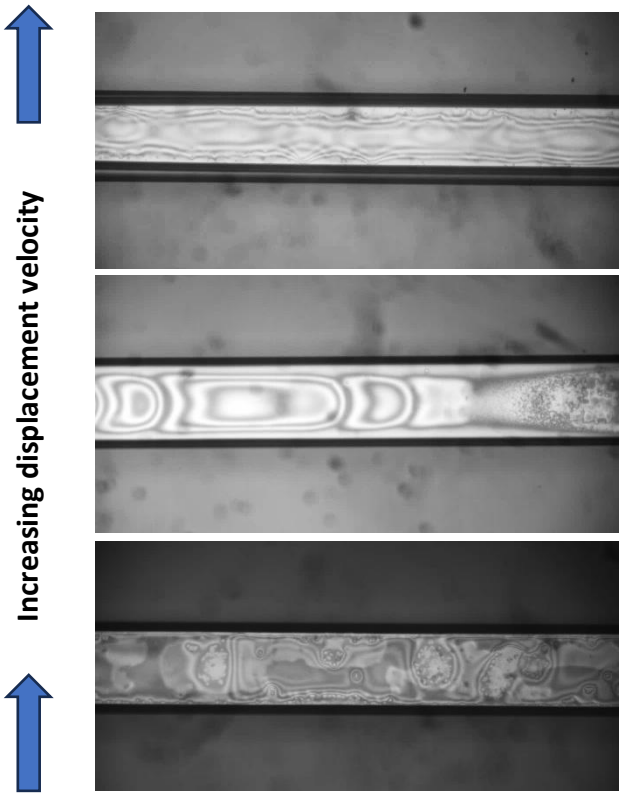

Figure 99 The fluid film patterns acquired on top and bottom of microchannel surfaces. The images are acquired under no-flow conditions following the displacement of water with CO_2 in plasma treated 500 µm channels under 5x magnification in reflection mode.

Besides wettability, the thickness and the shape of the film patterns depend on the displacement velocity (Bretherton, 1961) as indicated in Figure 99. Water films along the microchannels

destabilize rapidly (within seconds) due to the flow. They form small droplets which move along the microchannel surfaces being propelled by the flow of CO_2.

The shape of the droplet interface during drainage experiments is always concave, looking from the CO_2 into the water phase (see Figure 100). The shape of the interface in contact with glass surfaces with the native wettability conditions is not smooth just like demonstrated in the imbibition section. Interestingly, after the plasma treatment, the interface often lies flush with the upper edge of the microchannel attached at the corners (see 23° conditions in Figure 100). With barely any curvature, it traps nearly the full capacity of the pocket.

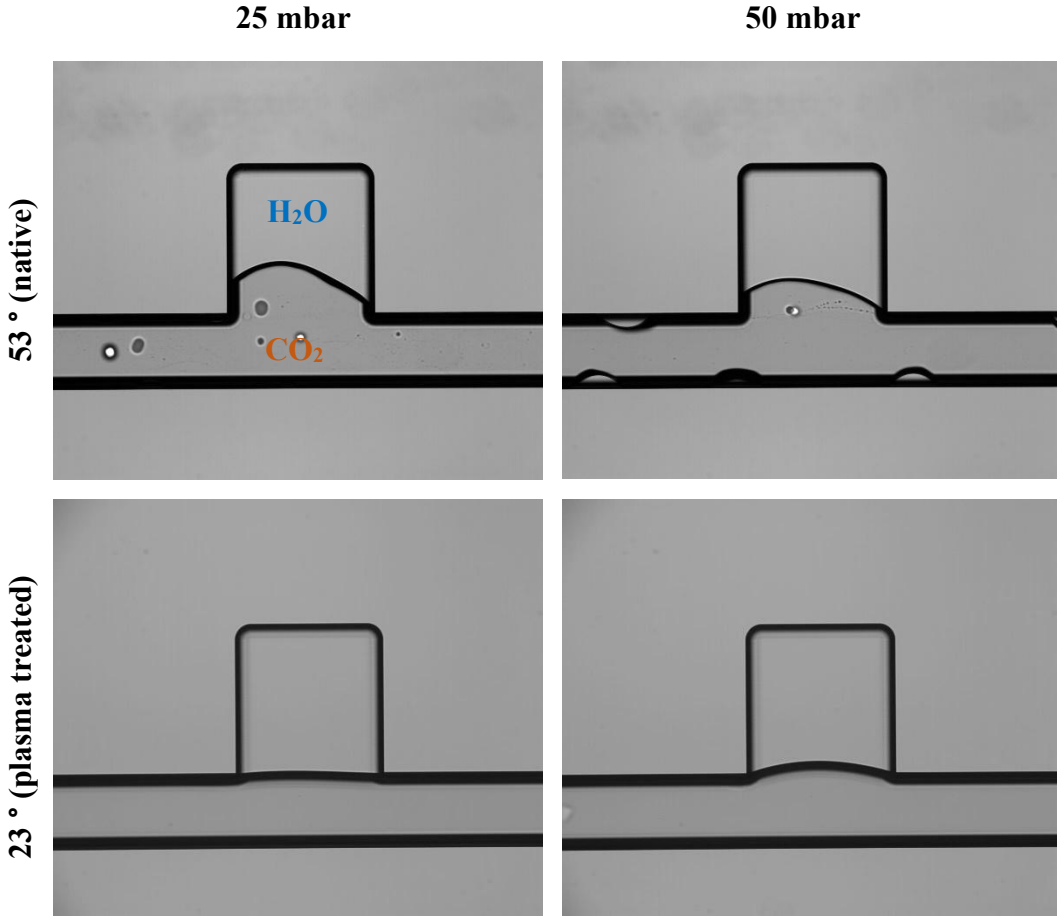

Figure 100 Variations of initial water droplet shape and size for two pressure differences and wettability conditions.

Overall, water droplets occupy a relatively larger portion of the pore, and their initial size is more stable with respect to the imposed pressure difference compared to gas bubbles during imbibition experiments (see Figure 101). This behavior is primarily due to the hydrophilic nature of glass surfaces, which have a higher affinity for water, allowing them to retain the droplet more effectively. Additionally, the higher density and viscosity of water increase its inertia, making it less susceptible to the viscous drag force exerted by the flowing gas phase. Thus, during drainage

on the 23° surface, nearly the full capacity of the trapping element is utilized for water retention, whereas during imbibition, typically only around 50% of the volume is filled with CO_2.

By looking at Figure 101, we can observe that in native moderately water-wet surfaces (53°), capillary trapping of water slightly increases with the imposed pressure difference. This behavior closely resembles CO_2 trapping during imbibition on the same native wettability surfaces. In contrast, on more hydrophilic surfaces (23°), the capillary trapping potential of water appears to decrease as the pressure difference increases. Namely, as the pressure difference increases, viscous forces begin to dominate over capillary forces, pulling a small portion of the trapped water out of the pocket into the microchannel. The contact angle is however not sufficiently low to create stable films and corner flows to drain the whole trapped volume out of the pocket.

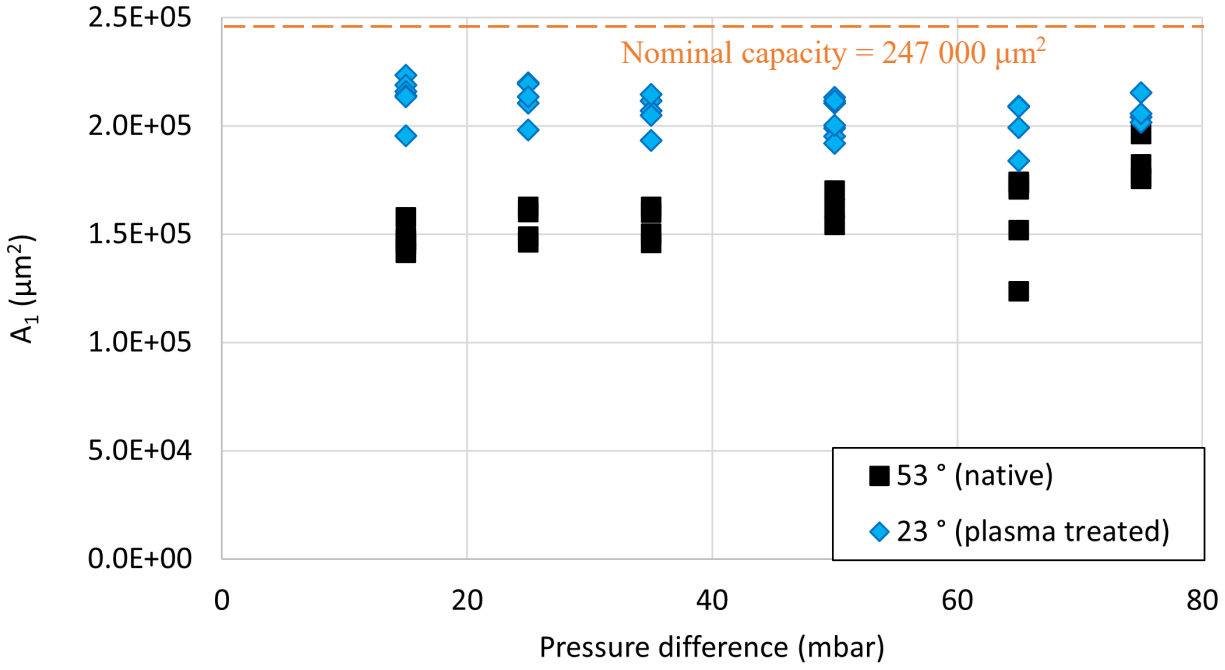

Figure 101 Initial water droplet size (A_1) scaling with the imposed pressure differences for the two wettability conditions. Nominal capacity denotes the measured area of a 500 × 500 µm trapping element.

Results on "L-pore" geometry

Displacement of water by a stream of CO_2 gas leaves behind residual water in the form of disrupted thin films and accumulated volumes along the corners of the microchannel geometry (see Figure 102). Despite comparable wettability to single pocket microfluidic devices (Micronit), the amount of trapped water in devices with L-pore geometry (Klearia) seems to be far superior, before and after the plasma treatment. By looking at the edges along the entire microchannel, it is visible that surface topology portrays far more striations, indicating a rougher surface finish. This implies that the glass surface in this microfluidic device resembles the Wenzel model (refer to Chapter 1), capable of retaining more of the wetting phase onto its surfaces. Supporting this statement is the

observation that droplet interfaces exhibit significantly less distortion when gliding over lubricating water films. In this case, the interface can smoothly adjust its shape to minimize surface energy, rather than becoming pinned and distorted by surface heterogeneities on a mostly dry substrate. While the concavity of the interface in the native moderately water-set state is comparable to the results on a single pocket device, the initial droplet of plasma altered surfaces indicates a highly curved interface. A possible explanation could be thick water films which could result in an outflow of the fluid through the corners of the microchannel, as shown in the PIV results.

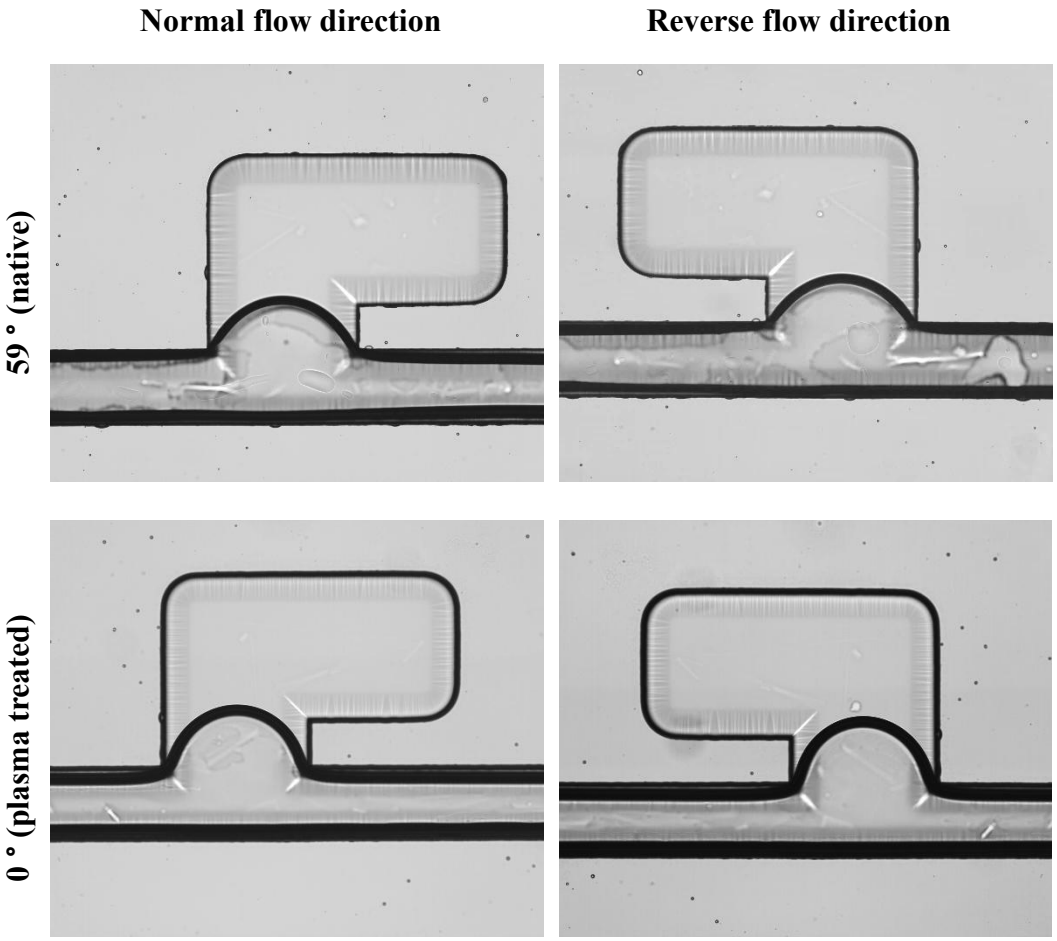

Figure 102 Variations of initial water droplet shape and size at 25 mbar of pressure difference for the two wettability conditions and the two flow directions (achieved by re-orienting the microfluidic device for consistent flow direction from left to right).

The initial droplet size, shown in Figure 103, increases with the imposed pressure difference across all cases, except for native surfaces under the normal flow direction. This deviation may be attributed to the limited number of data points, which may not fully capture the natural data dispersion statistics. The observed proportional behavior of droplet size with imposed pressure difference can be explained by the Wenzel wetting state, as discussed earlier, and is further amplified under highly hydrophilic conditions following plasma treatment. Specifically, after the initial displacement, thicker liquid films tend to form at higher displacement velocities, consistent

with Bretherton's law. In the moments following displacement, these films rapidly break and part of them retracts into the primary trapped volume to minimize surface free energy. Consequently, at higher pressure differences, thicker films contribute to the trapped water volume, leading to an increase in the initial droplet size.

Another key observation from Figure 103 are larger initial trapped volumes in the native, moderately water-wet environment compared to the highly water-wet conditions induced by plasma treatment, particularly at the lower pressure differences. However, at higher imposed pressure differences, this distinction becomes less pronounced. This behavior contrasts with the single-pocket geometry, where a larger volume was trapped on plasma-treated surfaces. However, it is important to note that the contact angles in these cases are not identical.

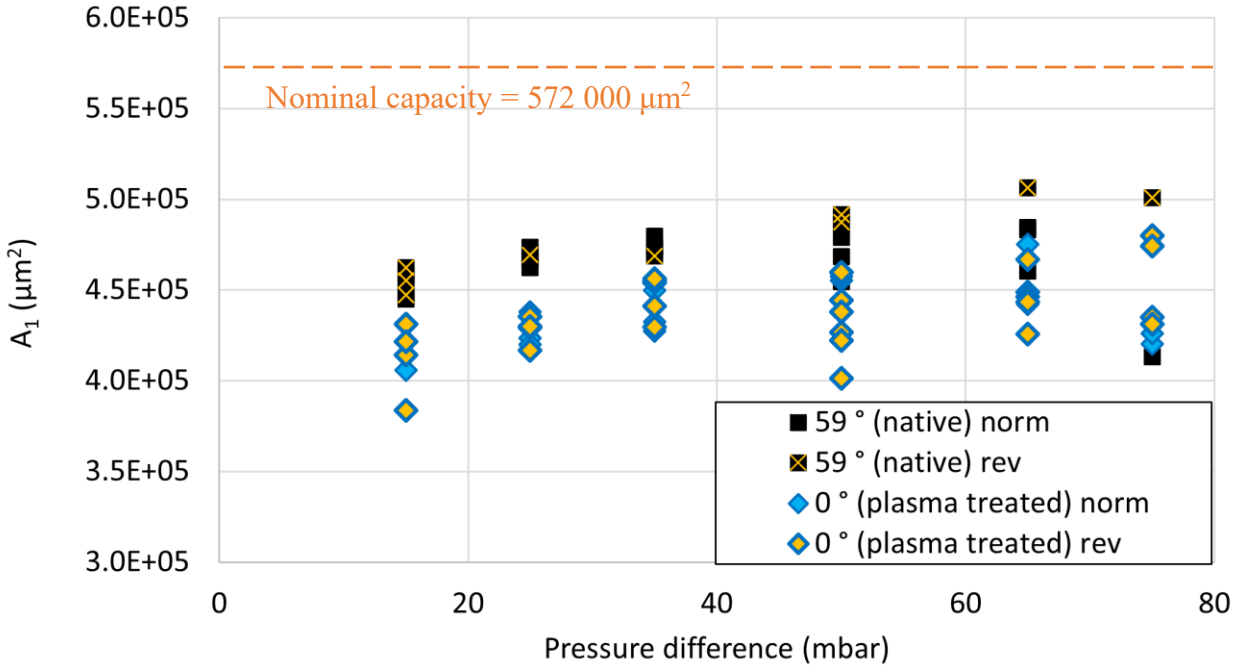

Figure 103 The initial water droplet size (A_1) scaling with the imposed pressure differences for the two wettability conditions and the two flow directions. "Norm" and "rev" stand for normal and reverse flow directions, respectively. Nominal capacity denotes the measured area of the L-pore trapping element.

Water evaporation dynamics

Results on "single pocket" geometry

During drainage, water evaporation is a mass transfer process of interest. Like in the case of imbibition, the onset of mass exchange through the interface is as soon as two fluids are in contact (in the T-valve) however, we only follow it after the initial displacement in the microchannel, leading to the entrapment of a water droplet in the pocket.

Before examining the specifics of water evaporation during drainage, it is important to note the variation in interface "thickness" (in 2D) across experiments conducted under different wettability

conditions. This difference is particularly pronounced in the single pocket geometry, as seen when comparing native and plasma-treated surfaces in Figure 104. Specifically, the interface on plasma-treated surfaces appears thicker, indicating greater curvature in the z-direction (depth) of the microchannel.

Within the scope of this thesis, direct measurements of curvature in the z-direction are not performed. Given that the microchannel depth (100 µm) is considerably smaller than its other dimensions (500 µm wide), we assume that the interface is a straight projection of the perimeter into the depth. Consequently, the absolute values of our results remain comparable to actual conditions.

Mass transfer dynamics

The characteristic events during the drainage following the initial displacement (t_0) are illustrated in Figure 104. Due to the hydrophilic nature of the glass surfaces, the passage of the CO_2 front leaves behind residual water in the form of corner volumes, thin films, and small droplets (see orange arrow markings at t_0), with their distribution depending on the specific contact angle. While at 53° the water volumes will tend to stay in place, at 23° those volumes will be advected by the stream of flowing gas (CO_2), resulting in the refilling events. These refilling events contribute to the growth of the main droplet within the trapping element, as observed at t_1.

While significant water volumes remain in the underlying microchannel, the movement of the main water droplet interface is slower on 53° surfaces. This is because the flowing CO_2 becomes presaturated with water vapor due to upstream evaporation from these residual volumes, which reduces its capacity to further evaporate the main droplet. On the contrary, the interface movement on 23° surfaces seems to accelerate and decelerate with no particular patterns. Hence, corner inflow and outflow from the main trapping element are assumed to be the drivers of these changes.

Once all residual water has evaporated (time t_1 at 53° and t_2 at 23°), the interface movement accelerates as dry CO_2 directly contacts the main droplet. While the interface is symmetrical with respect to the central pocket axis throughout evaporation at 23°, at 53°, it starts off-centered to one side (t_0) and then shifts toward the opposite sidewall of the pocket as visible at t_2. With the interface reaching the end of the pocket, the main water droplet splits into two smaller droplets (see time t_3). At 53°, the asymmetry of the interface results in two unequally sized droplets, whose complete evaporation times are proportional to their respective sizes. In contrast, at 23°, the droplets are equal in size and evaporate simultaneously.

53 ° (native)
23 ° (plasma treated)
t0
t0
t1 = t0 +19x30s (dry period)
t1 = t0 +1x30s (refilling)
t2 = t0 +43x30s (tilting)
t2 = t0 +49x30s (dry period)

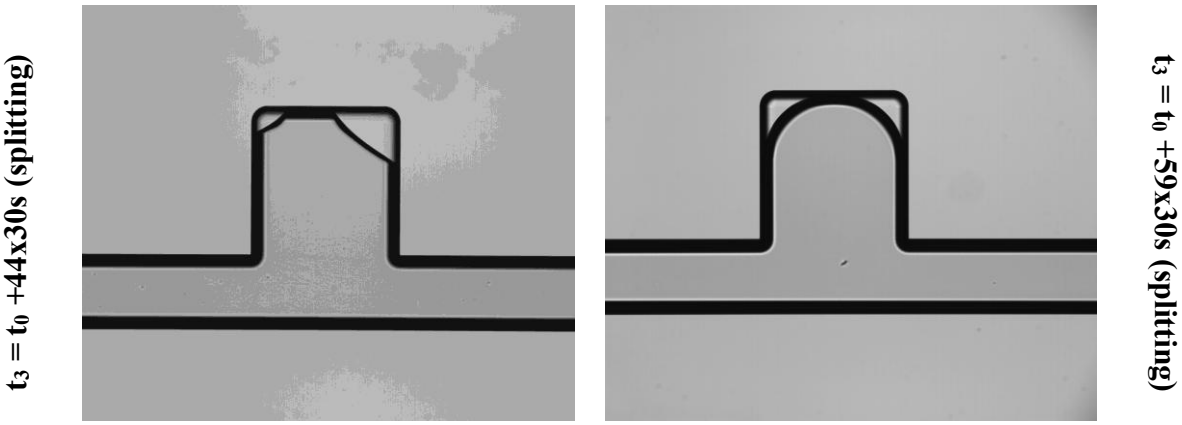

Figure 104 Water evaporation evolution during drainage under 25 mbar. The central axis of the pocket is shown with the dashed lines. Locations marked by the orange arrows point to the residual water volumes (droplets) outside the main trapping element.

From the images (Figure 104), data were extracted to characterize the evaporation behavior and patterns using four key parameters. A general description of the process is provided based on the results shown in Figure 105, which includes representative examples for both wettability conditions. The overall evaporation behavior during drainage can be categorized into two distinct phases: a "wet" period and a "dry" period. The wet period begins immediately after displacement, during which considerable volumes of water persist within the microchannels and tubing for both wettability conditions.

At 53°, average evaporation rates (see Figure 105d) remain low as the CO_2 stream is already presaturated with water vapor, limiting its capacity to evaporate the main droplet. Consequently, the main droplet experiences only a minor reduction in size (Figure 105b). The perimeter (see Figure 105a) stays stable as the evaporation is characterized predominantly by the translatory movement of the interface. Overall, the observed trends across all four parameters indicate smooth and continuous behavior, with no abrupt transitions. At this wettability condition, the water remains immobilized, resulting in neither inflow nor outflow from the primary trapping element. Consequently, the evaporation behavior is governed solely by the mass transfer process.

At 23°, the presence of significant mobile water volumes along the microchannel and tubing leads to considerable variability in evaporation patterns, resulting in unpredictable behavior characterized by multiple trends and strong nonlinearity. Several co-occurring mechanisms are proposed to influence the evolution of the main droplet during this period. The most prominent of these is droplet inflow from the underlying channel, which results in refilling events. These distinct events are observable as increases in droplet volume (Figure 105b) and negative evaporation rates (Figure 105d), marked by blue arrows in the respective graphs. Additionally, less abrupt increases of droplet area could be attributed to water inflow into the trapping element (pocket) through films and corners.

In the continuation of the wet evaporation process at 23°, a slowdown or stalling of droplet area evolution is also frequently observed (Figure 105b), making this phase last a significant portion of the total evaporation time. Slowdown and stalling could be a result of gradual water film inflow, droplet swelling due to CO_2 dissolution (not explicitly observed), or even interface pinning in the underlying microchannel. However, unlike the distinct refilling events with droplets, droplet swelling and water exchange through films and corners are difficult to detect due to the absence of flow indicators. Additionally, pinning in the underlying microchannel often occurs outside the observation camera's field of view, however, it has been noticed on other geometries.

The evaporation into the humid CO_2 and possibly the outflow through films and corner volumes are assumed to be causing a reduction in droplet size. As a result of competition between various mechanisms, droplet area dynamics during the wet period is characterized by multiple evaporation trends.

The displacement and/or evaporation of all the retained water volumes upstream from the trapping element marks the onset of the dry period (see dashed lines in all graphs). During the dry period, the perimeter of the main water droplet stays nearly constant (Figure 105a) while the area evolution in time follows an essentially linear trend (Figure 105b). The linear behavior lasts until the interface reaches the end of the pocket, causing the droplet to split into two parts. The asymmetric tilting on native (53°) surfaces before splitting (see time t_2 in Figure 104) causes a slight increase in perimeter. During the dry period, the evaporation rates are elevated and stay relatively constant until the splitting (see Figure 105d after the respective dashed lines until the orange arrow markings).

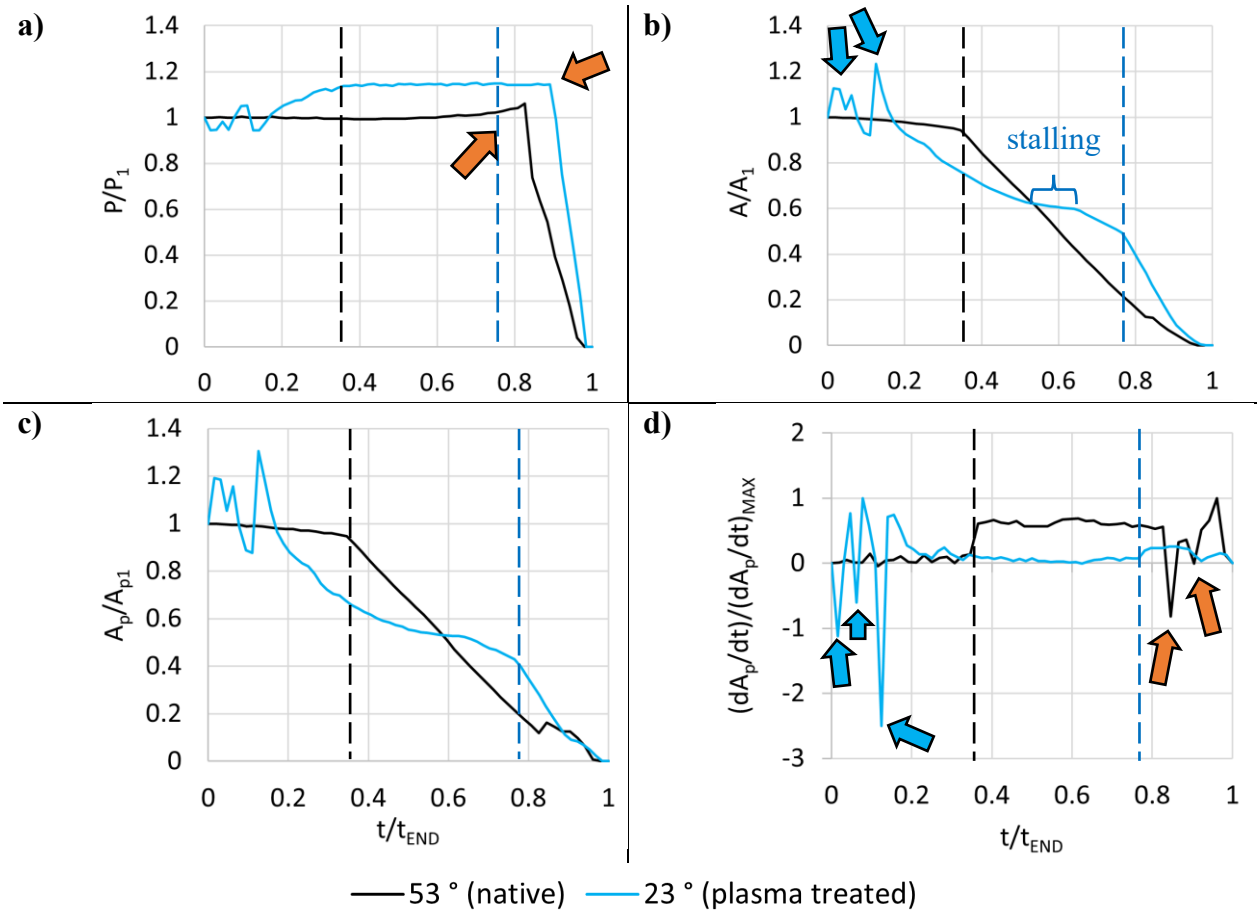

Figure 105 The patterns of the droplet evaporation process, given for 25 mbar of pressure difference at two wettability conditions. The process is tracked through the normalized perimeter – P/P_1 (a), normalized area - A/A_1 (b), normalized perimeter area – A_p/A_{p1} (c) and normalized interval dissolution rate - $(dA_p/dt) / (dA_p/dt)_{MAX}$ (d). Dashed lines indicate the transition between the fast and slow evaporation periods for each respective wettability condition. Orange arrows in graphs a) and d) mark the moment when the liquid interface contacts the far pocket wall, resulting in the division of the water body into two segments. Blue arrows in graphs b) and d) highlight abrupt refilling events.

Mass transfer rates

In Figure 106, we present the average evaporation rates as a function of the imposed pressure difference during the wet period, dry period, and across the entire experimental duration. The wet period values are calculated from the time following the last refilling event, while the dry period includes only the linear phase leading up to droplet splitting. The overall values account for both exclusions, specifically, incorporating the time interval from the last refilling event up to the moment of droplet splitting.

During the wet period (Figure 106a), evaporation rates on 53° surfaces remain relatively constant and low, on the order of 10^{-2} µm/s. In contrast, on 23° surfaces, evaporation rates scale with applied pressure, reaching values on the order of 1 µm/s, highlighting a clear distinction in mass transfer

behavior between the two wettability conditions. Notably, data dispersion increases with applied pressure difference, particularly on the 23° surface.

During the dry period (Figure 106b), mass transfer rates on 53° surfaces exhibit a linear relationship with the imposed pressure difference. However, on 23° surfaces, mass transfer rates do not follow a straightforward linear trend with pressure, having no clear physical explanation. The average mass transfer rates during this period are on the order of 10^{-1} μm/s for both surfaces, indicating that wettability effects are not pronounced. In contrast to the wet period, data dispersion decreases with increasing pressure difference, particularly on 23° surfaces, highlighting the importance of advection for this period.

When comparing these two periods, mass transfer rates on 53° surfaces tend to be higher during the dry period, whereas the wet period favors higher rates on 23° surfaces. This difference can be attributed to proximity to the underlying microchannel through distinct mechanisms. On 53° surfaces, the dry period begins with only a minor reduction in initial droplet size, maintaining close contact with the primary advection zones, thereby sustaining higher mass transfer rates. Conversely, on 23° surfaces, the same proximity of the interface to the underlying microchannel may facilitate water outflow through films and corners, contributing to elevated average rates during the wet period compared to the subsequent dry period.

Finally, mass transfer rates over the entire experimental duration (Figure 106c) reflect a combined influence of both periods, weighted by their respective durations and magnitudes. Due to its longer duration, the wet period predominantly influences the overall values on 23° surfaces, whereas the dry period has a greater impact on 53° surfaces. At lower pressure differences, mass transfer rates are nearly identical for both wettability conditions, but they diverge as the pressure difference increases, with 23° surfaces again exhibiting a steeper rise. The values of normalized and lumped mass transfer coefficient (the latter is not shown here) remain predominantly within the order of 10^{-1} μm/s and 10^{2} $\mu m^2/s$, respectively, with resembling trends over the pressure difference range.

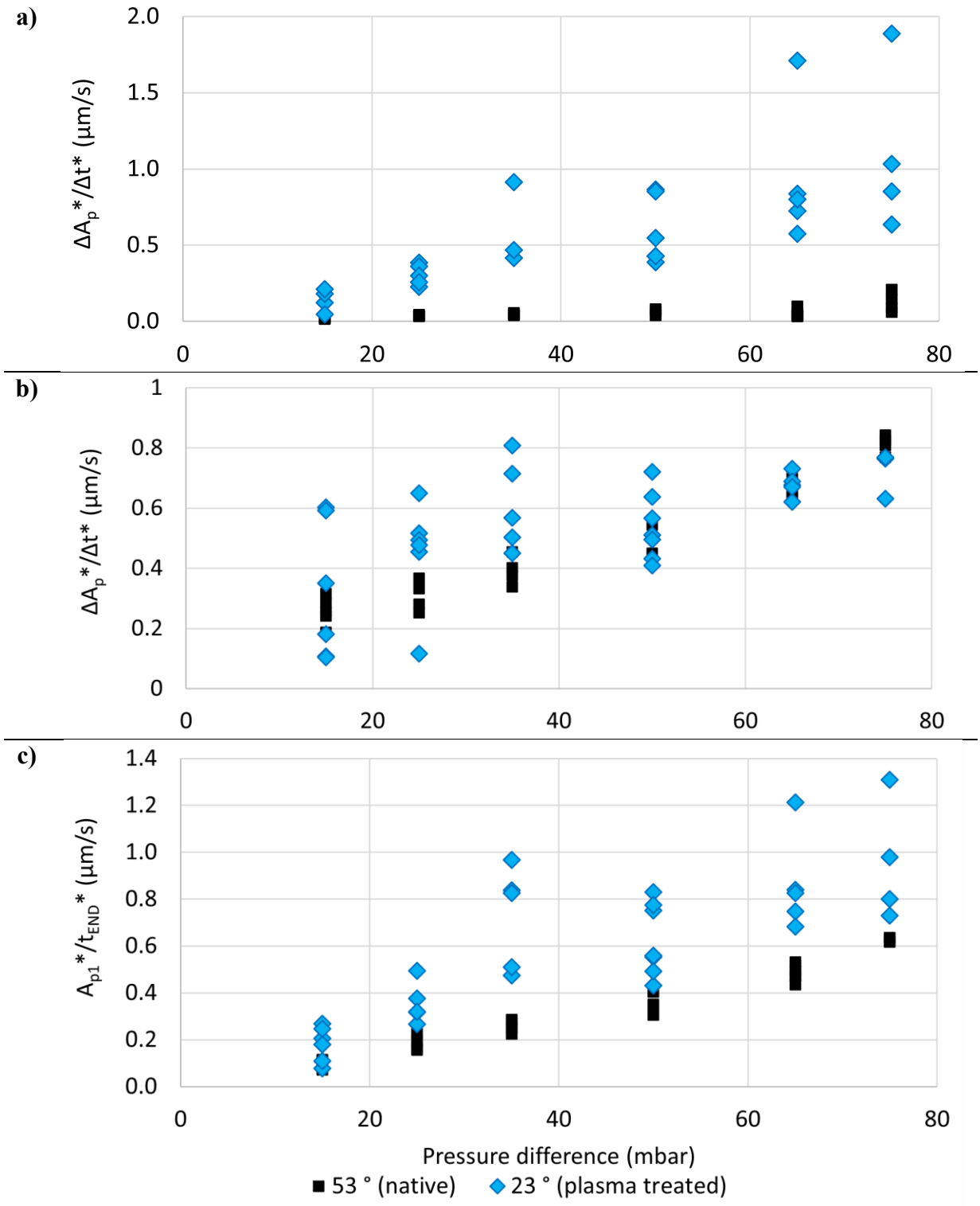

*Figure 106 The average perimeter-normalized evaporation rates during the wet period (a), dry period (b and overall (c) * taken without refilling events and before splitting. The results are presented as a function of an imposed pressure difference for two wettability conditions.*

By evaluating four key parameters extracted through image processing, characteristic evaporation patterns were identified, consistently exhibiting two distinct temporal regimes: a wet period followed by a dry period. During the wet period, significant volumes of water remain along the microchannel and tubing, presaturating the CO_2 stream with water vapor and thereby limiting the evaporation of the main water droplet. The transition to the dry period is marked by the depletion of all residual water volumes except the main droplet, after which evaporation proceeds under drier gas conditions.

Wettability predominantly governs the behavior of the water phase in the main trapping element during the initial wet period. Specifically, on more hydrophilic surfaces (23°), the water remains mobile and is thus more strongly influenced by pressure-driven advective forces. This results in increased water movement (into and) out of the trapping element (via corner flow), in addition to evaporation. Consequently, surfaces with a 23° contact angle exhibit higher mass transfer rates than those with a 53°. This behavior is also reflected in the overall mass transfer values. Additionally, both 23° and 53° surfaces show a positive scaling of mass transfer rates with pressure. At 23°, this scaling is primarily attributed to enhanced fluid advection during the wet phase, as previously discussed. In contrast, at 53°, advection maintains a steep concentration gradient in the gas phase by rapidly supplying dry CO_2 during the dry phase.

Furthermore, the agreement in behavior and trends between the normalized and lumped mass transfer coefficient formulations suggests that, beyond the enhancement of interfacial area, wettability influences mass transfer through additional mechanisms, potentially involving modifications in interface morphology or contact line dynamics.

To relate this observation to capillary trapping, at higher hydrophilicity (23°), the system exhibits larger initial droplet volumes along with elevated evaporation rates. As a result, at the scale of a single pore, the overall dissolution times are comparable to those observed under less hydrophilic conditions (53°), where smaller trapped volumes evaporate at a slower rate. While water is generally not the targeted storage phase, if retention of the aqueous phase were of interest, such behavior would suggest enhanced storage security via a combination of capillary trapping and increased mass transfer efficiency under hydrophilic conditions.

Finally, comparison between the magnitudes of water evaporation and CO_2 dissolution reveals that water evaporates approximately one order of magnitude more slowly than CO_2 dissolves into the aqueous phase. This expected observation stems from the inherent differences in intermolecular bonding, with water's strong hydrogen bonding resulting in a lower vapor pressure and consequently slower phase transfer. This physical characteristic is mirrored in its relatively high capacity to dissolve CO_2, reinforcing the aqueous phase as a favorable medium for solubility trapping in carbon storage applications. Moreover, while water evaporation rates increase with the applied pressure difference, CO_2 dissolution appears to remain largely unaffected.

Results on "L-pore" geometry

During drainage in the L-pore geometry, we observed a rapid decrease in droplet area over time. Consistent with the PIV results, the observations in Figure 107 show that water is drained from the trapping element primarily through film and corner flow (see arrow markings). On average, water drainage up to residual films takes 15s on native (59°) surfaces and 6s on plasma-treated (0°) surfaces.

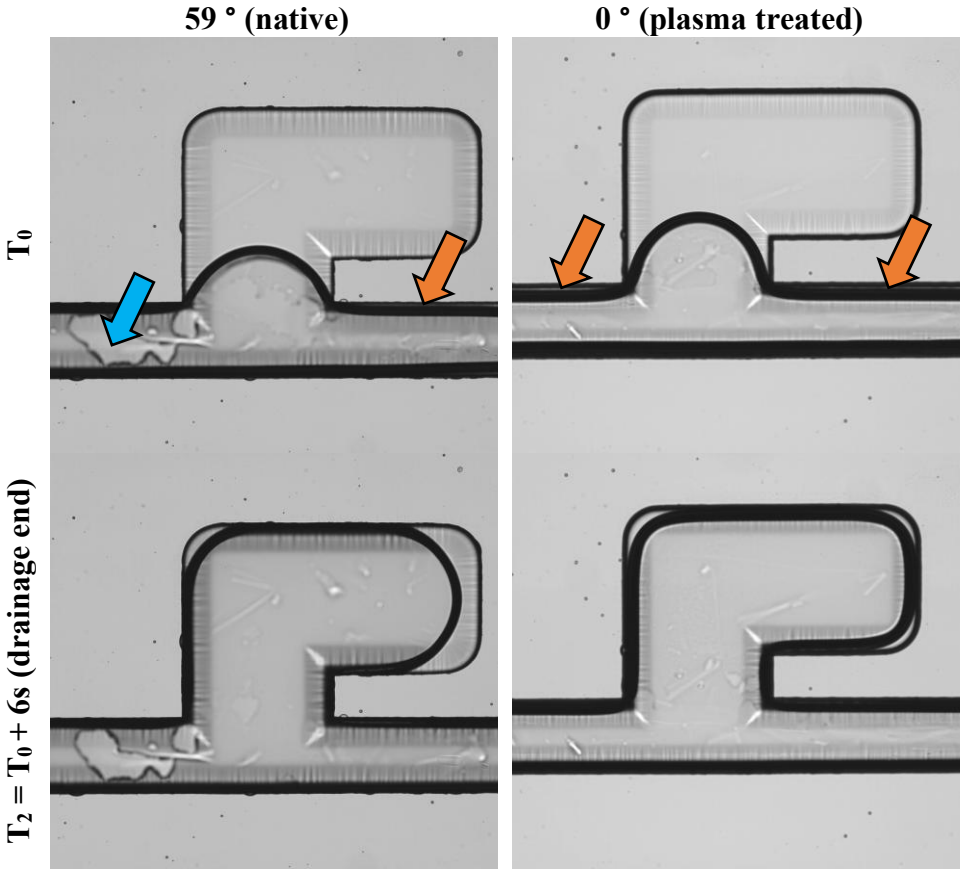

Figure 107 Water evaporation evolution during drainage under 25 mbar. Blue arrow marks the existence of films, while orange arrows mark the existence of corner volumes.

These observations are further quantified through overall water drainage rates shown in Figure 108. Across all experimental conditions, nearly all measured rates exceed 10^4 and even 10^5 $\mu m^2/s$. Interfacial mass transfer is thus highly unlikely to be the responsible mechanism as values obtained on single pocket geometry contrast these results by at least two orders of magnitude. The results below 10^4 $\mu m^2/s$, indicated with the orange arrow, could potentially have superimposed film and corner flow drainage (gradual displacement) with still influential fluid-fluid interfacial mass transfer. While the flow direction does not make a difference on 0° surfaces, 59° surfaces tend to exhibit higher drainage rates in the normal flow direction, likely due to the alignment of the trapping element geometry with the main flow. Water drainage rates in the L-pore initially start at comparable values across wettability conditions but diverge at higher pressure differences, favoring

increased drainage rates at 0° wettability. This behavior is similar to wettability-influenced evaporation rate trends observed on the single pocket geometry shown just earlier (Figure 106c).

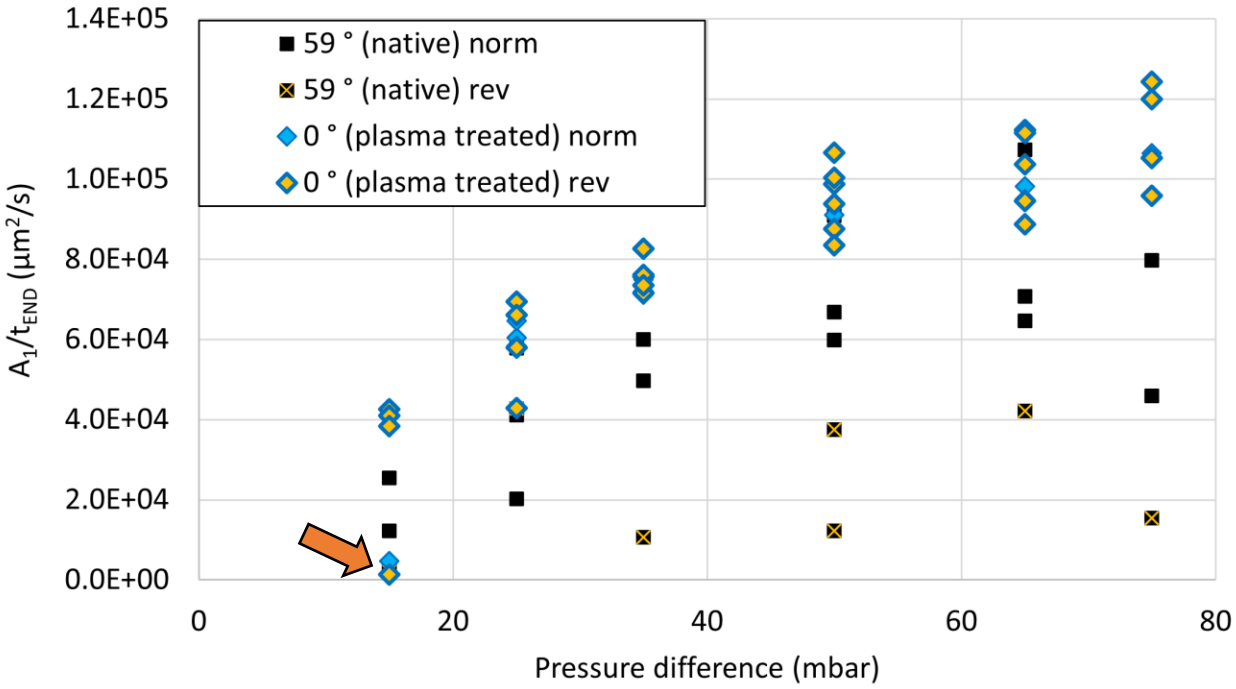

Figure 108 Overall water drainage rates (A_1/t_{END}) presented as a function of pressure for two wettability conditions. A few selected points with the lowest observed rates are marked with an orange arrow.

Consequently, the experimental data do not provide insight into interfacial mass transfer on L-pore geometry during the drainage but rather indicate two mechanisms of mass transfer - dominant physical advection through water films and corner flows, and less dominant evaporation. With the current setup we are unable to experimentally quantify the contribution of each mechanism. Despite this, the effect of wettability is still observable, favoring drainage rates on superhydrophilic surfaces. While the wettability itself explains the behavior on 0°surfaces, we hypothesize that the behavior on 59° surfaces can be attributed to surface roughness creating small channels within the geometry draining (advecting) the fluid from the main trapping element and increasing the interfacial area for mass transfer. Thus, the presence of significant water films and corner volumes is expected to enhance overall mass transfer by evaporation through the creation of an extensive interfacial area.

The absence of direct measurements of evaporation limits our ability to compare with dissolution mass transfer rates within the L-pore geometry and further hinders a comprehensive comparison of mass transfer efficiency between the two geometries. We hypothesize that the observations made at the single-pore scale can be extrapolated, suggesting that evaporation would proceed more slowly than dissolution. Furthermore, if the same wettability conditions were compared between the two geometries, evaporation would likely be higher in the single-pocket configuration than in

the L-pore geometry. This is primarily due to the simpler geometry of the single pocket, which allows for better exposure of the interface to the flowing CO_2 stream, resulting in locally higher Reynolds numbers.

IV. Conclusion

The main objective of this chapter was to evaluate the impact of wettability on capillary trapping and interfacial mass transfer within the CCUS framework using a microfluidic approach. The experiments were performed on two microfluidic geometries using CO_2 and water as proxies for injection and reservoir fluid. In each geometry, we performed drainage and imbibition. During the drainage, the goal was to trap water and study the evaporation as representative mass transfer while in imbibition we aimed to immobilize CO_2 and evaluate dissolution patterns. Results from each geometry are evaluated on two distinct wettability conditions over the range of imposed pressure differences simulating different flow conditions.

Prior to the main experiments, we aimed to characterize and constrain the range of flow properties in our geometry designs for single- and two-phase flow using particle experiments. Analysis of flow patterns in the primary geometrical features during single-phase water flow revealed that the onset of the first recirculation patterns occurs around 65 mbar, marking a deviation from the creeping flow regime. In this pressure difference range, the Reynolds number remained below 20 while the corresponding capillary number during two-phase flow was approximately 10^{-3}, both of which could be encountered during typical CCUS projects. During drainage, we observed advective motion with a trapped water droplet, driven by momentum transfer at the interface from the underlying gas flow. Additionally, on plasma-treated surfaces, drainage was characterized by a strong presence and flow of film and corner volumes. Both observations turned out to be crucial for the interpretation of mass transfer behavior.

With the necessary flow testing completed, we now shift to the main research focus – capillary trapping and mass transfer. By providing an overview of the experimental conditions in Table 14 and Table 15, we aim to achieve a clearer perspective on the results and their implications.

1. Capillary trapping

Table 14 The overview of the experimental conditions used to assess capillary trapping. The abbreviation dp stands for pressure difference.

CAPILLARY TRAPPING	**CO_2 trapping**	**Water trapping**
Single pocket	53° vs 23° @ dp 15 – 75 mbar	53° vs 23° @ dp 15 – 75 mbar
L-pore	53° vs 23° & flow direction @ dp 15 – 75 mbar	53° vs 23° & flow direction @ dp 15 – 75 mbar

a) CO_2 trapping

During imbibition, the initial CO_2 bubble exhibits a wide range of shapes influenced by both pore geometry and wettability. At lower contact angles, the bubble interface remains more rounded and curved, predominantly guided by interfacial tension rather than the geometry of the trapping element. In single pocket geometry, the bubble consistently remains in contact with the solid

surface, whereas in L-pore geometry under superhydrophilic conditions (0°), the bubble does not come into contact with the glass surfaces.

Wettability does not appear to significantly affect the initial bubble size in single pocket geometry. Likewise, the initial bubble size on L-pore geometry does not show dependency on wettability or flow anisotropy. However, in L-pore geometry, CO_2 bubble displacement is consistently observed under superhydrophilic conditions (0°) when the imposed pressure difference exceeds 35 mbar in the normal flow direction. This finding suggests that the combined effect of flow anisotropy and wettability can influence the capillary trapping potential of CO_2.

b) Water trapping

Due to the hydrophilic nature of glass surfaces, significant water volumes remain trapped following the initial displacement during drainage. These trapped volumes are present as water films, droplets, and corner volumes along the microchannels and tubes, in addition to the principal volume within the trapping element.

In single pocket geometry, the interface of the principal water droplet on 53° surfaces is asymmetric with respect to the central pocket axis. On 23° surfaces, it is pinned at the corners and aligns flat with the microchannel edges instead of being curved. The interface of the principal water droplet in L-pore geometry seems to be rounder regardless of the wettability, only showing a difference in the curvature (higher curvature at lower contact angle).

When assessing the amount of trapped water in single pocket geometry following initial displacement, significantly larger volumes are retained at 23° compared to 53°. Surprisingly, in L-pore geometry, comparable moderately water-wet surfaces (59°) retain on average more water than superhydrophilic surfaces (0°). While the exact influence of wettability remains unclear, its effect is evident, suggesting that an additional factor may contribute to the observed trapping behavior. Furthermore, no significant differences in water trapping were observed in L-pore geometry when altering flow direction.

c) Comparative analysis and conclusion

Considering both geometries and both fluids, wettability effects are most pronounced in capillary trapping of water during drainage, while they appear negligible for CO_2 trapping. This discrepancy likely arises because all tested surfaces were hydrophilic, ensuring consistent contact with water, whereas CO_2, as a non-wetting phase, remains largely unaffected by variations in solid wettability.

When comparing trapped volumes of different fluids within the same geometry, the single pocket geometry retains more water than CO_2, whereas in the L-pore geometry, no significant difference is observed between the two fluids. While hydrophilic media are expected to favor greater water retention, the increased complexity of porous media appears to mitigate this effect, resulting in comparable trapping behavior for both fluids in L-pore geometry.

Thus, compared to other studies, the novelty of our approach lies in using a single-pore microfluidic platform with engineered simple pockets and L-shaped pore geometries to uniquely isolate wettability as the controlled variable. By testing both water and CO_2 in the same controlled pore, we show for the first time that wettability strongly governs water retention but not CO_2 entrapment - a finding made possible by eliminating geometry heterogeneity, unlike in most prior multi-pore experiments (Massimiani *et al*., 2023).

2. Mass transfer

Table 15 The overview of the experimental conditions used to assess mass transfer. The abbreviation dp stands for pressure difference.

MASS TRANSFER	**CO_2 dissolution**	**Water evaporation**
Single pocket	59° vs 0° @ dp 15 – 75 mbar	59° vs 0° @ dp 15 – 75 mbar
L-pore	59° vs 0° & flow direction @ dp 15 – 75 mbar	59° vs 0° & flow direction @ dp 15 – 75 mbar

a) CO_2 dissolution

Single pocket geometry

Dissolution patterns in single pocket geometry exhibit two distinct phases: an initial fast dissolution period dominated by advection and a subsequent slower phase controlled by diffusion. While wettability does not significantly influence the fast dissolution phase, both the slow phase and the overall mass transfer coefficient values show a clear trend, with higher dissolution rates observed at a lower contact angle (23°). The average mass transfer rates are on the order of a few µm/s, aligning well with findings from previous studies. A comparison of mass transfer formulations with and without normalization to the interfacial area (perimeter) reveals that wettability influences dissolution not only by increasing the interfacial area but also by modifying interfacial curvature, which alters capillary pressure.

Furthermore, a static experiment demonstrated that CO_2 dissolution in such conditions would take months. This underscores the importance of ensuring CO_2 containment in the initial period through physical trapping mechanisms, such as structural and capillary trapping, before chemical mechanisms like dissolution and mineralization can ensure long-term storage security.

L-pore geometry

On L-pore geometry, we experience many challenges due to bubble displacement which occurred initially or later on during the experiments. This highlights the potential instability of capillary trapping but also limits the statistical robustness of our mass transfer data. Additionally, bubble growth was observed on native wettability surfaces when reversing flow direction, suggesting an exsolution process rather than dissolution.

Despite the scarcity of experimental data and the significant impact of wettability, trapping element geometry, and its anisotropy on dissolution patterns, the characteristic fast and slow dissolution

periods remain distinguishable. Similar to single pocket geometry, the initial fast dissolution phase shows no major dependence on wettability, whereas the slow phase and overall mass transfer rates exhibit a clear trend favoring faster dissolution at lower contact angles (0°). On moderately hydrophilic surfaces (59°), overall dissolution rates are on the order of 10^{-1} μm/s, while on superhydrophilic surfaces (0°), rates range between 10^{0} and 10^{1} μm/s. Flow direction does not appear to substantially affect overall mass transfer rates.

b) Water evaporation

Single pocket geometry

Water evaporation during drainage follows a two-phase behavior, consisting of a wet period and a dry period. During the wet period, significant water volumes in the form of films, small droplets, and corner volumes remain on microchannel surfaces. During the dry period, only the principal droplet volume within the trapping element persists. Thus, wettability conditions largely impact evaporation patterns by altering the type and amount of volumes during the wet period. On 53° surfaces, the main droplet size follows a linear trend in time, one in each period. The steeper slope observed during the dry period indicates that evaporation rates are higher when the CO_2 stream is unsaturated with water vapor. In contrast to essentially immobilized volumes on 53° surfaces, water volumes on 23° surfaces are moving, flowing in and out of the trapping element at various unpredictable rates, creating multiple non-linear trends during the wet period.

Hence, experimental data of mass transfer rates on 53° surfaces show less dispersion, with a clear rising trend in overall mass transfer with applied pressure difference. At lower applied pressure differences, both wettability conditions exhibit similar overall evaporation rates. However, as pressure differences increase, evaporation rates diverge, favoring the lower contact angle surface (23°). Overall evaporation rates are on the order of 10^{-1} μm/s, which is an order of magnitude lower than CO_2 dissolution rates.

Experimental studies on water evaporation into CO_2 at the pore scale are extremely scarce, particularly using microfluidic platforms. Some numerical studies have only touched upon this topic incidentally while investigating other phenomena (e.g., capillary-driven flow or salt precipitation) without focusing specifically on evaporation kinetics. As a result, experimental validation remains limited and is critically needed to calibrate and improve pore-scale models. Our study thus addresses this gap by providing direct experimental observations of water evaporation into CO_2, identifying two distinct regimes ("wet" and "dry" periods) that describe the kinetics of evaporation. Additionally, our measurements report overall evaporation rates on the order of 10^{-1} μm/s, offering rare experimental benchmarks for future modeling efforts in the context of geological CO_2 storage.

L-pore geometry

Evaporation behavior in the L-pore geometry is more difficult to analyze as there is gradual but rapid water drainage from the trapping element through film and corner flow. The near-complete

drainage of the principal droplet from the trapping element occurs within approximately 15 seconds on 59° surfaces and just 6 seconds on 0° surfaces, corresponding to drainage rates as high as 10^5 $\mu m^2/s$. Thus, drainage is a prevalent process compared to interfacial mass transfer. These results highlight a fundamental difference in the nature of a process occurring during drainage. Hence, direct comparison between evaporation rates of the two geometries, as well as the comparison between dissolution and evaporation rates on this geometry is unfeasible.

Concluding remarks and implications

Overall, this research reveals that wettability, pore geometry, and applied pressure differences collectively influence the complexity of mass transfer behavior. Despite variations in mechanisms, a two-period behavior is consistently observed, regardless of the mass transfer direction. Wettability becomes a more dominant factor typically in only one period, albeit for different reasons:

- During imbibition and CO_2 dissolution, wettability influences mass transfer primarily in the second period, when advection weakens, allowing its effects to become more pronounced.
- During drainage and water evaporation, wettability plays a more critical role in the initial wet period, where hydrophilic surfaces promote the formation and advection of water films and corner volumes. This alters droplet size evolution patterns and modifies the mechanism of evaporation.

Overall, mass transfer, whether through dissolution or evaporation, tends to be more efficient under hydrophilic conditions. This enhancement occurs through multiple mechanisms, including increased interfacial area, elevated capillary pressure due to higher interfacial curvature, and the presence of films and corner volumes, which not only expand the available interfacial area but also regulate the trapped volume through direct inflow and outflow dynamics.

The findings of this study have meaningful implications for reducing uncertainties and improving forecasting models related to CO_2 geological storage in saline aquifers. In particular, the observed influence of wettability on both capillary and solubility trapping underlines the necessity of incorporating wettability effects into predictive models, especially considering that these effects become dominant during later stages under diffusion-controlled conditions. By elucidating fundamental mass transfer mechanisms based on first principles of physics within the context of CO_2 storage, these insights can also be extended to a broad range of two-phase systems in porous media environments.

Chapter 5 - *In situ* Raman Spectroscopy for Quantitative Dissolution Analysis

Micro-Raman spectroscopy is introduced as the method of choice to complement the visual observations presented in Chapter 4**,** by enabling in situ monitoring of chemical species during interfacial mass transfer. The goal of this chapter is to develop an *in situ* method for qualitative and semi-quantitative analysis of species evolution during mass transfer, with a particular focus on tracking CO_2 dissolution in water. We begin with a brief overview of the state of the art, followed by a description of our experimental setup and acquisition procedure with optimized parameters. The main part of the chapter presents results demonstrating the feasibility of detecting both water and CO_2 species, as well as capturing the kinetics of the dissolution process. The chapter concludes with a short discussion and outlook on advancing the technique toward full quantitative analysis in future work.

I. Introduction

Raman spectroscopy is a widely used, non-destructive technique for the qualitative and (semi-) quantitative analysis of species in gaseous, liquid, and solid states. It is based on the interaction of monochromatic light with molecules, as illustrated schematically in Figure 109. When the energy of an incident photon falls between vibrational and electronic transitions, the molecule is excited to a short-lived virtual energy state. The return to a lower energy state involves the emission of a photon. In elastic (Rayleigh) scattering, there is no energy exchange, and the emitted photon retains the same energy (frequency) as the incident light. However, inelastic scattering, i.e., the Raman effect, involves an energy shift in the emitted photons. If the molecule occupies its ground state and relaxes to a higher vibrational level, the emitted photon has lower energy (Stokes scattering). Conversely, if the molecule is initially in an excited vibrational state and returns to the ground state, the emitted photon has higher energy (anti-Stokes scattering).

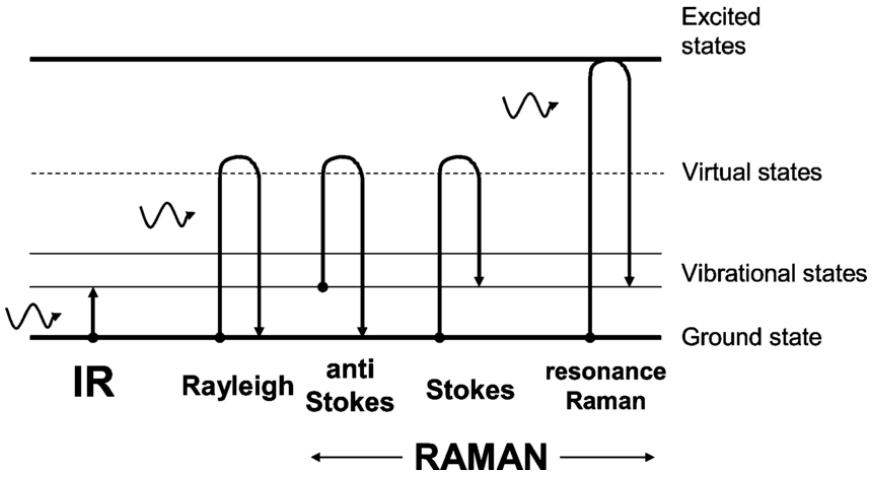

Figure 109 The scheme of infrared absorption (IR) versus elastic (Rayleigh) and inelastic Raman (Stokes/anti-Stokes) scattering of light. Taken from Ellis and Goodacre (2006).

The Raman-scattered signal is inherently weak, with only about one in every 10^7 photons undergoing Raman scattering (Neuville *et al*., 2014). In contrast, Rayleigh scattering is several orders of magnitude stronger and must be removed before detection to prevent detector saturation (Neuville *et al*., 2014). The remaining signal consists of both Stokes and anti-Stokes components (see Figure 110), each providing a molecular fingerprint with intensities proportional to concentration in mixtures, and to density in gases. Under ambient conditions, Stokes scattering is typically more intense due to the lower population of molecules in excited vibrational states, making it the preferred signal for analysis. By referencing both the incident (λ_0) and scattered (λ_S) wavelengths through the concept of wavenumber ($\Delta\nu = \lambda_0 - 1/\lambda_S$), the resulting Raman spectra are independent of the laser excitation wavelength.

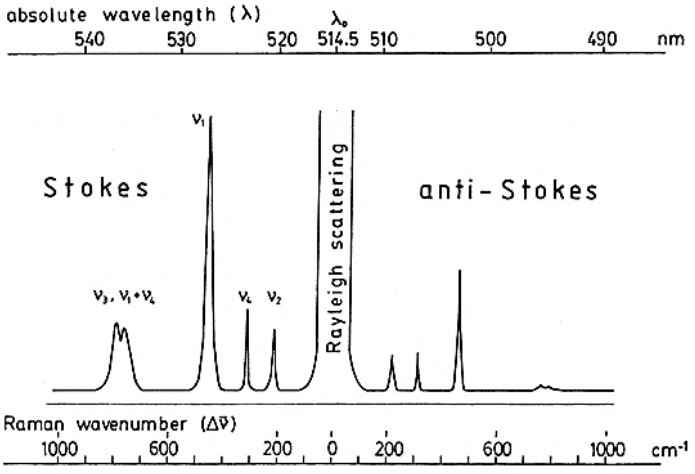

Figure 110 Raman signal from Stokes and anti-Stokes scattering, shown in perspective of wavelength and wavenumber. Modified from Van Den Kerkhof (1988).

There are six main types of molecular vibrational modes: two stretching modes - symmetric and asymmetric stretching; and four bending modes - rocking, scissoring, twisting, and wagging (Nasdala *et al.*, 2004; Tuschel, 2014). The number of vibrational modes a molecule exhibits depends on its number of atoms (N) and the linearity of the molecule itself (3N-5 for linear and 3N-6 for non-linear geometry), but it can also be predicted through bond stiffness and the masses of the atoms (Fayed, 2016). As molecular vibrations for a given molecule have a discrete energy, they serve as a molecular fingerprint, allowing for the identification of chemical species and structure.

It is important to note that not all molecules are suitable for this technique, as species of interest need to be Raman active. The activity and magnitude of the Raman effect are largely linked to the polarizability of the bonds in the molecule. Due to a rule of mutual exclusion within centrosymmetric molecules, one can study substances that are not Raman active with complementary techniques like Fourier Transform Infra-Red (FTIR) spectroscopy or Inelastic Incoherent Neutron Scattering (IINS) (Larkin, 2011; Wikipedia, 2023). Water and CO_2, for example, exhibit vibrational modes that are both Raman and infrared active. This means that their molecular vibrations can be detected using both Raman spectroscopy and infrared (IR) spectroscopy, as they involve changes in polarizability and dipole moment, respectively. One advantage of using Raman spectroscopy is that water generates a relatively weak Raman signal compared to other vibrational techniques such as FTIR. In FTIR, strong OH absorption may obscure the signals of other species. Raman spectroscopy reduces this challenge, enabling clearer detection and analysis of dissolved components like CO_2 in aqueous systems (Chrimes *et al.*, 2013).

When combined with a microscope, the micro-Raman setup goes hand in hand with the scale of investigation of microfluidics to provide close-to-real-time in-situ tracking of the processes and analysis of the matter. Several studies have already demonstrated the added value of combining the

two techniques on the topic of multiphase flow, mass transfer on fluid/fluid interfaces, and similar (Liu *et al*., 2012; Panneerselvam *et al*., 2022; Pinho and Hartman, 2017; Poonoosamy *et al*., 2020).

However, while microfluidic systems excel at controlling dynamic chemical processes, Raman detection often lags in space/time resolution. Confocal microscopes equipped with Raman spectroscopy can resolve ≈ 1 μm, but 2D and 3D mapping is slow, suitable mostly for non-evolving samples. Capturing transient events, millisecond-scale flow, and concentration gradients within microfluidic channels remains challenging due to the difficulty of combining high spectral sensitivity with rapid acquisition. Potential directions include parallelizing detection (e.g., multispot Raman) or opting for faster techniques like coherent Raman spectroscopy to enhance time resolution.

Furthermore, natural samples, particularly within microfluidic devices, often result in numerous overlapping Raman bands. Multiple overlapping Raman bands together with presence of fluorescence can make the signal of targeted species can be obscured or distorted. Thus, analysis of multiple Raman active chemical species in microfluidic devices makes spectral analysis challenging.

1. Raman signal of water and CO_2

In this section, we introduce the Raman signal of water and CO_2.

a) Water

Raman spectrum of water, as one of the most studied and widespread substances on earth, is still the subject of research (Ito *et al*., 2016; Pattenaude *et al*., 2018). Interest in its Raman features dates back to the discovery of Raman scattering (Raman and Krishnan, 1928), with early work such as that by Cross *et al*. (1937) laying the foundation. The complexity of water's Raman spectrum stems from its non-linear molecular geometry and hydrogen bonding which give rise to intra- and intermolecular vibrations. The general Raman signal of liquid water can be seen in several wavenumber regions, each associated with broad bands as shown in Figure 111. Of principal interest are the three fundamental vibrational modes: OH bending located around 1640 cm^{-1}, and symmetric and asymmetric OH stretching located in the region around 2800 – 3800 cm^{-1}. With Gaussian analysis, each band can be decomposed into several vibrational peaks, giving information about the water structure in a particular environment (Carey and Korenowski, 1998; He *et al*., 2024; Mozhdehei *et al*., 2024). The stretching band is particularly sensitive to pressure (Carey and Korenowski, 1998), temperature (Suzuki *et al*., 2012) and composition dependent (Terpstra *et al*., 1990). On the contrary, the bending band seems to be more stable and thus more suitable for the function of a standard reference (Li *et al*., 2018). However, the details about deconvolution and interpretation of water spectra are not our direct interest at this stage of the study hence, they will not be further discussed.

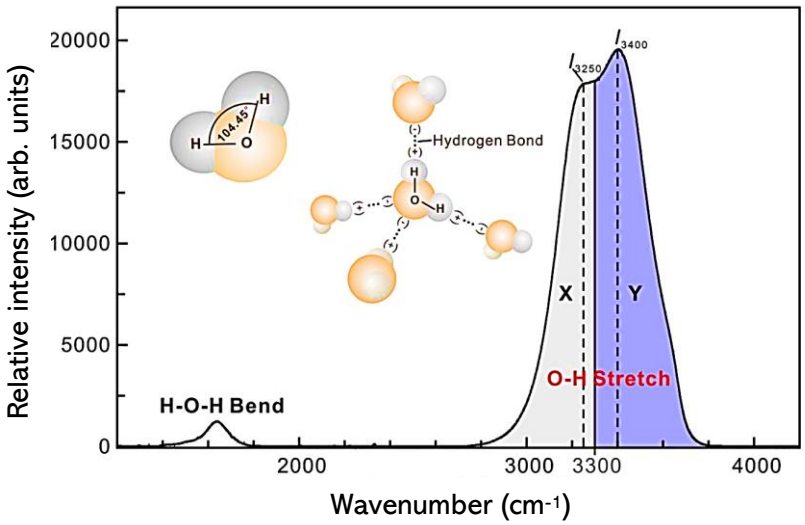

Figure 111 The Raman spectrum of water bending and stretching. Adapted from Tian et al. (2020).

b) $CO_{2\,(g)}$

Due to its linear symmetry of three atoms in the CO_2 molecule, there are four degrees of freedom, hence four vibrating modes. These are namely: symmetric in-phase stretching (ν1), symmetric bending (ν2 or also written as 2ν2) consisting of two sublevels (2ν2a and 2ν2b) with the same frequency but opposite vibration directions and asymmetric out-of-phase mode (ν3) (Herzberg, 1945). The latter two vibration modes are infrared active while the first one is only Raman active (Herzberg, 1945). Thus, the Raman "fingerprint" of CO_2 (see Figure 112) has two strong peaks located around 1285 cm^{-1} and 1388 cm^{-1} in ambient conditions (Hagiwara *et al*., 2018). These two peaks are famously known as the "Fermi diad" (Fermi, 1931). The Fermi diad is a consequence of the resonance effect, which is essentially an inharmonic mixing of the overtone of the symmetric bending mode 2ν2 with the symmetric stretching ν1. Since this 2a sublevel of the bending mode 2ν2 has nearly the same frequency as the symmetric stretching ν1, they perturb each other in an excited state. Additionally, as shown in Figure 112, a part of the characteristic CO_2 signal are also hot bands (1265 and 1409 cm^{-1}) and a peak of carbon 13 isotope (1370 cm^{-1}).

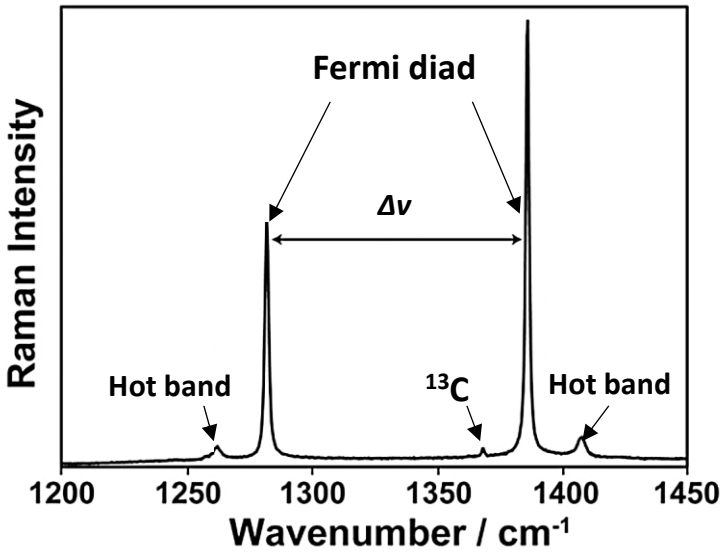

Figure 112 Raman signal of gaseous CO_2. Adapted from Hagiwara et al. (2018).

The exact position and intensity of the Fermi diad peaks are not fixed but vary with several parameters, primarily pressure (i.e., gas density), as well as temperature and fluid composition. Pressure-dependent divergence of Fermi diad peaks has been widely used in geosciences for non-destructive *in situ* pressure estimation in fluid inclusions (Burke, 2001; Frezzotti *et al*., 2012; Wang *et al*., 2011). Studies have shown that while temperature has a minor effect, the diad splitting increases with CO_2 density, often showing a linear correlation above the critical pressure (Le *et al*., 2019; Fall *et al*., 2011). The addition of other gases, particularly nitrogen and methane (see Figure 113), significantly alters the diad position and splitting (Hagiwara *et al*., 2020; Seitz *et al*., 1996).

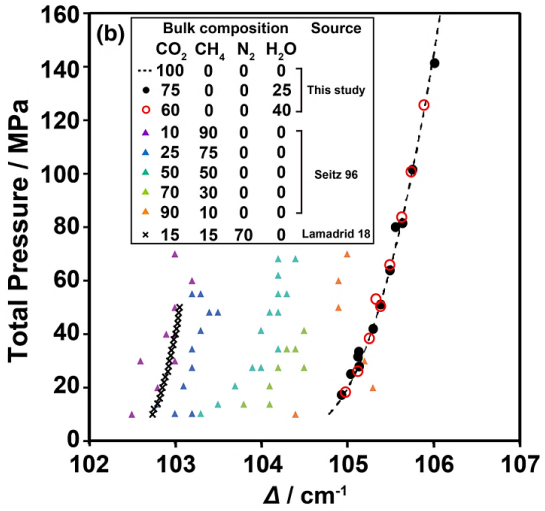

Figure 113 The Fermi diad split in relation to pressure in different gas mixtures. Taken from Hagiwara et al. (2020).

c) $CO_{2\,(aq)}$

The dissolution of CO_2 in water results in weak interaction with water molecules, therefore most CO_2 in water is present in aqueous form ($CO_{2(aq)}$) (Lam *et al*., 2015; Leung *et al*., 2007; Prasetyo and Hofer, 2018), while only a minor part gets converted into carbonic acid and further breaks down into ions (HCO_3^- and CO_3^{2-}) (Soli and Byrne, 2002). In other words, the dissolution of CO_2 in water is rather a physical process and not a chemical reaction (Hu *et al*., 2019). Hence, Raman spectra of CO_2 in pure water will predominantly come from $CO_{2\,(aq)}$ species (He *et al*., 2024). The characteristic spectrum of the $CO_{2\,(aq)}$ species is presented in Figure 114. The signal closely resembles that of gaseous CO_2, with the key difference being that the two peaks of the Fermi diad are broadened and shifted toward lower wavenumbers. The lower band is located around 1276 cm^{-1} while the upper band is visible around 1383 cm^{-1} (Caumon *et al*., 2016). Since the Raman signal intensity is proportional to the amount of species undergoing scattering, under higher pressure, where there is more dissolved CO_2 in the water, the signal becomes more intense, as shown in Figure 114.

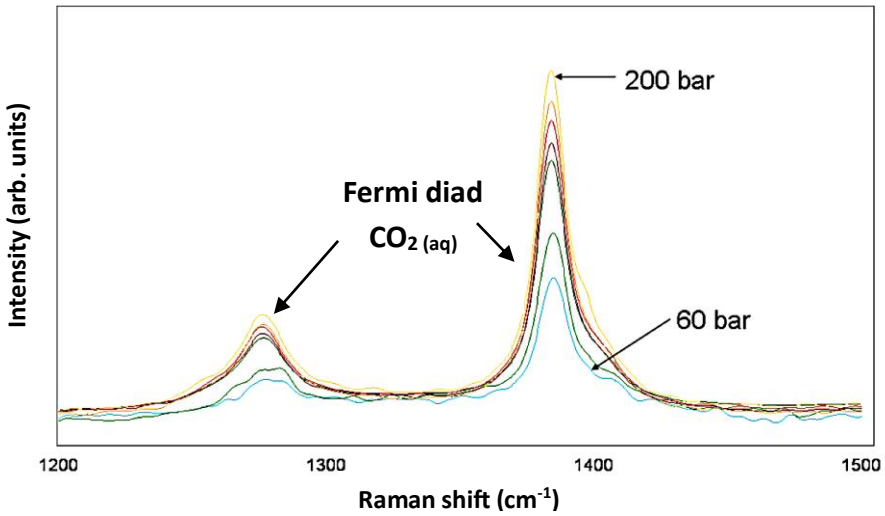

Figure 114 Raman signal of $CO_{2\,(aq)}$ species dissolved in water as a function of pressure. Adapted from (Sterpenich et al., 2017).

2. Micro-Raman investigation of CO_2 dissolution

The following paragraphs present key studies on interfacial mass transfer at the micrometer scale between water and CO_2, conducted in glass capillaries and microfluidic devices, where Raman spectroscopy was employed as a principal analytical tool.

In a work of Deleau *et al*. (2020), mass transfer coefficients (kLa) between water and CO_2 were experimentally determined with the help of Raman spectroscopy. Note: kL is the liquid mass transfer coefficient (m/s), while a is the specific surface normalized to the volume of the liquid slug. The principal component of a setup was a 297 µm diameter fused silica capillary through which co-injection of CO_2 and water was established under elevated pressures (up to 10 MPa) and moderate temperature (303 K). The glass capillary was incorporated within the Raman setup with an optical fiber in the way shown in Figure 115.

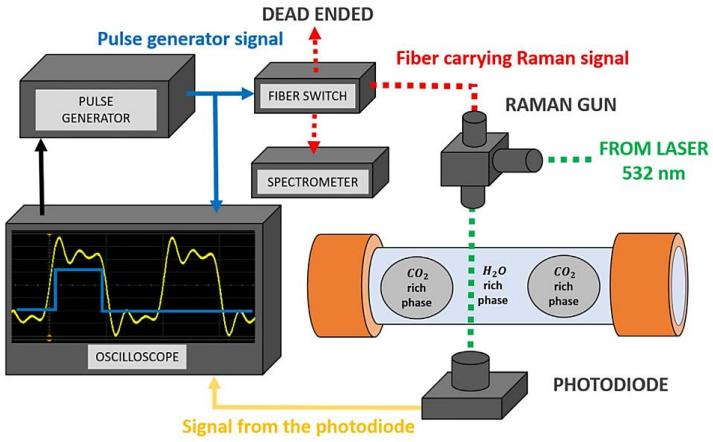

Figure 115 Glass capillary incorporated in the Raman setup. Taken from Deleau et al. (2020).

To calculate mass transfer coefficients, the peak area ratio between CO_2 and water, obtained from Raman signal analysis, was first related to the respective molar fraction ratio via the modified Henry's law. The peak area for $CO_{2\,(aq)}$ was taken in the range between 1200 and 1450 cm^{-1}, while for water, between 2700 and 3900 cm^{-1}. Molar fraction ratio together with the mixture density model served as an input for the determination of the dissolved CO_2 concentration profile. The volumetric liquid mass transfer coefficient was then computed along the length of the capillary. Experimentally derived k_La values were in the range between 10^{-3} and 10^{-2} s^{-1}.

The study of Belgodere *et al*. (2015) had a very similar scope. The goal was to determine the CO_2 diffusion coefficient in aqueous solutions under pressure (4 MPa) and room temperature via Raman spectroscopy and highlight the effect of solution salinity (up to 6.0 molNaCl/kgH_2O). A 100 µm internal diameter fused silica capillary with one closed end was placed under a micro-Raman setup and the signal of CO_2 and water was recorded. A normalized peak area ratio was calculated with the $CO_{2\,(aq)}$ band around 1383 cm^{-1} and the bending (v2) band of water (see Figure 116). The CO_2 diffusion coefficient in the aqueous solution was then determined by fitting the experimental data with a numerical solution of the second Fick's law using the least squares method. The CO_2 diffusion coefficient in pure water came out at 1.7×10^{-9} m^2/s, decreasing with salt concentration. The raw data showing the evolution of the Raman signal as a function of time is depicted in Figure 116a) and as a function of distance from the gas inlet in Figure 116b). At a fixed position, we observe the signal of $CO_{2\,(aq)}$ increasing with time as the concentration increases due to dissolution, while at the fixed point in time, the intensity falls with the distance from the interface increases.

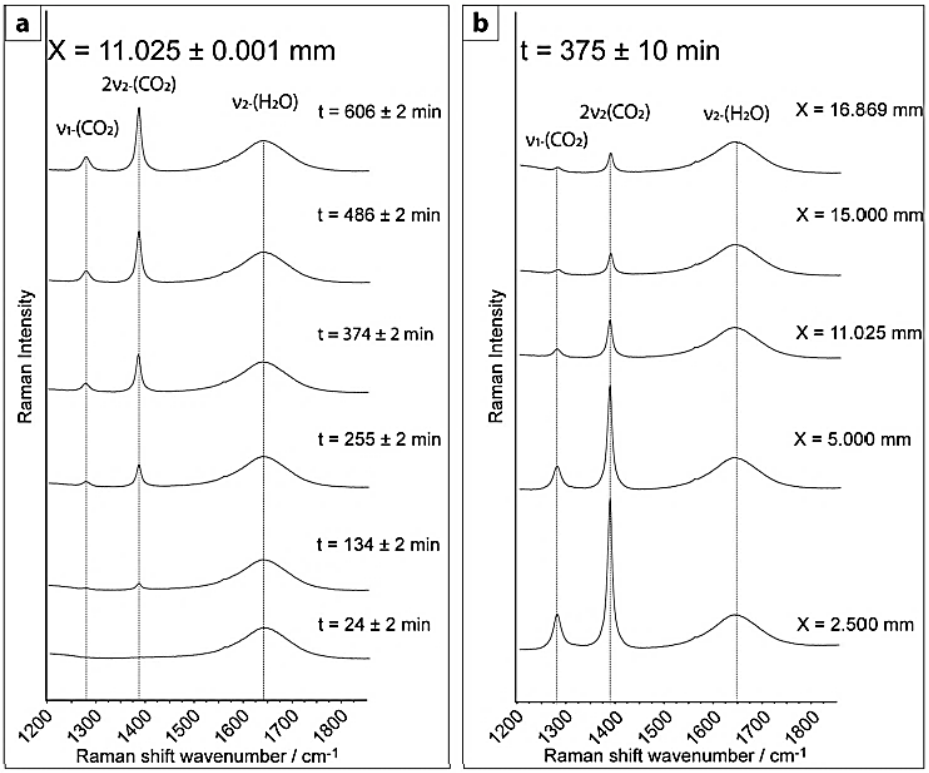

Figure 116 The change of Raman spectra with time (a) and distance from the CO_2 interface (b). Taken from Belgodere et al. (2015).

In a microfluidic study by Liu *et al*. (2012), confocal Raman microscopy and optical characterization were used for studying CO_2 solubility in deionized water and brine (1-3 M of NaCl) in the context of CCUS (Figure 117). The silicon-Pyrex micromodel with 1 m long, 200 µm wide and 100 µm deep microchannel was used to create slug flow in the liquid under various pressure (1.1 – 10 MPa) and temperature conditions (295 – 373 K). Raman spectra were acquired after a 10-minute equilibration period. The equilibration period (t_D) was calculated to be in the order of 25 s by following relation: $t_D \sim x^2/2D$, where x is half the distance between two CO_2 slugs (200 µm) and D (0.8×10^{-9} m^2/s) is the diffusion coefficient estimated from the Stokes-Einstein equation. This estimation is also experimentally validated to be under one minute, based on the temporal evolution of the 1385 cm^{-1} band. Thus, 10 minutes was selected to ensure extra time for proper equilibration between the two phases.

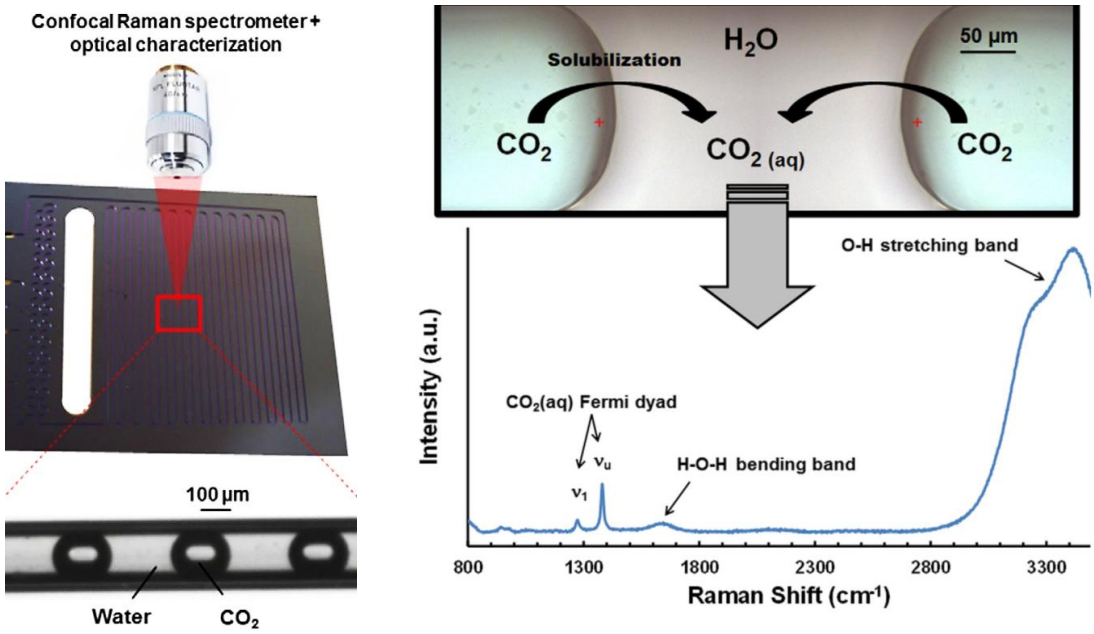

Figure 117 Confocal Raman microfluidics analysis method for studying CO_2 dissolution in water/brine. Adapted from Liu et al. (2012).

To estimate CO_2 solubility from the Raman signal, intensity values were extracted for $CO_{2\,(aq)}$ at 1385 cm^{-1} and water at 3430 cm^{-1}. When the CO_2-to-water intensity ratios were plotted against solubility coefficients obtained from the thermodynamic model of Duan and Sun (2003) under specific conditions (see Figure 118), a positive correlation with CO_2 solubility was observed. In more concentrated saline solutions, the relationship deviates from the linear trend seen in deionized water. This deviation is attributed to the steric hindrance effects of salt ions on the Fermi resonance.

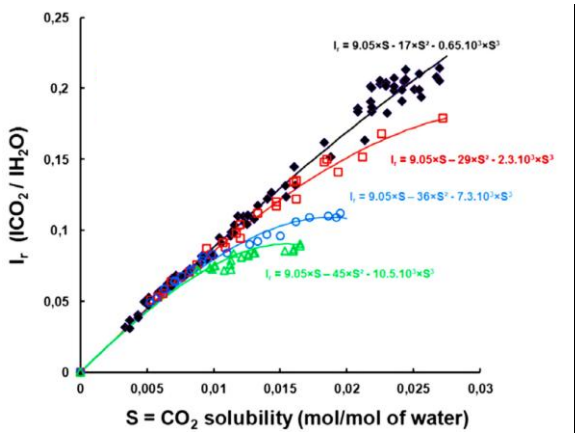

Tested experimental conditions:

	Salinity (M)	Pressure (MPa)	Temperature (K)
◆	0	1.1-10	295-373
□	1	3-10	303-373
○	2	4-10	303-373
△	3	7-9.5	308-328

Figure 118 The CO_2 to water band intensity ratio in relation to CO_2 solubility. Adapted from Liu et al. (2012).

Guo *et al*. (2014) utilized the same Raman bands to develop their model that takes into account temperature effects on CO_2 solubility. The solubility was calculated from visual observation of CO_2

volume change over a broader pressure (10 - 120 MPa) and temperature range (273 - 573 K) using a 300 µm inner diameter glass capillary. They normalized the peak intensity (height) ratio (HR) and peak area ratio (PAR) to solubility and compared the performance. Both HR and PAR approaches (see Figure 119) seem to show little dispersion with pressure and linear trends with temperature. While the PAR approach gives only one trend, the HR approach shows two trends. Despite the focus on higher pressures and temperature-driven effects, which lie outside the operating range of our current study, the findings of Guo *et al*. (2014) provide valuable insight into how Raman spectral features, particularly peak intensity and area ratios, can reflect CO_2 solubility behavior. Their results highlight the potential of Raman spectroscopy not only for capturing temperature effects but also for guiding the development of robust calibration strategies applicable across a range of experimental conditions relevant to CO_2 dissolution studies.

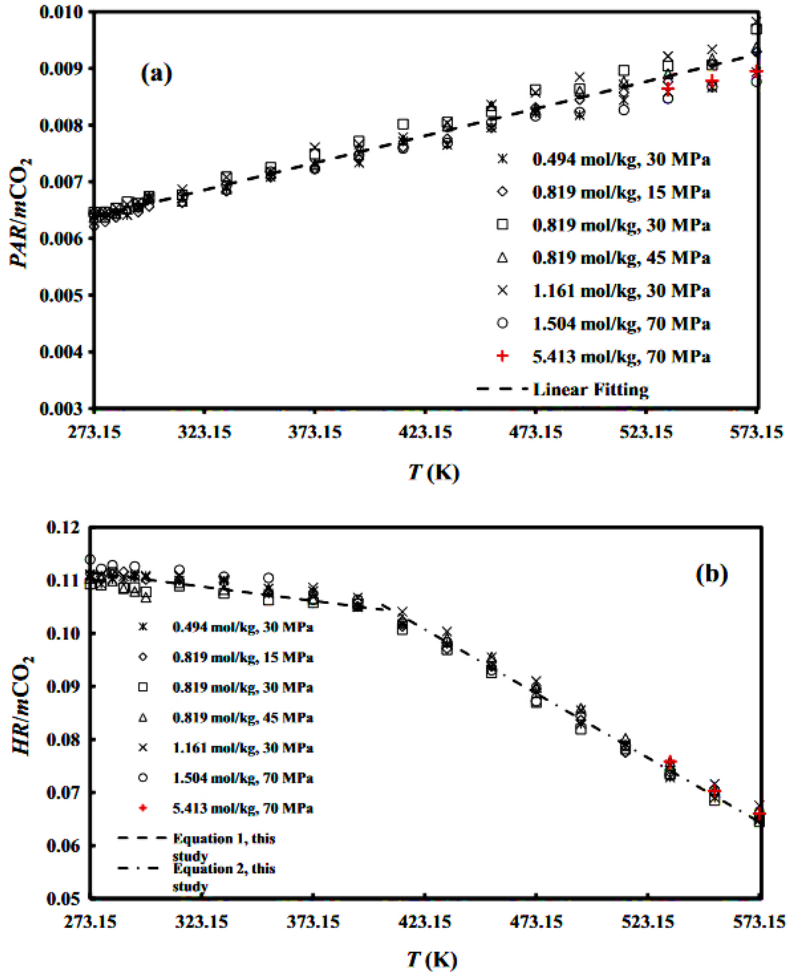

Figure 119 The scaling of solubility (mCO_2) normalized peak area ratio – PAR (a) and peak intensity ratio - HR (b) with temperature for various conditions. Taken from Guo et al. (2014).

In summary, the reviewed studies demonstrate the feasibility of both qualitative and semi-quantitative analysis of CO_2 dissolution using Raman spectroscopy, in microscale systems such as microfluidic devices and glass capillaries. Quantitative assessments are typically achieved by calibrating peak intensity or area ratios of CO_2 and water against thermodynamic models or supporting visual data. These spectral ratios are influenced by key parameters including pressure, temperature, and salinity, and have been shown to correlate with dissolved CO_2 concentration, giving the prerequisites for the estimation of mass transfer coefficients.

However, despite the promising progress, several challenges remain. The underlying mechanisms governing the observed spectral dependencies are not yet fully understood, and current models often fail to universally capture non-linear effects, particularly at higher pressures or in saline systems. Most critically, there is a significant gap in experimental data for low-pressure systems (<1 MPa), which are especially relevant for environmental and low-pressure research applications like ours. Future research should focus on expanding datasets in this range and refining mechanistic interpretations to improve the robustness and transferability of Raman-based analytical approaches.

II. Material and methods

1. Setup

The Raman setup at ISTO, where experiments are conducted, features an open laser beam configuration as shown in Figure 120. The setup is comprised of an upright microscope with a motorized stage and a camera (Chapter 2) that houses a microfluidic device, enabling its precise control in the three spatial directions. A laser device (Genesis MX SLM from Coherent) generates a beam of green light (λ = 532 nm) with a maximum power output of 500 mW (class 4 laser). The beam is then guided through a series of lenses and mirrors to the microscope, which focuses and condenses it to micrometer-scale dimensions, thereby enhancing the spatial resolution of the analysis.

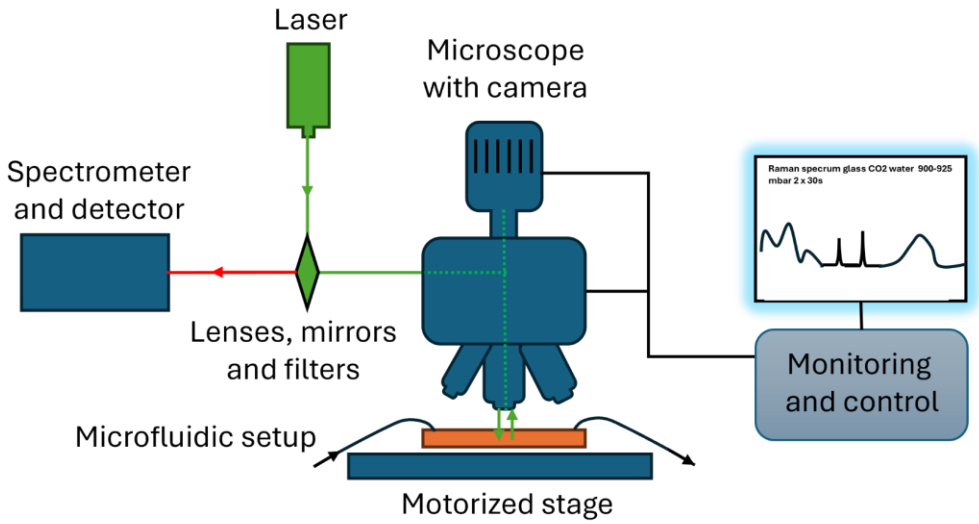

Figure 120 Micro-Raman setup in ISTO adapted for microfluidic investigations.

Specifically, from the numerical aperture (NA) of a given objective and laser wavelength (λ) we calculated a theoretical laser spot diameter (d) based on the following equation *(11)*:

$$d = (1.22 * \lambda)/NA, \quad (11)$$

and the depth of field (d.o.f.) according to the next one *(12)*:

$$d.o.f. = \frac{4\lambda}{NA^2}. \quad (12)$$

The dimensions of the laser spot dependent on the selected objective are available in Table 16.

Table 16 Objective specifications and corresponding laser spot size (d) and depth of field (d.o.f).

Magnification	Numerical aperture (NA)	d (µm)	d.o.f. (µm)
5x	0.15	4.3	94.6
20x	0.45	1.4	10.5
40x	0.6	1.1	5.9
50x	**0.7**	**0.9**	**4.3**
100x	0.8	0.8	3.3

On the signal acquisition side of a setup, the backscattered light signal is passed through an Edge filter to remove the Rayleigh and anti-Stokes light before entering the Andor Shamrock 500i spectrometer equipped with a Peltier-cooled back-illuminated CCD Andor Newton detector. There are three different gratings one can choose to balance the size and resolution of the spectral window. Gratings of 600, 1200 and 1800 lines/mm offer spectral resolutions of 1.2, 0.8, and 0.4 cm^{-1} with window sizes of around 2500, 900 and 670 cm^{-1}, respectively.

The acquisition of spectra is performed with Andor Solis software while for the data treatment (baseline correction, normalization, deconvolutions, etc), we opted for Fityk, an open source software (Wojdyr, 2010).

2. Procedure and optimization

At the beginning of every lab session and in case of gratings change, the Raman signal is manually calibrated with silicon based on its characteristic peak at 520.3 cm^{-1}. After calibration, a microfluidic device is positioned under the microscope and previously determined optimal operational parameters (see Table 17) are set. The aim of optimization is to improve the signal-to-noise ratio. The optimization was performed beforehand on microchannels saturated with CO_2 gas under pressure (up to 4 bar) due to the convenience and simplicity of detecting and adjusting the Raman signal in these conditions. We optimized for gratings, microscope objective, output power, laser spot focus in depth, acquisition time and pressure. All optimization parameters are summarized in Table 17.

Table 17 The optimized operational parameters for Raman acquisition within glass micromodels and CO_2-water system.

Optimized parameter	Value	Reason
Gratings	1200 mm^{-1}	A compromise between the size of the spectral window and resolution
Objective	50x	Maximum signal intensity
Power output	300 mW	A compromise between signal intensity and to prevent heating
Focus in depth	Middle of depth	Maximum signal intensity
Acquisition time	2 x 30s	Balance signal to noise ratio and the time scale of the process
Pressure difference	25 -50 mbar	To capture the evolution of the process with the selected acquisition time
Confining pressure	Max possible	Pressure increases the density, which intensifies the signal. Pressure regulator up to 4 bar & pressure pump up to 1 bar

The laser spot is then aligned with the location of interest, which is 100 µm from the end of the trapping element as indicated in Figure 121. The location is chosen sufficiently far from the interface to track the evolution of dissolved CO_2 species, yet not too close to the wall to ensure that the laser spot remains within the fluid phase and not in the glass. Once the microfluidic experiment is initiated, spectral acquisition can begin.

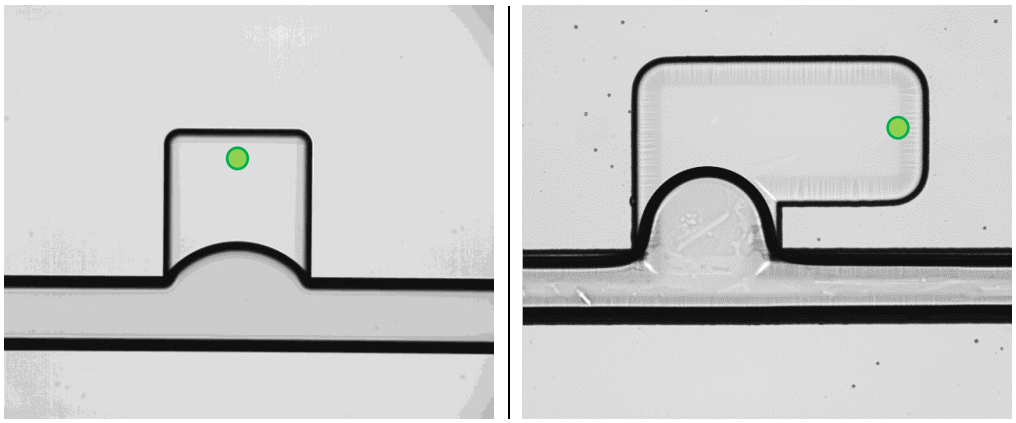

Figure 121 Laser spot location (green dot) in single pocket and L-pore geometry.

After Raman signal acquisition, the spectra are imported into Fityk software and the data treatment is performed in the following manner (see Figure 122). At first (Step 1), the baseline is stripped by making relatively straight lines through the lowest data points. In the background-corrected spectrum, the centers of peaks are positioned and the Voigt profile is used to deconvolute the data points (Step 2). The glass signal within the spectral window is deconvolved into five peaks, while dissolved CO_2 and water are each represented by two peaks. (Semi-)quantitative analysis is

performed by comparing the relative intensities of the Raman modes rather than the area under the deconvolved peaks. This approach is chosen because baseline subtraction introduces significant user-dependent error as even a small shift in the baseline can result in a substantial change of the integrated area due to the broad base of the peaks or bands.

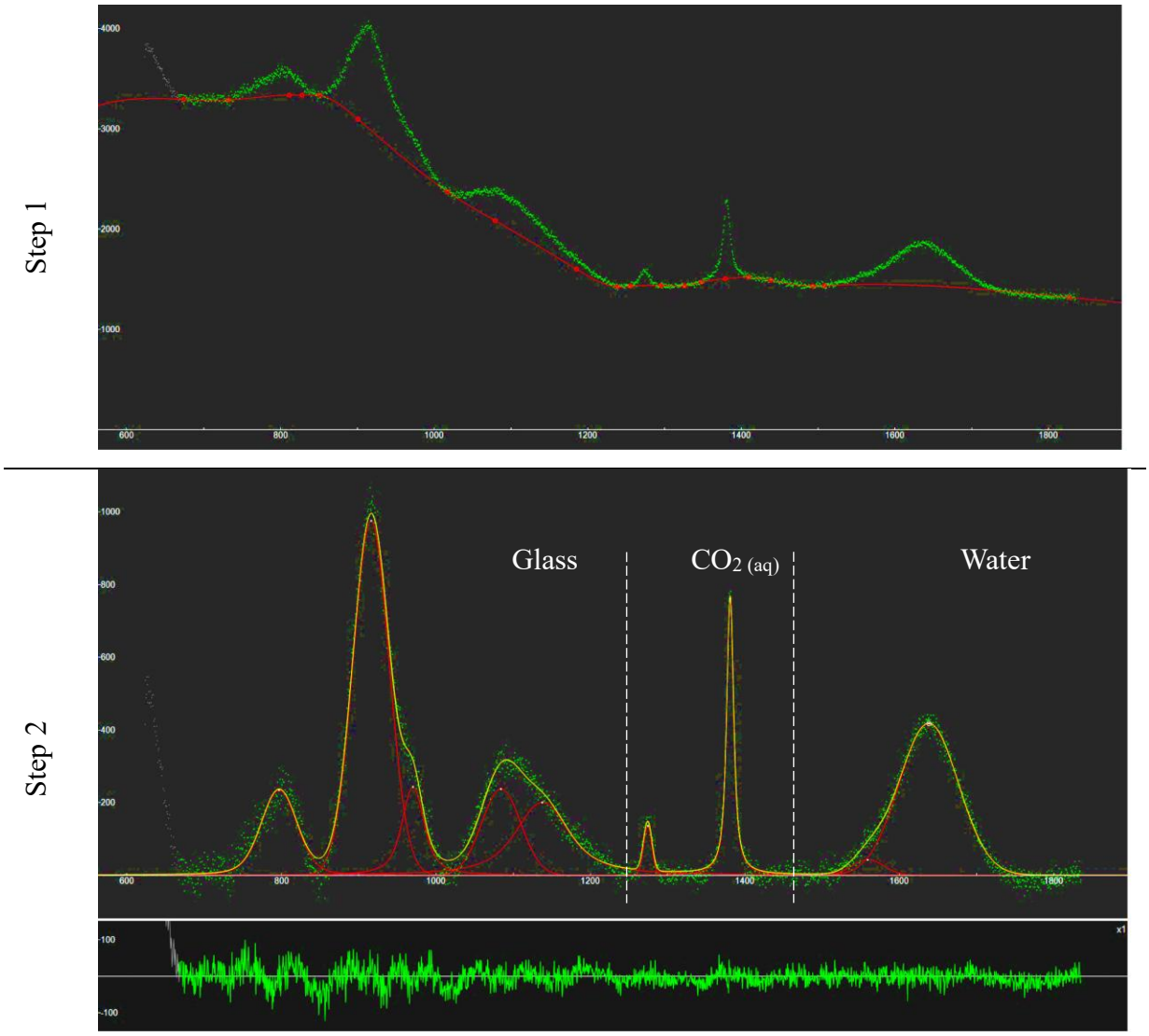

Figure 122 Raman spectra treatment with Fityk. Example of signal acquired in water pre-equilibrated with CO_2 and under 4 bars of confining pressure on a single pocket geometry (Micronit device). STEP 1: example of baseline correction, STEP 2: example of deconvolution of Raman bands

III. Results

A schematic representation of the principal mass transfer processes during drainage and imbibition is shown in Figure 123. In this study, we focus on Raman analysis of CO_2 dissolution during drainage (highlighted in red). In comparison, Chapter 4 focused on tracking water evaporation during drainage and CO_2 dissolution during imbibition. The choice of drainage over imbibition stems from the compatibility of acquisition times with the speed of interfacial movement necessary to obtain a reliable signal-to-noise ratio. Drainage also avoids the ambiguity associated with bubble detachment typically encountered in the later stages of imbibition. Furthermore, CO_2 dissolution during imbibition is limited by the small size of the gas bubble and the low resulting concentration of dissolved CO_2, which is quickly advected away. Evaporation processes, on the other hand, cannot be tracked in the current Raman setup, as the signal from water vapor or thin films remains below the detection limit.

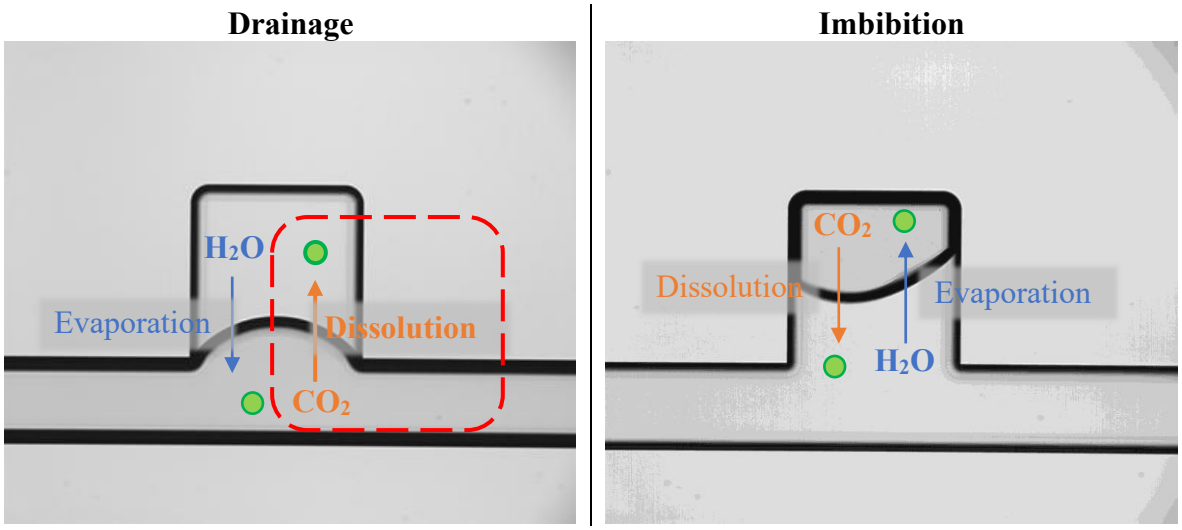

Figure 123 Schematics of dominant mass transfer processes during drainage and imbibition experiments. The laser spot location is marked with a green dot.

Thus, the result section is structured in two parts. Section 1 introduces the characteristic Raman signal of glass species coming from microfluidic devices, followed by the signal of water and CO_2, in both gaseous and dissolved form. The aim was to establish a semi-quantitative calibration between the signal intensity of dissolved CO_2 species and pressure under equilibrium conditions. Section 2 focuses on tracking the kinetics of CO_2 dissolution during drainage.

1. Species identification

a) Glass

The Raman spectrum of borosilicate glass is characterized by broad, overlapping bands of silicate network extending up to 1250 cm^{-1} as shown in Figure 124. Micronit and Klearia devices show matching spectral profiles in this region, confirming identical material composition. As shown in Figure 124, plasma treatment did not alter the Raman spectra of glass in either Micronit or Klearia

devices. Namely, plasma wettability treatments affect only the surface without altering the bulk material, penetrating only a few nanometers in depth and therefore not producing chemical alterations that are sufficiently intense to be detectable by Raman spectroscopy.

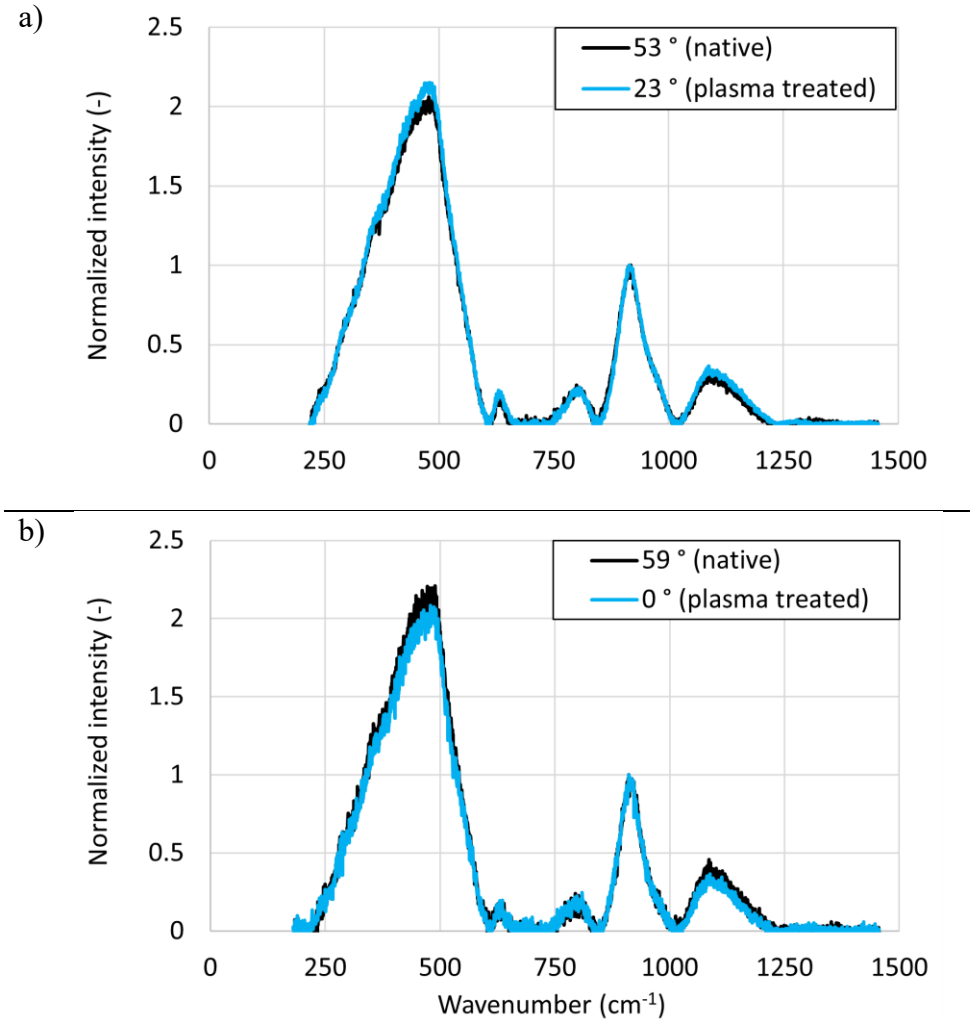

Figure 124 Raman signal of glass before and after plasma treatment on single pore (Micronit) (a)and L-pore (Klearia) devices (b), normalized to the glass peak at 916 cm^{-1}.

However, a significant difference between the two micromodel devices emerges in the higher wavenumber region (> 2000 cm^{-1}), as shown in Figure 125. Namely, Klearia devices show a nearly flat response, whereas Micronit ones exhibit a rapid increase in intensity with increasing wavenumber. This increase can be attributed to fluorescence, which likely occurs due to impurities within the bulk glass structure. Following the plasma treatment, Micronit devices experienced a decrease in relative fluorescence intensity, which is discussed later in section c). Additionally, in the Raman spectra of both devices a small peak at 1555 cm^{-1} is attributed to oxygen, while the peak at 2330 cm^{-1} corresponds to nitrogen, both originating from ambient air.

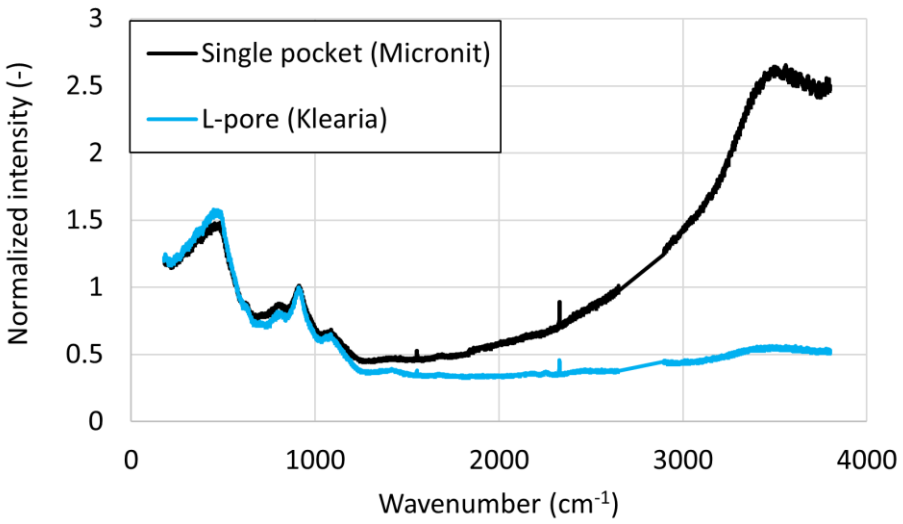

Figure 125 Raman spectra indicating fluorescence on Micronit devices. The spectra are acquired on native surfaces and depict raw data normalized to the glass peak at 916 cm^{-1}.

b) CO_2 gas

The signal of gaseous CO_2 (Figure 126) is characterized by two main peaks of the Fermi diad located at 1284 and 1387 cm^{-1}. In general, on any device, at higher pressure (e.g., at 4 bar), we can also observe hot bands positioned at 1263 and 1408 cm^{-1} and a very weak peak around 1369 cm^{-1} that can be assigned to the ^{13}C isotope.

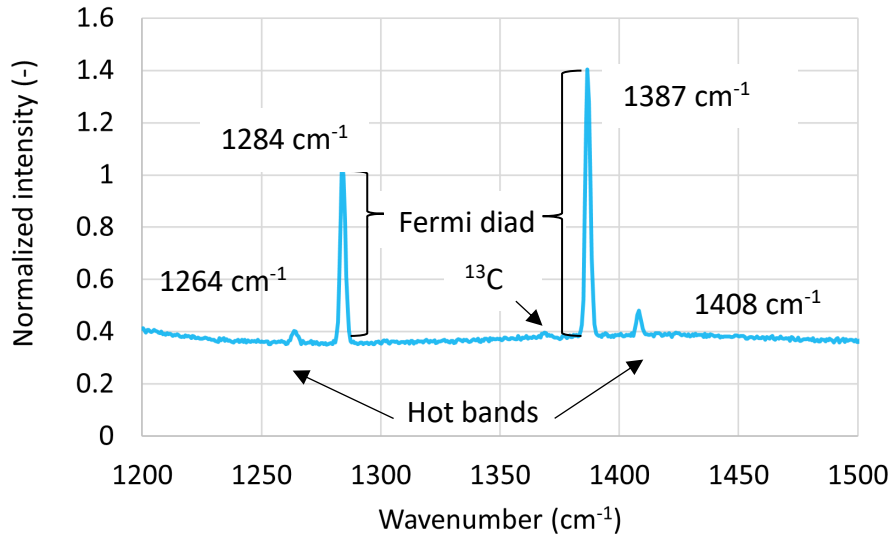

Figure 126 The Raman signal of gaseous CO_2 visible through the Fermi diad and hot bands. The spectrum is acquired on a plasma treated single pocket (Micronit) device under 4 bars of pressure and normalized to the glass peak at 916 cm^{-1}.

Since CO_2 gas is a compressible fluid, implying that its density changes with pressure, we are able to follow the increase in signal intensity with pressure. To do so, we took the difference in intensity

between the two peaks of the Fermi diad (I_{C2}-I_{C1}) as a form of internal calibration and further normalized it to the intensity of the glass band around 916 cm^{-1} (I_{G916}). As shown in Figure 127, the scaling of normalized $CO_{2\,(g)}$ intensity is a linear function with applied pressure, giving nearly identical results on both Micronit and Klearia devices.

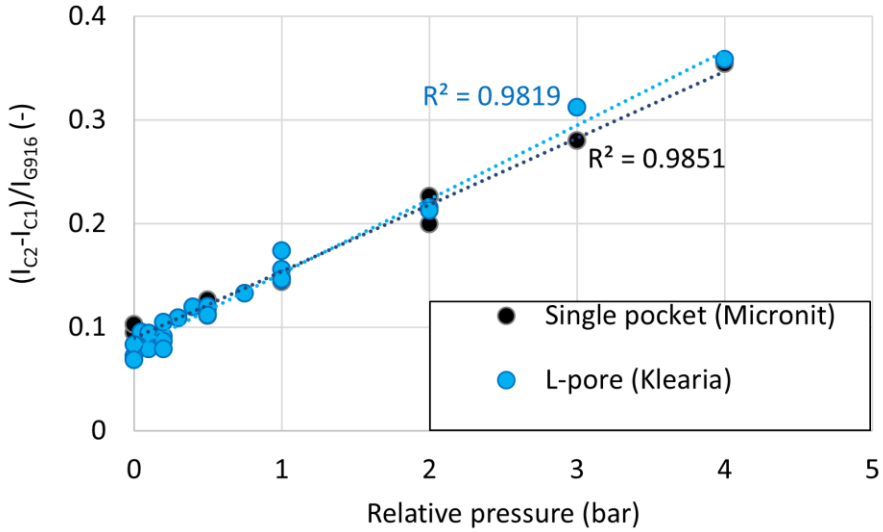

Figure 127 The scaling of normalized $CO_{2\,(g)}$ intensity ($(I_{C2}$-$I_{C1})/I_{G916}$) with pressure on plasma treated devices.

c) Water and $CO_{2\,(aq)}$

The water signal has two principal bands: bending observed around 1640 cm^{-1} and stretching centered at 3400 cm^{-1}. In Micronit devices, the water stretching band (Figure 128) is partially masked by the fluorescence which seems to decrease by half after plasma treatment of microchannels (compare the intensities at 3750 cm^{-1}). This correlates with the surface cleaning effect of plasma explained in Chapter 3. In Klearia devices, no significant difference in the water stretching signal is observed. Moreover, the presence of CO_2 has no impact on the Raman vibrational signature of the water band, which is consistent with the literature (He *et al*., 2024; Hu *et al*., 2019).

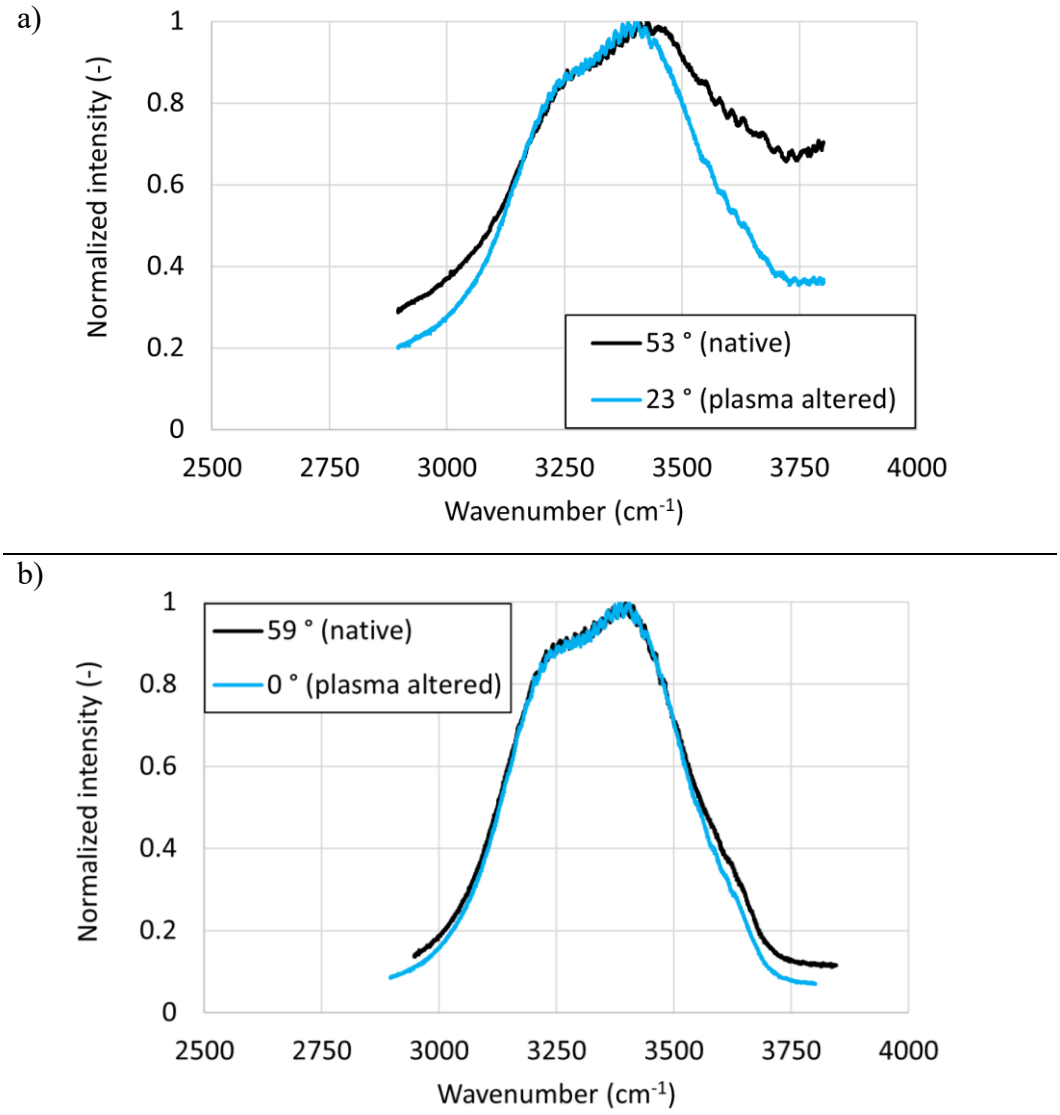

Figure 128 Raman stretching bands of water single pore (Micronit) (a)and L-pore (Klearia) glass (b). The normalization is performed on maximum intensity.

Water bending Raman band and the modes assigned to dissolved CO_2 are shown in Figure 129. The spectra are obtained on microchannels filled with single-phase water presaturated with CO_2. The presaturation is achieved by mixing a small amount of water (< 10 mL) in a CO_2-pressurized glass bottle (100 mL) for 10 minutes. After the equilibration, water with dissolved CO_2 is then injected under pressure into the microchannel to prevent exsolution and formation of gas bubbles. The *in situ* analysis shows that after a few minutes of mixing, time no longer has an effect on signal intensity, indicating that 10 minutes is more than enough to reach equilibrium conditions. Additionally, once the microfluidic device is sealed using the valves, the pressure sensor on the pump confirms stabilization, showing no drop in CO_2 pressure and indicating that no further dissolution is occurring.

Water bending Raman mode is characterized by a broad band located around 1640 cm^{-1}. Dissolved CO_2 is comprised of two bands located around 1274 and 1382 cm^{-1}. The Raman signature of dissolved CO_2 can still be detected as a characteristic Fermi diad, but with the Raman peaks shifted to lower wavenumbers and increased full widths in comparison with gaseous CO_2. As the molar density (mol/m^3) of dissolved CO_2 is lower than that of gaseous CO_2, the signal intensity in the dissolved state is always less intense in comparison to gas. Thus, the first band (around 1274 cm^{-1}) is sometimes difficult to detect at lower pressure as it blends in with noise. Broadening of CO_2 peaks is attributed to the water environment (solvatation) impacting the vibrational mode through intermolecular interactions.

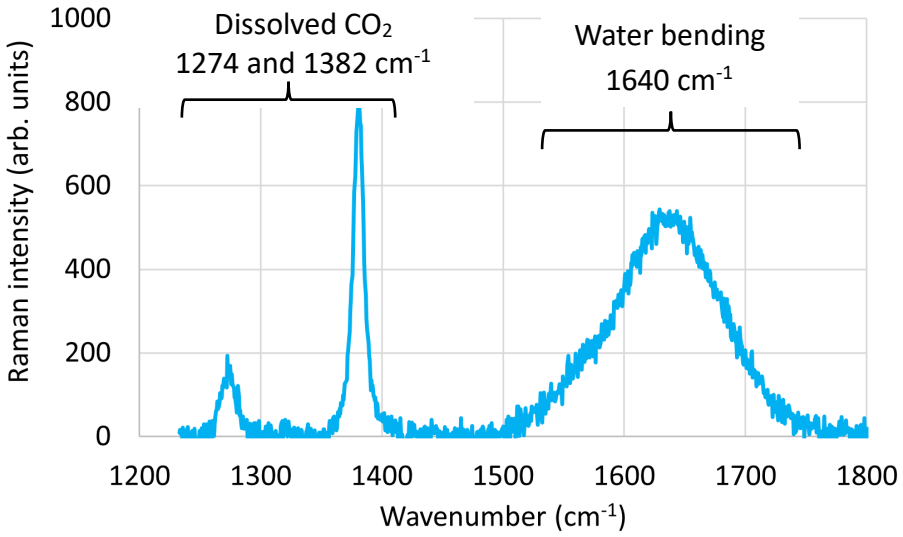

Figure 129 Raman spectrum showing water bending and dissolved CO_2 at a pressure of 4 bar in plasma treated devices.

Given its spectral proximity to dissolved CO_2 and its reported use as an internal reference in the literature (Belgodere *et al*., 2015), the water bending mode was evaluated for internal calibration in two-phase experiments and compared to the glass peak at 916 cm^{-1}. The evaluation of water and glass signal intensity over the pressure range is shown in Figure 130a while its time evolution in two-phase flow experiments under constant applied pressure is shown in Figure 130b. As may be observed, the bending mode of water shows better stability of signal intensity with imposed pressure and in time on both microfluidic devices. Hence, the signal of water bending at 1640 cm^{-1} is used to normalize the dissolved CO_2 species in further analysis.

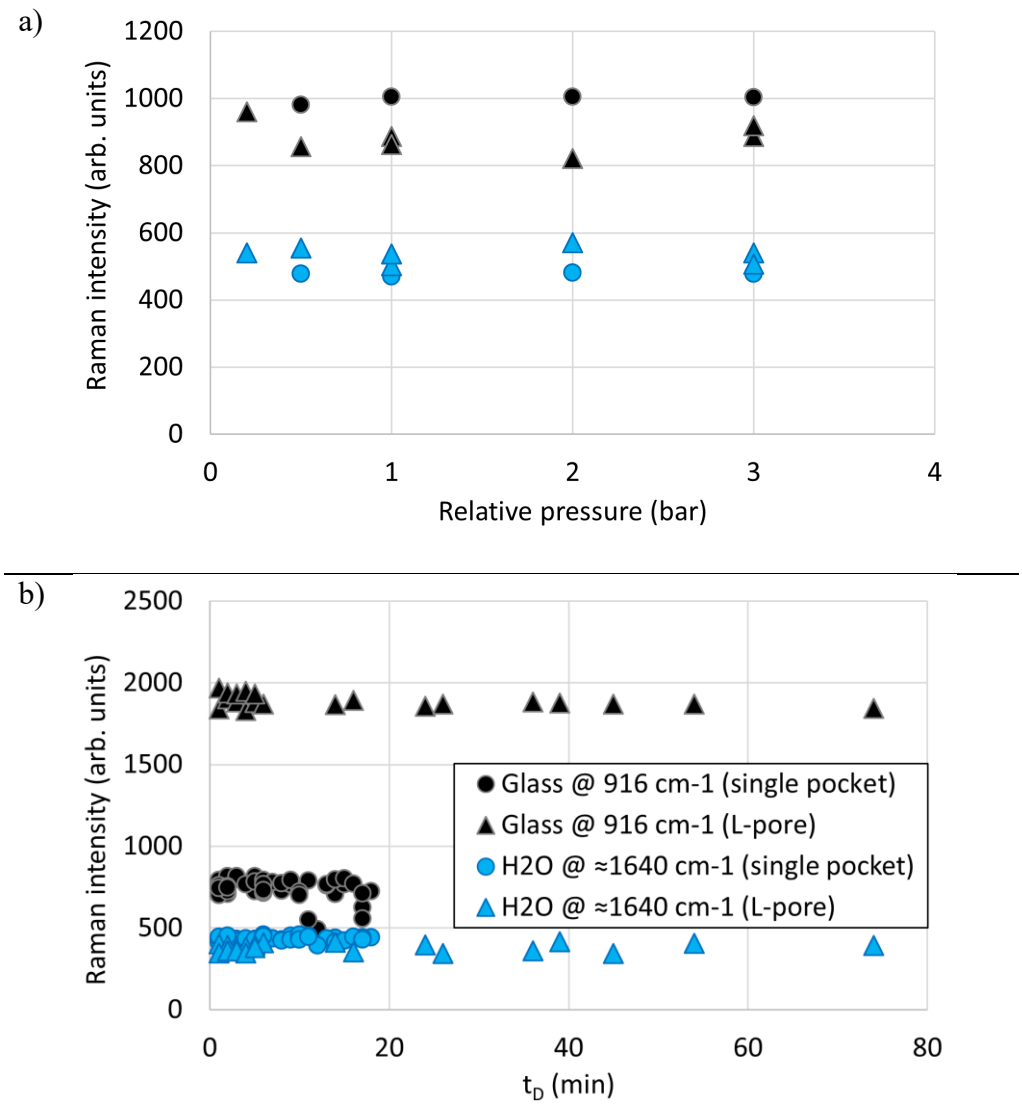

Figure 130 The scaling of water bending and glass signal (at 916 cm^{-1}) as a function of imposed pressure a) and with (post-displacement) time (t_D) during the two-phase experiments at fixed relative pressure of 900 mbar (b).

To obtain the calibration curve, the Raman spectra were acquired in the microchannel on the water that had been equilibrating with CO_2 for 10 minutes in the bottle, as described earlier in the text. Similar to the behavior observed for gaseous CO_2, a normalized signal of dissolved CO_2 ($(I_{C2}-I_{C1})/(I_{H2O\_1640})$) increases linearly with applied pressure (see Figure 131). This is due to an increase in the concentration of CO_2 species in water. Thus, Raman intensity can be treated as a proxy for concentration and used to describe the process of CO_2 dissolution in water.

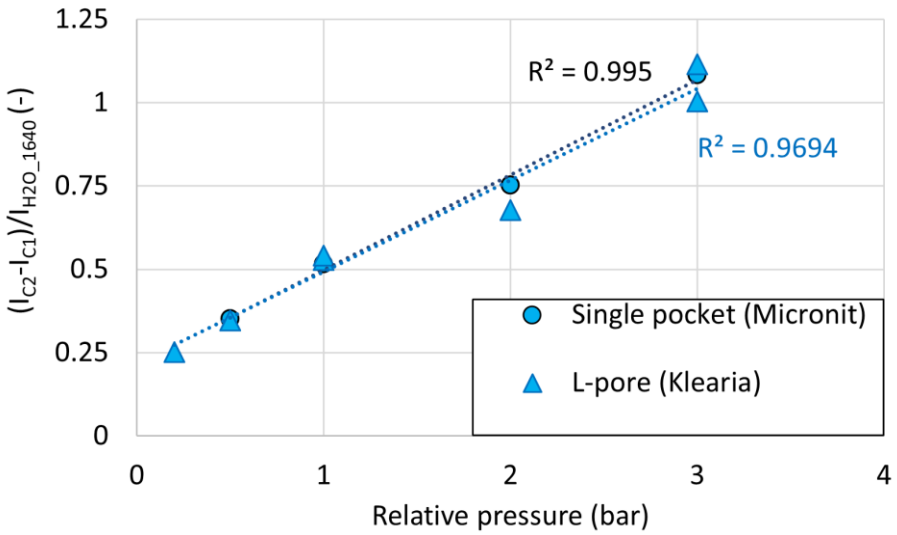

Figure 131 The scaling of the normalized dissolved CO_2 intensity on plasma treated surfaces.

2. Tracking CO_2 dissolution kinetics via *in situ* Raman measurements

With all species identified and the normalization strategy established, Raman signal intensity will serve as a proxy for species concentration, enabling semi-quantitative analysis of dynamic flow experiments. The primary objective is to monitor the kinetics of the CO_2 dissolution process by measuring the temporal evolution of Raman signal intensity for relevant species at a fixed location within the microfluidic device. To enhance the probability of detecting dissolved CO_2, all experiments were conducted under a relative pressure of 900 mbar (applied by the pumps at inlet and outlet), with pressure differences of 25 and 50 mbar to drive the flow.

Figures 132 andFigure 133 show the evolution of Raman spectra recorded during the drainage process in the two respective geometries (single pocket and L-pore). For easier visualization of the process, each spectrum is attributed to a characteristic visual change. Each time step (t) corresponds to one minute of acquisition time. Initially, the system is fully saturated with water (t_0), and as a result, only the water bending band is detected in the Raman spectrum. Upon the initial displacement of water with gaseous CO_2, we begin to observe the signal of dissolved CO_2 in the water ($\geq t_1$). By comparing Figure 132 and Figure 133, we can observe that the increase of dissolved CO_2 signal intensity at the beginning of the dissolution process is more gradual in L-pore compared to single pocket. Namely, the evolution of Raman intensity is influenced by both the pore geometry (its complexity and shear volume) and the applied pressure difference. Shortly after, the system enters a steady state with no qualitative or quantitative changes observed in spectra. As water evaporation progresses, the fluid interface moves and eventually crosses the laser spot location. The Raman signal response during this transition depends on the speed of interface movement which is typically on the order of one acquisition time, i.e., 1 minute. Consequently, interface transition is characterized by the superposition of dissolved and gaseous CO_2 signals in the acquired spectrum. The subsequent spectrum reveals a weak signal of water, likely from a water film, along

with a reduced-intensity gaseous CO_2 signal. Finally, once the interface moved even further due to evaporation, the laser spot is fully immersed in gaseous CO_2, which is clearly observed in the Raman spectrum by the maximum intensity of the Fermi diad (at a given pressure).

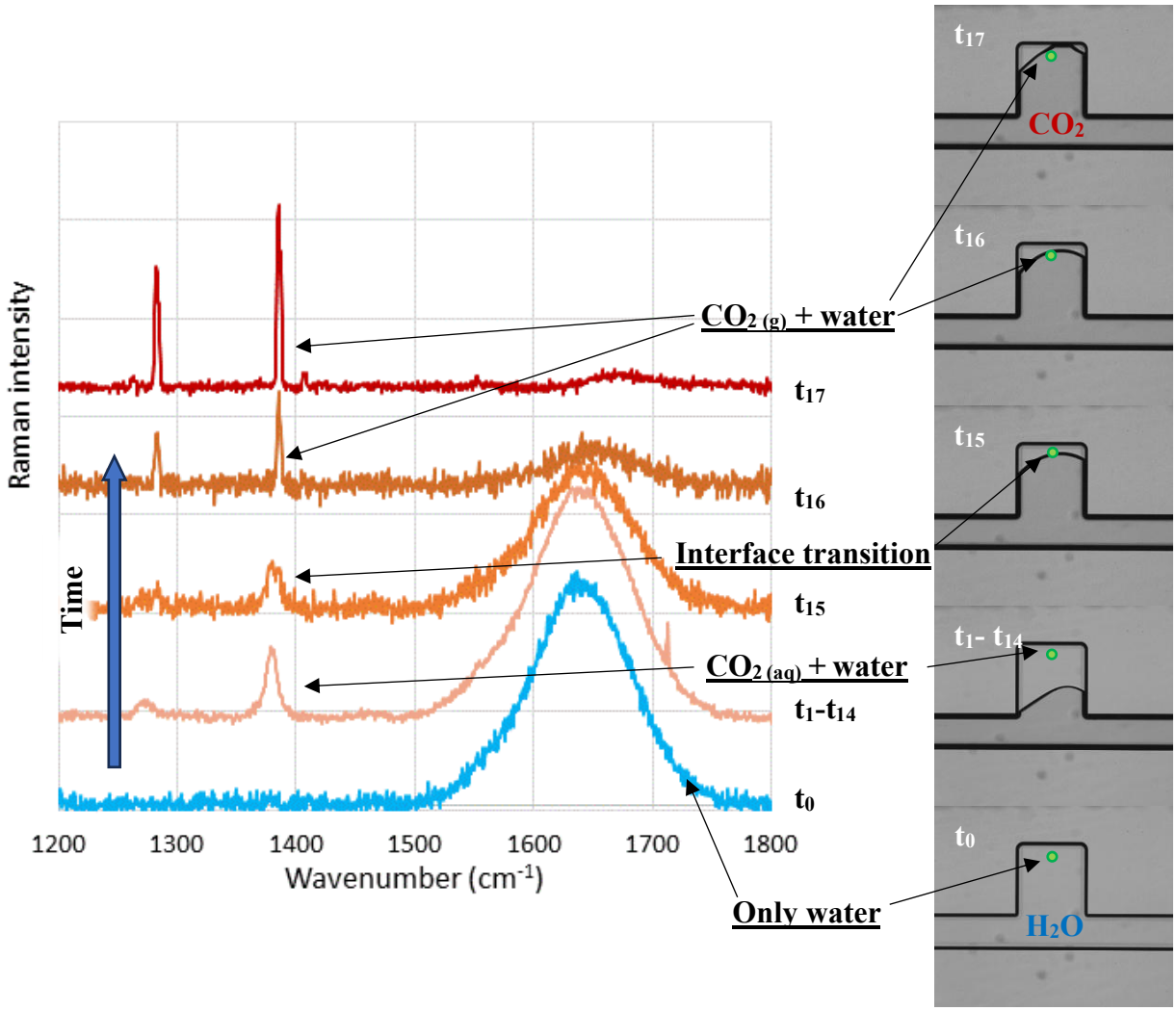

Figure 132 The time-lapse of CO_2 dissolution during drainage followed through consecutive acquisitions of Raman spectra (each 2 × 30s). An example is shown on the 53° contact angle single pocket (Micronit) device for a pressure difference of 50 mbar. The laser spot is represented by a green dot.

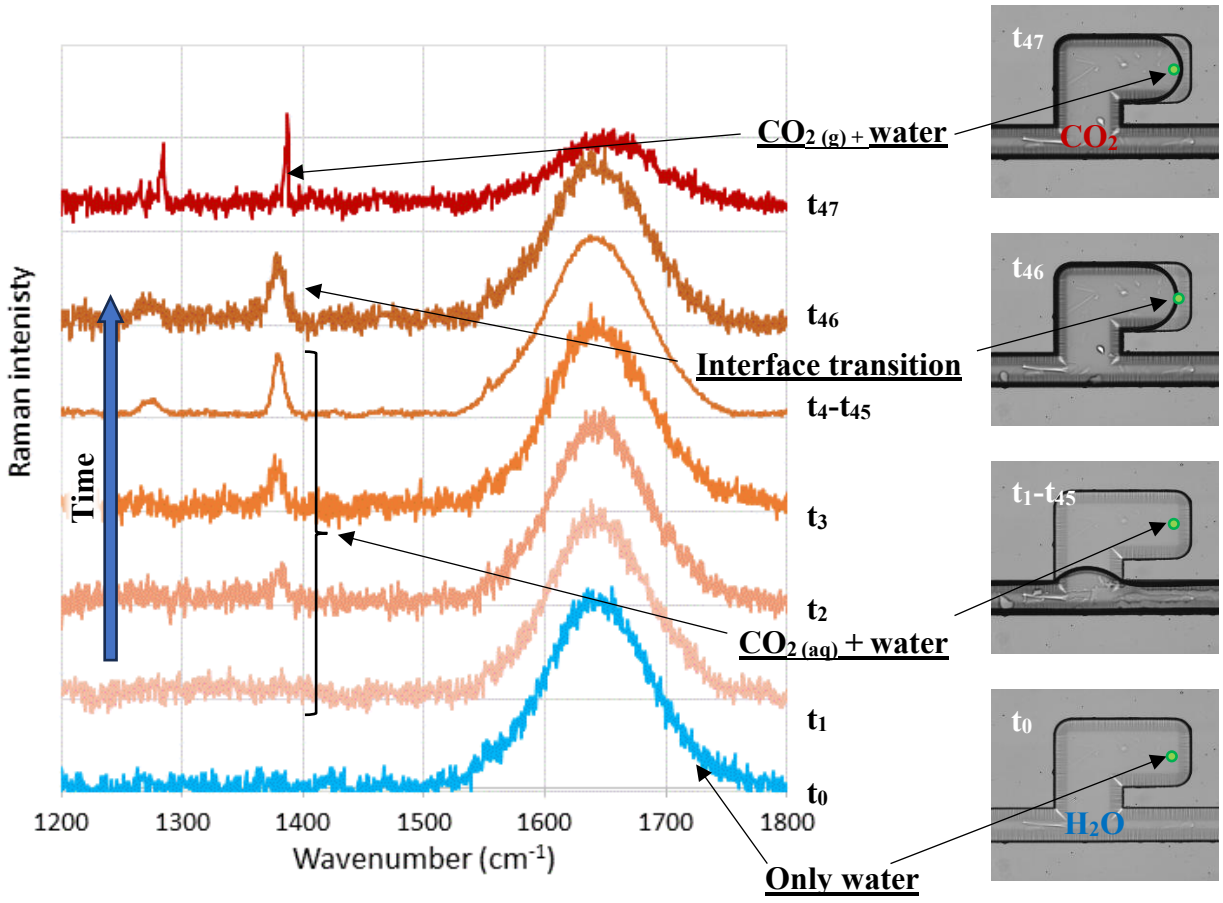

Figure 133 The time-lapse of CO_2 dissolution during drainage followed through consecutive acquisitions of Raman spectra (each 2 × 30s). An example is shown on the 59° contact angle L-pore (Klearia) device for a pressure difference of 50 mbar. The laser spot is represented by a green dot.

The presented kinetic Raman spectra are deconvolved as described in the Procedure and optimization section, enabling quantitative analysis of the dissolved species signal. The results of spectral processing, showing the time evolution of normalized Raman intensity, are presented in Figure 134.

For the single-pocket geometry (Figure 134a), the data reveal a rapid increase in dissolved CO_2 intensity, mostly within the first minute (equivalent to one spectral acquisition). Subsequent spectra exhibit minor oscillations in dissolved CO_2 intensity until the fluid interface passes the laser spot, at which point the dissolved CO_2 signal fades and drops to zero, getting replaced by a signal of gaseous CO_2.

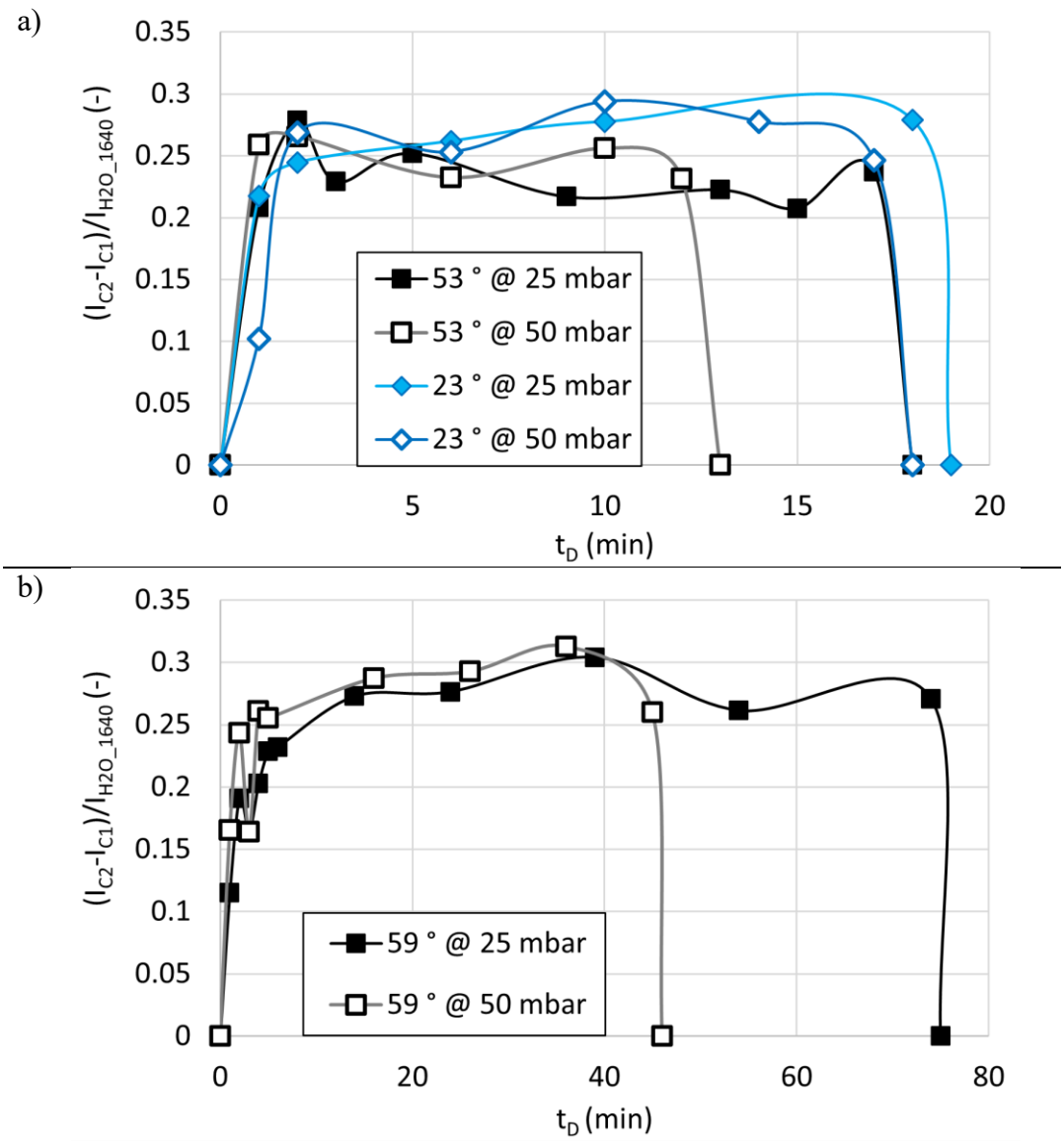

Figure 134 The time-lapse of the CO_2 dissolution process followed through normalized Raman intensity ($(I_{C2}-I_{C1})/I_{H2O\_1640}$) on a single pocket for two values of the contact angle (a) and a L-pore (b) microfluidic device.

To interpret the initial rapid signal increase, we propose two equally plausible explanations. The first is that CO_2 begins diffusing into the water while still in the tubing, so the arriving water is already partially equilibrated with CO_2. The second explanation is based on recirculating flow within the trapped water droplet (see Chapter 4, Flow Properties section), which promotes advective mixing and leads to rapid equilibration. It is also likely that the observed effect results from a combination of both mechanisms. Regardless of the exact cause, the fluid system typically reaches a steady state within one to two minutes, depending on the alignment between the onset of initial displacement and the start of signal acquisition.

Oscillations observed during the steady-state phase may thus be attributed to fluctuations in CO_2 concentration caused by the recirculation pattern, in addition to device- or user-related errors. No significant quantitative differences in signal intensity were observed between surfaces of differing wettability or across the tested pressure differences.

In the L-pore geometry (Figure 134b), which features a slightly larger volume and increased structural complexity, the signal evolution shows a more gradual rise in intensity, suggesting slower equilibration during the initial phase. A consistent dip in signal intensity is observed after two minutes, indicating a lower dissolved CO_2 concentration. This finding further supports the hypothesis that recirculation patterns influence the spatiotemporal distribution of dissolved CO_2.

In both geometries, the signal stabilizes between normalized intensity values of approximately 0.25 and 0.3, indicating a consistent final state across experiments. This consistency supports the physical interpretation of the normalized Raman intensity as a measure of CO_2 concentration in water, suggesting that the system reaches a comparable level of CO_2 saturation regardless of geometry, surface wettability, or applied pressure difference.

IV. Conclusion

In this chapter, we demonstrated the applicability of micro-Raman spectroscopy as a complementary tool to monitor and analyze interfacial mass transfer processes between CO_2 and water in microfluidic systems. Building upon a review of the current state of the art, we established the rationale for employing Raman spectroscopy, particularly its capacity to detect both gaseous and dissolved chemical species. Our aim was not only to validate the feasibility of Raman-based measurements in microfluidic environments but also to develop an optimized experimental setup capable of capturing key chemical signatures under dynamic conditions at low pressure. To that end, we designed a procedure tailored for glass microfluidic devices, addressing the specific challenges encountered during signal acquisition. Particular attention was given to the suppression of fluorescence effects, which appeared above 2000 cm^{-1} and interfered with the OH stretching water signal. Fortunately, the main signal of CO_2, the Fermi diad, appears in a region weakly affected by fluorescence, allowing us to focus on CO_2 behavior in both the gas phase and in solution.

For gaseous CO_2, a linear scaling of the Fermi diad peak intensity with pressure was observed, consistent with previous studies and confirming the sensitivity of Raman spectra to pressure variations. Upon dissolution of CO_2 in water, the Fermi diad peaks broadened and shifted to lower wavenumbers, consistent with literature findings. The ultimate goal was to track reaction kinetics *in situ* by monitoring the evolution of chemical species during CO_2 dissolution under dynamic drainage conditions. Drainage mode was selected over imbibition due to its slower interfacial movement, which permitted longer acquisition times and thus improved signal-to-noise ratio at low pressure (< 1 bar). This marks a significant difference from most literature studies, which typically operate under higher pressure and thus benefit from stronger Raman signals. Despite these less favorable conditions, relatively stable signal intensities were obtained on single pocket geometry, suggesting fast dissolution and near-equilibrium between the CO_2 and water phases within the acquisition time. Minor variations in Raman intensity were observed across different wettability states and pressure gradients, but they were not significant enough to alter the overall trend or signal interpretation. However, we were able to qualitatively observe the influence of different wettability states and imposed pressure gradients at the moment the gas-liquid interface crossed the laser spot (positioned 100 µm from the farthest wall of the geometry), marked by a distinguishable shift in the Raman signal from $CO_{2(aq)}$ to $CO_{2(g)}$, indicating the approach of dissolution completion. The increased geometrical complexity of L-pore devices resulted in more gradual intensity evolution over time, likely due to the larger distance of the laser spot relative to the gas-liquid interface.

These results confirm that Raman spectroscopy can qualitatively and semi-quantitatively track the chemical evolution of CO_2 during mass transfer in confined geometries, even under low-pressure conditions. However, full quantitative interpretation remains limited by the lack of direct correlation between the Raman signal and the actual concentration of dissolved species. Future work will aim to address this limitation through calibration against known standards or

thermodynamic models. Additionally, enhancements to the system, such as incorporating lasers with alternative wavelengths to mitigate fluorescence, using faster detectors to capture transient dynamics and implementing spatial mapping techniques, are expected to broaden the method's applicability. Slower-reacting systems, such as methane-water, could also be explored to further probe mass transfer kinetics in a more controlled manner and to expand the research to other fluid pairs. Together, these improvements will pave the way toward robust, spatially resolved, and quantitative Raman analysis of interfacial processes in microfluidics.

Chapter 6 - Summary, conclusion and perspectives

In the context of carbon capture, utilization, and storage (CCUS), understanding the underlying mechanisms of CO_2 sequestration within geological porous media is critical for ensuring the long-term stability and effectiveness of storage systems. This thesis was motivated by the need to address a persistent gap in fundamental knowledge regarding interfacial mass transfer and capillary trapping at the pore scale, using experimental approaches. Given the critical role of these mechanisms in determining the fate of CO_2 in subsurface storage, advancing our understanding at a fundamental level is essential to improve the calibration of both pore- and reservoir-scale models and to enhance the interpretation of field-scale storage behavior.

The primary objective of this research was to experimentally investigate the influence of porous media wettability on fluid-fluid interfacial mass transfer and capillary trapping processes. Wettability, defined as the preferential affinity of a fluid to adhere to a solid surface, is a fundamental property in porous media. Due to significant interaction between solid and fluids generated through extensive fluid–solid interfaces in porous media environment, surface properties like wettability can significantly affect fluid phases behavior with the solid (capillary trapping) and between each other (mass transfer). Thus, understanding the mechanisms of how wettability affects CO_2 trapping and dissolution is crucial for improving long-term storage predictions.

To address the complexity of CO_2 trapping processes, a pore-scale experimental approach needed to be adopted to isolate fundamental mechanisms and capture dynamic mass transfer within an accessible timeframe. A multidisciplinary methodology combining microfluidics, µRaman spectroscopy, and plasma surface treatment was deployed to enable this investigation. Microfluidic devices with two geometries (single pocket and L-pore) were designed to replicate simplified rock structures, allowing visual observation of fluid configurations and precise control over surface properties. Advanced image processing techniques were applied to analyze fluid displacement and trapping patterns. *In situ* chemical species evolution during interfacial mass transfer was monitored using micro-Raman spectroscopy. Atmospheric pressure plasma treatment was employed to modify wettability inside closed microfluidic devices. This experimental platform enabled a detailed investigation of the physical and chemical mechanisms governing wettability-driven CO_2 storage at the pore scale, particularly under dynamic drainage conditions that are representative of realistic subsurface processes.

Building on this foundation, the specific scientific questions addressed in this thesis were:

1. Can plasma be propagated and utilized for *in situ* wettability treatment of closed glass microfluidic devices?
2. How does wettability influence capillary trapping and interfacial mass transfer between CO_2 and water at the pore scale?
3. Can the fluid-fluid interfacial mass transfer process be effectively monitored by tracking chemical species evolution using Raman spectroscopy?

By answering these questions, this work advances the understanding of pore-scale CO_2 sequestration mechanisms and provides a foundation for refining larger-scale models and field-scale storage assessments. Building upon the experimental insights gained through this integrated approach, the following sections summarize the key findings of the thesis, discuss their implications for pore- and reservoir-scale CO_2 storage, and outline recommendations for future research directions.

The first challenge that we addressed was to control the wettability of our microfluidic devices. A significant challenge in studying wettability in microfluidic systems lies in the difficulty of modifying wettability in a controlled, reversible, and localized manner. For this purpose, we developed atmospheric pressure plasma treatment as an innovative solution to alter wettability in a microfluidic setting. Compared to classical chemical treatments plasma treatment is fast, simple, and modifies only the surface without affecting the bulk material. However, plasma-based methods used to suffer from aging effects, where the induced wettability gradually diminishes over time. Moreover, low-pressure plasma treatments were associated with propagation challenges in confined spaces, making it difficult to treat the surfaces of closed microfluidic devices. To tackle those challenges, our setup deploys atmospheric pressure plasma optimized for *in situ* treatment. By using a kHz helium plasma in a dielectric barrier discharge (DBD)-like configuration, we demonstrated that plasma treatment could efficiently alter the wettability of closed glass microfluidic devices, enabling the creation of surfaces with varying degrees of hydrophilicity.

Specifically, we demonstrated effective plasma propagation in microfluidic devices of varying complexity, with channel cross-sections as small as 250 × 100 µm. Our results showed that plasma treatment could rapidly modify the surface wettability of glass, achieving significant reductions in contact angle, up to 60°, within just one minute of exposure. The treated surfaces exhibited enhanced wettability stability, maintaining hydrophilic states for up to three days when stored in water and one day in air, both representing improvements over previously reported values. While air-stored devices gradually returned to their original wettability after two weeks, water-stored samples retained much of the induced hydrophilicity, remaining stable for up to 70 days. Importantly, devices are successfully retreated with plasma, restoring their hydrophilic performance and demonstrating their reusability. The plasma-induced wettability changes were attributed to the cleaning and functionalization of the glass surface, which reduced carbon contamination and introduced various hydrophilic functional groups (e.g., carboxyl and amino groups) that enhanced the surface's affinity for water. This novel *in situ* modification of wettability in closed microfluidic devices enabled us to study the effect of wettability on mass transfer processes in a well-controlled way.

This work paves the way for expanding the plasma-based platform toward a full range of contact angles, including mixed-wet conditions, to better mimic natural porous media. Future efforts will focus on applying this approach to more complex geometries and diverse materials, while also continuing to improve the long-term stability of wettability treatments.

To explore the influence of wettability on capillary and dissolution trapping of CO_2, we conducted a series of two-phase microfluidic experiments in drainage and imbibition injection mode, across a range of pressure potentials in two microfluidic geometries. In drainage, we trap water by displacing it from the microchannel with CO_2 and in imbibition, we trap CO_2 by displacing it with water. By using CO_2 and water as analogs for injection and reservoir fluids, we were able to simulate processes during geological storage of CO_2, focusing on characteristic patterns of capillary and solubility trapping at the pore scale.

We assessed capillary trapping behavior by measuring the initial volume of fluids retained in the main geometrical feature. The CO_2 capillary trapping potential during imbibition showed minimal variation of the initially trapped gas volume across the tested contact angle range, irrespective of the complexity of the geometry.

In contrast, drainage experiments revealed that water trapping potential was strongly influenced by surface wettability, although the complexity of the trapping element geometry also contributed. Namely, single pocket geometry traps more water at a lower contact angle (23°), while L-pore tends to trap more water at a higher contact angle (59°). Moreover, at lower contact angles, especially on superhydrophilic surfaces, substantial water volumes in the form of films, droplets, and corner accumulations remain mobile and well-connected along the microchannel walls. As the contact angle increased, the trapped water volumes became less mobile and more spatially disconnected.

When comparing the capillary trapping potential between the two fluids, we observe that relatively more water is trapped in the single pocket geometry as microchannel surfaces are hydrophilic. However, a more complex L-pore geometry did not exhibit a noteworthy preference for trapping one or the other fluid regardless of wettability. Relative to the theoretical maximum capacity, the highest overall fluid trapping in the main geometrical feature was observed during the drainage in a single pocket design at a contact angle of 23°, where nearly the full feature capacity was utilized for trapping water.

After trapping one of the fluid phases in the feature of the channel, we evaluated pore-scale mass transfer. During imbibition and in the context of CO_2 dissolution, we observed 2 regimes of dissolution: the initial one dominated by advection and the later one dominated by diffusion. Through analysis of experimental data, wettability was found to play a more prominent role in the later stages of mass transfer, where diffusion dominates. More hydrophilic surfaces exhibited faster dissolution rates due to increased interfacial area and capillary pressure. These trends were consistent across both evaluated geometries. Quantitatively, in the single pocket geometry, the overall mass transfer coefficient was on the order of a few μm/s. In the L-pore geometry, moderately hydrophilic surfaces showed mass transfer rates around 10^{-1} μm/s, while superhydrophilic surfaces reached values between 10^{0} and 10^{1} μm/s. These results suggest that both wettability and geometric complexity influence mass transfer. Within the tested range, no strong dependence of the overall dissolution rate on imposed pressure difference was observed.

During drainage, we identified two regimes: the initial “wet” and the following “dry” regime. During the “wet” regime, hydrophilic surfaces facilitated strong water transport in and out of the trapping element, not only due to interfacial mass transfer but also due to the contribution of film and corner flows. Once all residual water in the microchannel and tubing has evaporated, the CO_2 stream is no longer pre-saturated with water vapor, marking the start of the “dry” evaporation regime. In the single pocket geometry, wettability played a critical role in water evaporation, particularly during the initial “wet surface” phase. During this period, lower contact angles resulted in higher evaporation rates, with divergence between different wettability conditions becoming more pronounced as the imposed pressure difference increased. The resulting overall mass transfer coefficients increased with pressure difference and were predominantly on the order of 10^{-1} μm/s. In contrast, the dominant mass transfer mechanism in the L-pore geometry was corner flow, which led to significantly higher rates reaching up to 10^5 μm/s, favored at superhydrophilic conditions. The overall rates in both geometries correlated proportionately with imposed pressure differences.

Thus, when comparing the two mass transfer directions, dissolution is a faster process than evaporation, however, transport through film and corner flow on superhydrophilic surfaces during drainage outperforms them both. The total time required for complete dissolution or evaporation of trapped fluids is influenced by both capillary trapping (trapped volume) and the rate of interfacial mass transfer. These findings underscore the importance of wettability in both trapping and pore-scale transport. While wettability strongly affects the early-stage process of water evaporation during drainage, its influence during imbibition becomes even more critical during the diffusion-limited phase of CO_2 dissolution.

Since the emphasis is on CO_2 storage, this study confirms that while wettability in the tested hydrophilic range does not significantly influence capillary trapping, it plays a critical role in interfacial mass transfer during CO_2 dissolution. Specifically, more hydrophilic surfaces enhance mass transfer rates, which may contribute to more efficient and secure long-term CO_2 storage. Although previous research has linked wettability to interfacial mass transfer, primarily through its impact on interfacial area, experimental evidence at the pore scale has remained limited. This thesis addresses that gap by providing direct observations and quantification of mass transfer processes under controlled wettability conditions. Importantly, the findings suggest that wettability influences mass transfer not only through changes in interfacial area but also via capillary pressure driven by interface curvature, and potentially through surface roughness effects. By identifying distinct mass transfer regimes and highlighting those where wettability exerts the strongest effect, this work advances our understanding of pore-scale phenomena relevant to geological carbon sequestration.

Future research on interfacial mass transfer using microfluidics should focus on implementing more complex geometries, particularly parallel and serial arrangements of trapping elements. This will allow for a slight upscaling of the system and help assess potential interactions between adjacent pore bodies. Our findings have shown that residual water volumes along microchannels and tubing create a persistent wet regime, suggesting that such effects may influence neighboring elements in more realistic pore networks. Additionally, investigating the impact of mixed

wettability in these complex geometries will be essential for better representing natural porous media.

Another key perspective involves collaboration with Heriot-Watt University, which will enable the comparison of experimental results with numerical simulations. This offers a valuable opportunity to validate and calibrate pore-scale models, thereby improving the accuracy of predictions related to CO_2 storage performance. Challenges that may emerge during this calibration process could, in turn, require new experimental investigations to address unresolved phenomena (e.g., the influence of supercritical CO_2).

To complement the visual observations of mass transfer dynamics, we incorporated micro-Raman spectroscopy as a powerful tool for real-time, *in situ* chemical analysis of the species evolution during CO_2 dissolution. Despite the difficulty with fluorescence coming from the material of the microfluidic devices, following the signal optimization, we were able to qualitatively and semi-quantitatively describe the process. At first, we identified the species, putting a primary focus on the CO_2 species. Besides the bending and stretching band of water, the Fermi diad of gaseous CO_2, with the spectral analysis we were able to observe a signal of dissolved, hydrated CO_2 species ($CO_{2(aq)}$). The signal of $CO_{2(aq)}$ is essentially a Fermi diad shifted to lower wavenumber with broad peaks. The signals of carbonic acid or its byproducts, carbonate and bicarbonate ions, were not detected, which is consistent with the literature. The intensity of both $CO_{2(g)}$ and $CO_{2(aq)}$ signal reveals linear scaling with pressure, indicating the signal intensity as a good proxy of the quantity of CO_2 in the system.

The application of Raman spectroscopy also allowed us to observe CO_2 dissolution kinetics and evaluate the impact of surface wettability by pointing the laser at the fixed location and tracking the species evolution in time. The results on the single pocket indicate a rapid increase in $CO_{2(aq)}$ signal intensity within the first minute or two of the process, while on L-pore, the evolution is more gradual. Following the initial period, the signal intensity appears to enter a steady state with minor differences influenced by the wettability and applied pressure differences. This behavior indicates that mass transfer in the case of CO_2 dissolution is a rapid process with the time-scale dependent on pore volume and architecture. With these results, we demonstrate the potential of Raman spectroscopy for qualitative and semi-quantitative tracking of CO_2 dissolution in microfluidic systems.

The perspectives in the domain of spectroscopic analysis include improving the platform with hardware updates to provide better time resolution of kinetic experiments and developing a more robust framework for quantifying dissolution dynamics. Furthermore, comparison of experimental data with models shall be established as well.

In conclusion, this multidisciplinary experimental study sheds new light on how wettability influences mass transfer at the pore scale, offering critical insights into the behavior of CO_2 in porous media. By identifying distinct mass transfer regimes and clarifying when wettability plays a decisive role, the research highlights that more hydrophilic conditions generally promote higher

CO_2 dissolution rates. These findings deepen our fundamental understanding of pore-scale processes and address a key knowledge gap in wettability-dependent mass transfer. The results are directly relevant to carbon storage, as they support the calibration of pore-scale models that can, in turn, improve larger-scale reservoir simulations. Through such model integration and upscaling strategies, insights from controlled microfluidic experiments can inform more accurate predictions of CO_2 trapping efficiency and long-term storage security. Ultimately, this work contributes to the design of safer and more effective geological storage strategies.

References

1. Abou Rich, S., Leroy, P., Dufour, T., Wehbe, N., Houssiau, L., Reniers, F., 2014. In-depth diffusion of oxygen into LDPE exposed to an Ar–O_2 atmospheric post-discharge: a complementary approach between AR-XPS and Tof-SIMS techniques. Surface & Interface Analysis 46, 164–174. https://doi.org/10.1002/sia.5403

2. Agada, S., Kolster, C., Williams, G., Vosper, H., MacDowell, N., Krevor, S., 2017. Sensitivity Analysis of the Dynamic CO2 Storage Capacity Estimate for the Bunter Sandstone of the UK Southern North Sea. Energy Procedia 114, 4564–4570. https://doi.org/10.1016/j.egypro.2017.03.1575

3. Agaoglu, B., Copty, N.K., Scheytt, T., Hinkelmann, R., 2015. Interphase mass transfer between fluids in subsurface formations: A review. Advances in Water Resources 79, 162–194. https://doi.org/10.1016/j.advwatres.2015.02.009

4. Ajayi, T., Gomes, J.S., Bera, A., 2019. A review of CO2 storage in geological formations emphasizing modeling, monitoring and capacity estimation approaches. Pet. Sci. 16, 1028–1063. https://doi.org/10.1007/s12182-019-0340-8

5. Akbarabadi, M., Piri, M., 2013. Relative permeability hysteresis and capillary trapping characteristics of supercritical CO2/brine systems: An experimental study at reservoir conditions. Advances in Water Resources 52, 190–206. https://doi.org/10.1016/j.advwatres.2012.06.014

6. Akbari, R., Antonini, C., 2021. Contact angle measurements: From existing methods to an open-source tool. Advances in Colloid and Interface Science 294, 102470. https://doi.org/10.1016/j.cis.2021.102470

7. Al-Harbi, L.M., Darwish, M.S.A., Khowdiary, M.M., Stibor, I., 2018. Controlled Preparation of Thermally Stable Fe-Poly(dimethylsiloxane) Composite by Magnetic Induction Heating. Polymers 10, 507. https://doi.org/10.3390/polym10050507

8. Al-Khdheeawi, E.A., Vialle, S., Barifcani, A., Sarmadivaleh, M., Iglauer, S., 2018. Effect of wettability heterogeneity and reservoir temperature on CO2 storage efficiency in deep saline aquifers. International Journal of Greenhouse Gas Control 68, 216–229. https://doi.org/10.1016/j.ijggc.2017.11.016

9. Al-Khdheeawi, E.A., Vialle, S., Barifcani, A., Sarmadivaleh, M., Iglauer, S., 2017. Influence of Rock Wettability on CO2 Migration and Storage Capacity in Deep Saline Aquifers. Energy Procedia 114, 4357–4365. https://doi.org/10.1016/j.egypro.2017.03.1587

10. Amarasinghe, W., Fjelde, I., Rydland, J.-A., Guo, Y., 2019. Effects of Permeability and Wettability on CO2 Dissolution and Convection at Realistic Saline Reservoir Conditions: A Visualization Study, in: Day 4 Thu, June 06, 2019. Presented at the SPE Europec featured

at 81st EAGE Conference and Exhibition, SPE, London, England, UK, p. D041S008R003. https://doi.org/10.2118/195469-MS

11. Aminu, M.D., Nabavi, S.A., Rochelle, C.A., Manovic, V., 2017. A review of developments in carbon dioxide storage. Applied Energy 208, 1389–1419. https://doi.org/10.1016/j.apenergy.2017.09.015

12. Anderson, W.G., 1987a. Wettability Literature Survey- Part 4: Effects of Wettability on Capillary Pressure. Journal of Petroleum Technology 39, 1283–1300. https://doi.org/10.2118/15271-PA

13. Anderson, W.G., 1987b. Wettability Literature Survey Part 5: The Effects of Wettability on Relative Permeability. Journal of Petroleum Technology 39, 1453–1468. https://doi.org/10.2118/16323-PA

14. Anderson, W.G., 1986. Wettability Literature Survey- Part 1: Rock/Oil/Brine Interactions and the Effects of Core Handling on Wettability. Journal of Petroleum Technology 38, 1125–1144. https://doi.org/10.2118/13932-PA

15. Ansari, A., Imoukhuede, P.I., 2018. Plenty more room on the glass bottom: Surface functionalization and nanobiotechnology for cell isolation. Nano Res. 11, 5107–5129. https://doi.org/10.1007/s12274-018-2177-7

16. Arif, M., Abu-Khamsin, S.A., Iglauer, S., 2019. Wettability of rock/CO2/brine and rock/oil/CO2-enriched-brine systems:Critical parametric analysis and future outlook. Advances in Colloid and Interface Science 268, 91–113. https://doi.org/10.1016/j.cis.2019.03.009

17. Arif, M., Al-Yaseri, A.Z., Barifcani, A., Lebedev, M., Iglauer, S., 2016. Impact of pressure and temperature on CO 2 –brine–mica contact angles and CO 2 –brine interfacial tension: Implications for carbon geo-sequestration. Journal of Colloid and Interface Science 462, 208–215. https://doi.org/10.1016/j.jcis.2015.09.076

18. Arif, M., Lebedev, M., Barifcani, A., Iglauer, S., 2017. CO2 storage in carbonates: Wettability of calcite. International Journal of Greenhouse Gas Control 62, 113–121. https://doi.org/10.1016/j.ijggc.2017.04.014

19. Arkles, B., 2011. Hydrophobicity, hydrophilicity and silane surface modification [WWW Document]. Gelest technical library. URL https://technical.gelest.com/brochures/hydrophobicity-hydrophilicity-and-silane-surface-modification/hydrophobicity-hydrophilicity-and-silane-surface-modification/

20. Aryana, S.A., Kovscek, A.R., 2012. Experiments and analysis of drainage displacement processes relevant to carbon dioxide injection. Phys. Rev. E 86, 066310. https://doi.org/10.1103/PhysRevE.86.066310

21. Avramov, I., Vassilev, Ts., Penkov, I., 2005. The glass transition temperature of silicate and borate glasses. Journal of Non-Crystalline Solids 351, 472–476. https://doi.org/10.1016/j.jnoncrysol.2005.01.044

22. Aziz, G., Thukkaram, M., De Geyter, N., Morent, R., 2017. Plasma parameters effects on the properties, aging and stability behaviors of allylamine plasma coated ultra-high molecular weight polyethylene (UHMWPE) films. Applied Surface Science 409, 381–395. https://doi.org/10.1016/j.apsusc.2017.03.027

23. Babich, L., Loiko, T.V., 2016. Generalized Paschen's Law for Overvoltage Conditions. IEEE Trans. Plasma Sci. 44, 3243–3248. https://doi.org/10.1109/TPS.2016.2629022

24. Bachu, S., Adams, J.J., 2003. Sequestration of CO2 in geological media in response to climate change: capacity of deep saline aquifers to sequester CO2 in solution. Energy Conversion and Management 44, 3151–3175. https://doi.org/10.1016/S0196-8904(03)00101-8

25. Bae, G., Park, T., Song, I.-H., 2022. Surface Modification of Polymethylmethacrylate (PMMA) by Ultraviolet (UV) Irradiation and IPA Rinsing. Micromachines 13, 1952. https://doi.org/10.3390/mi13111952

26. Bandara, U.C., Tartakovsky, A.M., Palmer, B.J., 2011. Pore-scale study of capillary trapping mechanism during CO2 injection in geological formations. International Journal of Greenhouse Gas Control 5, 1566–1577. https://doi.org/10.1016/j.ijggc.2011.08.014

27. Belgodere, C., Dubessy, J., Vautrin, D., Caumon, M., Sterpenich, J., Pironon, J., Robert, P., Randi, A., Birat, J., 2015. Experimental determination of CO_2 diffusion coefficient in aqueous solutions under pressure at room temperature via Raman spectroscopy: impact of salinity (NaCl). J Raman Spectroscopy 46, 1025–1032. https://doi.org/10.1002/jrs.4742

28. Berg, S., Armstrong, R., Ott, H., Georgiadis, A., Klapp, S.A., Schwing, A., Neiteler, R., Brussee, N., Makurat, A., Leu, L., Enzmann, F., Schwarz, J.-O., Wolf, M., Khan, F., Kersten, M., Irvine, S., Stampanoni, M., 2014. Multiphase Flow in Porous Rock Imaged Under Dynamic Flow Conditions with Fast X-Ray Computed Microtomography. Petrophysics - The SPWLA Journal of Formation Evaluation and Reservoir Description 55, 304–312.

29. Berndt, J., Acid, H., Kovacevic, E., Cachoncinlle, C., Strunskus, Th., Boufendi, L., 2013. Deposition and tuning of nanostructured hydrocarbon deposits: From superhydrophobic to superhydrophilic and back. Journal of Applied Physics 113, 063302. https://doi.org/10.1063/1.4789949

30. Bhattacharya, S., Datta, A., Berg, J.M., Gangopadhyay, S., 2005. Studies on surface wettability of poly(dimethyl) siloxane (PDMS) and glass under oxygen-plasma treatment

and correlation with bond strength. J. Microelectromech. Syst. 14, 590–597. https://doi.org/10.1109/JMEMS.2005.844746

31. Biesinger, M., 2021. Using Adventitious Carbon for Charge Correcting [WWW Document]. X-ray Photoelectron Spectroscopy (XPS) Reference Pages. URL http://www.xpsfitting.com/search/label/Adventitious

32. Bigelow, W.C., Pickett, D.L., Zisman, W.A., 1946. Oleophobic monolayers: I. Films adsorbed from solution in non-polar liquids☆. Journal of Colloid Science 1, 513–538.

33. Blunt, M.J., Scher, H., 1995. Pore-level modeling of wetting. Phys. Rev. E 52, 6387–6403. https://doi.org/10.1103/PhysRevE.52.6387

34. Boeuf, J.-P., Yang, L.L., Pitchford, L.C., 2013. Dynamics of a guided streamer ('plasma bullet') in a helium jet in air at atmospheric pressure. J. Phys. D: Appl. Phys. 46, 015201. https://doi.org/10.1088/0022-3727/46/1/015201

35. Booth, J.-P., Mozetič, M., Nikiforov, A., Oehr, C., 2022. Foundations of plasma surface functionalization of polymers for industrial and biological applications. Plasma Sources Sci. Technol. 31, 103001. https://doi.org/10.1088/1361-6595/ac70f9

36. Borcia, G., Brown, N.M.D., 2007. Hydrophobic coatings on selected polymers in an atmospheric pressure dielectric barrier discharge. J. Phys. D: Appl. Phys. 40, 1927–1936. https://doi.org/10.1088/0022-3727/40/7/015

37. Bouquet, S., Bruel, D., de Fouquet, C., 2013. Influence of Heterogeneities and Upscaling on CO2 Storage Prediction at Large Scale in Deep Saline Aquifer. Energy Procedia 37, 4445–4456. https://doi.org/10.1016/j.egypro.2013.06.349

38. Brahme, A., Chang, Z., Zhao, N., Kondeti, V.S.S.K., Bruggeman, P.J., 2018. Penetration of Ar and He RF-driven plasma jets into micrometer-sized capillary tubes. J. Phys. D: Appl. Phys. 51, 414002. https://doi.org/10.1088/1361-6463/aad883

39. Brandenburg, R., 2017. Dielectric barrier discharges: progress on plasma sources and on the understanding of regimes and single filaments. Plasma Sources Sci. Technol. 26, 053001. https://doi.org/10.1088/1361-6595/aa6426

40. Breden, D., Miki, K., Raja, L.L., 2012. Self-consistent two-dimensional modeling of cold atmospheric-pressure plasma jets/bullets. Plasma Sources Sci. Technol. 21, 034011. https://doi.org/10.1088/0963-0252/21/3/034011

41. Bretherton, F.P., 1961. The motion of long bubbles in tubes. J. Fluid Mech. 10, 166–188. https://doi.org/10.1017/S0022112061000160

42. Broseta, D., Tonnet, N., Shah, V., 2012. Are rocks still water-wet in the presence of dense CO 2 or H 2 S?: Wettability alteration of rocks by acid gases. Geofluids 12, 280–294. https://doi.org/10.1111/j.1468-8123.2012.00369.x

43. Burke, E.A., 2001. Raman microspectrometry of fluid inclusions. Lithos 55, 139–158.

44. Busch, A., Müller, N., 2011. Determining CO2 /brine relative permeability and capillary threshold pressures for reservoir rocks and caprocks: Recommendations for development of standard laboratory protocols. Energy Procedia 4, 6053–6060. https://doi.org/10.1016/j.egypro.2011.02.610

45. Butt, H.-J., Liu, J., Koynov, K., Straub, B., Hinduja, C., Roismann, I., Berger, R., Li, X., Vollmer, D., Steffen, W., Kappl, M., 2022. Contact angle hysteresis. Current Opinion in Colloid & Interface Science 59, 101574. https://doi.org/10.1016/j.cocis.2022.101574

46. Carey, D.M., Korenowski, G.M., 1998. Measurement of the Raman spectrum of liquid water. The Journal of Chemical Physics 108, 2669–2675. https://doi.org/10.1063/1.475659

47. Cassie, A.B.D., Baxter, S., 1944. Wettability of porous surfaces. Trans. Faraday Soc. 40, 546. https://doi.org/10.1039/tf9444000546

48. Caumon, M.-C., Sterpenich, J., Randi, A., Pironon, J., 2016. Measuring mutual solubility in the H2O–CO2 system up to 200bar and 100°C by in situ Raman spectroscopy. International Journal of Greenhouse Gas Control 47, 63–70. https://doi.org/10.1016/j.ijggc.2016.01.034

49. Celia, M.A., Bachu, S., Nordbotten, J.M., Bandilla, K.W., 2015. Status of CO_2 storage in deep saline aquifers with emphasis on modeling approaches and practical simulations: STATUS OF CO_2 STORAGE IN DEEP SALINE AQUIFERS. Water Resour. Res. 51, 6846–6892. https://doi.org/10.1002/2015WR017609

50. Chalbaud, C., Robin, M., Békri, S., Egermann, P., 2007. Wettability impact on CO2 storage in aquifers: visualization and quantification using micromodel tests, pore network model and reservoir simulations. SCA International Symposium, Calgary, September.

51. Chang, C., Zhou, Q., Oostrom, M., Kneafsey, T.J., Mehta, H., 2017. Pore-scale supercritical CO2 dissolution and mass transfer under drainage conditions. Advances in Water Resources 100, 14–25. https://doi.org/10.1016/j.advwatres.2016.12.003

52. Chang, Z.-S., Zhang, G.-J., Shao, X.-J., Zhang, Z.-H., 2012. Diagnosis of gas temperature, electron temperature, and electron density in helium atmospheric pressure plasma jet. Physics of Plasmas 19, 073513. https://doi.org/10.1063/1.4739060

53. Chatzis, I., Morrow, N.R., Lim, H.T., 1983. Magnitude and Detailed Structure of Residual Oil Saturation. Society of Petroleum Engineers Journal 23, 311–326. https://doi.org/10.2118/10681-PA

54. Chaudhary, K., Bayani Cardenas, M., Wolfe, W.W., Maisano, J.A., Ketcham, R.A., Bennett, P.C., 2013. Pore-scale trapping of supercritical CO_2 and the role of grain wettability and shape: PORE-SCALE CONTROLS ON TRAPPING OF s-CO_2. Geophys. Res. Lett. 40, 3878–3882. https://doi.org/10.1002/grl.50658

55. Chen, L., Wang, M., Kang, Q., Tao, W., 2018. Pore scale study of multiphase multicomponent reactive transport during CO2 dissolution trapping. Advances in Water Resources 116, 208–218. https://doi.org/10.1016/j.advwatres.2018.02.018

56. Chevalier, R.B., Dwyer, J.R., 2021. Optimizing noncontact oxygen-plasma treatment to improve the performance of a top-down nanofabricated surface enhanced Raman spectroscopy substrate with structurally responsive, high-aspect-ratio nanopillar array. J Raman Spectroscopy 52, 608–615. https://doi.org/10.1002/jrs.6050

57. Chiquet, P., Broseta, D., Thibeau, S., 2007. Wettability alteration of caprock minerals by carbon dioxide. Geofluids 7, 112–122. https://doi.org/10.1111/j.1468-8123.2007.00168.x

58. Choi, K.Y., Sultan, Md.T., Ajiteru, O., Hong, H., Lee, Y.J., Lee, Ji Seung, Lee, H., Lee, O.J., Kim, S.H., Lee, Joong Seob, Park, S.-J., Eden, J.G., Park, C.H., 2021. Treatment of Fungal-Infected Diabetic Wounds with Low Temperature Plasma. Biomedicines 10, 27. https://doi.org/10.3390/biomedicines10010027

59. Chrimes, A.F., Khoshmanesh, K., Stoddart, P.R., Mitchell, A., Kalantar-zadeh, K., 2013. Microfluidics and Raman microscopy: current applications and future challenges. Chem. Soc. Rev. 42, 5880. https://doi.org/10.1039/c3cs35515b

60. Chuah, Y.J., Koh, Y.T., Lim, K., Menon, N.V., Wu, Y., Kang, Y., 2015. Simple surface engineering of polydimethylsiloxane with polydopamine for stabilized mesenchymal stem cell adhesion and multipotency. Sci Rep 5, 18162. https://doi.org/10.1038/srep18162

61. Chung, T.-H., Stancampiano, A., Sklias, K., Gazeli, K., André, F., Dozias, S., Douat, C., Pouvesle, J.-M., Santos Sousa, J., Robert, É., Mir, L., 2020. Cell Electropermeabilisation Enhancement by Non-Thermal-Plasma-Treated PBS. Cancers 12, 219. https://doi.org/10.3390/cancers12010219

62. Clement, F., Svarnas, P., Marlin, L., Gkelios, A., Held, B., 2011. Atmospheric-Pressure Plasma Microjet of Argon–Nitrogen Mixtures Directed by Dielectric Flexible Tubes. IEEE Trans. Plasma Sci. 39, 2364–2365. https://doi.org/10.1109/TPS.2011.2159246

63. Clingerman, J., Bebak, J., Mazik, P.M., Summerfelt, S.T., 2007. Use of avoidance response by rainbow trout to carbon dioxide for fish self-transfer between tanks. Aquacultural Engineering 37, 234–251. https://doi.org/10.1016/j.aquaeng.2007.07.001

64. Concus, P., Finn, R., 1969. ON THE BEHAVIOR OF A CAPILLARY SURFACE IN A WEDGE. Proc. Natl. Acad. Sci. U.S.A. 63, 292–299. https://doi.org/10.1073/pnas.63.2.292

65. Craig, F.C., 1971. The Reservoir Engineering Aspects of Waterflooding. Monograph Series, Society of Petroleum Engineers of AIME.

66. Cross, P.C., Burnham, J., Leighton, P.A., 1937. The Raman Spectrum and the Structure of Water. J. Am. Chem. Soc. 59, 1134–1147. https://doi.org/10.1021/ja01285a052

67. Da Silva, A.R.M., Farias, M.L., Da Silva, D.L.S., Vitoriano, J.O., De Sousa, R.C., Alves-Junior, C., 2017. Using atmospheric plasma to increase wettability, imbibition and germination of physically dormant seeds of Mimosa Caesalpiniafolia. Colloids and Surfaces B: Biointerfaces 157, 280–285. https://doi.org/10.1016/j.colsurfb.2017.05.063

68. Dai, X., Stogin, B.B., Yang, S., Wong, T.-S., 2015. Slippery Wenzel State. ACS Nano 9, 9260–9267. https://doi.org/10.1021/acsnano.5b04151

69. Danckwerts, P.V., 1951. Significance of Liquid-Film Coefficients in Gas Absorption. Ind. Eng. Chem. 43, 1460–1467. https://doi.org/10.1021/ie50498a055

70. De Chalendar, J.A., Garing, C., Benson, S.M., 2018. Pore-scale modelling of Ostwald ripening. J. Fluid Mech. 835, 363–392. https://doi.org/10.1017/jfm.2017.720

71. Deleau, T., Fechter, M.H.H., Letourneau, J.-J., Camy, S., Aubin, J., Braeuer, A.S., Espitalier, F., 2020. Determination of mass transfer coefficients in high-pressure two-phase flows in capillaries using Raman spectroscopy. Chemical Engineering Science 228, 115960. https://doi.org/10.1016/j.ces.2020.115960

72. Delshad, M., Najafabadi, N.F., Anderson, G.A., Pope, G.A., Sepehrnoori, K., 2009. Modeling Wettability Alteration by Surfactants in Naturally Fractured Reservoirs. SPE Reservoir Evaluation & Engineering 12, 361–370. https://doi.org/10.2118/100081-PA

73. Deng, X., Kamal, M.S., Patil, S., Hussain, S.M.S., Zhou, X., 2020. A Review on Wettability Alteration in Carbonate Rocks: Wettability Modifiers. Energy Fuels 34, 31–54. https://doi.org/10.1021/acs.energyfuels.9b03409

74. Dodds, W.S., Stutzman, L.F., Sollami, B.J., 1956. Carbon Dioxide Solubility in Water. Ind. Eng. Chem. Chem. Eng. Data Series 1, 92–95. https://doi.org/10.1021/i460001a018

75. Dou, Y., Li, F., Tang, B., Zhou, G., 2021. Surface Wettability Tuning of Acrylic Resin Photoresist and Its Aging Performance. Sensors 21, 4866. https://doi.org/10.3390/s21144866

76. Douat, C., Kacem, I., Sadeghi, N., Bauville, G., Fleury, M., Puech, V., 2016. Space-time resolved density of helium metastable atoms in a nanosecond pulsed plasma jet: influence of high voltage and pulse frequency. J. Phys. D: Appl. Phys. 49, 285204. https://doi.org/10.1088/0022-3727/49/28/285204

77. Duan, Z., Sun, R., 2003. An improved model calculating CO2 solubility in pure water and aqueous NaCl solutions from 273 to 533 K and from 0 to 2000 bar. Chemical Geology 193, 257–271. https://doi.org/10.1016/S0009-2541(02)00263-2

78. Duan, Z., Sun, R., Zhu, C., Chou, I.-M., 2006. An improved model for the calculation of CO2 solubility in aqueous solutions containing Na+, K+, Ca2+, Mg2+, Cl−, and SO42−. Marine Chemistry 98, 131–139. https://doi.org/10.1016/j.marchem.2005.09.001

79. Egghe, T., Narimisa, M., Ghobeira, R., Nisol, B., Onyshchenko, Y., Hoogenboom, R., Morent, R., De Geyter, N., 2022. Comparison of the physicochemical properties and aging behavior of two different APTES-derived plasma polymer-based coatings. Surface and Coatings Technology 449, 128945. https://doi.org/10.1016/j.surfcoat.2022.128945

80. Eiken, O., 2019. Twenty Years of Monitoring CO2 Injection at Sleipner, in: Davis, T.L., Landrø, M., Wilson, M. (Eds.), Geophysics and Geosequestration. Cambridge University Press, pp. 209–234. https://doi.org/10.1017/9781316480724.014

81. Ellis, D.I., Goodacre, R., 2006. Metabolic fingerprinting in disease diagnosis: biomedical applications of infrared and Raman spectroscopy. Analyst 131, 875. https://doi.org/10.1039/b602376m

82. Encyclopedia Britannica, 2012. ionization energy. Encyclopedia Britannica.

83. Espinoza, D.N., Santamarina, J.C., 2010. Water-CO_2 -mineral systems: Interfacial tension, contact angle, and diffusion-Implications to CO_2 geological storage: WATER CO_2 MINERAL SYSTEMS. Water Resour. Res. 46. https://doi.org/10.1029/2009WR008634

84. Farajzadeh, R., Zitha, P.L.J., Bruining, J., 2009. Enhanced Mass Transfer of CO_2 into Water: Experiment and Modeling. Ind. Eng. Chem. Res. 48, 6423–6431. https://doi.org/10.1021/ie801521u

85. Favier, B., Chamakos, N.T., Papathanasiou, A.G., 2017. A precise goniometer/tensiometer using a low cost single-board computer. Meas. Sci. Technol. 28, 125302. https://doi.org/10.1088/1361-6501/aa8e25

86. Fayed, T.A., 2016. Vibrational Spectroscopy (Infrared, IR-Spect.).

87. Fermi, E., 1931. Über den ramaneffekt des kohlendioxyds. Zeitschrift für Physik 71, 250–259.

88. Ferreira, P., Alves, P., Coimbra, P., Gil, M.H., 2015. Improving polymeric surfaces for biomedical applications: a review. J Coat Technol Res 12, 463–475. https://doi.org/10.1007/s11998-015-9658-3

89. Fioravante, I., Nunes, R., Acciari, H., Codaro, E., 2019. Films Formed on Carbon Steel in Sweet Environments - A Review. J. Braz. Chem. Soc. https://doi.org/10.21577/0103-5053.20190055

90. Fleury, M., Pironon, J., Le Nindre, Y.M., Bildstein, O., Berne, P., Lagneau, V., Broseta, D., Pichery, T., Fillacier, S., Lescanne, M., Vidal, O., 2010. Evaluating Sealing Efficiency of Caprocks for CO $_2$ Storage: an Overview of the Geocarbone-Integrity Program and Results. Oil Gas Sci. Technol. – Rev. IFP 65, 435–444. https://doi.org/10.2516/ogst/2010007

91. Frezzotti, M.L., Tecce, F., Casagli, A., 2012. Raman spectroscopy for fluid inclusion analysis. Journal of Geochemical Exploration 112, 1–20. https://doi.org/10.1016/j.gexplo.2011.09.009

92. Furre, A.-K., Meneguolo, R., Pinturier, L., Bakke, K., 2020. Planning deep subsurface CO2 storage monitoring for the Norwegian full-scale CCS project. First Break 38, 55–60. https://doi.org/10.3997/1365-2397.fb2020074

93. Gao, Z., Henthorn, D.B., Kim, C.-S., 2008. Enhanced wettability of a SU-8 photoresist through a photografting procedure for bioanalytical device applications. J. Micromech. Microeng. 18, 045013. https://doi.org/10.1088/0960-1317/18/4/045013

94. Gaus, I., 2010. Role and impact of CO2–rock interactions during CO2 storage in sedimentary rocks. International Journal of Greenhouse Gas Control 4, 73–89. https://doi.org/10.1016/j.ijggc.2009.09.015

95. Geistlinger, H., Ataei-Dadavi, I., Mohammadian, S., Vogel, H., 2015. The impact of pore structure and surface roughness on capillary trapping for 2-D and 3-D porous media: Comparison with percolation theory. Water Resources Research 51, 9094–9111. https://doi.org/10.1002/2015WR017852

96. Gerhard, C., Weihs, T., Tasche, D., Brückner, S., Wieneke, S., Viöl, W., 2013. Atmospheric Pressure Plasma Treatment of Fused Silica, Related Surface and Near-Surface Effects and Applications. Plasma Chem Plasma Process 33, 895–905. https://doi.org/10.1007/s11090-013-9471-7

97. Glass, N.R., Tjeung, R., Chan, P., Yeo, L.Y., Friend, J.R., 2011. Organosilane deposition for microfluidic applications. Biomicrofluidics 5, 036501. https://doi.org/10.1063/1.3625605

98. Goebel, D.M., Katz, I., 2008. Basic Plasma Physics, in: Fundamentals of Electric Propulsion. John Wiley & Sons, Ltd, pp. 37–90. https://doi.org/10.1002/9780470436448.ch3

99. Goncalves Canane, P.A., 2019. Surface Modification Strategies for Microfluidic Devices (Master thesis). Universidade de Lisboa.

100. Gong, H., Li, Y., Dong, M., Ma, S., Liu, W., 2016. Effect of wettability alteration on enhanced heavy oil recovery by alkaline flooding. Colloids and Surfaces A: Physicochemical and Engineering Aspects 488, 28–35. https://doi.org/10.1016/j.colsurfa.2015.09.042

101. Gredicak, V., Douat, C., Slodczyk, A., Dozias, S., Roman, S., 2025. Wettability alteration of closed glass microfluidic devices by in situ plasma. Microfluidics and Nanofluidics 29, 22. https://doi.org/10.1007/s10404-025-02793-9

102. Guo, H., Chen, Y., Hu, Q., Lu, W., Ou, W., Geng, L., 2014. Quantitative Raman spectroscopic investigation of geo-fluids high-pressure phase equilibria: Part I. Accurate calibration and determination of CO2 solubility in water from 273.15 to 573.15 K and from 10 to 120 MPa. Fluid Phase Equilibria 382, 70–79. https://doi.org/10.1016/j.fluid.2014.08.032

103. Guragain, R.P., Baniya, H.B., Banset, N., Pradhan, S.P., Dhungana, S., Chhetri, G.K., Panta, G.P., Sedhai, B., Shrestha, B., Shrestha, S., Guragain, D.P., Joshi, U.M., Pandey, B.P., Subedi, D.P., 2022. Effects of Plasma-Activated Water on Soybean and Wheat: Germination and Seedling Development. Plasma Med 12, 27–43. https://doi.org/10.1615/PlasmaMed.2022042374

104. Hagiwara, Y., Takahata, K., Torimoto, J., Yamamoto, J., 2018. CO_2 Raman thermometer improvement: Comparing hot band and Stokes and anti-Stokes Raman scattering thermometers. J Raman Spectroscopy 49, 1776–1781. https://doi.org/10.1002/jrs.5461

105. Hagiwara, Y., Torimoto, J., Yamamoto, J., 2020. Pressure measurement and detection of small H_2O amounts in high-pressure H_2O–CO_2 fluid up to 141 MPa using Fermi diad splits and bandwidths of CO_2. J Raman Spectroscopy 51, 1003–1018. https://doi.org/10.1002/jrs.5865

106. Han, D., Moon, S.Y., 2015. Rapid Formation of Transparent Superhydrophobic Film on Glasses by He/CH_4 /C_4F_8 Plasma Deposition at Atmospheric Pressure: Rapid Formation of Transparent Superhydrophobic. Plasma Process. Polym. 12, 172–179. https://doi.org/10.1002/ppap.201400145

107. Han, J., Eimer, D.A., Melaaen, M.C., 2013. Liquid Phase Mass Transfer Coefficient of Carbon Dioxide Absorption by Water Droplet. Energy Procedia 37, 1728–1735. https://doi.org/10.1016/j.egypro.2013.06.048

108. Hansen, G., Hamouda, A.A., Denoyel, R., 2000. The effect of pressure on contact angles and wettability in the mica/water/n-decane system and the calcite+stearic acid/water/n-decane system. Colloids and Surfaces A: Physicochemical and Engineering Aspects 172, 7–16. https://doi.org/10.1016/S0927-7757(99)00498-7

109. He, X., Wang, W.-Q., Liu, Y.-Z., Sun, Q., 2024. Raman Quantitative Measurement on the Cl- Molarity of H2O-NaCl-CO2 System: Application to Fluid Inclusions.

110. Herring, A.L., Sheppard, A., Andersson, L., Wildenschild, D., 2016. Impact of wettability alteration on 3D nonwetting phase trapping and transport. International Journal of Greenhouse Gas Control 46, 175–186. https://doi.org/10.1016/j.ijggc.2015.12.026

111. Herzberg, G., 1945. Molecular spectra and molecular structure. Vol. 2: Infrared and Raman spectra of polyatomic molecules. Molecular spectra and molecular structure. Vol. 2: Infrared and Raman spectra of polyatomic molecules.

112. Hesse, M.A., Orr, F.M., Tchelepi, H.A., 2008. Gravity currents with residual trapping. J. Fluid Mech. 611, 35–60. https://doi.org/10.1017/S002211200800219X

113. Higbie, R., 1935. The Rate of Absorption of a Pure Gas into a Still Liquid during Short Periods of Exposure.

114. Holmberg, K., Matthews, A., 2009. Coatings tribology: properties, mechanisms, techniques and applications in surface engineering, 2. ed. ed, Tribology and interface engineering series. Elsevier, Amsterdam Heidelberg.

115. Holtzman, R., Segre, E., 2015. Wettability Stabilizes Fluid Invasion into Porous Media via Nonlocal, Cooperative Pore Filling. Phys. Rev. Lett. 115, 164501. https://doi.org/10.1103/PhysRevLett.115.164501

116. Hu, Q., Zhao, H., Li, H., Dong, Y., Liu, Z., 2019. Understanding the Raman spectroscopic quantification and dissolving behaviors of CO2 for the CO2–H2O system from water structure. Chemical Physics Letters 717, 47–52. https://doi.org/10.1016/j.cplett.2019.01.005

117. Hu, R., Wan, J., Kim, Y., Tokunaga, T.K., 2017. Wettability impact on supercritical CO $_2$ capillary trapping: Pore-scale visualization and quantification: WETTABILITY ON CO $_2$ CAPILLARY TRAPPING. Water Resour. Res. 53, 6377–6394. https://doi.org/10.1002/2017WR020721

118. Huh, C., Scriven, L.E., 1971. Hydrodynamic model of steady movement of a solid/liquid/fluid contact line. Journal of Colloid and Interface Science 35, 85–101. https://doi.org/10.1016/0021-9797(71)90188-3

119. IEA, 2021a. About CCUS [WWW Document]. URL https://www.iea.org/reports/about-ccus (accessed 9.7.22).

120. IEA, 2021b. Global Energy Review: CO2 Emissions in 2021 Global emissions rebound sharply to highest ever level.

121. Iglauer, S., 2017. CO_2 –Water–Rock Wettability: Variability, Influencing Factors, and Implications for CO_2 Geostorage. Acc. Chem. Res. 50, 1134–1142. https://doi.org/10.1021/acs.accounts.6b00602

122. Iglauer, S., 2011. Dissolution Trapping of Carbon Dioxide in Reservoir Formation Brine – A Carbon Storage Mechanism, in: Nakajima, H. (Ed.), Mass Transfer - Advanced Aspects. InTech. https://doi.org/10.5772/20206

123. Iglauer, S., Paluszny, A., Pentland, C.H., Blunt, M.J., 2011. Residual CO_2 imaged with X-ray micro-tomography: RESIDUAL CO_2 IMAGED WITH TOMOGRAPHY. Geophys. Res. Lett. 38, n/a-n/a. https://doi.org/10.1029/2011GL049680

124. Iglauer, S., Pentland, C.H., Busch, A., 2015. CO_2 wettability of seal and reservoir rocks and the implications for carbon geo-sequestration. Water Resour. Res. 51, 729–774. https://doi.org/10.1002/2014WR015553

125. Iglauer, S., Salamah, A., Sarmadivaleh, M., Liu, K., Phan, C., 2014. Contamination of silica surfaces: Impact on water–CO2–quartz and glass contact angle measurements. International Journal of Greenhouse Gas Control 22, 325–328. https://doi.org/10.1016/j.ijggc.2014.01.006

126. IPCC (Ed.), 2005. IPCC special report on carbon dioxide capture and storage, 1. publ. ed. Cambridge Univ. Press, Cambridge.

127. Ito, H., Hasegawa, T., Tanimura, Y., 2016. Effects of Intermolecular Charge Transfer in Liquid Water on Raman Spectra. J. Phys. Chem. Lett. 7, 4147–4151. https://doi.org/10.1021/acs.jpclett.6b01766

128. Ivanova, A., Mitiurev, N., Cheremisin, A., Orekhov, A., Kamyshinsky, R., Vasiliev, A., 2019. Characterization of Organic Layer in Oil Carbonate Reservoir Rocks and its Effect on Microscale Wetting Properties. Sci Rep 9, 10667. https://doi.org/10.1038/s41598-019-47139-y

129. Jafari, M., Jung, J., 2018. Variation of Contact Angles in Brine/CO_2 /Mica System considering Short-Term Geological CO_2 Sequestration Condition. Geofluids 2018, 1–15. https://doi.org/10.1155/2018/3501459

130. Jahanbakhsh, A., Wlodarczyk, K.L., Hand, D.P., Maier, R.R.J., Maroto-Valer, M.M., 2020. Review of Microfluidic Devices and Imaging Techniques for Fluid Flow Study in Porous Geomaterials. Sensors 20, 4030. https://doi.org/10.3390/s20144030

131. Jain, S., Bruggeman, P.J., 2023. Penetration of a Pulsed Guided Streamer Discharge into Micrometer-Sized Capillary Tubes. Plasma 6, 663–679. https://doi.org/10.3390/plasma6040046

132. Jansen, R.J.J., Van Bekkum, H., 1995. XPS of nitrogen-containing functional groups on activated carbon. Carbon 33, 1021–1027. https://doi.org/10.1016/0008-6223(95)00030-H

133. Javanmard, S., Pouryoussefi, S.G., 2023. Comparison of characteristics of atmospheric pressure plasma jets using argon and helium working gases. Current Applied Physics 46, 61–69. https://doi.org/10.1016/j.cap.2022.12.002

134. Jiang, N., Ji, A., Cao, Z., 2009. Atmospheric pressure plasma jet: Effect of electrode configuration, discharge behavior, and its formation mechanism. Journal of Applied Physics 106, 013308. https://doi.org/10.1063/1.3159884

135. Jitsomboonmit, P., Nisoa, M., Dangtip, S., 2012. Experimental Study of Current-Voltage Characteristics and Optical Emission of Various Gases in Dielectric Barrier Discharge at Atmospheric Pressure. Physics Procedia 32, 723–731. https://doi.org/10.1016/j.phpro.2012.03.625

136. Jõgi, I., Talviste, R., Raud, J., Piip, K., Paris, P., 2014. The influence of the tube diameter on the properties of an atmospheric pressure He micro-plasma jet. J. Phys. D: Appl. Phys. 47, 415202. https://doi.org/10.1088/0022-3727/47/41/415202

137. Johnson, V.S., Zhu, W., Wang, R., Lo Re, J., Sivaram, S., Mahoney, J., Lopez, J.L., 2011. A Cold Atmospheric-Pressure Helium Plasma Generated in Flexible Tubing. IEEE Trans. Plasma Sci. 39, 2360–2361. https://doi.org/10.1109/TPS.2011.2160737

138. Juanes, R., Spiteri, E.J., Orr, F.M., Blunt, M.J., 2006. Impact of relative permeability hysteresis on geological CO_2 storage: IMPACT OF HYSTERESIS ON GEOLOGICAL CO_2 STORAGE. Water Resour. Res. 42. https://doi.org/10.1029/2005WR004806

139. Jung, M., Brinkmann, M., Seemann, R., Hiller, T., Sanchez de La Lama, M., Herminghaus, S., 2016. Wettability controls slow immiscible displacement through local interfacial instabilities. Phys. Rev. Fluids 1, 074202. https://doi.org/10.1103/PhysRevFluids.1.074202

140. Kakei, R., Ogino, A., Iwata, F., Nagatsu, M., 2010. Production of ultrafine atmospheric pressure plasma jet with nano-capillary. Thin Solid Films 518, 3457–3460. https://doi.org/10.1016/j.tsf.2009.11.055

141. Kassa, A.M., Gasda, S.E., Kumar, K., Radu, F.A., 2020. Impact of Time-Dependent Wettability Alteration on the Dynamics of Capillary Pressure. Advances in Water Resources 142, 103631. https://doi.org/10.1016/j.advwatres.2020.103631

142. Khan, C., Amin, R., Madden, G., 2013. Carbon dioxide injection for enhanced gas recovery and storage (reservoir simulation). Egyptian Journal of Petroleum 22, 225–240. https://doi.org/10.1016/j.ejpe.2013.06.002

143. Kitsara, M., Revet, G., Vartanian-Grimaldi, J.-S., Simon, A., Minguy, M., Miche, A., Humblot, V., Dufour, T., Agbulut, O., 2022. Cyto- and bio-compatibility assessment of plasma-treated polyvinylidene fluoride scaffolds for cardiac tissue engineering. Front. Bioeng. Biotechnol. 10, 1008436. https://doi.org/10.3389/fbioe.2022.1008436

144. König, U., Nitschke, M., Pilz, M., Simon, F., Arnhold, C., Werner, C., 2002. Stability and ageing of plasma treated poly(tetrafluoroethylene) surfaces. Colloids and Surfaces B: Biointerfaces 25, 313–324. https://doi.org/10.1016/S0927-7765(01)00333-2

145. Koutsoyiannis, D., 2012. Clausius–Clapeyron equation and saturation vapour pressure: simple theory reconciled with practice. Eur. J. Phys. 33, 295–305. https://doi.org/10.1088/0143-0807/33/2/295

146. Kovach, K.M., Capadona, J.R., Sen Gupta, A., Potkay, J.A., 2014. The effects of PEG-based surface modification of PDMS microchannels on long-term hemocompatibility: PEG-Based Surface Modification Of PDMS Microchannels. J. Biomed. Mater. Res. n/a-n/a. https://doi.org/10.1002/jbm.a.35090

147. Kovalev, A.V., Yagodnitsyna, A.A., Bilsky, A.V., 2020. Experimental study of dynamic contact angles in liquid-liquid microfluidic plug flow with partial wetting. J. Phys.: Conf. Ser. 1677, 012064. https://doi.org/10.1088/1742-6596/1677/1/012064

148. Kuchin, I., Starov, V., 2015. Hysteresis of Contact Angle of Sessile Droplets on Smooth Homogeneous Solid Substrates via Disjoining/Conjoining Pressure. Langmuir 31, 5345–5352. https://doi.org/10.1021/acs.langmuir.5b01075

149. Kwok, D.Y., Neumann, A.W., 1999. Contact angle measurement and contact angle interpretation. Advances in Colloid and Interface Science 81, 167–249. https://doi.org/10.1016/S0001-8686(98)00087-6

150. Lam, R.K., England, A.H., Smith, J.W., Rizzuto, A.M., Shih, O., Prendergast, D., Saykally, R.J., 2015. The hydration structure of dissolved carbon dioxide from X-ray absorption spectroscopy. Chemical Physics Letters 633, 214–217. https://doi.org/10.1016/j.cplett.2015.05.039

151. Lamour, G., Hamraoui, A., Buvailo, A., Xing, Y., Keuleyan, S., Prakash, V., Eftekhari-Bafrooei, A., Borguet, E., 2010. Contact Angle Measurements Using a Simplified Experimental Setup. J. Chem. Educ. 87, 1403–1407. https://doi.org/10.1021/ed100468u

152. Larkin, P.J., 2011. Infrared and raman spectroscopy: principles and spectral interpretation, 2e ed. ed. Elsevier, Amsterdam.

153. Laroussi, M., Akan, T., 2007. Arc-Free Atmospheric Pressure Cold Plasma Jets: A Review. Plasma Process. Polym. 4, 777–788. https://doi.org/10.1002/ppap.200700066

154. Larson, R.G., Scriven, L.E., Davis, H.T., 1977. Percolation theory of residual phases in porous media. Nature 268, 409–413. https://doi.org/10.1038/268409a0

155. Launay, G., 2018. PyDSA: Drop shape analysis in python.

156. Lee, J.H., Lee, K.S., 2017. Enhanced Wettability Modification and CO $_2$ Solubility Effect by Carbonated Low Salinity Water Injection in Carbonate Reservoirs. Journal of Chemistry 2017, 1–10. https://doi.org/10.1155/2017/8142032

157. Leetaru, H.E., Brown, A.L., Lee, D.W., Senel, O., Coueslan, M.L., 2012. CO2 Injectivity, Storage Capacity, Plume Size, and Reservoir and Seal Integrity of the Ordovician St. Peter Sandstone and the Cambrian Potosi Formation in the Illinois Basin (No. DOE/FE0002068-1). 1 Illinois State Geological Survey Board of Trustees of the University of Illinois.

158. Lefortier, S.G.R., Hamersma, P.J., Bardow, A., Kreutzer, M.T., 2012. Rapid microfluidic screening of CO2 solubility and diffusion in pure and mixed solvents. Lab Chip 12, 3387. https://doi.org/10.1039/c2lc40260b

159. Lehtinen, N.G., 2021. Physics and Mathematics of Electric Streamers. Radiophys Quantum El 64, 11–25. https://doi.org/10.1007/s11141-021-10108-5

160. Leiweke, R.J., Sands, B.L., Ganguly, B.N., 2011. Effect of Gas Mixture on Plasma Jet Discharge Morphology. IEEE Trans. Plasma Sci. 39, 2304–2305. https://doi.org/10.1109/TPS.2011.2139228

161. Lepoetre, A., Ognier, S., Zhang, M., Wengler, J., Al Ayoubi, S., Ollivier, C., Fensterbank, L., Duten, X., Tatoulian, M., 2021. Amination of Cyclohexane by Dielectric Barrier Discharge Processing in a Continuous Flow Microreactor: Experimental and Simulation Studies. Plasma Chem Plasma Process 41, 351–368. https://doi.org/10.1007/s11090-020-10140-9

162. Leung, K., Nielsen, I.M.B., Kurtz, I., 2007. *Ab Initio* Molecular Dynamics Study of Carbon Dioxide and Bicarbonate Hydration and the Nucleophilic Attack of Hydroxide on CO_2. J. Phys. Chem. B 111, 4453–4459. https://doi.org/10.1021/jp068475l

163. Levich, V.G., 1962. Physicochemical hydrodynamics, 2. ed. ed, Prentice Hall international series in the physical and chemical engineering sciences. Prentice-Hall, Englewood Cliffs, NJ.

164. Lewis, W.K., Whitman, W.G., 1924. Principles of Gas Absorption. Ind. Eng. Chem. 16, 1215–1220. https://doi.org/10.1021/ie50180a002

165. Li, D., Xiong, M., Wang, Song, Chen, X., Wang, Shen, Zeng, Q., 2020. Effects of low-temperature plasma treatment on wettability of glass surface: Molecular dynamic

simulation and experimental study. Applied Surface Science 503, 144257. https://doi.org/10.1016/j.apsusc.2019.144257

166. Li, L., Zhang, X., Luan, Z., Du, Z., Xi, S., Wang, B., Cao, L., Lian, C., Yan, J., 2018. In Situ Quantitative Raman Detection of Dissolved Carbon Dioxide and Sulfate in Deep-Sea High-Temperature Hydrothermal Vent Fluids. Geochem Geophys Geosyst 19, 1809–1823. https://doi.org/10.1029/2018GC007445

167. Li, Y., Liu, H., Bai, Q., Lu, L., Zhang, P., Shen, R., Yuan, X., Miao, X., Han, W., Yao, C., 2023. Atomistic investigation on interfacial properties of glass surfaces modeling plasma modification and the influence of wettability conditions on adhesion. International Journal of Adhesion and Adhesives 122, 103330. https://doi.org/10.1016/j.ijadhadh.2023.103330

168. Lieberman, M.A., Lichtenberg, A.J., 2005. Principles of plasma discharges and materials processing, Second edition. ed. Wiley-Interscience, Hoboken, NJ.

169. Lienhard, J.H., Washington State University Technical Extension Service, Washington State University College of Engineering Research Division, 1966. Synopsis of lift, drag, and vortex frequency data for rigid circular cylinders, Bulletin (Washington State University. College of Engineering. Research Division); Bulletin (Washington State University. College of Engineering. Research Division); 300. Technical Extension Service, Washington State University, Pullman, Wash.

170. Lim, K.-B., Lee, D.-C., 2004. Surface modification of glass and glass fibres by plasma surface treatment. Surf. Interface Anal. 36, 254–258. https://doi.org/10.1002/sia.1682

171. Lin, L., Rui, L., Li, C., Liu, Q., Li, S., Xia, Y., Hu, H., Yang, W., Xu, H., 2021. Study on CO2-based plasmas for surface modification of polytetrafluoroethylene and the wettability effects. Journal of CO2 Utilization 53, 101752. https://doi.org/10.1016/j.jcou.2021.101752

172. Liu, N., Aymonier, C., Lecoutre, C., Garrabos, Y., Marre, S., 2012. Microfluidic approach for studying CO2 solubility in water and brine using confocal Raman spectroscopy. Chemical Physics Letters 551, 139–143. https://doi.org/10.1016/j.cplett.2012.09.007

173. Liu, Q., Liu, Y., Xu, J., Teng, Y., Ling, Z., Zhang, Y., Jiang, L., Song, Y., 2023. A review of the gas hydrate phase transition with a microfluidic approach. Energy Reviews 2, 100011. https://doi.org/10.1016/j.enrev.2022.100011

174. Liu, X., Zhang, J., Liu, Y., Huang, H., Liu, Z., 2018. Main factors controlling the wettability of gas shales: A case study of over-mature marine shale in the Longmaxi

Formation. Journal of Natural Gas Science and Engineering 56, 18–28. https://doi.org/10.1016/j.jngse.2018.05.017

175. Liu, Z., Cheng, Y., Wang, Y., Wang, L., Li, W., 2019. Experimental investigation of CO2 injection into coal seam reservoir at in-situ stress conditions for enhanced coalbed methane recovery. Fuel 236, 709–716. https://doi.org/10.1016/j.fuel.2018.09.062

176. Loeb, L.B., Kip, A.F., 1939. Electrical Discharges in Air at Atmospheric Pressure The Nature of the Positive and Negative Point-to-Plane Coronas and the Mechanism of Spark Propagation. Journal of Applied Physics 10, 142–160. https://doi.org/10.1063/1.1707290

177. Lu, X., Laroussi, M., Puech, V., 2012. On atmospheric-pressure non-equilibrium plasma jets and plasma bullets. Plasma Sources Sci. Technol. 21, 034005. https://doi.org/10.1088/0963-0252/21/3/034005

178. Lu, X., Naidis, G.V., Laroussi, M., Ostrikov, K., 2014. Guided ionization waves: Theory and experiments. Physics Reports 540, 123–166. https://doi.org/10.1016/j.physrep.2014.02.006

179. Luque, A., Ratushnaya, V., Ebert, U., 2008. Positive and negative streamers in ambient air: modelling evolution and velocities. J. Phys. D: Appl. Phys. 41, 234005. https://doi.org/10.1088/0022-3727/41/23/234005

180. Ma, C., Nikiforov, A., Hegemann, D., De Geyter, N., Morent, R., Ostrikov, K. (Ken), 2023. Plasma-controlled surface wettability: recent advances and future applications. International Materials Reviews 68, 82–119. https://doi.org/10.1080/09506608.2022.2047420

181. Macgregor-Ramiasa, M.N., Vasilev, K., 2016. Plasma Polymer Deposition: A Versatile Tool for Stem Cell Research, in: Tiwari, A., Garipcan, B., Uzun, L. (Eds.), Advanced Surfaces for Stem Cell Research. John Wiley & Sons, Inc., Hoboken, NJ, USA, pp. 199–232. https://doi.org/10.1002/9781119242642.ch8

182. Mackie, N.M., Dalleska, N.F., Castner, D.G., Fisher, E.R., 1997. Comparison of Pulsed and Continuous-Wave Deposition of Thin Films from Saturated Fluorocarbon/H_2 Inductively Coupled rf Plasmas. Chem. Mater. 9, 349–362. https://doi.org/10.1021/cm960388q

183. Maes, J., Geiger, S., 2018. Direct pore-scale reactive transport modelling of dynamic wettability changes induced by surface complexation. Advances in Water Resources 111, 6–19. https://doi.org/10.1016/j.advwatres.2017.10.032

184. Maes, J., Soulaine, C., 2018. A new compressive scheme to simulate species transfer across fluid interfaces using the Volume-Of-Fluid method. Chemical Engineering Science 190, 405–418. https://doi.org/10.1016/j.ces.2018.06.026

185. Maho, T., Binois, R., Brulé-Morabito, F., Demasure, M., Douat, C., Dozias, S., Escot Bocanegra, P., Goard, I., Hocqueloux, L., Le Helloco, C., Orel, I., Pouvesle, J.-M., Prazuck, T., Stancampiano, A., Tocaben, C., Robert, E., 2021. Anti-Bacterial Action of Plasma Multi-Jets in the Context of Chronic Wound Healing. Applied Sciences 11, 9598. https://doi.org/10.3390/app11209598

186. Mansouri-Boroujeni, M., 2022. A microfluidic study of the physical and chemical mechanisms induced by CO2 injection in deep saline aquifers (phdthesis). Université d'Orléans.

187. Mansouri-Boroujeni, M., Soulaine, C., Azaroual, M., Roman, S., 2023. How interfacial dynamics controls drainage pore-invasion patterns in porous media. Advances in Water Resources 171, 104353. https://doi.org/10.1016/j.advwatres.2022.104353

188. Marmur, A., Della Volpe, C., Siboni, S., Amirfazli, A., Drelich, J.W., 2017a. Contact angles and wettability: towards common and accurate terminology. Surface Innovations 5, 3–8. https://doi.org/10.1680/jsuin.17.00002

189. Marmur, A., Della Volpe, C., Siboni, S., Amirfazli, A., Drelich, J.W., 2017b. Contact angles and wettability: towards common and accurate terminology. Surface Innovations 5, 3–8. https://doi.org/10.1680/jsuin.17.00002

190. Marre, S., Baek, J., Park, J., Bawendi, M.G., Jensen, K.F., 2009. High-Pressure/High-Temperature Microreactors for Nanostructure Synthesis. JALA: Journal of the Association for Laboratory Automation 14, 367–373. https://doi.org/10.1016/j.jala.2009.06.005

191. Martynov, D., 2022. Numerical Study of Formation Dry-out and Salt Precipitation due to Supercritical CO2 Injection (Master's Thesis).

192. Masalmeh, S.K., 2003. The effect of wettability heterogeneity on capillary pressure and relative permeability. Journal of Petroleum Science and Engineering 39, 399–408. https://doi.org/10.1016/S0920-4105(03)00078-0

193. Massey, S., Duboin, A., Mantovani, D., Tabeling, P., Tatoulian, M., 2012. Stable modification of PDMS surface properties by plasma polymerization: Innovative process of allylamine PECVD deposition and microfluidic devices sealing. Surface and Coatings Technology 206, 4303–4309. https://doi.org/10.1016/j.surfcoat.2012.04.047

194. Massimiani, A., Panini, F., Marasso, S.L., Cocuzza, M., Quaglio, M., Pirri, C.F., Verga, F., Viberti, D., 2023. 2D Microfluidic Devices for Pore-Scale Phenomena Investigation: A Review. Water 15, 1222. https://doi.org/10.3390/w15061222

195. Meek, J.M., 1940. A Theory of Spark Discharge. Phys. Rev. 57, 722–728. https://doi.org/10.1103/PhysRev.57.722

196. Mehmani, A., Kelly, S., Torres-Verdín, C., Balhoff, M., 2019. Capillary Trapping Following Imbibition in Porous Media: Microfluidic Quantification of the Impact of Pore-Scale Surface Roughness. Water Resources Research 55, 9905–9925. https://doi.org/10.1029/2019WR025170

197. Menawat, A., Joseph, H., Siriwardane, R., 1984. Control of surface energy of glass by surface reactions: Contact angle and stability. Journal of Colloid and Interface Science 101, 110–119. https://doi.org/10.1016/0021-9797(84)90012-2

198. Mericam-Bourdet, N., Laroussi, M., Begum, A., Karakas, E., 2009. Experimental investigations of plasma bullets. J. Phys. D: Appl. Phys. 42, 055207. https://doi.org/10.1088/0022-3727/42/5/055207

199. Mestre, E., Gibert, T., Dozias, S., Douat, C., 2024. Comparison of helium and argon for the production of carbon monoxide (CO) by a plasma jet for biomedical applications. Eur. Phys. J. Appl. Phys. 99, 13. https://doi.org/10.1051/epjap/2024230213

200. Mishra, S., Ganesh, P., Schuetter, J., He, J., Jin, Z., Durlofsky, L., 2015. SIMPLIFIED PREDICTIVE MODELS FOR CO2 SEQUESTRATION PERFORMANCE ASSESSMENT (No. 1238355). https://doi.org/10.2172/1238355

201. Mojica, E.-R.E., Abbas, N., Wyan, L.O., Vedad, J., Desamero, R.Z.B., 2018. Solvent Sensitivity of the −C≡N Group: A Raman Spectroscopic Study, in: Sonntag, M.D. (Ed.), ACS Symposium Series. American Chemical Society, Washington, DC, pp. 181–197. https://doi.org/10.1021/bk-2018-1305.ch011

202. Morais, S., Liu, N., Diouf, A., Bernard, D., Lecoutre, C., Garrabos, Y., Marre, S., 2016. Monitoring CO_2 invasion processes at the pore scale using geological labs on chip. Lab Chip 16, 3493–3502. https://doi.org/10.1039/C6LC00830E

203. Morent, R., De Geyter, N., Trentesaux, M., Gengembre, L., Dubruel, P., Leys, C., Payen, E., 2010. Influence of Discharge Atmosphere on the Ageing Behaviour of Plasma-Treated Polylactic Acid. Plasma Chem Plasma Process 30, 525–536. https://doi.org/10.1007/s11090-010-9233-8

204. Morrow, N.R., 1970. Physics and Thermodynamics of Capillary Action in Porous Media. Ind. Eng. Chem. 62, 32–56. https://doi.org/10.1021/ie50726a006

205. Mozhdehei, A., Mercury, L., Slodczyk, A., 2024. Ubiquity of the Micrometer-Thick Interface along a Quartz–Water Boundary. Langmuir 40, 13025–13041. https://doi.org/10.1021/acs.langmuir.4c00742

206. Müller, N., 2011. Supercritical CO2-Brine Relative Permeability Experiments in Reservoir Rocks—Literature Review and Recommendations. Transp Porous Med 87, 367–383. https://doi.org/10.1007/s11242-010-9689-2

207. Munkejord, S.T., Hammer, M., Ervik, Å., Odsæter, L.H., Lund, H., 2021. Coupled CO2-well-reservoir simulation using a partitioned approach: effect of reservoir properties on well dynamics. Greenhouse Gas Sci Technol 11, 103–127. https://doi.org/10.1002/ghg.2035

208. Musbah, A., Eljaafari, W., Fessatwi, E., Elsahli, Y., 2022. Comparison Between Chemical Vapor Deposition CVD and Physical Vapor Deposition PVD Coating Techniques: A Review Paper.

209. Nasdala, L., Smith, D.C., Kaindl, R., Ziemann, M.A., 2004. Raman spectroscopy: Analytical perspectives in mineralogical research, in: Spectroscopic Methods in Mineralogy. Mineralogical Society of Great Britain and Ireland, Germany, pp. 281–343. https://doi.org/10.1180/EMU-notes.6.7

210. Ndiaye, M., Gadoin, E., Gentric, C., 2018. CO 2 gas–liquid mass transfer and k L a estimation: Numerical investigation in the context of airlift photobioreactor scale-up. Chemical Engineering Research and Design 133, 90–102. https://doi.org/10.1016/j.cherd.2018.03.001

211. Nemes, L., Mohai, M., Donkó, Z., Bertóti, I., 2000. Detection of CN radicals in DC nitrogen plasma used for deposition of CNx layers. Spectrochimica Acta Part A: Molecular and Biomolecular Spectroscopy 56, 761–767. https://doi.org/10.1016/S1386-1425(99)00159-6

212. Neuville, D.R., De Ligny, D., Henderson, G.S., 2014. Advances in Raman Spectroscopy Applied to Earth and Material Sciences. Reviews in Mineralogy and Geochemistry 78, 509–541. https://doi.org/10.2138/rmg.2013.78.13

213. Nežerka, V., Somr, M., Trejbal, J., 2018. Contact Angle Measurement Tool Based on Image Analysis. Exp Tech 42, 271–278. https://doi.org/10.1007/s40799-017-0231-0

214. Nguyen, P.Q.M., Yeo, L.-P., Lok, B.-K., Lam, Y.-C., 2014. Patterned Surface with Controllable Wettability for Inkjet Printing of Flexible Printed Electronics. ACS Appl. Mater. Interfaces 6, 4011–4016. https://doi.org/10.1021/am4054546

215. Nijdam, S., Teunissen, J., Ebert, U., 2020. The physics of streamer discharge phenomena. Plasma Sources Sci. Technol. 29, 103001. https://doi.org/10.1088/1361-6595/abaa05

216. Niu, B., Al-Menhali, A., Krevor, S.C., 2015. The impact of reservoir conditions on the residual trapping of carbon dioxide in B erea sandstone. Water Resources Research 51, 2009–2029. https://doi.org/10.1002/2014WR016441

217. Nordbotten, J.M., Celia, M.A., Bachu, S., 2005. Injection and Storage of CO2 in Deep Saline Aquifers: Analytical Solution for CO2 Plume Evolution During Injection. Transp Porous Med 58, 339–360. https://doi.org/10.1007/s11242-004-0670-9

218. Nordin, N.H., Ahmad, Z., 2015. Monitoring Chemical Changes on the Surface of Borosilicate Glass Covers during the Silanisation Process. Journal of Physical Science 26.

219. Norouzisadeh, M., Leroy, P., Soulaine, C., 2024. A lubrication model with slope-dependent disjoining pressure for modeling wettability alteration. Computer Physics Communications 298, 109114. https://doi.org/10.1016/j.cpc.2024.109114

220. Oliveira, R., Blunt, M.J., Bijeljic, B., 2023. Impact of Physical Heterogeneity and Transport Conditions on Effective Reaction Rates in Dissolution. Transp Porous Med 146, 113–138. https://doi.org/10.1007/s11242-022-01836-x

221. Onyshchenko, I., De Geyter, N., Nikiforov, A.Y., Morent, R., 2015. Atmospheric Pressure Plasma Penetration inside Flexible Polymeric Tubes: Atmospheric Pressure Plasma Penetration…. Plasma Process. Polym. 12, 271–284. https://doi.org/10.1002/ppap.201400190

222. Ozkan, O., Turkoglu Sasmazel, H., 2018. Dielectric barrier discharge and jet type plasma surface modifications of hybrid polymeric poly (ε-caprolactone)/chitosan scaffolds. J Biomater Appl 32, 1300–1313. https://doi.org/10.1177/0885328218755571

223. Panneerselvam, R., Sadat, H., Höhn, E.-M., Das, A., Noothalapati, H., Belder, D., 2022. Microfluidics and surface-enhanced Raman spectroscopy, a win–win combination? Lab on a Chip 22, 665–682. https://doi.org/10.1039/D1LC01097B

224. Park, J., Kim, J.-A., Ahn, H., Bae, J., Jin, J., 2019. A Review of Thickness Measurements of Thick Transparent Layers Using Optical Interferometry. Int. J. Precis. Eng. Manuf. 20, 463–477. https://doi.org/10.1007/s12541-019-00105-0

225. Patmonoaji, A., Suekane, T., 2017. Investigation of CO2 dissolution via mass transfer inside a porous medium. Advances in Water Resources 110, 97–106. https://doi.org/10.1016/j.advwatres.2017.10.008

226. Pattenaude, S.R., Streacker, L.M., Ben-Amotz, D., 2018. Temperature and polarization dependent Raman spectra of liquid H2O and D2O. Journal of Raman Spectroscopy 49, 1860–1866. https://doi.org/10.1002/jrs.5465

227. Pearse, R.W.B., Gaydon, A.G., 1976. The identification of molecular spectra, 4th ed. ed. Chapman & Hall, London.

228. Perkins, E., 2003. Fundamental Geochemical Processes Between CO2, Water and Minerals 250.

229. Pinho, B., Hartman, R.L., 2017. Microfluidics with in situ Raman spectroscopy for the characterization of non-polar/aqueous interfaces. Reaction Chemistry & Engineering 2, 189–200. https://doi.org/10.1039/C6RE00177G

230. Plug, W.-J., Bruining, J., 2007. Capillary pressure for the sand–CO2–water system under various pressure conditions. Application to CO2 sequestration. Advances in Water Resources 30, 2339–2353. https://doi.org/10.1016/j.advwatres.2007.05.010

231. Poonoosamy, J., Soulaine, C., Burmeister, A., Deissmann, G., Bosbach, D., Roman, S., 2020. Microfluidic flow-through reactor and 3D Raman imaging for *in situ* assessment of mineral reactivity in porous and fractured porous media. Lab Chip 20, 2562–2571. https://doi.org/10.1039/D0LC00360C

232. Prasetyo, N., Hofer, T.S., 2018. Structure, Dynamics, and Hydration Free Energy of Carbon Dioxide in Aqueous Solution: A Quantum Mechanical/Molecular Mechanics Molecular Dynamics Thermodynamic Integration (QM/MM MD TI) Simulation Study. J. Chem. Theory Comput. 14, 6472–6483. https://doi.org/10.1021/acs.jctc.8b00557

233. Preibisch, S., Saalfeld, S., Tomancak, P., 2009. Globally optimal stitching of tiled 3D microscopic image acquisitions. Bioinformatics 25, 1463–1465. https://doi.org/10.1093/bioinformatics/btp184

234. Primc, G., Mozetič, M., 2022. Hydrophobic Recovery of Plasma-Hydrophilized Polyethylene Terephthalate Polymers. Polymers 14, 2496. https://doi.org/10.3390/polym14122496

235. Primkulov, B.K., Pahlavan, A.A., Fu, X., Zhao, B., MacMinn, C.W., Juanes, R., 2021. Wettability and Lenormand's diagram. J. Fluid Mech. 923, A34. https://doi.org/10.1017/jfm.2021.579

236. Prodanovic, M., Esteva, M., Hanlon, M., Nanda, G., Agarwal, P., 2015. Digital Rocks Portal: A repository for porous media images. https://doi.org/10.17612/P7CC7K

237. Qi, Z., Xu, L., Xu, Y., Zhong, J., Abedini, A., Cheng, X., Sinton, D., 2018. Disposable silicon-glass microfluidic devices: precise, robust and cheap. Lab Chip 18, 3872–3880. https://doi.org/10.1039/C8LC01109E

238. Quinet, O., Champagne, B., Rodriguez, V., 2006. Experimental and theoretical investigation of the Raman and hyper-Raman spectra of acetonitrile and its derivatives. The Journal of Chemical Physics 124, 244312. https://doi.org/10.1063/1.2208350

239. Radmilovic-Radjenovic, M., Radjenovic, B., Klas, M., Bojarov, A., Matejcik, S., 2013. The breakdown mechanisms in electrical discharges: The role of the field emission effect in direct current discharges in microgaps. Acta Physica Slovaca 63, 105–205. https://doi.org/10.2478/apsrt-2013-0003

240. Raether, H., 1939. Die Entwicklung der Elektronenlawine in den Funkenkanal: Nach Beobachtungen in der Nebelkammer. Z. Physik 112, 464–489. https://doi.org/10.1007/BF01340229

241. Raizer, Y.P., Milikh, G.M., Shneider, M.N., 2010. Streamer- and leader-like processes in the upper atmosphere: Models of red sprites and blue jets: MODELS OF RED SPRITES AND BLUE JETS. J. Geophys. Res. 115. https://doi.org/10.1029/2009JA014645

242. Raman, C.V., Krishnan, K.S., 1928. A New Type of Secondary Radiation. Nature 121, 501–502. https://doi.org/10.1038/121501c0

243. Rasheed, Z., Raza, A., Gholami, R., Rabiei, M., Ismail, A., Rasouli, V., 2020. A numerical study to assess the effect of heterogeneity on CO2 storage potential of saline aquifers. Energy Geoscience 1, 20–27. https://doi.org/10.1016/j.engeos.2020.03.002

244. Riaz, A., Hesse, M., Tchelepi, H.A., Orr, F.M., 2006. Onset of convection in a gravitationally unstable diffusive boundary layer in porous media. J. Fluid Mech. 548, 87. https://doi.org/10.1017/S0022112005007494

245. Ringrose, P., 2020. How to Store CO2 Underground: Insights from early-mover CCS Projects. Springer International Publishing, Cham. https://doi.org/10.1007/978-3-030-33113-9

246. Robert, E., Vandamme, M., Brullé, L., Lerondel, S., Le Pape, A., Sarron, V., Riès, D., Darny, T., Dozias, S., Collet, G., Kieda, C., Pouvesle, J.M., 2013. Perspectives of endoscopic plasma applications. Clinical Plasma Medicine 1, 8–16. https://doi.org/10.1016/j.cpme.2013.10.002

247. Roels, S.M., Ott, H., Zitha, P.L.J., 2014. μ-CT analysis and numerical simulation of drying effects of CO2 injection into brine-saturated porous media. International Journal of Greenhouse Gas Control 27, 146–154. https://doi.org/10.1016/j.ijggc.2014.05.010

248. Roman, S., Soulaine, C., AlSaud, M.A., Kovscek, A., Tchelepi, H., 2016. Particle velocimetry analysis of immiscible two-phase flow in micromodels. Advances in Water Resources 95, 199–211. https://doi.org/10.1016/j.advwatres.2015.08.015

249. Roman, S., Soulaine, C., Kovscek, A.R., 2020. Pore-scale visualization and characterization of viscous dissipation in porous media. Journal of Colloid and Interface Science 558, 269–279. https://doi.org/10.1016/j.jcis.2019.09.072

250. Saadatpoor, E., Bryant, S.L., Sepehrnoori, K., 2010. New Trapping Mechanism in Carbon Sequestration. Transp Porous Med 82, 3–17. https://doi.org/10.1007/s11242-009-9446-6

251. Sabbatini, L., De Giglio, E. (Eds.), 2022. Polymer Surface Characterization. De Gruyter. https://doi.org/10.1515/9783110701098

252. Sabirzyanov, A.N., Il'in, A.P., Akhunov, A.R., Gumerov, F.M., 2002. Solubility of Water in Supercritical Carbon Dioxide 40.

253. Sagbana, P.I., Sarkodie, K., Nkrumah, W.A., 2022. A critical review of carbonate reservoir wettability modification during low salinity waterflooding. Petroleum S2405656122000128. https://doi.org/10.1016/j.petlm.2022.01.006

254. Saraf, S., Bera, A., 2021. A review on pore-scale modeling and CT scan technique to characterize the trapped carbon dioxide in impermeable reservoir rocks during sequestration. Renewable and Sustainable Energy Reviews 144, 110986. https://doi.org/10.1016/j.rser.2021.110986

255. Saraji, S., Goual, L., Piri, M., Plancher, H., 2013. Wettability of Supercritical Carbon Dioxide/Water/Quartz Systems: Simultaneous Measurement of Contact Angle and Interfacial Tension at Reservoir Conditions. Langmuir 29, 6856–6866. https://doi.org/10.1021/la3050863

256. Schmidt-Bleker, A., Norberg, S.A., Winter, J., Johnsen, E., Reuter, S., Weltmann, K.D., Kushner, M.J., 2015. Propagation mechanisms of guided streamers in plasma jets: the influence of electronegativity of the surrounding gas. Plasma Sources Sci. Technol. 24, 035022. https://doi.org/10.1088/0963-0252/24/3/035022

257. Sell, A., Fadaei, H., Kim, M., Sinton, D., 2013. Measurement of CO2 Diffusivity for Carbon Sequestration: A Microfluidic Approach for Reservoir-Specific Analysis. Environ. Sci. Technol. 47, 71–78. https://doi.org/10.1021/es303319q

258. Seo, S., Mastiani, M., Hafez, M., Kunkel, G., Ghattas Asfour, C., Garcia-Ocampo, K.I., Linares, N., Saldana, C., Yang, K., Kim, M., 2019. Injection of in-situ generated CO2 microbubbles into deep saline aquifers for enhanced carbon sequestration. International Journal of Greenhouse Gas Control 83, 256–264. https://doi.org/10.1016/j.ijggc.2019.02.017

259. Shakeri, A., Khan, S., Didar, T.F., 2021. Conventional and emerging strategies for the fabrication and functionalization of PDMS-based microfluidic devices. Lab Chip 21, 3053–3075. https://doi.org/10.1039/D1LC00288K

260. Shao, T., Wang, R., Zhang, C., Yan, P., 2018. Atmospheric-pressure pulsed discharges and plasmas: mechanism, characteristics and applications. High Voltage 3, 14–20. https://doi.org/10.1049/hve.2016.0014

261. Shariati Pour, S., Pickup, G.E., Mackay, E.J., Heinemann, N., 2012. Flow Simulation of CO2 Storage in Saline Aquifers Using Black Oil Simulator, in: Carbon Management Technology Conference. Presented at the Carbon Management Technology Conference, Carbon Management Technology Conference, Orlando, Florida, USA. https://doi.org/10.7122/151042-MS

262. Sifuentes, W.F., Giddins, M.A., Blunt, M.J., 2009. Modeling CO2 Storage in Aquifers : Assessing the key contributors to uncertainty, in: All Days. Presented at the SPE Offshore Europe Oil and Gas Conference and Exhibition, SPE, Aberdeen, UK, p. SPE-123582-MS. https://doi.org/10.2118/123582-MS

263. Sinha, P.K., Wang, C.-Y., 2007. Pore-network modeling of liquid water transport in gas diffusion layer of a polymer electrolyte fuel cell. Electrochimica Acta 52, 7936–7945. https://doi.org/10.1016/j.electacta.2007.06.061

264. Soli, A.L., Byrne, R.H., 2002. CO2 system hydration and dehydration kinetics and the equilibrium CO2/H2CO3 ratio in aqueous NaCl solution. Marine Chemistry 78, 65–73. https://doi.org/10.1016/S0304-4203(02)00010-5

265. Soulaine, C., Maes, J., Roman, S., 2021. Computational Microfluidics for Geosciences. Front. Water 3, 643714. https://doi.org/10.3389/frwa.2021.643714

266. Stalder, A.F., Kulik, G., Sage, D., Barbieri, L., Hoffmann, P., 2006. A snake-based approach to accurate determination of both contact points and contact angles. Colloids and Surfaces A: Physicochemical and Engineering Aspects 286, 92–103. https://doi.org/10.1016/j.colsurfa.2006.03.008

267. Stalder, A.F., Melchior, T., Müller, M., Sage, D., Blu, T., Unser, M., 2010. Low-bond axisymmetric drop shape analysis for surface tension and contact angle measurements of sessile drops. Colloids and Surfaces A: Physicochemical and Engineering Aspects 364, 72–81. https://doi.org/10.1016/j.colsurfa.2010.04.040

268. Sterpenich, J., Dubessy, J., Pironon, J., Renard, S., Caumon, C., Leisen, M., Jaubert, J.-N., Favre, E., Roizard, D., Parmentier, M., Azaroual, M., Lachet, V., Creton, B., El, E., Lagneau, V., Mouronval, G., Hy-Billiot, J., Chiquet, P., 2017. Experimental and numerical simulation of thermodynamic properties of water-salt-gas mixtures (CO2 + co-contaminant) under geological storage conditions. Energy Procedia.

269. Sun, Y., Yu, H., Yang, B., 2024. Impact of Wettability on CO_2 Dynamic Dissolution in Three-Dimensional Porous Media: Pore-Scale Simulation Using the Lattice Boltzmann Method. Langmuir 40, 22658–22672. https://doi.org/10.1021/acs.langmuir.4c02412

270. Sun, Z., Mehmani, A., Torres-Verdín, C., 2021. Subpore-Scale Trapping Mechanisms Following Imbibition: A Microfluidics Investigation of Surface Roughness Effects. Water Resources Research 57, e2020WR028324. https://doi.org/10.1029/2020WR028324

271. Suzuki, H., Matsuzaki, Y., Muraoka, A., Tachikawa, M., 2012. Raman spectroscopy of optically levitated supercooled water droplet. The Journal of Chemical Physics 136, 234508. https://doi.org/10.1063/1.4729476

272. Taheri, A., Wessel-Berg, D., Torsaeter, O., Soroush, M., 2012. The Effects of Anisotropy and Heterogeneity on CO2 Dissolution in Deep Saline Aquifers, in: Carbon Management Technology Conference. Presented at the Carbon Management Technology Conference, Carbon Management Technology Conference, Orlando, Florida, USA. https://doi.org/10.7122/151345-MS

273. Tan, S.H., Nguyen, N.-T., Chua, Y.C., Kang, T.G., 2010. Oxygen plasma treatment for reducing hydrophobicity of a sealed polydimethylsiloxane microchannel. Biomicrofluidics 4, 032204. https://doi.org/10.1063/1.3466882

274. Tang, T., Yuan, Y., Yalikun, Y., Hosokawa, Y., Li, M., Tanaka, Y., 2021. Glass based micro total analysis systems: Materials, fabrication methods, and applications. Sensors and Actuators B: Chemical 339, 129859. https://doi.org/10.1016/j.snb.2021.129859

275. Tatomir, A., Dimache, A.-N., Iulian, I., Sauter, M., 2019. Modelling of CO_2 storage in geological formations with DuMu^x, a free-open-source numerical framework. A possible tool to assess geological storage of carbon dioxide in Romania. E3S Web Conf. 85, 07002. https://doi.org/10.1051/e3sconf/20198507002

276. Taylor, R., Krishna, R., 1993. Multicomponent mass transfer, Wiley series in chemical engineering. Wiley, New York.

277. Teng, H., Yamasaki, A., 1998. Mass transfer of CO2 through liquid CO2-water interface. Heat Mass Transfer. https://doi.org/10.1016/S0017-9310(98)00173-2

278. Terpilowski, K., Rymuszka, D., 2016. Surface properties of glass plates activated by air, oxygen, nitrogen and argon plasma. Glass Phys Chem 42, 535–541. https://doi.org/10.1134/S1087659616060195

279. Terpstra, P., Combes, D., Zwick, A., 1990. Effect of salts on dynamics of water: A Raman spectroscopy study. The Journal of Chemical Physics 92, 65–70. https://doi.org/10.1063/1.458418

280. Thielicke, W., Stamhuis, E.J., 2014. PIVlab – Towards User-friendly, Affordable and Accurate Digital Particle Image Velocimetry in MATLAB. Journal of Open Research Software 2. https://doi.org/10.5334/jors.bl

281. Tian, Z., Zhang, X., Liu, C., Meng, Q., Du, Z., Yan, J., 2020. Characterization of the Influence of Hydrated Ions on the Oxygen–Hydrogen Stretching Vibration of Water by Raman Spectroscopy. Analytical Letters 53, 2034–2046. https://doi.org/10.1080/00032719.2020.1728294

282. Tokunaga, T.K., Wan, J., 2013. Capillary Pressure and Mineral Wettability Influences on Reservoir CO2 Capacity. Reviews in Mineralogy and Geochemistry 77, 481–503. https://doi.org/10.2138/rmg.2013.77.14

283. Trantidou, T., Elani, Y., Parsons, E., Ces, O., 2017. Hydrophilic surface modification of PDMS for droplet microfluidics using a simple, quick, and robust method via PVA deposition. Microsyst Nanoeng 3, 16091. https://doi.org/10.1038/micronano.2016.91

284. Turkoglu Sasmazel, H., Alazzawi, M., Kadim Abid Alsahib, N., 2021. Atmospheric Pressure Plasma Surface Treatment of Polymers and Influence on Cell Cultivation. Molecules 26, 1665. https://doi.org/10.3390/molecules26061665

285. Tuschel, D., 2014. Practical Group Theory and Raman Spectroscopy, Part I: Normal Vibrational Modes. Spectroscopy 29, 14.

286. Van Den Kerkhof, A.M., 1988. Phase transitions and molar volumes of CO2-CH4-N2 inclusions. bulmi 111, 257–266. https://doi.org/10.3406/bulmi.1988.8046

287. Van Gorcum, M., 2019. Dynamics of Soft Wetting (PhD). University of Twente, Enschede, The Netherlands. https://doi.org/10.3990/1.9789036547376

288. van Rooijen, W., Hashemi, L., Boon, M., Farajzadeh, R., Hajibeygi, H., 2022. Microfluidics-based analysis of dynamic contact angles relevant for underground hydrogen storage. Advances in Water Resources 164, 104221. https://doi.org/10.1016/j.advwatres.2022.104221

289. Vandenbossche, M., Hegemann, D., 2018. Recent approaches to reduce aging phenomena in oxygen- and nitrogen-containing plasma polymer films: An overview. Current Opinion in Solid State and Materials Science 22, 26–38. https://doi.org/10.1016/j.cossms.2018.01.001

290. Vandu, C.O., Liu, H., Krishna, R., 2005. Mass transfer from Taylor bubbles rising in single capillaries. Chemical Engineering Science 60, 6430–6437. https://doi.org/10.1016/j.ces.2005.01.037

291. Vizireanu, S., Ionita, M.D., Ionita, R.E., Stoica, S.D., Teodorescu, C.M., Husanu, M.A., Apostol, N.G., Baibarac, M., Panaitescu, D., Dinescu, G., 2017. Aging phenomena and wettability control of plasma deposited carbon nanowall layers. Plasma Process Polym 14, 1700023. https://doi.org/10.1002/ppap.201700023

292. Vledder, P., Fonseca, J.C., Wells, T., Gonzalez, I., Ligthelm, D., Park, K., Rijswijk, G., 2010. Low Salinity Water Flooding: Proof Of Wettability Alteration On A Field Wide Scale.

293. Vukovic, T., Røstad, J., Farooq, U., Torsæter, O., van der Net, A., 2023. Systematic Study of Wettability Alteration of Glass Surfaces by Dichlorooctamethyltetrasiloxane Silanization─A Guide for Contact Angle Modification. ACS Omega 8, 36662–36676. https://doi.org/10.1021/acsomega.3c02448

294. Wägli, P., Homsy, A., De Rooij, N.F., 2010. Norland optical adhesive (NOA81) microchannels with adjustable surface properties and high chemical resistance against IR-transparent organic solvents. Procedia Engineering 5, 460–463. https://doi.org/10.1016/j.proeng.2010.09.146

295. Wagner, H.-E., Brandenburg, R., Kozlov, K.V., Sonnenfeld, A., Michel, P., Behnke, J.F., 2003. The barrier discharge: basic properties and applications to surface treatment. Vacuum 71, 417–436. https://doi.org/10.1016/S0042-207X(02)00765-0

296. Wan, J., Kim, Y., Tokunaga, T.K., 2014. Contact angle measurement ambiguity in supercritical CO2–water–mineral systems: Mica as an example. International Journal of Greenhouse Gas Control 31, 128–137. https://doi.org/10.1016/j.ijggc.2014.09.029

297. Wan, Y., Jia, C., Zhao, W., Jiang, L., Chen, Z., 2023. Micro-Scale Lattice Boltzmann Simulation of Two-Phase CO2–Brine Flow in a Tighter REV Extracted from a Permeable Sandstone Core: Implications for CO2 Storage Efficiency. Energies 16, 1547. https://doi.org/10.3390/en16031547

298. Wang, S., Edwards, I.M., Clarens, A.F., 2013. Wettability Phenomena at the CO_2 – Brine–Mineral Interface: Implications for Geologic Carbon Sequestration. Environ. Sci. Technol. 47, 234–241. https://doi.org/10.1021/es301297z

299. Wang, T., Shi, L., Lv, L., Liu, J., 2020. Homogeneous surface hydrophilization on the inner walls of polymer tubes using a flexible atmospheric cold microplasma jet. Plasma Processes & Polymers 17, 2000056. https://doi.org/10.1002/ppap.202000056

300. Wang, X., Chou, I.-M., Hu, W., Burruss, R.C., Sun, Q., Song, Y., 2011. Raman spectroscopic measurements of CO2 density: Experimental calibration with high-pressure optical cell (HPOC) and fused silica capillary capsule (FSCC) with application to fluid inclusion observations. Geochimica et Cosmochimica Acta 75, 4080–4093. https://doi.org/10.1016/j.gca.2011.04.028

301. Wenzel, R.N., 1936. Resistance of solid surfaces to wetting by water. Ind. Eng. Chem. 28, 988–994. https://doi.org/10.1021/ie50320a024

302. Wenzel, R.N.N., 1949. Surface Roughness and Contact Angle. The journal of physical chemistry. 53.

303. Wikipedia, 2023. Raman spectroscopy [WWW Document]. URL https://en.wikipedia.org/wiki/Raman_spectroscopy

304. Williams, D.L., Kuhn, A.T., Amann, M.A., Hausinger, M.B., Konarik, M.M., Nesselrode, E.I., 2010. Computerised Measurement of Contact Angles.

305. Williams, G.A., Chadwick, R.A., Vosper, H., 2018. Some thoughts on Darcy-type flow simulation for modelling underground CO 2 storage, based on the Sleipner CO 2 storage operation. International Journal of Greenhouse Gas Control 68, 164–175. https://doi.org/10.1016/j.ijggc.2017.11.010

306. Winter, J., Brandenburg, R., Weltmann, K.-D., 2015. Atmospheric pressure plasma jets: an overview of devices and new directions. Plasma Sources Sci. Technol. 24, 064001. https://doi.org/10.1088/0963-0252/24/6/064001

307. Wojdyr, M., 2010. *Fityk* : a general-purpose peak fitting program. J Appl Crystallogr 43, 1126–1128. https://doi.org/10.1107/S0021889810030499

308. Worden, R.H., 2023. Value of core for reservoir and top-seal analysis for carbon capture and storage projects. SP 527, SP527-2022–38. https://doi.org/10.1144/SP527-2022-38

309. Wu, S., Guo, Y., Ouyang, F., Zhou, B., Hu, B., Cheng, H., 2023. Characteristics of the plasma sheath in helium discharge within dielectric tubes. Plasma Sci. Technol. 25, 045402. https://doi.org/10.1088/2058-6272/ac9e93

310. Wu, S., Lu, X., Yue, Y., Dong, X., Pei, X., 2016. Effects of the tube diameter on the propagation of helium plasma plume via electric field measurement. Physics of Plasmas 23, 103506. https://doi.org/10.1063/1.4964280

311. Wu, S., Wu, F., Liu, X., Mao, W., Zhang, C., 2018. A Bipolar DC-Driven Touchable Helium Plasma Jet Operated in Self-Pulsed Mode. IEEE Trans. Plasma Sci. 46, 4091–4098. https://doi.org/10.1109/TPS.2018.2868234

312. Wu, S.-T., Huang, C.-Y., Weng, C.-C., Chang, C.-C., Li, B.-R., Hsu, C.-S., 2019. Rapid Prototyping of an Open-Surface Microfluidic Platform Using Wettability-Patterned Surfaces Prepared by an Atmospheric-Pressure Plasma Jet. ACS Omega 4, 16292–16299. https://doi.org/10.1021/acsomega.9b01317

313. Xiong, Q., Lu, X., Ostrikov, K., Xiong, Z., Xian, Y., Zhou, F., Zou, C., Hu, J., Gong, W., Jiang, Z., 2009. Length control of He atmospheric plasma jet plumes: Effects of discharge parameters and ambient air. Physics of Plasmas 16, 043505. https://doi.org/10.1063/1.3119212

314. Xiong, Z., Kushner, M.J., 2012. Atmospheric pressure ionization waves propagating through a flexible high aspect ratio capillary channel and impinging upon a target. Plasma Sources Sci. Technol. 21, 034001. https://doi.org/10.1088/0963-0252/21/3/034001

315. Xiong, Z., Robert, E., Sarron, V., Pouvesle, J.-M., Kushner, M.J., 2012. Dynamics of ionization wave splitting and merging of atmospheric-pressure plasmas in branched dielectric tubes and channels. J. Phys. D: Appl. Phys. 45, 275201. https://doi.org/10.1088/0022-3727/45/27/275201

316. Xu, H.M., Yu, J.S., Chen, G.L., Qiu, X.P., Hu, W., Chen, W.X., Bai, H.Y., 2015. Exploring the polymerization of bioactive nano-cones on the inner surface of an organic tube by an atmospheric pressure pulsed micro-plasma jet. Applied Surface Science 359, 349–355. https://doi.org/10.1016/j.apsusc.2015.10.149

317. Xu, R., Li, R., Huang, F., Jiang, P., 2017. Pore-scale visualization on a depressurization-induced CO2 exsolution. Science Bulletin 62, 795–803. https://doi.org/10.1016/j.scib.2017.04.023

318. Xu, T., Apps, J.A., Pruess, K., 2003. Reactive geochemical transport simulation to study mineral trapping for CO $_2$ disposal in deep arenaceous formations: TRANSPORT SIMULATION FOR CO $_2$ DISPOSAL. J. Geophys. Res. 108. https://doi.org/10.1029/2002JB001979

319. Yadav, V.K., Sathyanarayana, K., Bora, D., 2008. Electron cyclotron resonance breakdown studies in a linear plasma system. Pramana - J Phys 70, 487–501. https://doi.org/10.1007/s12043-008-0064-6

320. Yakimov, A.S., Pryazhnikov, A.I., Pryazhnikov, M.I., Skorobogatova, A.D., Minakov, A.V., 2023. Plasma Surface Modification of PDMS-Glass Microfluidic Chips for Oil Recovery Studies. Applied Sciences 13, 6365. https://doi.org/10.3390/app13116365

321. Yamasaki, H., Terao, K., Suzuki, T., Simokawa, F., Takao, H., 2013. Patternable atmospheric-pressure plasma jets with gas discharge in microfluidic channel array, in: 2013 IEEE 26th International Conference on Micro Electro Mechanical Systems (MEMS). Presented at the 2013 IEEE 26th International Conference on Micro Electro Mechanical Systems (MEMS), IEEE, Taipei, Taiwan, pp. 205–208. https://doi.org/10.1109/MEMSYS.2013.6474213

322. Yang, J., Tsai, P.A., 2024. Microfluidic mass transfer of supercritical CO2 in brine. Chemical Engineering Science 300, 120543. https://doi.org/10.1016/j.ces.2024.120543

323. Yang, X.M., Zhong, Z.W., Diallo, E.M., Wang, Z.H., Yue, W.S., 2014. Silicon wafer wettability and aging behaviors: Impact on gold thin-film morphology. Materials Science in Semiconductor Processing 26, 25–32. https://doi.org/10.1016/j.mssp.2014.03.044

324. Yekeen, N., Padmanabhan, E., Sevoo, T.A., Kanesen, K.A., Okunade, O.A., 2020. Wettability of rock/CO2/brine systems: A critical review of influencing parameters and recent advances. Journal of Industrial and Engineering Chemistry 88, 1–28. https://doi.org/10.1016/j.jiec.2020.03.021

325. Yirijor, J., Danyuo, Y., Salifu, A.A., Ezenwafor, T., McBagonluri, F., 2022. Surface coating and wettability study of PDMS-based composites: Effect on contact angle and cell-surface interaction. MRS Advances 7, 656–662. https://doi.org/10.1557/s43580-022-00299-y

326. Young, T., 1805. An essay on the cohesion of fluids. Phil. Trans. R. Soc. 95, 65–87. https://doi.org/10.1098/rstl.1805.0005

327. Zanini, S., Barni, R., Pergola, R.D., Riccardi, C., 2014. Modification of the PTFE wettability by oxygen plasma treatments: influence of the operating parameters and investigation of the ageing behaviour. J. Phys. D: Appl. Phys. 47, 325202. https://doi.org/10.1088/0022-3727/47/32/325202

328. Zarghami, S., Boukadi, F., Al-Wahaibi, Y., 2017. Diffusion of carbon dioxide in formation water as a result of CO2 enhanced oil recovery and CO2 sequestration. J Petrol Explor Prod Technol 7, 161–168. https://doi.org/10.1007/s13202-016-0261-7

329. Zeng, X., Xu, G., Gao, Y., An, Y., 2011. Surface Wettability of (3-Aminopropyl)triethoxysilane Self-Assembled Monolayers. J. Phys. Chem. B 115, 450–454. https://doi.org/10.1021/jp109259b

330. Zhao, B., MacMinn, C.W., Juanes, R., 2016. Wettability control on multiphase flow in patterned microfluidics. Proc. Natl. Acad. Sci. U.S.A. 113, 10251–10256. https://doi.org/10.1073/pnas.1603387113

331. Zheng, X., Mahabadi, N., Yun, T.S., Jang, J., 2017. Effect of capillary and viscous force on CO_2 saturation and invasion pattern in the microfluidic chip: CO_2 INVASION INTO MICROFLUIDIC CHIP. J. Geophys. Res. Solid Earth. https://doi.org/10.1002/2016JB013908

332. Zhong, Y., Li, Q., Gao, W., Wen, Y., Zhang, Y., 2025. A review of microfluidic technology for CO2 sequestration in saline aquifers. Journal of Rock Mechanics and

Geotechnical Engineering S167477552500054X. https://doi.org/10.1016/j.jrmge.2025.01.018

333. Zhu, P., Wang, L., 2022. Microfluidics-Enabled Soft Manufacture of Materials with Tailorable Wettability. Chem. Rev. 122, 7010–7060. https://doi.org/10.1021/acs.chemrev.1c00530

Viktor GREDICAK

Approche microfluidique du transfert de masse aux interfaces fluide–fluide dans les milieux poreux avec contrôle de mouillabilité par plasma et analyse par spectroscopie Raman

Cette thèse de doctorat s'inscrit dans le cadre du projet INTER-AQ porté par le CNRS, une initiative de recherche interdisciplinaire visant à élucider les dynamiques complexes et couplées du transfert de masse et de la redistribution des fluides aux interfaces fluide-fluide dans les milieux poreux. Le projet combine la microfluidique expérimentale pour reproduire des environnements souterrains, la spectroscopie Raman pour la quantification chimique in situ, et des techniques innovantes à base de plasma pour moduler les propriétés de surface des pores. Ces approches intégrées ciblent des enjeux énergétiques majeurs, tels que le stockage géologique du CO_2. Dans ce cadre, la recherche doctorale apporte une contribution à l'échelle des pores, en développant des méthodes expérimentales permettant d'analyser comment les phénomènes interfaciaux influencent le comportement des fluides dans les systèmes poreux.

Cette thèse vise à combler une lacune essentielle dans la compréhension du transfert de masse à l'échelle des pores, en s'intéressant spécifiquement à l'impact de la mouillabilité sur les échanges aux interfaces fluide–fluide et sur les mécanismes de piégeage. Cette étude présente le développement d'une plateforme expérimentale intégrant la microfluidique et la spectroscopie µRaman. Les dispositifs microfluidiques sont des réseaux de pores transparents constitués de canaux, simulant des environnements poreux souterrains et permettant une visualisation directe des comportements des fluides. Cette étude propose, pour la première fois, l'utilisation in situ du traitement plasma à pression atmosphérique comme outil de contrôle de la mouillabilité. Les connaissances acquises sur le transfert de masse interfacial en fonction des propriétés de mouillabilité devraient permettre d'améliorer l'étalonnage des modèles numériques à l'échelle des pores comme à l'échelle du réservoir, augmentant ainsi la précision des prévisions pour le stockage du carbone dans les réservoirs géologiques.

L'étude s'articule autour de trois questions de recherche principales. Premièrement, la faisabilité de la propagation d'un plasma atmosphérique dans des canaux microfluidiques fermés est examinée pour contrôler la mouillabilité des surfaces. Le travail démontre qu'un jet de plasma à pression atmosphérique peut être introduit et contrôlé avec succès dans les dispositifs, permettant une modification fiable de la mouillabilité des canaux. Les résultats obtenus par mesure in situ de l'angle de contact sur images indiquent un traitement homogène avec un accroissement des propriétés hydrophiles. La mouillabilité obtenue sur le verre avec notre configuration montre une stabilité pouvant atteindre 70 jours, selon les paramètres de traitement plasma et de stockage. Deuxièmement, l'étude examine comment les conditions de mouillabilité affectent le piégeage capillaire et le transfert de masse interfacial. En utilisant des dispositifs microfluidiques de complexité géométrique croissante, les expériences révèlent que la mouillabilité de surface influence effectivement le piégeage résiduel, l'évaporation de l'eau et la dissolution du CO_2 sous différentes conditions d'écoulement. Troisièmement, le potentiel de la spectroscopie µRaman pour une analyse in situ semi-quantitative de la dissolution du CO_2 est évalué. L'analyse Raman permet de capturer l'évolution temporelle des espèces dissoutes, fournissant des données chimiques complémentaires aux observations visuelles des écoulements, et permettant la quantification des taux de transfert de masse interfaciale.

En résumé, cette recherche intègre les plasmas atmosphériques, la microfluidique et la spectroscopie µRaman, pour l'étude du transfert de masse à l'échelle des pores sous conditions de mouillabilité contrôlées. La thèse apporte de nouvelles connaissances sur les mécanismes régissant le piégeage du CO_2 dans les milieux poreux, essentiels à la conception et à l'optimisation des stratégies de séquestration du carbone.

Mots clés : microfluidique, milieux poreux, écoulement multiphasique, stockage de CO_2, traitement plasma, mouillabilité

Microfluidic Study of Mass Transfer at Fluid–Fluid Interfaces in Porous Media with Plasma-Induced Wettability Control and Raman Spectroscopy

This PhD thesis is part of the INTER-AQ project within CNRS, an interdisciplinary research initiative aiming to unravel the complex and coupled dynamics of mass transfer and fluid redistribution at fluid-fluid interfaces within porous media. The project combines experimental microfluidics to replicate subsurface environments, vibrational spectroscopy for in situ chemical quantification, and novel plasma-based techniques to tailor pore surface properties. These integrated approaches target key environmental and energy challenges, such as geological CO_2 storage. Within this framework, the PhD research contributes to a pore-scale perspective, advancing experimental methods to investigate how interfacial phenomena influence fluid behavior in porous systems.

The objective of this thesis is to address a fundamental gap in our understanding of mass transfer at the pore scale, specifically how wettability affects fluid/fluid interfacial mass transfer processes and fluid trapping in geological porous media. The research focuses on the development of an experimental platform that integrates microfluidics and µRaman spectroscopy to track CO_2-water interfacial mass transfer in real time. Microfluidic devices are transparent pore networks made of channels of rectangular cross-sections, mimicking subsurface porous environments and allowing direct visualization of fluid behaviors. Crucially, the study introduces in situ atmospheric pressure plasma treatment as a new tool for modifying wettability within closed glass microfluidic devices. This allows precise control over surface characteristics, enabling systematic investigation of wettability impacts on interfacial dynamics. The insights of wettability influenced interfacial mass transfer gained in this study are expected to improve the calibration of both pore- and field-scale models, increasing the accuracy of predictions for carbon storage in geological reservoirs.

Three core research questions structure the investigation. First, the feasibility of propagating atmospheric plasma within closed microfluidic channels is explored to determine whether in situ wettability tuning is technically viable. The work demonstrates that plasma jets can be successfully introduced and controlled within the devices, enabling reliable alteration of surface wettability. Results obtained by in situ contact angle measurement on images indicate uniform wettability treatment with increased hydrophilic properties after only 1 min of plasma treatment. The wettability achieved on glass with our setup offers stability for up to 70 days, depending on the plasma treatment and storage parameters. Second, the study examines how wettability conditions affect capillary trapping and interfacial mass transfer. By employing microfluidic devices with increasing geometrical complexity, the experiments reveal how surface wettability indeed influences fluid displacement/ retention, water evaporation and CO_2 dissolution under a range of flow conditions. Our results demonstrate the influence of wettability on fluid-fluid displacement and mass transfer processes. Third, the potential of µRaman spectroscopy for in situ, semi-quantitative analysis of CO_2 dissolution is assessed. Raman analyses is able to capture the temporal evolution of dissolved species, providing complementary chemical data to visual flow observations and enabling the quantification of interfacial mass transfer rates.

In summary, this research establishes an integrated atmospheric-plasma-microfluidic-µRaman experimental framework that allows for the systematic study of pore-scale interfacial mass transfer under controlled wettability conditions. By leveraging plasma technology for surface modification and spectroscopic techniques for chemical analysis on microfluidic devices, the thesis delivers new insights into the mechanisms that govern CO_2 trapping in porous media and that are critical for the design and optimization of carbon sequestration strategies.

Keywords : microfluidics, porous media, multiphase flow, CO_2 storage, plasma treatment, wettability

Institut des Sciences de la Terre d'Orléans (ISTO)

1A Rue de la Ferollerie Campus Géosciences, 45100 Orléans, France